Photophysics and Photochemistry of Conjugated Systems and Photochromic Molecules

Dissertation zur Erlangung des
Doktorgrades der Naturwissenschaften (Dr. rer. nat.)
dem Department Physik der Fakultät für Naturwissenschaften
der Universität Paderborn
vorgelegt von

Christian Wiebeler

Paderborn, den 31.03.2015

Eingereicht am: 31.03.2015

Promotionskommission

Vorsitzender:	Prof. Dr. Cedrik Meier
Erstgutachter:	Jun.-Prof. Dr. Stefan Schumacher
Zweitgutachter:	Prof. Dr. Torsten Meier
Beisitzer:	Dr. Simone Sanna

Archiv
Elektronische Dissertationen und Habilitationen der Universität Paderborn:
`http://ubdok.upb.de/`

Contents

1 Abstract/ Zusammenfassung

1.1 Abstract

Molecular materials play an important role in applications such as organic photovoltaics, organic electronics, and organic light-emitting diodes. Going one step further, all-optically switchable hybrid structures that contain photochromic molecules for functionalization can be tailored. For these applications, the photophysical and photochemical properties of molecular materials have to be understood and they are mainly influenced by the presence, shape and topology of a molecule's extended conjugated system.

In this dissertation, we investigate the photophysical and photochemical properties of a number of molecules that are of relevance for experimental applications. To this end we employ state of the art quantum chemical calculations. The first system we study in this thesis are conjugated polymers with a focus on charged molecules and charge generation. Here, we used time-dependent density functional theory to study the electronic and optical properties and to analyze the electronic transitions.[1] Graphene Quantum Dots are studied as a system where the conjugated electronic system extends into two dimensions. For this molecule we employed the nuclear-ensemble approach to simulate the absorption spectrum and demonstrate intensity borrowing.[2] Perylene derivatives are smaller two dimensional conjugated systems. We simulated the vibronic progression that is found in the absorption spectrum of some perylene derivatives by employing quantum chemical calculations based on the quantum mechanical Franck-Condon principle.[3] The diarylethene CMTE is used for the functionalization of microdisk resonators in experiment. We studied its properties employing quantum chemical calculations and the photochemical reaction that is of importance for the use as all-optical switch is investigated in detail using nonadiabatic ab initio molecular dynamics.[4] Diarylethenes can be classified into two types and both types are of interest for applications like all-optical switches. To understand the fundamental difference in the photochemical reaction for the two types of diarylethenes, we investigated prototypical molecules using nonadiabatic ab initio molecular dynamics.[5] Finally, the ultrafast photophysical process of charge separation of an oligomer based on a conjugated polymer is of high interest due to potential applications of this oligomer in organic photovoltaics.[6] We used the aforementioned type of dynamics to model this process in detail.

Most of our research is based on collaborations with experiment. So all of our results have been directly related to experimental applications. Our theoretical calculations do not only allow to understand the photophysical and photochemical properties of molecular materials that are used by these groups, but also to predict properties of new materials. Taking into account the versatility of synthetic chemistry, this opens the avenue to tailor specific molecular materials for specific applications.

1.2 Zusammenfassung

Molekulare Materialien sind von besonderer Bedeutung für technische Anwendungen, z.B. organische Photovoltaik, organische Elektronik und organische Leuchtdioden. Einen Schritt weiter geht die gezielte Herstellung von rein optisch schaltbaren Hybridstrukturen, die photochrome Moleküle zur Funktionalisierung verwenden. Für diese Anwendungen müssen die photophysikalischen und photochemischen Eigenschaften molekularer Materialien verstanden werden. Sie werden hauptsächlich durch Gegenwart, Form und Topologie des konjugierten Systems der Moleküle beeinflusst.

In dieser Dissertation untersuchen wir die photophysikalischen und photochemischen Eigenschaften einer Vielzahl von Molekülen, die für experimentelle Anwendungen von Interesse sind. Für diesen Zweck verwenden wir modernste quantenchemische Rechnungen. Das erste System, das wir in dieser Arbeit anschauen, sind konjugierte Polymere mit einem Fokus auf geladenen Molekülen und Ladungserzeugung. Dafür verwendeten wir zeitabhängige Dichtefunktionaltheorie, um die elektronischen und optischen Eigenschaften zu untersuchen und elektronische Übergänge zu analysieren.[1] Graphenquantenpunkte werden als ein System untersucht, in dem sich das konjugierte System in zwei Dimensionen ausdehnt. Für dieses Molekül benutzten wir den nuklearen Ensemble-Ansatz, um das Absorptionsspektrum zu simulieren und das Ausleihen von Intensität nachzuweisen.[2] Derivate des Perylens sind kleinere zweidimensionale konjugierte Systeme. Wir simulierten die vibronische Progression, die sich in den Absorptionsspektren dieser Derivate findet, mithilfe quantenchemischer Rechnungen, die dem quantenmechanischen Franck-Condon-Prinzip Rechnung tragen.[3] Das Diarylethen CMTE wird für die Funktionalisierung von Resonatoren, die aus einer Mikrodisk bestehen, im Experiment verwendet. Dessen Eigenschaften untersuchten wir mit quantenchemischen Rechnungen und die photochemische Reaktion, die für die experimentelle Anwendung von Bedeutung ist, wurde im Detail mit nichtadiabatischer ab initio Molekulardynamik angeschaut.[4] Diarylethene können in zwei Arten eingeteilt werden und beide sind für Anwendungen, wie z.B. rein optische Schalter, von Interesse. Um den fundamentalen Unterschied in der photochemischen Reaktion dieser zwei Arten von Diarylethenen zu verstehen, untersuchten wir prototypische Moleküle unter Verwendung nichtadiabatischer ab initio Molekulardynamik.[5] Schließlich ist der ultraschnelle photophysikalische Prozess der Ladungstrennung in einem Oligomer, das auf einem konjugierten Polymer basiert, aufgrund möglicher Anwendungen in organischer Photovoltaik von besonderem Interesse.[6] Wir benutzten die zuvor genannte Art der Molekulardynamik, um diesen Vorgang im Detail zu modellieren.

Ein Großteil unserer Forschung basiert auf Kollaborationen mit Experiment und alle unsere Ergebnisse wurden in direktem Bezug mit experimentellen Anwendungen gesetzt. Unsere theoretischen Rechnungen erlaubt nicht nur das Verständnis der photophysikalischen und photochemischen Eigenschaften molekularer Materialien, die bereits verwendet werden, sondern auch die Vorhersage von Eigenschaften neuer Materialien. Unter Berücksichtigung der Vielseitigkeit der synthetischen Chemie eröffnet dies die Möglichkeit, gezielt molekulare Materialien für Anwendungen maßzuschneidern.

2 Abbreviations

Abbreviation	Full name
6-31+G*	6-31G* with additional diffuse functions at heavy atoms
6-31G*	Pople-style, double-ζ basis set with d-functions at heavy atoms
A	Acceptor
B3LYP	Becke, three-parameter, Lee-Yang-Parr (hybrid functional)
BHJ	Bulk heterojunction
BHJSC	Bulk heterojunction solar cell
BOA	Born-Oppenheimer approximation
BOMD	Born-Oppenheimer molecular dynamics
BPT	1-(2-methyl-3-benzothienyl)-2-(2,4dimethyl-5-phenyl-3-thienyl)-perfluorocyclopentene
BT	Benzothiadiazole
C132	Graphene quantum dot made of 132 carbon atoms
CAM	Used as synonym for CAM-B3LYP
CAM-B3LYP	Coulomb-attenuating method B3LYP (long-range corrected hybrid functional)
cc-pVDZ	Correlation-consistent polarized valence Double-ζ basis set
CF	Closed form (isomer of a diarylethene)
CI	conical intersection
CMTE	cis-1,2-dicyano-1,2-bis(2,4,5-trimethyl-3-thienyl)ethene
CPDT	Cyclopentadithiophene
CPDT-BT	Cyclopentadithiophene-benzothiadiazole
CPDT-BBT	Cyclopentadithiphene-bis-benzothiadiazole
CT	Charge transfer
D	Donor
DAE	Diarylethene
def2-SVP	Ahlrichs type split-valence basis set with polarization functions
DFT	Density functional theory
EX	Exciton absorption
FC	Franck-Condon
FCA	Franck-Condon approximation
FCHTA	Method employing FCA and HTA
FCP	Franck-Condon principle
GB	Ground state bleaching
GQD	Graphene quantum dot
HTA	Herzberg-Teller approximation
HOMO	Highest occupied molecular orbital

HONTO	Highest occupied natural transition orbital
ITO	Indium tin oxide
LD	Local diabatization (method for time propagation of quantum amplitudes)
LR-TDDFT	Linear-response time-dependent density functional theory
LUMO	Lowest unoccupied molecular orbital
LUNTO	Lowest unoccupied natural transition orbital
MO	Molecular orbital
NA-AIMD	Nonadiabatic ab initio molecular dynamics
NAC	Nonadiabatic couplings
NACME	Nonadiabatic coupling matrix elements
NACV	Nonadiabatic coupling vectors
NEA	Nuclear-ensemble approach
NTO	Natural transition orbital
OF	Open form (isomer of a diarylethene)
OPV	Organic photovoltaics
OVL	Wave function overlaps used as method for time propagation of quantum amplitudes
P1	Polaron absorption
PBE0	Hybrid functional based on the GGA-functional PBE (Perdew, Burke, Ernzerhof)
PCBM	Phenyl-C61-byturic acid methyl ester
PCPDT	Poly-cyclopentadithiophene
PCPDT-BT	Poly-cyclopentadithiophene-benzothiadiazole
PEDOT:PSS	Poly-ethylene-dioxythiophene:Poly-styrene sulfonate
PES	Potential energy surface
RI-ADC(2)	Resolution of identity algebraic diagrammatic construction to second order
RI-CC2	Resolution of identity approximate coupled cluster singles and doubles
S_0	Singlet ground state
S_n	n-th excited singlet state
SE	Stimulated emission
TDA	Tamm-Dancoff approximation (Used for TDDFT-calculations)
TDDFT	Time-dependent density functional theory
TEM	Transmission electron microscopy
TFSA	Tully's fewest switches algorithm
TSH	Trajectory surface hopping
VEA	Vertical excitation approximation

3 Introduction

> Arriving at a correct understanding of the fundamentals of science is the final aim that has always to be kept in mind. However, to make some progress in science, it is imperative to study specific problems.
>
> *(Karl Weierstraß {translated by the author from [7]})*

2015 has been declared the "International Year of Light and Light-based Technologies" by the United Nations.[8] Light-based technologies hold the promise of solving many global challenges of the 21st century and research in this field is an interdisciplinary endeavor. As an example, locally, physicists, chemists and electrical engineers are working together in the "Center for Optoelectronics and Photonics Paderborn" to advance light-based technologies.[9] On a larger scale, humans have always been interested in the interaction between light and matter and the resulting consequences.

Since the antiquity, mankind has been using dyes. As an example, it is known that indigo was already utilized in ancient egypt 4000 B.C. Furthermore, this dye has been used in china and india for millenia. Closely related to it is another natural dye, Tyrian purple that was a status symbol in ancient times and is made of 6,6'-dibromoindigo. However, dyes did not only play a crucial role in ancient and medieval times, but have also been of high importance for the beginning of the modern chemical industry, see for example the history of the chemical companies Bayer, Hoechst, and BASF (Badische Anilin- und Sodafabrik). In addition, natural dyes like chlorophyll that is related to porphine and carotene are known from everyday life, see figure 3.1. The examples given are taken from references [10] and [11], wherein further information on organic dyes can be found.

As can be seen from the molecular structures of the organic dyes, they consist of sp^2 hybridized carbon atoms forming a **conjugated system**. The π electrons of this system are delocalized giving rise to absorption of light in the visible region of the electromagnetic spectrum. So the origin of color for these compounds can be traced back to the existence, shape and topology of their conjugated systems. In order to understand the interaction of light with molecular materials, the photophysics and photochemistry of these materials have to be understood.

To explain this process, potential energy surfaces (PESs) of ground and electronic excited states are often sketched and discussed, see figure 3.2. These surfaces can be for-

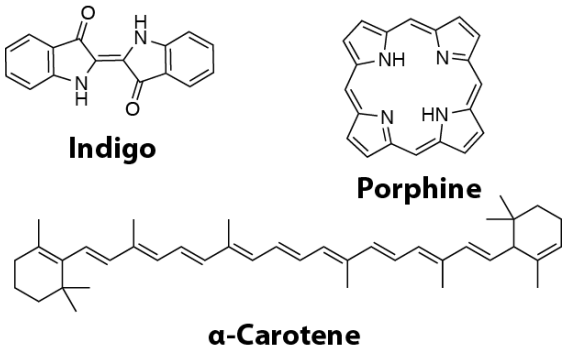

Figure 3.1: Illustration of some important organic dyes. Indigo is the blue of blue jeans. Porphine is an aromatic, heterocyclic compound. It is closely related to hemoglobin and chlorophyll. The former is responsible for the color of blood and the latter for the green color of plants. α-carotene belongs to the family of carotenes that are for example causing the color of carrots. All compounds posses an extended conjugated system of delocalized π-electrons.

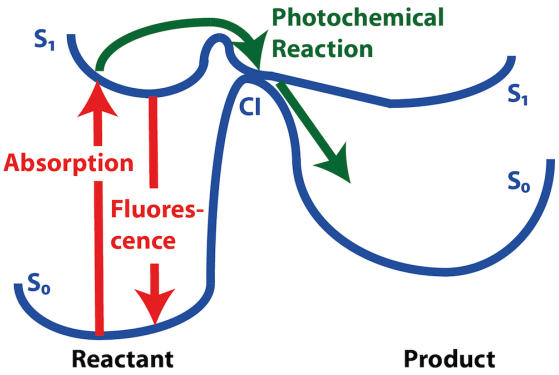

Figure 3.2: Schematic representation to explain the photophysical processes of absorption and fluorescence (red). Furthermore, a photochemical reaction is indicated in green. Shown are the ground and first excited singlet states (S_0 and S_1, respectively). Absorption starts in the minimum of S_0 and the molecule is vertically excited to S_1. Fluorescence begins in the minimum of the excited states and the molecule transfers back to S_0 via emission of a photon. The initial situation for the depicted photochemical reaction is the excited molecule. This molecule passes a potential barrier in the first excited state and reaches a conical intersection (CI), i.e. a region of the PESs, where two electronic states become degenerate. The molecule can then transfer back to S_0 without emission of a photon. Finally, two outcomes of this process are possible: In the unreactive case, the molecule relaxes back to the initial S_0 structure, i.e. ultrafast deactivation, and in the reactive case the molecule reaches a different minimum of S_0, i.e. photochemical reaction.

mally derived by starting from the time-dependent Hamiltonian of the molecular system, employing a Born-Oppenheimer expansion of the molecular wave function and using the Born-Oppenheimer Approximation (BOA).[12] This allows in principle the calculation of the potential energies in dependence of the molecular structure or some reactive coordinate and is the basis of electronic structure calculations in quantum chemistry.[13]

Following reference [14], **photophysical processes** are processes that do not involve chemical reactions. Therefore, the molecular structure does not change much during such processes and in general the displacements of the nuclei are relatively small. Due to this, the description of photophysical phenomena is relatively straightforward and not as involved as for photochemical ones. Two fundamental photophysical processes are absorption and fluorescence that are sketched in figure 3.2.

In order to describe absorption, it is assumed that the molecule is in its ground electronic and vibrational state. Then, the absorption can be estimated based on different levels of approximations, i.e. classical, semiclassical and quantum mechanical interpretation of the Franck-Condon principle (FCP).[15,16] For the classical approximation, the molecular structure is optimized and the vertical excitation energies are calculated subsequently. This type of calculation is widely used and will be denoted as vertical excitation approximation (VEA). In order to employ the semiclassical approximation, the zero-point vibrational motion of the molecule is taken into account giving rise to the nuclear-ensemble approach (NEA). Finally, for the quantum mechanical treatment also the overlap of the vibrational wave functions has to be considered. This method is named Franck-Condon Approach (FCA). Fluorescence occurs after relaxation of the excited molecule to the minimum of the S_1 PES according to Kasha's rule.[17] It can be treated analogously to the case of absorption discussed before, but the corresponding molecular structure of S_1 has to be used. VEA and NEA are discussed in more detail in chapter 5 and information regarding the FCA can be found in chapter 6.

During **photochemical processes**, the molecule reaches a new minimum on the S_0 PES and a new chemical species is formed.[14] Photochemical reactions normally involve large displacements of the nuclei. Furthermore, the BOA often breaks down due to the fact that electronic states may come close to each other during such reactions. Therefore, approaches going beyond the BOA are needed and an example is trajectory surface hopping (TSH) that is discussed in more detail in chapter 9 and can be used for nonadiabatic ab initio molecular dynamics (NA-AIMD). TSH is not only used for the investigation of ultrafast photochemical processes, but also ultrafast photophysical processes like radiationless relaxation can be studied.[18]

The considerations presented so far concerning molecular photophysics and photochemistry are general in nature. However, 2015 is not only the "International Year of Light", but also the "Paderborner Weierstraß-Jahr".[19] Karl Weierstraß was born 1815, graduated 1834 from the Gymnasium Theodorianum Paderborn, and according to reference [20], he is the founder of modern analysis. Regarding his quote given at the beginning of this chapter, the photophysical and photochemical concepts described so far dealt with a correct understanding of the fundamentals of science. However, to make real progress in science, these concepts have to be applied to some specific problems. In our case the specific problems are properties of molecules that have been determined in

experiment and that are modeled theoretically based on the described concepts. Such an approach does not only allow the assessment of the accuracy of the employed models, but also makes it possible to interpret and understand experimental observations and going one step further, even to predict properties of similar molecules. The remainder of this thesis is organized as follows:

In **chapter 4** the electronic and optical properties of conjugated polymers that consist of a one dimensional conjugated system are modeled. It starts with the introduction of fundamental approaches to characterize electronic transitions and explains an approach to determine the properties of conjugated polymers based on oligomers. These methods are used in the included paper to discuss the photophysical properties of a specific copolymer based on VEA. In the end, a promising potential application for these materials is explained in more detail

Chapter 5 deals with the simulation of the absorption spectrum of the Graphene Quantum Dot (GQD) C132 that is made of an extended two dimensional conjugated system. For this purpose, classical and semiclassical FCP are explained. In the included paper, VEA and NEA are used to model the photophysical properties of the molecule and some further investigations based on these calculations are presented at the end.

The perylene derivatives that are studied in **chapter 6** have a smaller conjugated system than the GQD C132. The reduced size allows the application of the quantum-mechanical approach for this molecule. After the corresponding concept has been introduced in more detail, photophysical properties obtained from VEA and FCA are discussed in the included paper. Finally, a more thorough analysis of the latter approach is done to demonstrate its capabilities and compare the results with NEA.

A specific photochromic diarylethene (DAE), cis-1,2-dicyano-1,2-bis(2,4,5-trimethyl-3-thienyl)ethene (CMTE), is investigated in **chapter 7**. DAEs consist of a conjugated system that can be switched between two different forms. After a summary of the main findings regarding the photophysics and photochemistry of DAEs discussed in the master's thesis,[21] further photophysical and photochemical properties of CMTE are presented in the included paper. Apart from properties that are of special relevance for the experimental application, also the perceived color is estimated from the calculated absorption spectra. In the end, some validations of the method used for the modeling of the photochemical reaction of CMTE and further calculations are discussed.

Chapter 8 is dedicated to the photochemical reaction involved in the photoisomerization of photochromic DAEs that leads to the switching between the two conjugated systems. The reaction is classified in the beginning, the different dynamics of the photochemical reaction for two prototypical DAEs are analyzed in the included paper and at the end of the chapter the reaction dynamics for further DAEs are presented.

However not only the dynamics of a photochemical process are investigated in this work, but also first results concerning the dynamics of the photophysical process of ultrafast relaxation after excitation leading to charge separation are shown. Therefore, **chapter 9** starts with a derivation and discussion of the method that is used for the investigation of ultrafast dynamics. Then the included paper is used as a motivation for the studies presented at the end of the chapter regarding ultrafast charge seperation.

Due to the fact that this PhD-thesis is not a traditional German dissertation, but a cumulative one, some remarks are in order:

- The presentation focuses on the photophysics and photochemistry of the corresponding molecules. Therefore, no introduction to electronic structure theory, density functional theory (DFT), and time-dependent density functional theory (TDDFT) is given. Information regarding these topics can be found in the master's thesis.[21] Complementary to this, there are some review articles regarding the accuracy of DFT-based calculations for organic molecules.[22–24]
- Each of the following six chapters is written around an article that has been published in a peer-reviewed journal.
- The original article is always fully included, but only the parts of the supporting information are reproduced that are of special relevance for this thesis.
- Some introductory ideas, concepts, and theoretical models are presented in the beginning of each chapter giving some background information.
- After the article, further discussions are found in each chapter to give additional information about some topics that have been described before.
- Only the literature needed in the texts written around the article is included in the bibliography. In general, further references can be found in the included articles.
- If not otherwise noted, the molecular structures were visualized using Gaussview.[25]
- A documentation of the advanced quantum chemical methods used to obtain the results presented in this work can be found in chapter 10

4 Conjugated Polymers as One Dimensional Extended Conjugated Systems

> [...] conducting polymers offered the promise of achieving a new generation of polymers: Materials which exhibit the electrical and optical properties of metals and semiconductors and which retain the attractive mechanical properties and processing advantages of polymers.
>
> *(Alan J. Heeger[26])*

The synthesis of long conjugated systems can be achieved by linking small molecules with conjugated systems to one another giving rise to conjugated polymers. Such a polymer consists of a conjugated system that is delocalized over the whole molecular chain exhibiting electronic properties similar to metals and semiconductors.[27] These polymers are also termed conducting or semiconducting polymers. The combination of the special electronic properties with processing advantages and mechanical properties of "conventional" polymers makes conjugated polymers promising candidates for numerous applications. Potential applications can be found in the field of polymer electronics, for example organic semiconductor lasers, organic photonics for communications, and also the use of organic electronics in biological systems.[28–31] This chapter is dedicated to the investigation of photophysical properties of polymers. Natural transition orbitals (NTOs) as a means for the investigation and characterization of electronic transitions are explained. Then quantum chemical calculations are used to analyze the properties of the building blocks and oligomers that are derived from conjugated polymers. Based on these results, the oligomer-approach is introduced and the electronic and optical properties of a specific conjugated polymer are discussed in the article that is included in this chapter.[1] At the end of the chapter, the use of conjugated polymers in organic photovoltaics (OPV) will be explained in more detail.

4.1 Characterization of Excited Electronic States

Fundamental for understanding the photophysics and photochemistry of conjugated systems is the characterization of the involved electronic transitions. First information, i.e. energy levels and oscillator strengths of electronic transitions, are readily obtained

by quantum chemical calculations, e.g. TDDFT, and can be used to construct level schemes. Furthermore, the transitions can be understood in more detail by investigating appropriate orbitals. The orbitals can either be molecular orbitals (MOs) or NTOs.

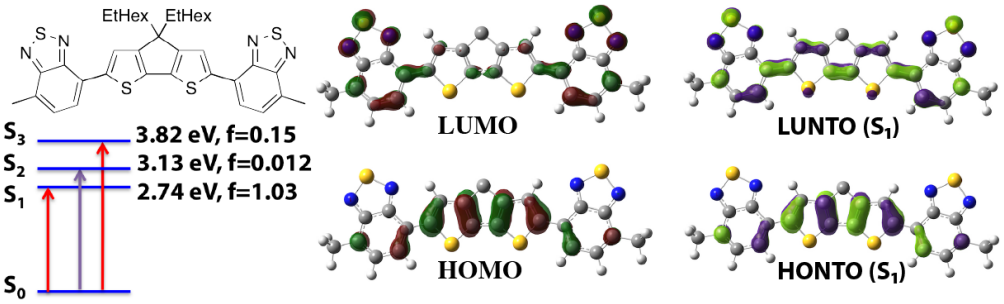

Figure 4.1: On the left, molecular structure of CPDT-BBT (upper part) and level scheme of the singlet ground state S_0 and the first three excited singlet states (S_1, S_2 and S_3) with energies relative to S_0 and oscillator strength of the electronic transitions (lower part); In the middle, visualization of the HOMO and LUMO; On the right, visualization of the highest occupied natural transition orbital (HONTO) and lowest unoccupied natural transition orbital (LUNTO) for the first electronic transition. Note that HOMO and HONTO look very similar, whereas LUMO and LUNTO mainly differ in the central part of the molecule. Based on the LUMO, one might infer that the hole is localized on some parts of the molecule, but it is delocalized along the whole molecule due to contributions from higher-lying LUMOs. Note that the color coding of the orbitals will be maintained throughout the text, therefore allowing the differentiation between MOs and NTOs based on the colors used. CAM-B3LYP/6-31G* was employed for the quantum chemical calculations. More information on CPDT-BBT are given in chapter 9.

The lowest-lying electronic transition in a conjugated system is in general an excitation from a bonding π orbital to an antibonding π orbital and is therefore denoted as a π-π^* transition. It is normally dominated by an excitation from the highest occupied molecular orbital (HOMO) to the lowest unoccupied molecular orbital (LUMO). In order to characterize such a transition, it is therefore sufficient to visualize the two corresponding MOs that are for example obtained by time-independent electronic structure calculations based on DFT. However, for higher-lying excited states or for some molecules, there will be transitions that are not dominated by one pair of MOs that is involved in the electronic transition and therefore more advanced methods have to be used.

One such method is based on NTOs. The central idea of NTOs is that separate unitary transformations are applied to the occupied and virtual orbitals and that the transition density as physically-relevant quantity remains the same.[32] In the best case, the electronic transition can be understood with one pair of occupied and virtual orbitals corresponding to hole and electron wave function, respectively. However, due to correlation, this might not be the case and more pairs of occupied and virtual orbitals

have to be considered. In addition, if an electronic transition is already well described by a pair of MOs, the NTOs will be similar to them and therefore yield the same result. For comparisons between these two types of orbitals, see the corresponding discussions in references [1] and [33]. In the latter, the difference of the electron density between an excited state and S_0 is analyzed and compared with NTOs as well. To sum things up, NTOs can always be used for the characterization of electronic transitions and might lead to an electron-hole picture. So they are mainly used for this purpose in the following discussions.

4.2 The Building Blocks of a Conjugated Polymer

There are two kinds of polymers: homopolymers and copolymers. The former consists of a single building block, e.g. cyclopentadithiophene (CPDT, see figure 4.2), that is used as monomer. Therefore, the complete polymer consists of a chain of CPDT and the corresponding homopolymer is named poly-cyclopendadithiophene (PCPDT). Copolymers consist of two building blocks that are used as monomer. In addition to CPDT, benzothiadiazole (BT, see figure 4.2) can be used to form the monomer cyclopentadithiophene-benzothiadiazole (CPDT-BT) and the polymer is an alternating chain of CPDT and BT. Therefore, it is named poly-cyclopentadithiophene-benzothiadiazole (PCPDT-BT). Note that CPDT and BT have a conjugated system and in the homo- and copolymer this system extends over the whole polymer chain resulting in semiconducting and metallic properties of the polymer. In this chapter, CPDT and BT will be discussed in more detail, due to the fact that they are the fundamental building blocks and determine the properties of the monomer.

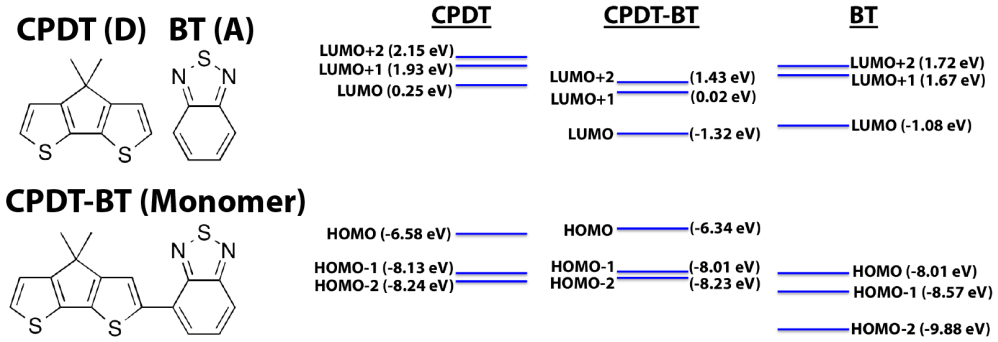

Figure 4.2: Left part of the figure, molecular structures of CPDT and BT (upper part) and of the copolymer made of CPDT and BT (lower part). The level scheme of the energies of the MOs of CPDT, CPDT-BT and BT is shown on the right for the first three HOMOs and LUMOs calculated with CAM-B3LYP/6-31G*. The HOMO energy of CPDT-BT is similar to the HOMO energy of the CPDT HOMO and the LUMO energy of the copolymer is close to the LUMO energy of BT. So it can be expected that the frontier orbitals of CPDT-BT are dominated by the corresponding orbital of CPDT and BT, respectively.

The energy levels of the MOs belonging to CPDT and BT are shown on the right of figure 4.2. Note that absolute values for MO energies have to be treated with care, but only the relative ordering and positions are relevant for this discussion and are more reliably determined. As can be seen there, the HOMO energy of CPDT is higher than the corresponding energy of BT. Therefore, the ionization potential is lower for the former. Furthermore, the LUMO energy of BT is lower than the corresponding energy of CPDT. Due to this, the electron affinity of BT is higher than the one of CPDT. This leads to the notion that the lowest energy excitation transfers an electron from the HOMO of the CPDT unit to the LUMO of the BT unit. In this case, CPDT acts as an electron donor (D) and BT is the electron acceptor (A).

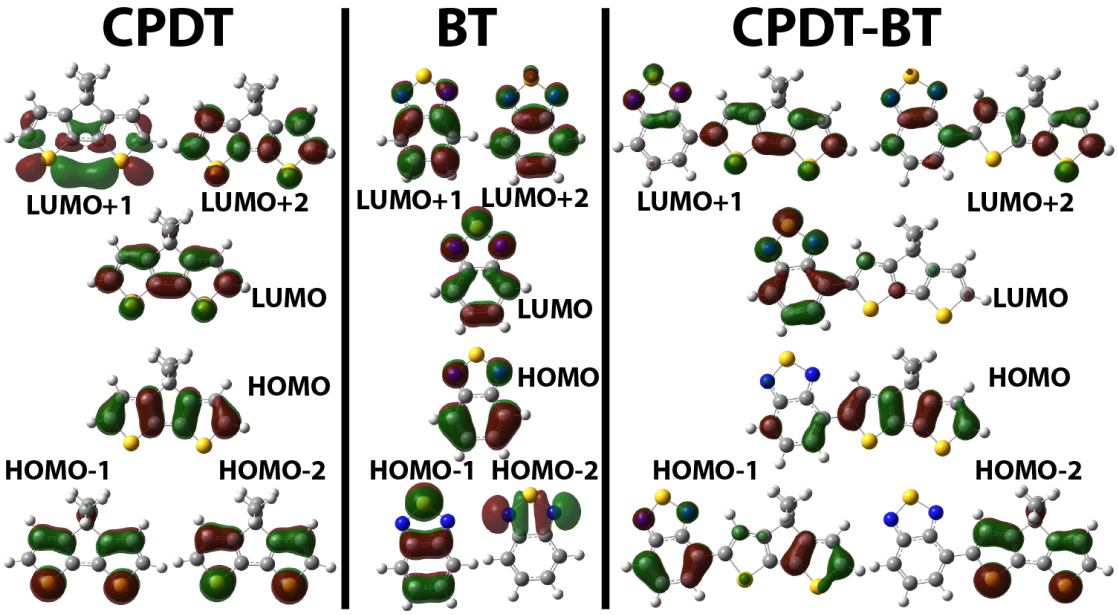

Figure 4.3: Visualization of the first three HOMOs and LUMOs of CPDT (left), BT (middle), and CPDT-BT (right) obtained with CAM-B3LYP/6-31G*. The LUMO of CPDT-BT is dominated by the LUMO of BT and the HOMO of the monomer is dominated by the HOMO of CPDT. Similar findings are obtained for the other shown MOs of CPDT-BT: The left part of HOMO-1 of CPDT-BT is similar to the HOMO of BT and HOMO-2 looks like HOMO-1 of CPDT. The right part of LUMO+1 of CPDT-BT resembles the LUMO of CPDT and the left part of LUMO+2 is akin to LUMO+2 of BT.

To further analyze this, the MOs of the building blocks and of the monomer can be visualized. After CPDT and BT are covalently linked, new MOs arise for CPDT-BT and therefore the energy levels and shapes of the MOs change, see right part of figure 4.2 and figure 4.3. Comparing the frontier orbitals, it is evident that the LUMO of CPDT-BT is dominated by the LUMO of BT and that the HOMO of CPDT-BT is dominated by the HOMO of CPDT. For the latter, however, the MO extends to the lower part of BT. Similar correspondences can be found for all the frontier orbitals of CPDT-BT that are

shown in figure 4.3.

Having discussed the electronic properties of CPDT-BT, the next step is the investigation of the optical properties. In order to understand the nature of excitations in CPDT-BT, the absorption spectrum and orbitals involved in the electronic transitions of this compound are compared with the corresponding properties of the building blocks.

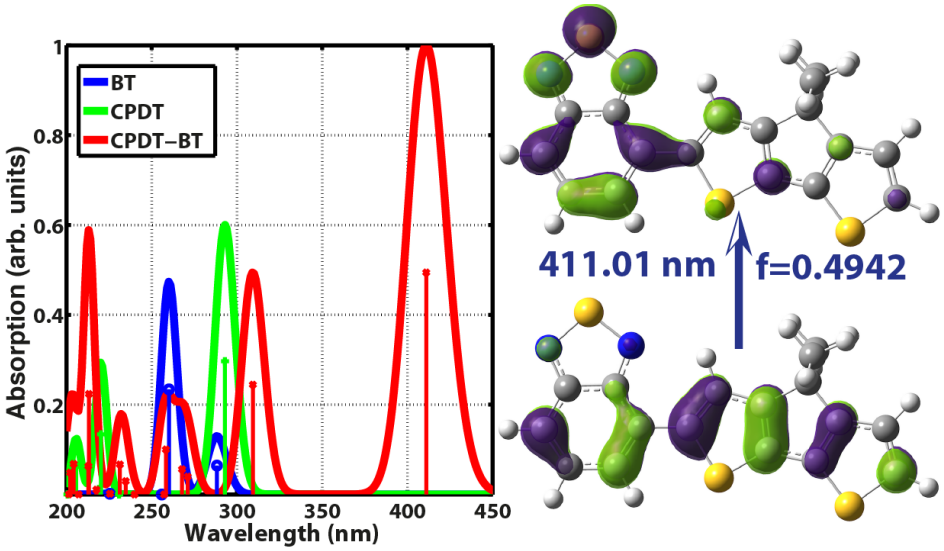

Figure 4.4: On the left, the absorption spectra of BT (blue), CPDT (green), and CPDT-BT (red) normalized to the absorption maximum of CPDT-BT and the corresponding stick spectra are shown. On the right, the NTOs for the first excitation together with the excitation energy and oscillator strength are shown. The calculations were done using CAM-B3LYP/6-31G*. The absorption spectrum of CPDT-BT is not only the sum of the absorption spectra of its constituents, but shape and position of it change due to the extension of the conjugated system. The absorption in the visible is determined by the lowest-energy excitation and the corresponding NTOs show the orbitals involved in the electronic transition.

Neither BT nor CPDT absorb light in the visible range. So only due to the extended conjugated system in PCPDT-BT, absorption in the visible is possible, see left part of figure 4.4. Furthermore, the change in the conjugated system has a strong influence on the position and shape of the whole spectrum. This makes it mandatory to analyze each electronic transition using NTOs, in order to unravel the shape of the orbitals that are involved in a certain electronic transition.

A prominent feature of the absorption spectrum of CPDT-BT is the strong absorption of the first electronic transition. Furthermore, this low-energy absorption makes PCPDT-BT a promising candidate for applications in OPV. This justifies a closer investigation of the orbitals involved in this electronic transition. There are two pairs of MOs mainly contributing to the excitation: HOMO to LUMO with a weight of 92.7 % and HOMO-1 to LUMO with a weight of 3.7 %. To get a clearer picture, the NTOs of

this transition have been determined, see right part of figure 4.4. The contribution of the shown pair is 97.7 %. The HONTO has a similar shape as the HOMO. The LUNTO is not only centered at the BT unit, but extends also to the CPDT unit. So it mainly shows the structure of the LUMO with some contributions from LUMO+1.

The presented results for the analysis of the monomer, i.e. CPDT-BT, and its building blocks, i.e. CPDT and BT, are similar to the discussion found in reference [34], where a monomer made of different building blocks is analyzed. Note that in the reference the building block that is used as A is not only made of BT but of dithiophene-benzothiadiazole and therefore it is already a D-A-D component. Due to this, more direct comparisons are hampered.

4.3 Oligomer Approach

Having broken down the monomer to its constituents and analyzed them, the next step is investigating the change of some properties for oligomers made of an increasing number of monomers. The monomers are arranged in a regular fashion following reference [35]. The change of the energies of HOMO and LUMO with increasing chain length is of special interest, because the gap between the both determines the electronic properties, i.e. it is connected to the change from insulating to semiconducting or metallic properties. Furthermore, the absorption in the visible range is of interest for potential applications and therefore not only the change in the vertical excitation energy, but also the change of the absorption spectrum in this spectral region will be traced.

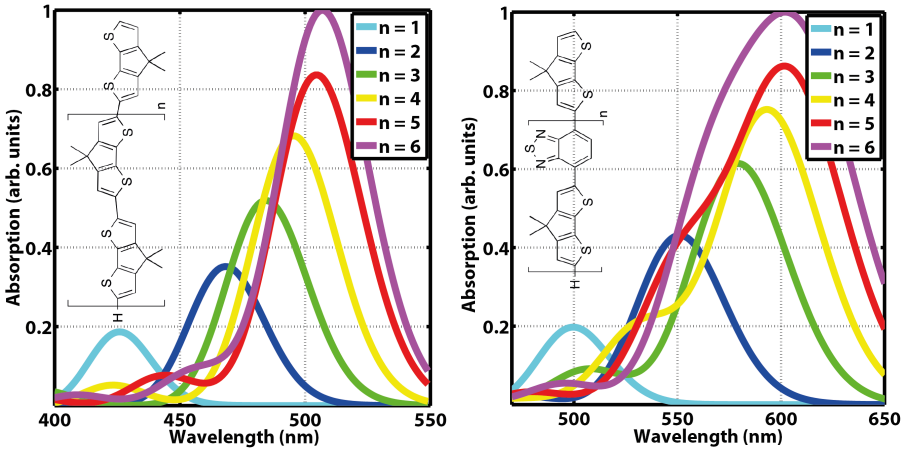

Figure 4.5: Absorption spectra of oligomers made of CPDT (left) and CPDT-BT (right) as monomers. The molecular structures used for the calculations are shown as insets. Color coded is the number of repeating units and each spectrum is normalized to the maximum absorption of the longest oligomer of the series. The calculations were done using CAM-B3LYP/6-31G*. Increasing chain length leads to a red-shift of the first electronic excitation and the absorption of a single oligomer also increases.

The absorption spectra shown for homo- and copolymer in figure 4.5 exhibit similar trends: Increasing chain length leads to red-shifts of the absorption peak, the red-shifts are saturated for oligomers made of 5 or more repeating units, and the absorption strength increases approximately linearly with chain length. Note that there is a deviation from the latter trend for longer PCPDT-BT oligomers. Furthermore, these oligomers have also a second peak in the visible region with non-negligible oscillator strength. Both these findings are caused by the u-shape of the oligomer and disappear if the oligomer is arranged in a different fashion, e.g. as it was done in reference [1], yielding an approximately linear shape. The energy of both conformations is similar and the barrier for rotations around the dihedral angles between donor and acceptor units is small, so that in thermal equilibrium there will be a mixture of different conformations.

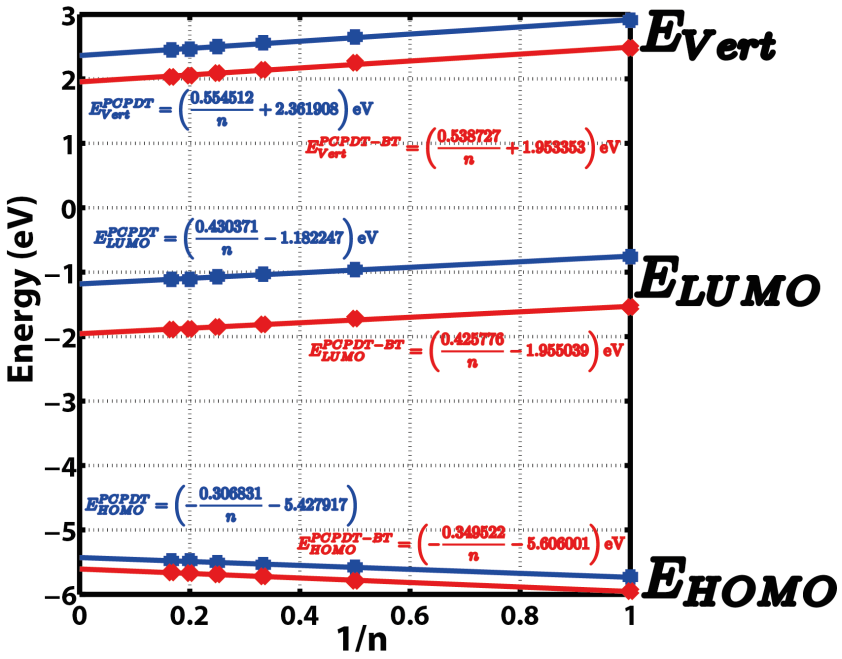

Figure 4.6: Energies of HOMO, LUMO, and vertical excitation for PCPDT (blue) and PCPDT-BT (red) plotted against the inverse of the number of repeating units. In addition to the data points, linear fits based on the equations included as insets are shown as lines. The values are obtained from CAM-B3LYP/6-31G* calculations. The linear correlations found between the energies and the inverse number of repeating units allow to estimate the values for infinite chain length as the intersection with the energy axis.

Following the procedure described in reference [36], the energies of the frontier orbitals and of the vertical excitation can be extrapolated to infinite chain length. To achieve this, the aforementioned energies are plotted against the inverse number of repeating units yielding linear correlations. Then, the corresponding energy can be found as the intersection of the linear fit with the energy axis, see figure 4.6. So to estimate the electronic and optical properties of a polymer used in experiment, quantum chemical

calculations for oligomers with sufficiently long chains can be done. This method is called oligomer approach and was used for the quantum chemical calculations that are found in the article that is included in the next section.[1] Furthermore, using oligomers instead of conjugated polymers is also an alternative for applications.[6,37,38] This is discussed in section 4.5 and in chapter 9.

4.4 "Spectral Signatures of Polarons in Conjugated Co-polymers"

This article has been published in "The Journal of Physical Chemistry B" and investigates the spectral signatures of polarons in PCPDT-BT. For this purpose, quantum chemical calculations of neutral and charged oligomers based on the oligomer approach were done and experimental measurements are also included in the article. we can trace back the differences in the absorption spectra of positively and negatively charged ions to the different nature of the involved MOs and NTOs. The findings can be generalized to other co-polymers. Finally, in section 4.5, OPV will be explained in more detail motivated by the fact, that bulk heterojunction solar cells (BHJSC) consisting of PCPDT-BT as donor material can reach high conversion efficiencies and materials based on this copolymer are promising for this application.

THE JOURNAL OF PHYSICAL CHEMISTRY B

Article

pubs.acs.org/JPCB

Spectral Signatures of Polarons in Conjugated Co-polymers

Christian Wiebeler,[†] Raphael Tautz,[‡] Jochen Feldmann,[‡] Elizabeth von Hauff,[§,∥] Enrico Da Como,[‡,⊥] and Stefan Schumacher*[,†,#]

[†]Physics Department and Center for Optoelectronics and Photonics Paderborn (CeOPP), Universität Paderborn, Warburger Strasse 100, 33098 Paderborn, Germany

[‡]Photonics and Optoelectronics Group, Department of Physics and CeNS, Ludwig-Maximilians-Universität München, Munich, Germany

[§]Fraunhofer Institute for Solar Energy Systems (ISE), 79110 Freiburg, Germany

[∥]Physikalisches Institut, Albert-Ludwigs-Universität Freiburg, 79104 Freiburg, Germany

[⊥]Department of Physics, University of Bath, Claverton Down, Bath, BA2 7AY, U.K.

[#]College of Optical Sciences, University of Arizona, Tucson, Arizona 85721, United States

Supporting Information

ABSTRACT: We study electronic and optical properties of the low-bandgap co-polymer PCPDT-BT (poly-cyclopentadithiophene-*co*-benzothiadiazole) and compare it with the corresponding homo-polymer PCPDT (poly-cyclopentadithiophene). We investigate the linear absorptivity in these systems for neutral molecules and for their singly charged ions based on quantum-chemical calculations and experiments. One of our main findings is that the ions of the homo-polymer show a polaron absorption that is symmetric between anion and cation, whereas for polaron excitations in the co-polymer this symmetry is strongly lifted. We demonstrate that this asymmetry can be attributed to the absence of symmetry between the high-lying occupied and low-lying unoccupied molecular orbitals in the co-polymer with type-II orbital alignment between the moieties constituting the chain. This notion is of importance for the qualitative and quantitative interpretation of spectroscopic polaron data and is not specific to the system studied here but similarly applies to other co-polymers.

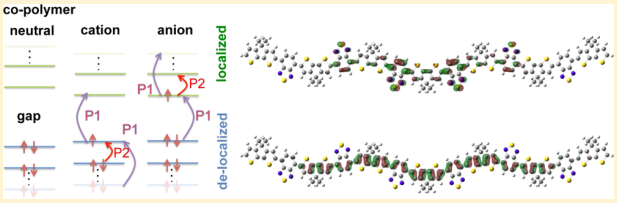

I. INTRODUCTION

Semiconducting conjugated polymers are an emerging class of materials that bear great promise for various applications in optoelectronics,[1] photonics,[2] and photovoltaics.[3] These molecular materials combine semiconductivity and desirable optical properties with attractive properties known from plastics such as mechanical flexibility, nontoxicity, affordability, and easiness to process. Through design of their molecular constituents, electronic and optical properties of these materials offer unprecedented flexibility. With more and more potential applications emerging, an increasing demand for the next generation of conjugated polymers has recently developed.

One promising route currently pursued in this field is the use of so-called co-polymers.[4,5] In these materials, different molecular segments with desirable electronic properties are systematically combined into a single polymer with new properties.[6] This way, novel low-band gap co-polymers have been designed, which are currently widely used and studied.[7] Due to their specific chemical and electronic structure, they exhibit favorable behavior for charge separation in photovoltaics[8]—one of the big technological challenges in this area. This can be further enhanced by appropriate molecular doping.[9,10] In nonlinear photonics, co-polymers can serve as well-controlled guest−host systems in which exciton−exciton annihilation as one of the major loss mechanisms is reduced.[11]

In the recent past, a large amount of research was dedicated to understanding the photophysics of these co-polymers.[12−16] In many cases, in addition to the molecular species, also their ionic counterparts play an important role. In photovoltaics, molecules carrying a net charge inevitably emerge as a desired product after successful charge separation. In optoelectronics, they contribute directly through electrical pumping or indirectly as an unwanted byproduct at elevated excitation densities. Charge carriers in semiconducting polymers—known as polarons—and their photophysical properties have previously been investigated in homo-polymers.[17−19] However, relatively little is known about the properties of charged species of co-polymers.[20] One way to obtain information about polaron properties is through spectroscopic studies.[21,22] The interpretation of spectroscopic polaron data is typically based on the assumption that the anion and cation show the same optical properties.[23] However, upon closer inspection, this is expected

Special Issue: Paul F. Barbara Memorial Issue

Received: August 27, 2012
Revised: November 12, 2012
Published: November 30, 2012

to be true only in systems with a sufficient degree of symmetry between high-lying occupied and low-lying unoccupied molecular orbitals.

Here we shed light on this aspect and present a combined theoretical and experimental study of polaron spectra in co-polymers with a type-II orbital alignment (PCPDT-BT and PCPDT-2T-BT co-polymers, in which the alignment between different moieties leads to high-lying occupied and low-lying unoccupied molecular orbitals that are partly localized on different sections of the chain) and compare these with the corresponding homo-polymer (PCPDT). We demonstrate that the missing symmetry between occupied and unoccupied orbitals in the co-polymers destroys the symmetry between anion and cation polaron wave functions and spectra. In our calculations, polaron signatures can be exclusively studied and are not overshadowed by other effects, such as the regular absorption of the neutral species, excited state absorption, triplet absorption, etc. This way we obtain detailed insight into the nature of the polaron excitations. Differences in the anion and cation absorption are traced back to differences in the respective wave functions in the excited system (electron and hole wave function). In addition to detailed quantum-chemical calculations, we also develop a simple physical picture explaining our observations qualitatively.

Our study highlights a fundamental difference between polaron absorption of homo- and co-polymers not previously studied. Our conclusions are expected to play an important role for the interpretation of spectroscopic polaron signatures in co-polymers in the future and are not specific to the system investigated but have general applicability to other co-polymer systems with a type-II orbital alignment.

II. THEORETICAL METHODS

All calculations are based on density-functional theory (DFT) and linear response time-dependent DFT (TD-DFT). The Gaussian 09 program suite[24] was used, and all results presented were obtained with the Coulomb-attenuating method Becke three-parameter Lee−Yang−Parr hybrid functional (CAM-B3LYP) and 6-31G* basis set. Orbitals were visualized using GaussView 5.[25] In the donor−acceptor co-polymers studied, significant charge separation is expected to occur in the ground state and also electronic transitions show pronounced charge-transfer (CT) character. The long-range character in the electronic exchange interaction required to describe these phenomena can be captured using the long-range corrected CAM-B3LYP functional.[14,19] For the charged species, all calculations were performed unrestricted. As successfully used in previous studies, calculations were done for long but finite-length oligomers to mimic properties of the corresponding polymers. To reduce the computational cost, alkyl side chains that are largely uninvolved in optical excitations were replaced by methyl groups. Furthermore, the spectra of smaller oligomers with and without symmetry constraints were compared and only small quantitative changes were observed. The dependence of the spectra on the length of the oligomers was studied, and no qualitative change is expected for longer chains than used in the present study. The total length of the different oligomers compared in this study is similar. The results for the longer PCPDT and PCPDT-BT oligomers reported in the present work were obtained using C_{2V} symmetry, and C_1 symmetry for PCPDT-2T-BT. Even without symmetry constraints in the calculations, we have observed only small changes in the overall molecular structures when charges were removed from or added to the PCPDT and PCPDT-BT oligomers. For PCPDT-2T-BT, we have found a relaxation toward a slightly more planar structure, similarly for anion and cation. For each of the molecular species studied (including their ions), we have first optimized the molecular geometry in the electronic ground state (coordinates of each of the equilibrium geometries of the neutral and charged molecules are provided in the Supporting Information) and then calculated the lowest 20 electronic transitions. A homogeneous broadening of 100 meV was applied to all electronic spectra shown (this leads to a wavelength-dependent broadening in the spectra shown). We find good agreement of our CAM-B3LYP/6-31G* DFT based calculations for the charged molecules with the experimental data justifying the choice of the method. We do not include counterions (see the Experimental Methods section below) in our calculations following ref 19, where no significant change of polaron spectra in fluorene oligomers was found when counterions were explicitly included. To obtain a qualitative picture of electronic excitations in the systems studied, we inspect the different molecular-orbital contributions to each transition. Visualizations of the molecular orbitals are included in the Supporting Information. The main tool we use to analyze the character of electronic transitions also quantitatively is the introduction of natural transition orbitals (NTOs). The NTOs cast each electronic transition into a minimum number of pairs of effective single-particle orbitals. Ideally, a reduction to only one relevant pair of NTOs can be achieved for each transition; however, if correlations play a significant role, a larger number of NTOs remains to be analyzed.

III. EXPERIMENTAL METHODS

For the chemical ionization measurements, the materials were solved in 1,2-dichlorobenzene (Sigma-Aldrich) with a concentration of 15 μg/mL. Only for measuring the neutral absorption spectrum of PCPDT, toluene (Sigma-Aldrich) was used, because interaction with pure 1,2-dichlorobenzene led to a small fraction of ionized polymer chains already. Absorption measurements of these solutions filled in fused silica cells (Spectrocell) with a light pass of 10 mm were done with an absorption spectrometer (Cary 5000, Varian) covering the spectral range from 175 to 3300 nm. Infrared absorption of the solvent above 3000 nm, below 290 nm, and from 2560 to 2860 nm limited the measurement to the spectral range shown. After measuring the absorptivity of neat (co-)polymer solutions, small amounts of a dilute $SbCl_5$ solution (90 μg/mL in 1,2-dichlorobenzene) in 1% wt steps (weight percent of dopant relative to polymer weight) were added. $SbCl_5$ is known to be a strong oxidizing agent and to generate a hole (positively charged) polaron in the ground state of most conjugated polymers.[27,28] Up to a doping ratio of 5%, the observed growth of ground state bleaching and polaronic signal due to the ions has been linear and started to saturate at ratios above 5%. Subtraction of normalized ground state absorption measured in undoped solutions led to the chemically induced differential absorption spectra of the investigated materials, as shown in Figure 4 in the main manuscript. Due to the high reactivity of $SbCl_5$ with air and moisture, all preparation steps were done in a nitrogen atmosphere. The use of airtight cells prevented any kind of degradation during the spectroscopic measurements.

We have tried two different techniques to measure the absorption spectra of anions (electron polarons), both of which were not successful for the materials studied here. Chemical

dx.doi.org/10.1021/jp3084869 | J. Phys. Chem. B 2013, 117, 4454−4460

doping with a NaK alloy, as it has been successfully applied to oligofluorenes recently,[19] did not result in anionic absorption bands as expected. The observation of a pronounced ground state bleaching upon doping without formation of absorption bands below the optical bandgap points toward a sensitivity and instability of the polymer chains to chemical reduction. As an alternative approach, charge modulation spectroscopy has been tried. However, no anionic spectral features but only pronounced electro-absorption could be observed in the materials studied in the present work, indicating charge injection problems between the Ca electrode and the LUMO levels of the polymers. The electro-absorption method was successfully applied to a co-polymer with a significantly lower optical bandgap than the materials studied here. Technical details are reported in ref 8.

IV. RESULTS AND DISCUSSION

Our discussion will be focused on a comparison of the PCPDT-BT low-band gap co-polymer with the PCPDT homo-polymer. In particular, we focus our attention on the properties of their singly charged ions. Further below, we complete the series by comparing with PCPDT-2T-BT, in which additional connector units are systematically inserted to separate BT and PCPDT units and thus to reduce the low-bandgap character compared with PCPDT-BT. Figure 1 shows the calculated absorptivity of PCPDT and PCPDT-BT for neutral and singly charged molecules. In the spectra of the neutral molecules, the low-bandgap character of the co-polymer compared to the homo-polymer is visible. The typical camelback structure we obtain for the absorptivity of the neutral co-polymer[4] is not clearly visible on the wavelength scale used in Figure 1. As a feature known for polaron spectra, for both charged species, two well resolved polaron peaks P_2 and P_1 are visible at longer wavelengths. For the homo-polymer, we observe symmetry between the anion and cation polaron spectrum in the long-wavelength range which is absent for the co-polymer.

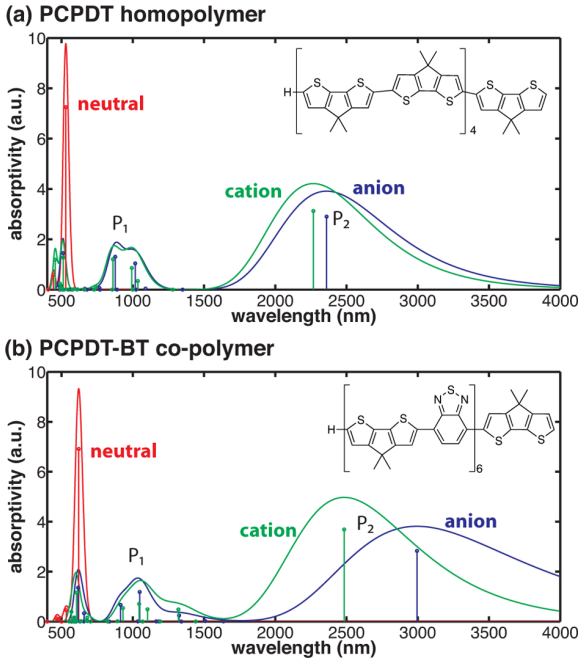

Figure 1. Calculated absorptivity of (a) PCPDT homo-polymer and (b) PCPDT-BT co-polymer. Results are for neutral species and singly charged ions; the insets show the structures used in the calculations. The sticks represent the wavelength and oscillator strength for each transition. While the absorptivity is almost symmetric between the anion and cation of the homo-polymer throughout the spectral range shown, for the co-polymer, this symmetry is lifted in the long-wavelength range due to asymmetry between the high-lying occupied and low-lying unoccupied molecular orbitals.

Before we turn our attention to details of the calculations, we provide a simple physical picture to explain the symmetry and asymmetry between anion and cation absorption spectra, respectively. For each of the polaron transitions in Figure 1, we have inspected the dominant molecular orbital contributions and energies. This leads us to the simple level scheme shown in Figure 2 for the interpretation of the different polaron peaks P_1 and P_2. Similar schemes have been discussed in previous studies on polarons in conjugated polymers.[21,29,30] The arrows in Figure 2 indicate the dominant contributions to the low-energy polaron transitions. The first, P_2, polaron peak can be interpreted as a transition between the lowest orbitals above the gap (anion) or a transition between the highest orbitals below the gap (cation), respectively. In the language of extended systems, the transitions are of "intraband" character. Although strictly speaking here we only study long oligomers, we will continue to use this language below as a convenient way to characterize transitions of different nature. The nature of the second peak, P_1, is slightly more subtle, as it is not clearly dominated by only a single transition in the molecular orbital picture but has strong contributions from multiple and different

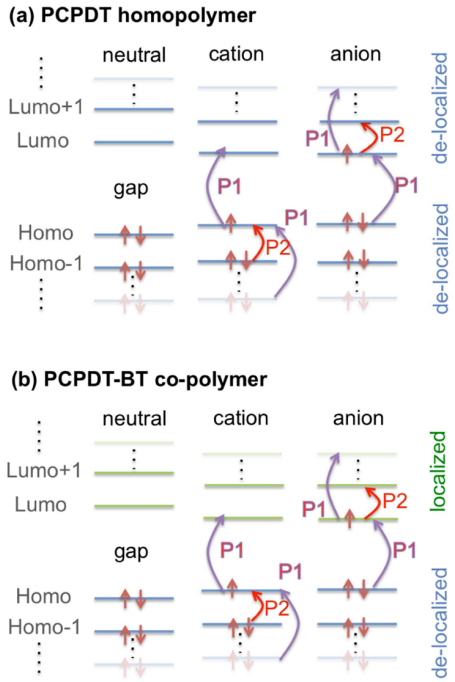

Figure 2. Schematic visualization of energy levels for (a) homo- and (b) co-polymer. Indicated by the arrows are the low-energy polaron transitions. For the co-polymer, these lowest polaron excitations have a different character for the anion and cation. For the anion, the lowest transition is between localized states on the BT unit and for the cation between states delocalized across the polymer. This difference is absent for the homo-polymer.

dx.doi.org/10.1021/jp3084869 | J. Phys. Chem. B 2013, 117, 4454–4460

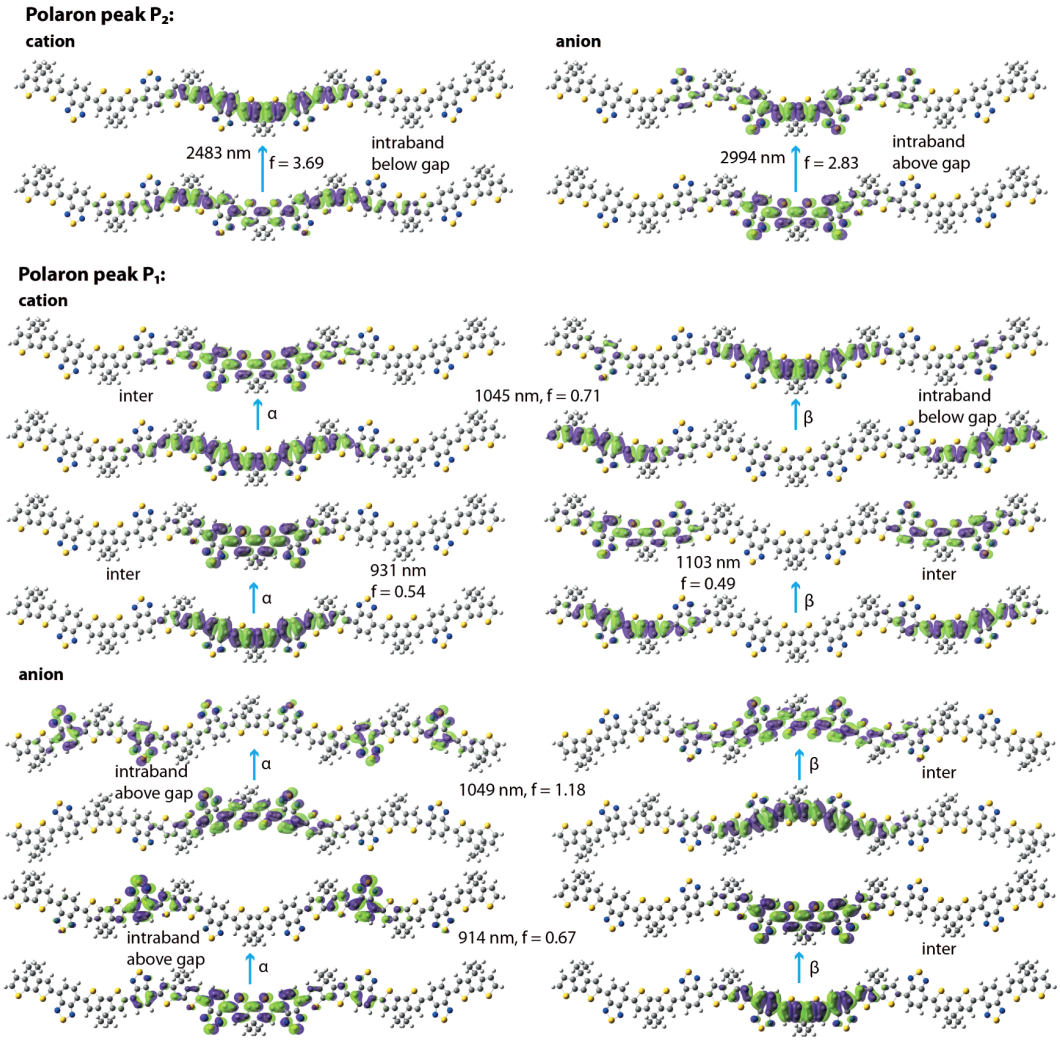

Figure 3. Analysis of long-wavelength polaron excitations in terms of natural transition orbitals for the PCPDT-BT co-polymer. Only one transition contributes to the P_2 polaron peak. Both for cation and anion, only one pair of NTOs significantly contributes to this P_2 transition. Clearly visible is the delocalized nature of the NTOs for the cation, whereas the NTOs for the anion are much more localized on the BT units. This result qualitatively coincides with the schematic interpretation in Figure 2. The NTO analysis of the polaron peak P_1 is more subtle. Multiple transitions significantly contribute to the P_1 peak; for the dominant transitions, the dominant NTOs are shown. The wavelength, oscillator strength f, spin character α or β, respectively, and dominant nature (inter- vs intraband) are noted for each pair of NTOs shown.

types of transitions. The first set of contributions stems from excitations across the gap involving several unoccupied and occupied orbitals ("interband" transitions). The second set of contributions stems from transitions between orbitals below or above the gap, respectively ("intraband" transitions), similar to P_2 but involving higher unoccupied or lower occupied molecular orbitals, respectively.

This interpretation is valid both for homo- and co-polymer. However, in the homo-polymer, states near the gap, both below and above the gap, show extended π-orbital character. In the co-polymer, states above the gap are well localized on the BT units,[31] whereas states below the gap show a similarly extended π-orbital nature as in the homo-polymer (the orbital alignment between the moieties constituting the chain in this co-polymer is similar to a type-II heterostructure, where states slightly below and above the gap are (at least partly) localized on different parts of the chain). Accordingly, for the anion of the co-polymer, the P_2 peak stems mostly from transitions between states localized on the BT unit, whereas for the cation the P_2 peak is dominated by transitions between delocalized molecular states. In the latter case, the P_2 transition in the co-polymer is similar in nature to the P_2 transition in the corresponding homo-polymer. Consequently, the P_2 absorption of co-polymer cation and homo-polymer cation is similar and only slightly different in energy. In the case of symmetry between highest occupied and lowest unoccupied orbitals ("electron−hole" symmetry) as in the homo-polymer, the qualitative difference between anion and cation is largely absent. We find that the spectral signatures of the P_1 polaron peak are very similar in anion and cation, both for homo- and co-polymer. This indicates that the energy of the transitions contributing to the P_1 peak (though not necessarily the oscillator strength) is mostly determined by the energy difference between the highest occupied molecular orbital (HOMO) and lowest unoccupied molecular orbital (LUMO).[29] This energy difference is independent of the character and energy separation between states below and above the gap, and consequently similar for anion and cation also in the co-polymer.

dx.doi.org/10.1021/jp3084869 | J. Phys. Chem. B 2013, 117, 4454−4460

Quantitative details of the different transitions will be further discussed below.

In the following, we solidify the reasoning presented above. In reality, when adding or taking away a charge to the molecular system, the molecular geometry changes according to the new electronic configuration, and the single-particle basis changes compared to the neutral species. Moreover, due to the doublet structure of the electronic ground state of the singly charged ions, the electronic spin-subsystems are not identical anymore and interpretation in terms of a single set of molecular orbitals only is not comprehensive. Excitations between states in different spin-subsystems have to be considered which contribute differently to the optical response of the system. These aspects have not been considered in the discussion of the previous paragraph; however, they are fully included in the quantum chemical calculations, and for a quantitative analysis, they need to be taken into account. One powerful method that allows us to analyze electronic excitations in the correlated electronic many-particle system more rigorously but still in relatively simple terms is the introduction of natural transition orbitals.[26]

We have numerically calculated the NTOs for the dominant low-energy polaron transitions in PCPDT-BT. Results are shown in Figure 3. The wavelength and oscillator strength f of each transition are noted in the figure. Only the dominant NTO contributions for each transition are shown—NTO pairs with a relative weight of less than 50% are not shown. The polaron peak P_2 in both cation and anion is dominated by a single NTO pair only. In this case, the NTOs can be interpreted analogous to electron and hole wave functions involved in the respective transition. For the cation, both NTOs are delocalized over a larger number of aromatic units. For the anion, the localized nature of the transition on the BT unit is clearly visible. This is in good agreement with the reasoning of the previous paragraph based on Figure 2. This difference between anion and cation NTOs of the P_2 transition can be attributed to the "type-II" orbital alignment in the co-polymer which results in a broken symmetry of high-lying occupied and low-lying unoccupied orbitals. This asymmetry is largely absent for the homo-polymer PCPDT. The shorter-wavelength polaron peak P_1 visible at about 1000 nm in Figure 1 stays more complicated even in the NTO picture. First, more than one electronic transition significantly contributes to this peak, as can be seen in the stick spectra included in Figure 1. For each of the relevant sticks at about 1000 nm, the dominant NTO contributions are shown in Figure 3. For the cation, the dominant contributions are at 1045, 1103, and 931 nm, with oscillator strengths $f = 0.71$, $f = 0.49$, and $f = 0.54$, respectively. For the anion, the dominant transitions are at 1049 and 914 nm with oscillator strengths $f = 1.18$ and $f = 0.67$. Second, each electronic transition possesses a more subtle underlying structure, as already indicated qualitatively in Figure 2. For the P_1 polaron, NTOs belonging to the different spin subsystems are denoted as α and β. We find that those transitions that have significant contributions from more than one NTO pair show both strong inter- and intraband character. For the cation, we note interband contributions in both spin channels. For the transitions inspected for the anion, interband contributions are in the β channel only. The intraband contributions for the cation are between delocalized states below the gap, whereas for the anion they are between states mostly localized on the BT units. Considering this different nature of the transitions in the P_1 peak for anion and cation, it is by no means safe to assume that there always exists symmetry for the higher-energy part of the spectrum of co-polymer anion and cation. The similarity of the anion and cation spectra we find for PCPDT-BT in the range of the P_1 peak in Figure 1 indicates that the energies of the transitions in this peak are mostly determined by the energy difference between the HOMO and LUMO.[29] This symmetry may be further lifted for other co-polymers, as is the case for anion and cation spectra for the three-component system PCPDT-2T-BT in Figure 4.

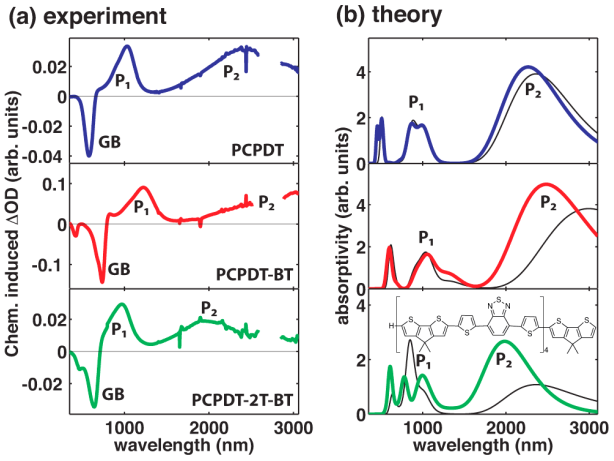

Figure 4. (a) Measured chemically induced change in optical density due to the presence of cations. (b) Calculated absorptivity for cations (colored) and anions (black).

We find that the intraband contributions to the P_1 peak have strong charge-transfer character; i.e., the NTOs within these pairs are localized at different regions of the molecule. We also note that in agreement with previous studies we find the low-energy polarons to be more localized than the extended π-orbitals of the corresponding neutral species (not shown). This is also true in the co-polymer; however, a difference in nature for the P_2 transitions in cation and anion (delocalized vs localized) remains clearly visible in Figure 3 and is reflected in the spectral properties in Figure 1.

We complete the discussion by comparing the theoretical data discussed so far with experiment. In this context, we extend the series studied by another co-polymer, PCPDT-2T-BT, resulting in a more representative series of homo- and co-polymers for this class of materials. In experiment, polaron absorption can be induced by chemically ionizing molecules (cf. the Experimental Methods section). For all three molecules in the series, in Figure 4, we show the measured chemically induced change in optical density due to the presence of cations. So far, we have not succeeded in measuring the corresponding anion spectra; details are given in the Experimental Methods section. In addition to the chemically induced polaron absorption features, the ground state bleach is visible as the negative change in optical density in the experiments. First, we turn our attention to the P_2 peak in the spectrum. Going from PCPDT to PCPDT-BT, the peak is slightly red-shifted. Moving on to PCPDT-2T-BT, the P_2 peak is significantly blue-shifted. These trends are similar but slightly less pronounced for the P_1 peak. We find good agreement between experiment in (a) and theory in (b). Comparing absolute numbers, we find that the calculated transition wavelengths are slightly blue-shifted with respect to the

dx.doi.org/10.1021/jp3084869 | J. Phys. Chem. B 2013, 117, 4454−4460

experimental data. We find a similar trend for the calculated spectra of the neutral molecules (not shown). However, this is not unexpected for the methodology used. All calculations are for finite (albeit long) oligomers. Furthermore, a blue-shift in the calculated spectra was noted before for an extended one-dimensional conjugated system using the CAM-B3LYP functional (cf. the Theoretical Methods section).[32] In addition to the P_1 and P_2 polaron peaks, in all three calculated spectra, an absorption feature can be identified close to the fundamental absorption line of the neutral molecules (see also spectra in Figure 1). This transition is also visible in the experimental data as a feature at the long-wavelength end of the ground state bleach for PCPDT-BT and PCPDT-2T-BT. The notion that there appears to remain some residual absorption of polarons at the fundamental resonance of the neutral molecule is not the main point of the present paper but could also be relevant for interpretation of spectral properties of charge carriers in these systems. Finally, we compare the calculated spectra for anion and cation for PCPDT-2T-BT. Here we note that the symmetry between anion and cation is further lifted. In this case, this is also true for the P_1 peak. Although the origin of the asymmetry is analogous to PCPDT-BT (missing symmetry between highest occupied and lowest unoccupied orbitals), due to the more complicated molecular structure, the inspection of the different transitions in PCPDT-2T-BT has not led us to a similarly clear physical picture as detailed above for PCPDT-BT.

V. CONCLUSIONS AND REMARKS

We have theoretically and experimentally studied optical properties of a series of co- (PCPDT-BT and PCPDT-2T-BT) and homo-polymers (PCPDT) and of their singly charged ions. These materials are currently widely used in organics-based photovoltaics and optoelectronics, and their ionic counterparts play a key role in the extraction and injection of charges. One of our main findings is that the ions of the homo-polymer show very similar polaron absorption (symmetric between anion and cation), whereas for polaron excitations in the co-polymer this symmetry between anion and cation is strongly lifted. On the basis of detailed quantum-chemical calculations, we trace the origin of this asymmetry back to differences in the orbitals contributing to the involved electronic transitions (caused by the absence of symmetry between occupied and unoccupied orbitals near the gap; missing "electron−hole" symmetry) in the co-polymer with type-II orbital alignment. This notion is of importance for future interpretation of spectroscopic polaron data and is expected to similarly apply to other homo- and co-polymer systems.

■ ASSOCIATED CONTENT

Supporting Information

Full author list of ref 24, comparison of the molecular orbitals of the homo- and co-polymer for the neutral species of PCPDT and PCPDT-BT, and equilibrium geometries of the neutral and charged oligomers of PCPDT, PCPDT-BT, and PCPDT-2T-BT. This material is available free of charge via the Internet at http://pubs.acs.org.

■ AUTHOR INFORMATION

Corresponding Author

*E-mail: stefan.schumacher@uni-paderborn.de.

Notes

The authors declare no competing financial interest.

■ ACKNOWLEDGMENTS

The Paderborn group acknowledges financial support from the DFG (GRK 1464), a grant for computing time at PC^2 Paderborn Center for Parallel Computing, and a start-up grant from the faculty of natural sciences, Universität Paderborn. The Munich group acknowledges financial support by the Excellence Cluster Nanosystems Initiative Munich (NIM) and by Solar Technologies Go Hybrid (Sol Tech) funded by the State of Bavaria.

■ REFERENCES

(1) Samuel, I. D. W.; Turnbull, G. A. *Chem. Rev.* **2007**, *107*, 1272−1295.
(2) Clark, J.; Lanzani, G. *Nat. Photonics* **2010**, *4*, 438−446.
(3) Günes, S.; Neugebauer, H.; Sariciftci, N. S. *Chem. Rev.* **2007**, *107*, 1324−1338.
(4) Jespersen, K. G.; Beenken, W. J. D.; Zaushitsyn, Y.; Yartsev, A.; Andersson, M.; Pullerits, T.; Sundström, V. *J. Chem. Phys.* **2004**, *121*, 12613−12617.
(5) Schmidtke, J. P.; Kim, J.-S.; Gierschner, J.; Silva, C.; Friend, R. H. *Phys. Rev. Lett.* **2007**, *99*, 167401.
(6) Milián-Medina, B.; Gierschner, J. *Org. Electron.* **2012**, *13*, 985−991.
(7) Liu, B.; Bazan, G. C. *J. Am. Chem. Soc.* **2006**, *128*, 1188−1196.
(8) Tautz, R.; da Como, E.; Limmer, T.; Feldmann, J.; Egelhaaf, H.-J.; von Hauff, E.; Lemaur, V.; Beljonne, D.; Yilmaz, S.; Dumsch, I.; Allard, S.; Scherf, U. *Nat. Commun.* **2012**, *3*, 970.
(9) Deschler, F.; Da Como, E.; Limmer, T.; Tautz, R.; Godde, T.; Bayer, M.; von Hauff, E.; Yilmaz, S.; Allard, S.; Scherf, U.; Feldmann, J. *Phys. Rev. Lett.* **2011**, *107*, 127402.
(10) Schubert, M.; Dolfen, D.; Frisch, J.; Roland, S.; Steyrleuthner, R.; Stiller, B.; Chen, Z.; Scherf, U.; Koch, N.; Facchetti, A.; Neher, D. *Adv. Energy Mater.* **2012**, *2*, 369−380.
(11) Amarasinghe, D.; Ruseckas, A.; Vasdekis, A. E.; Turnbull, G. A.; Samuel, I. D. W. *Adv. Mater.* **2009**, *21*, 107−110.
(12) Khalil, G. E.; Adawi, A. M.; Fox, A. M.; Iraqi, A.; Lidzey, D. G. *J. Chem. Phys.* **2009**, *130*, 044903.
(13) Huang, Y.-S.; Westenhoff, S.; Avilov, I.; Sreearunothai, P.; Hodgkiss, J. M.; Deleener, C.; Friend, R. H.; Beljonne, D. *Nat. Mater.* **2008**, *7*, 483−489.
(14) Fazzi, D.; Grancini, G.; Maiuri, M.; Brida, D.; Cerullo, G.; Lanzani, G. *Phys. Chem. Chem. Phys.* **2012**, *14*, 6367−6374.
(15) Banerji, N.; Gagnon, E.; Morgantini, P.-Y.; Valouch, S.; Mohebbi, A. R.; Seo, J.-H.; Leclerc, M.; Heeger, A. J. *J. Phys. Chem. C* **2012**, *116*, 11456−11469.
(16) Clark, J.; Nelson, T.; Tretiak, S.; Cirmi, G.; Lanzani, G. *Nat. Phys.* **2012**, *8*, 225−231.
(17) Beljonne, D.; Cornil, J.; Sirringhaus, H.; Brown, P. J.; Shkunov, M.; Friend, R. H.; Brédas, J.-L. *Adv. Funct. Mater.* **2001**, *11*, 229−234.
(18) Fratiloiu, S.; Grozema, F. C.; Koizumi, Y.; Seki, S.; Saeki, A.; Tagawa, S.; Dudek, S. P.; Siebbeles, L. D. A. *J. Phys. Chem. B* **2006**, *110*, 5984−5993.
(19) Zaikowski, L.; Kaur, P.; Gelfond, C.; Selvaggio, E.; Asaoka, S.; Wu, Q.; Chen, H.-C.; Takeda, N.; Cook, A. R.; Yang, A.; Rosanelli, J.; Miller, J. R. *J. Am. Chem. Soc.* **2012**, *134*, 10852−10863.
(20) Hwang, I.-W.; Cho, S.; Kim, J. Y.; Lee, K.; Coates, N. E.; Moses, D.; Heeger, A. J. *J. Appl. Phys.* **2008**, *104*, 033706.
(21) Brown, P. J.; Sirringhaus, H.; Harrison, M.; Shkunov, M.; Friend, R. H. *Phys. Rev. B* **2001**, *63*, 125204.
(22) Herrmann, D.; Niesar, S.; Scharsich, C.; Köhler, A.; Stutzmann, M.; Riedle, E. *J. Am. Chem. Soc.* **2011**, *133*, 18220−18233.
(23) Oberski, J. M.; Greiner, A.; Bässler, H. *Chem. Phys. Lett.* **1991**, *184*, 391−397.

(24) Frisch, M. J.; et al. *Gaussian 09*, revision B.01; Gaussian, Inc.: Wallingford, CT, 2009.
(25) Dennington, R.; Keith, T.; Millam, J. *GaussView*, version 5.0.9; Semichem, Inc.: Shawnee Mission, KS, 2009.
(26) Martin, R. L. *J. Chem. Phys.* **2003**, *118*, 4775−4777.
(27) Lewis, I. C.; Singer, L. S. *J. Chem. Phys.* **1965**, *43*, 2712−2727.
(28) Deussen, M.; Bässler, H. *Chem. Phys.* **1992**, *164*, 247−257.
(29) Campbell, D. K.; Bishop, A. R.; Fesser, K. *Phys. Rev. B* **1982**, *26*, 6862−6874.
(30) Fesser, K.; Bishop, A. R.; Campbell, D. K. *Phys. Rev. B* **1983**, *27*, 4804−4825.
(31) Risko, C.; McGehee, M. D.; Brédas, J.-L. *Chem. Sci.* **2011**, *2*, 1200−1218.
(32) Montgomery, N. A.; Hadley, G. J.; Ruseckas, A.; Denis, J.-C.; Schumacher, S.; Kanibolotsky, A. L.; Skabara, P. J.; Galbraith, I.; Turnbull, G. A.; Samuel, I. D. W. *Phys. Chem. Chem. Phys.* **2012**, *14*, 9176−9184.

Supporting Information for: Spectral Signatures of Polarons in Conjugated Co-Polymers

Christian Wiebeler, Raphael Tautz, Jochen Feldmann, Elizabeth von Hauff, Enrico Da Como, and Stefan Schumacher*

*Corresponding author: stefan.schumacher@uni-paderborn.de

Full Author List for Reference 24

Frisch, M. J.; Trucks, G. W.; Schlegel, H. B.; Scuseria, G. E.; Robb, M. A.; Cheeseman, J. R.; Scalmani, G.; Barone, V.; Mennucci, B.; Petersson, G. A.; Nakatsuji, H.; Caricato, M.; Li, X.; Hratchian, H. P.; Izmaylov, A. F.; Bloino, J.; Zheng, G.; Sonnenberg, J. L.; Hada, M.; Ehara, M.; Toyota, K.; Fukuda, R.; Hasegawa, J.; Ishida, M.; Nakajima, T.; Honda, Y.; Kitao, O.; Nakai, H.; Vreven, T.; Montgomery, Jr., J. A.; Peralta, J. E.; Ogliaro, F.; Bearpark, M.; Heyd, J. J.; Brothers, E.; Kudin, K. N.; Staroverov, V. N.; Kobayashi, R.; Normand, J.; Raghavachari, K.; Rendell, A.; Burant, J. C.; Iyengar, S. S.; Tomasi, J.; Cossi, M.; Rega, N.; Millam, J. M.; Klene, M.; Knox, J. E.; Cross, J. B.; Bakken, V.; Adamo, C.; Jaramillo, J.; Gomperts, R.; Stratmann, R. E.; Yazyev, O.; Austin, A. J.; Cammi, R.; Pomelli, C.; Ochterski, J. W.; Martin, R. L.; Morokuma, K.; Zakrzewski, V. G.; Voth, G. A.; Salvador, P.; Dannenberg, J. J.; Dapprich, S.; Daniels, A. D.; Farkas, Ö.; Foresman, J. B.; Ortiz, J. V.; Cioslowski, J.; Fox, D. J. *Gaussian 09, Revision B.01*, Gaussian, Inc., Wallingford CT, **2009**.

Visualization of molecular orbitals for the neutral oligomers of (a) PCPDT and (b) PCPDT-BT (CAM-B3LYP-6-31G(d)):

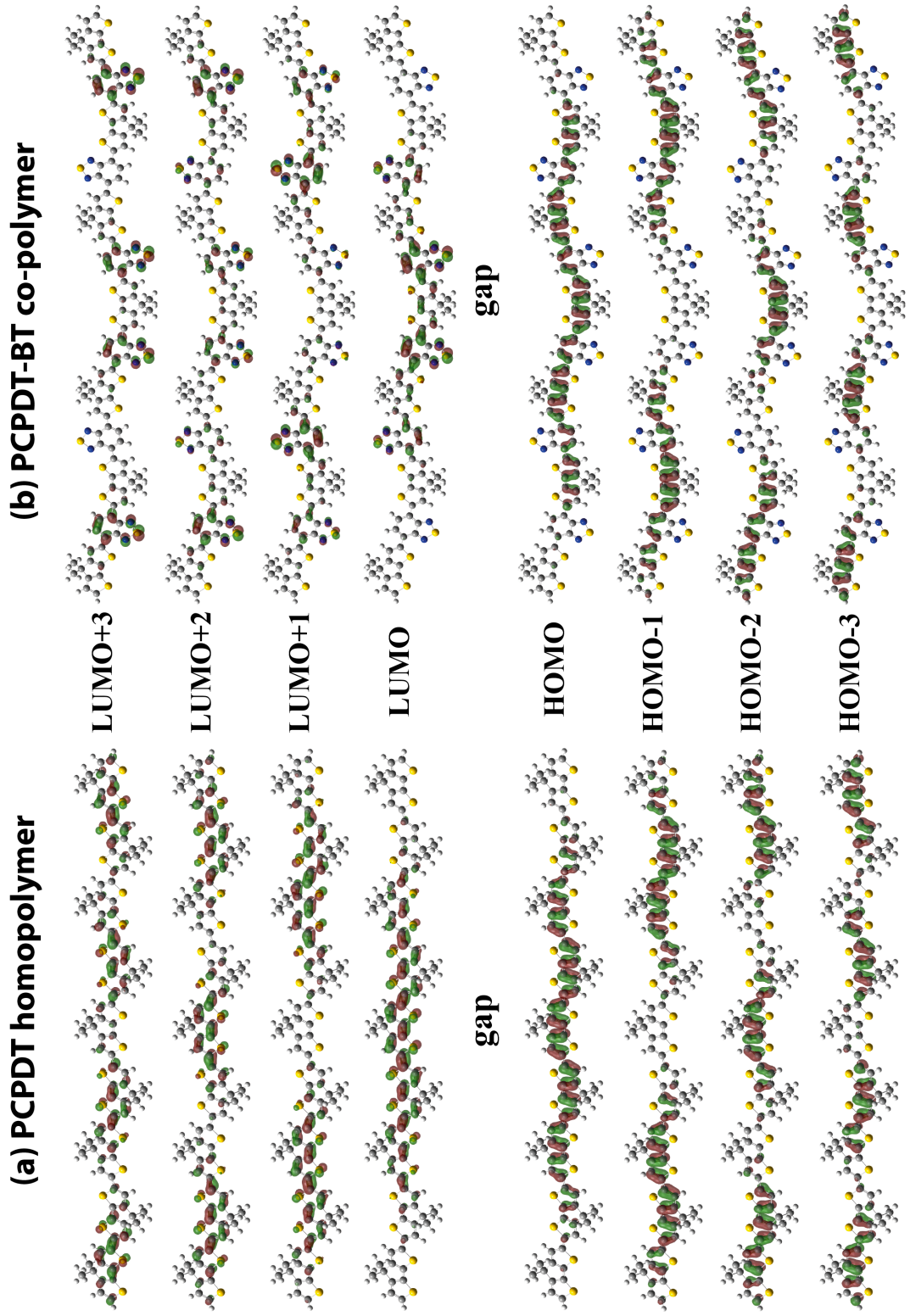

4.5 Organic Photovoltaics & Bulk Heterojunction Solar Cells

Currently, there is a high interest in the use of conjugated oligo- and polymers in solar cells, owing to their electronic properties, low cost, versatility of functionalization, thin film flexibility and ease of processing.[39] The first organic solar cell employing two layers of different organic molecules to obtain a heterojunction analogous to silicon-based solar cells has been developed by Tang.[40] A major improvement was achieved by introduction of BHJSC.[41] The structure of such a cell and the process of the conversion of solar energy to electric one are shown in figure 4.7. The donor is typically made of a conjugated polymer, e.g. PCPDT-BT, and the acceptor of a fullerene derivative, e.g. PCBM. Furthermore, oligomers can be used as donors in OPV.[37,38] In the following, the four steps of electric current generation in OPV will be discussed. The steps are: light absorption, exciton diffusion, exciton dissociation, and charge migration for collection at electrodes.

Conjugated polymers that are used as donors have typically large extinction coefficients for the absorption of visible light, allowing efficient light harvesting in layers with thicknesses of $100 - 200\,\mathrm{nm}$.[42] The absorption properties can be modeled by TDDFT-based calculations of a single polymer. The lowest-energy transition is typically a π-π^* transition. Excitation of a molecule in this state leads to the formation of a bound electron-hole pair, i.e. an exciton. In contrast to silicon, this exciton has a binding energy of $0.1 - 0.5\,\mathrm{eV}$, due to the lower dielectric constant and the smaller exciton radius. Therefore, dissociation into free charge carriers is not possible with thermal energy at room temperature, i.e. $25\,\mathrm{meV}$.[43]

Upon generation, the exciton diffuses until it recombines or it is separated into free charge carriers. The diffusion can be described by Förster-type incoherent energy transfer, which lowers the energy of the exciton.[39] Therefore, the exciton can either be trapped at a trap site or it reaches the interface between donor and acceptor material. Due to the finite lifetime, it might happen that a generated exciton is not able to reach the interface before it recombines. Therefore, the exciton diffusion length has to be larger than the distance to the interface. This is achieved in BHJSCs, due to their interpenetrating, phase-separated network of donor and acceptor regions and their nanoscale morphology.[42]

Exciton dissociation leading to charge separation is a controversial and critical issue for polymer solar cells. According to reference [44] the following statements hold at the moment: Interfacial charge transfer states exist in polymer:fullerene blends as evidenced by measurements. To a large amount, the charge separation is ultrafast and the influence of an external electric field depends on the material. However, the mechanism of charge carrier generation is disputed. This can either happen upon thermalization of the exciton or the "hot" exciton, i.e. exciton with excess kinetic energy, is separated without thermalization. As an example, transient absorption spectroscopy has been used to investigate this process, indicating the importance of hot excitons.[45] So far, this process has been mainly modeled by static quantum chemical calculations for systems consisting of donor and acceptor molecules.[43]

Upon successful charge separation, the hole that is located in the HOMO of the donor

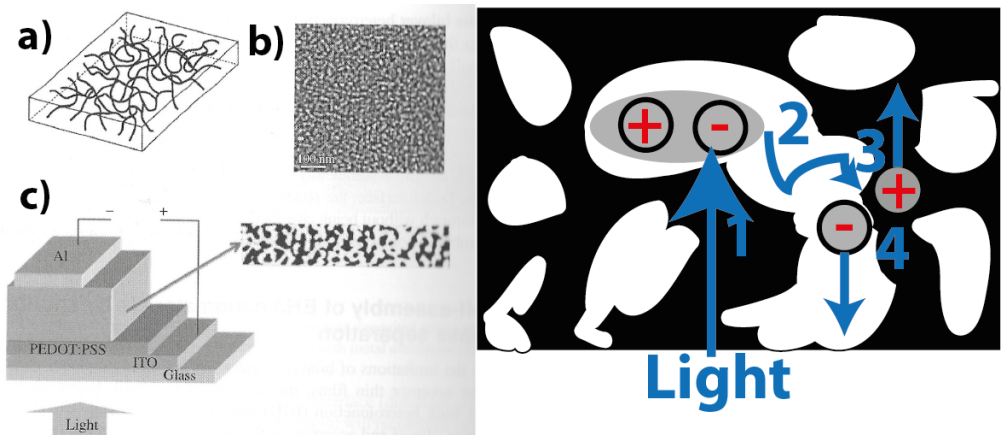

Figure 4.7: On the left, in a) the interpenetrating network of donor (black) and acceptor (white) material is shown; in b) the two different phases can be seen using TEM; in c) the principle structure of a BHJSC is sketched and as an inset the bulk heterojunction (BHJ) is shown. A BHJSC can consist of glass as substrate, of indium tin oxide (ITO) as conducting oxide for the bottom contact, of poly-ethylene-dioxythiophene:polystyrenesulfonic acid (PEDOT:PSS) as electron blocking layer, of the BHJ as active layer, and of aluminum (Al) as metal electrode on top. On the right, the process of current generation in the BHJ is sketched: 1) The incident light is absorbed in the donor (white) and a strongly bound electron-hole pair, i.e. an exciton, is formed. 2) The exciton diffuses to the interface between donor and acceptor. 3) The charges are separated at the interface, so the electron is transferred to an acceptor molecule and the hole remains in the donor phase forming a negatively charged polaron. 4) The charges migrate toward the corresponding electrode by hopping from one molecule to another one. The left part is taken and adapted from reference [27] and the sketch is own work.

drifts and diffuses towards the corresponding electrode as well as the electron that is found in the LUMO of the acceptor. The drift efficiencies of the charge carriers are determined by their mobilities. Charges located at a molecule or chain segment of the donor lead to a local geometry deformation giving rise to polarons due to the strong electron-phonon coupling.[42] Polarons hop from molecule to molecule and are extracted at the electrode. To simulate charge migration, coarse grained modeling can be used to describe larger systems than the ones used for the investigation of exciton dissociation.[43]

Overall, the external quantum efficiency, i.e. the probability that an absorbed photon generates an electron and a hole that are collected at the electrodes, is the product of the efficiencies of each step. In BHJSCs, the thickness of the layer can be chosen so that the corresponding efficiency is approximately one. Furthermore, the bottleneck of exciton diffusion is removed in such a cell. Therefore, the mechanisms of charge separation at the interface and of charge migration have to be understood.[37] The latter is mainly influenced by the morphology of the blend, whereas for the former the electronic states at the interface and the corresponding ultrafast dynamics have to be investigated.

5 Extended Two Dimensional Conjugated Systems: the GQD C132

> Our Science paper offered the first glimpse of graphene in its new avatar as a high quality 2D electronic system and beyond.
>
> *(Andre Geim[46])*

Graphene possesses an extended two dimensional conjugated system and therefore it can be seen as a two dimensional analogue to conjugated polymers that consist of a one dimensional extended conjugated system. The material is of high interest due to its particular mechanical and electronic properties.[47] As an example, it has been reported recently that the material can be used in conjunction with TiO_2 in thin film perovskite solar cells with conversion efficiencies up to 15.6 %.[48] Due to the fact that our calculations have been carried out without periodic boundary conditions, only systems with finite size, so called GQDs, have been investigated. However, also GQD are of great interest for experiment and can be produced by solution chemistry in a well-controlled manner. These graphene nanostructures are used in experiment allowing direct comparison between theory and experiment.[2] This chapter starts with the classical and semiclassical interpretation of the FCP and their application for spectrum simulation. Then the electronic and optical properties of the GQD C132 will be discussed employing the results of quantum chemical calculations that have been published in the paper that is included in this chapter.[2] In the last section, MOs and the simulated spectrum will be analyzed in more detail.

5.1 Franck-Condon Principle: Classical & Semiclassical Interpretation

The FCP can be stated as:[49] "Nuclei preserve their dynamical state during an electronic transition." Treating the nuclei as classical particles leads to the corresponding classical principle:[49] "Because nuclear masses are so much larger than the mass of an electron, an electronic transition occurs within a stationary nuclear framework." In this case, nuclear locations and their velocities remain the same during an electronic transition and readjust to the new electronic distribution after excitation.

At the top of figure 5.1, a classical harmonic oscillator model is shown to explain this principle in more detail.[50] In this picture, an electronic transition is a vertical excitation starting from the equilibrium geometry of S_0 and ending at the intersection between this

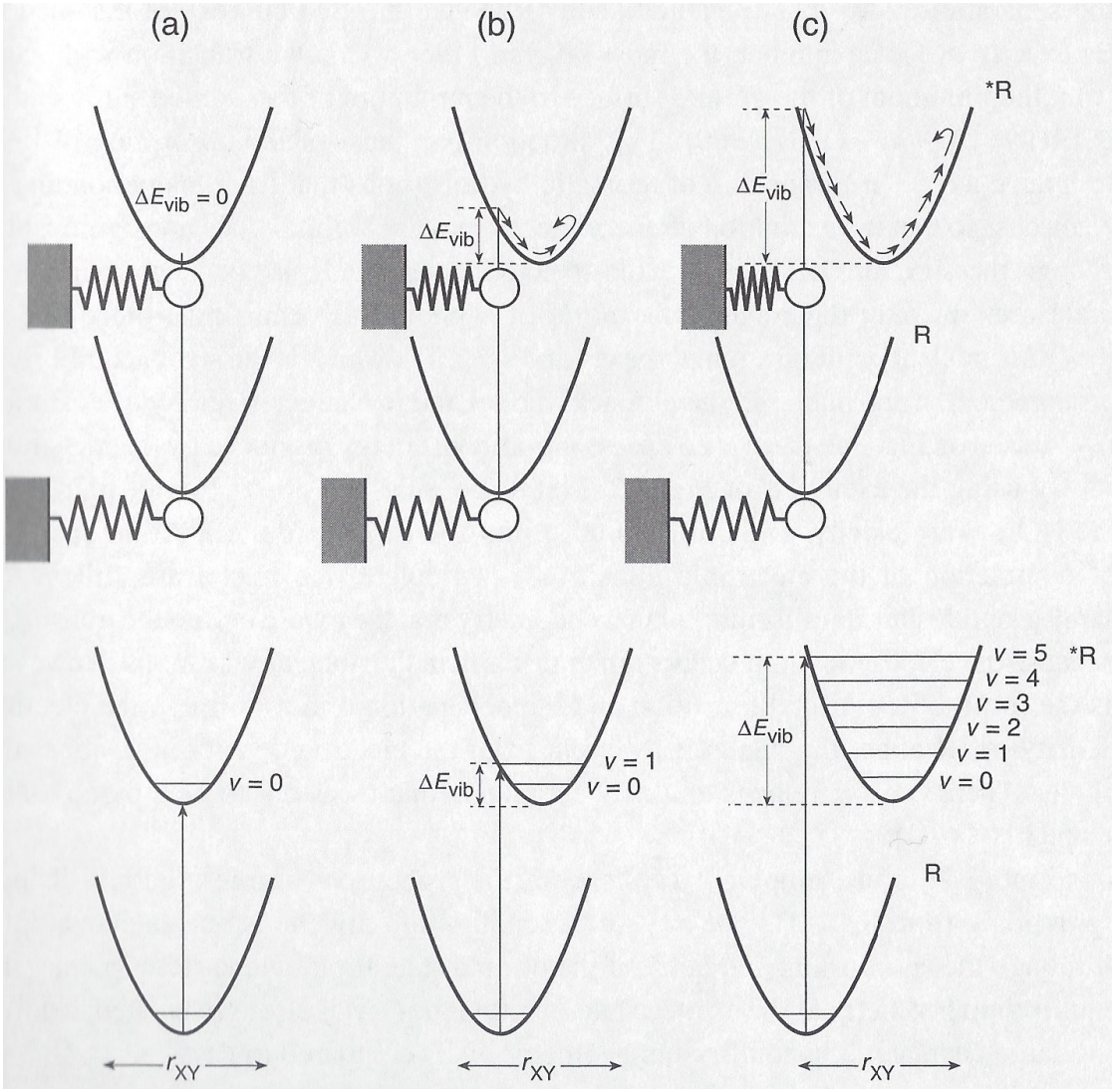

Figure 5.1: Illustration of the classical (top) and semiclassical (bottom) model of the FCP. In the classical case, the energy of the vibrational motion depends on the displacement between the equilibrium geometries of the two electronic states: the higher the displacement, the higher ΔE_{vib}. In the semiclassical model, the quantization of the vibrations is taken into account. This leads to the fact, that excitations start from a range of nuclear geometries and the probability of excitation of a specific vibrational mode depends on the displacements between the two parabolas: the higher the displacement, the more likely is the excitation of higher vibrational modes. The picture is taken from reference [50].

vertical line and the PES of S_1. Depending on the displacements between the parabolas of the PESs of S_0 and S_1, the energy stored in the vibrational motion is different. If there is no such displacement, the electronic transition will end in the equilibrium of the electronic excited state. Otherwise, the larger the displacement the higher is the vibrational energy.

In the semiclassical approximation as the next step, the quantization of the vibrational states can be taken into account leading to a semiclassical interpretation.[50] The transition now starts at the ground vibrational state of S_0. Therefore, electronic transitions do not start at a single optimized geometry but they are initiated from a range of nuclear geometries. The classical equilibrium geometry is at its center and the range of sampled geometries belongs to the zero-point vibrational motion. Depending on the displacements of the two parabolas, the most probable transition and with that the most probable vibrational mode excited can be different.

In a final step, not only the quantization of the vibrational states but also the corresponding vibrational wave functions have to be considered. This will be done in section 6.1. However, starting from an expression for the absorption spectrum the idea of spectrum simulation that is based on the semiclassical interpretation of the FCP can be understood. This will be explained in section 5.2.

5.2 Absorption Spectrum and Spectrum Simulation

In this section, only the fundamental equations that are needed for spectrum simulations will be presented. A more detailed discussion regarding the quantities involved in this equations as well as the phenomenon of intensity borrowing will be discussed in chapter 5. Also refer to the references given in this section for further explanations of the involved quantities and derivation of the formula. Note that throughout this chapter and the next one, an own notation has been used to increase the consistency and readability of the expressions.

Starting from the description of a classical light field, employing time-dependent perturbation theory, and applying the electric dipole approximation, the absorption of a molecule in the vibrational ground state of S_0 can be derived.[51] It can be written as:[52]

$$\sigma(E) = \frac{\pi}{3\hbar c \epsilon_0 n_r E} \sum_{nk} \int |\Delta E_{00,nk}(\boldsymbol{R}) \nu_{00}^*(\boldsymbol{R}) \langle \varepsilon_0 \,|\, \vec{\mu}_e(\boldsymbol{r};\boldsymbol{R}) \,|\, \varepsilon_n \rangle \, \nu_{nk}|^2 \, \delta(\Delta E_{00,nk}(\boldsymbol{R}) - E) \mathrm{d}\boldsymbol{R} \tag{5.1}$$

The prefactor consists of natural constants, the refractive index n_r of the material, and energy E. In this case, excitations from the ground vibrational state of S_0 are considered, the sum runs over all n electronic and k vibrational states of interest, and $\boldsymbol{r}$ and $\boldsymbol{R}$ denote the collective electronic and nuclear coordinates, respectively. The expression within the braket yields the electronic transition dipole moment and the energy difference $\Delta E_{00,nk}$ between the states of the transition also enters this equation. Finally, the overlap between the ground vibrational state ν_{00} and the excited state ν_{nk} has to be determined. To achieve this, the equation can be rewritten in time domain

and a phenomenological model for the temporal development of the overlap can be approximated. Using the approximation:[52]

$$\Delta E_{0n} \approx \langle \Delta E_{00,nk} \rangle_k \tag{5.2}$$

and defining oscillator strength and Lorentzian line shape as:

$$f_{0n} = \langle \varepsilon_0 \,|\, \vec{\mu}(\boldsymbol{r};\boldsymbol{R}) \,|\, \varepsilon_n \rangle^2 \, \frac{2m\Delta E_{0n}}{3\hbar^2 e^2} \tag{5.3}$$

$$g_L(E - \Delta E_{0,n}, \delta_n) = \frac{1}{\pi} \frac{\delta_n/2}{\left(E - \Delta E_{0,n}(\boldsymbol{R})\right)^2 + \left(\delta_n/2\right)^2} \tag{5.4}$$

yields the following final expression for the absorption:[52]

$$\sigma(E) = \frac{\pi\hbar e^2}{2mc\epsilon_0 n_r E} \sum_n \int |\nu_{00}(\boldsymbol{R})|^2 \, \Delta E_{0n}(\boldsymbol{R}) f_{0n}(\boldsymbol{R}) g_L(E - \Delta E_{0n}(\boldsymbol{R}), \delta_n) \mathrm{d}\boldsymbol{R} \tag{5.5}$$

Now, S_0 has to be sampled to simulate the absorption spectrum. To do so, a distribution of nuclear geometries can be created that is obtained in harmonic approximation using a Wigner-distribution described in references [52] and [53]. Having obtained such an ensemble of N_p normal coordinates, they can be converted into an ensemble of nuclear geometries. For each geometry, a calculation of transition energies and oscillator strengths for N_{fs} final states is done, e.g. using TDDFT. Then, the spectrum can be finally calculated using the following expression:[52]

$$\sigma(E) = \frac{\pi\hbar e^2}{2mc\epsilon_0 n_r E} \frac{1}{N_p} \sum_l^{N_p} \left[\sum_n^{N_{fs}} \Delta E_{0n}(\boldsymbol{R}_l) f_{0n}(\boldsymbol{R}_l) g_L(E - \Delta E_{0n}(\boldsymbol{R}_l), \delta_n) \right] \tag{5.6}$$

This formula allows semiclassical spectrum simulation taking into account the distribution of nuclear geometries of the ground vibrational state of S_0, but the vibrational states of the excited electronic states are not considered. The fact that this method uses an ensemble of nuclear geometries is the cause for its name: nuclear-ensemble approach, abbreviated NEA as already introduced. Classical spectrum simulation, i.e. spectrum calculation using VEA, is obtained using the optimized S_0 geometry as the only geometry to evaluate the expression in square brackets. A quantum mechanical treatment for the simulation of absorption spectra based on the FCP and discussion of its consequences will be discussed in the next chapter. In the remainder of this chapter, the GQD C132 will be used as an exemplar for the practical application of this kind of calculations.

5.3 "Optical Spectroscopy of Graphene Quantum Dots: The Case of C132"

This paper has been published in "The Journal of Physical Chemistry A" and is dedicated to the investigation of electronic and optical properties of a specific GQD consisting of 132 carbon atoms that is of special interest for experimental applications. We have used the NEA to show that the peaks and shoulders found in the experimental spectrum included in our paper are caused by the GQDs. A finding that cannot be derived from calculations employing VEA. In particular, our approach allows to clarify the role of potential impurities. In section 5.4, the electronic and optical structure will be analyzed in more detail and the spectrum will be decomposed into contributions of the different electronic states.

THE JOURNAL OF PHYSICAL CHEMISTRY A

Article

pubs.acs.org/JPCA

Optical Spectroscopy of Graphene Quantum Dots: The Case of C132

Hans Riesen,*[,†] Christian Wiebeler,[‡] and Stefan Schumacher[‡]

[†]School of Physical, Environmental and Mathematical Sciences, The University of New South Wales, Canberra, Australian Capital Territory 2600, Australia

[‡]Department of Physics and Center for Optoelectronics and Photonics Paderborn (CeOPP), University of Paderborn, Warburger Straße 100, 33098 Paderborn, Germany

Supporting Information

ABSTRACT: We have reinvestigated the optical spectroscopy of C132 graphene quantum dots by absorption, selective fluorescence, excitation and time-resolved spectroscopy, the external heavy atom effect, and DFT based quantum chemical calculations. In particular, wavelength-selective photobleaching provides strong evidence for the assignment of the intrinsic absorption and emission features of the quantum dots and indicates that emissions observed at ~670 and ~630 nm and associated relatively narrow features that display vibrational progressions in the selective excitation spectra are due to different species. The emitting state that leads to a broad emission (1700 cm^{-1}) centered around 750 nm appears to be a "near-dark" singlet state with a relatively long lifetime of ~30 ns. Simulated spectra, based on the nuclear ensemble approach, are in qualitative agreement with this finding and indicate very low oscillator strengths with some significant electron-vibrational intensity borrowing.

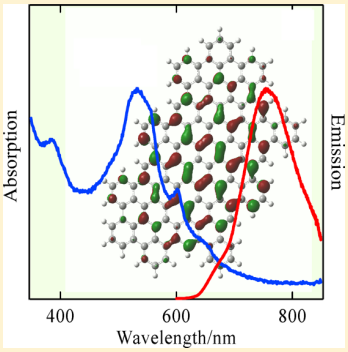

1. INTRODUCTION

With the discovery of C60, carbon nanotubes, and most recently graphene, carbonaceous materials have received a great deal of interest over the past 3 decades.[1−4] Also, nanodiamonds have been the subject of numerous investigations,[5] and this has been largely driven by their unique properties for applications as optical and magnetic probes.[6]

Over recent years, in particular graphene, consisting of two-dimensional (2D) single-atom carbon sheets, has been at the center of numerous investigations because of its high mechanical strength and high carrier mobility with possible electronic applications.[7,8] For example, it has been recently reported that graphene/TiO_2 nanocomposites can render solar cells with a ~15% conversion efficiency.[9] Other applications include the use of graphene as tunable antennas[10] and for the direct generation of terahertz laser pulses on the 100 fs time scale.[11] We note here that terahertz lasing has only been achieved indirectly to date.

In a series of papers, Li et al.[12−16] have reported spectroscopic properties of colloidal graphene quantum dots (GQDs), with solubilizing groups, that were made by a solution chemistry approach. GQDs are 0D quantum-confined systems with potential applications in photovoltaics, and they may also serve as model systems for studying properties of complex carbon materials.[17] The GQDs are held together by well-defined covalent bonds, including the solubilizing groups. Mueller et al. reported on the relaxation pathways in the photoexcited states.[12] From the observation that excitation spectra were highly dependent on the monitored luminescence wavelength, they concluded that relaxation pathways in C132 GQDs vary dramatically within the excited states, resulting in an emitting singlet and triplet state at ~670 and ~750 nm, respectively. Recent reviews of spectroscopic properties of a range of GQDs prepared by a variety of methods have been given in refs 17 and 18. Since a robust understanding of electronic states in GQDs is paramount for taking advantage of their extraordinary electronic properties, we report on our reinvestigation and findings of the spectroscopic properties of C132 GQDs in this article.

2. METHODS

Experiment. The C132 GQDs were kindly provided by Professor Liang-shi Li of Indiana University and were prepared as described previously by this research group.[15] Absorption spectra of the C132 GQDs in toluene and heptane were recorded on a GBC UV−vis 918 spectrometer in 1 and 5 cm cuvettes. Room temperature and 77 K fluorescence and excitation spectra were measured by using a Jobin Yvon Horiba Spex Fluoromax-3 fluorometer with a liquid nitrogen cryostat built in the laboratory. For temperatures below 77 K a Spex 1704 monochromator equipped with a Hamamatsu R928 photomultiplier was employed. In this latter case the signal was processed by using a Femto DLPCA-200 current voltage amplifier and a Stanford Research Systems SR810 lock-in amplifier. A 10 mW Nd:YAG laser was used as the excitation source, and for excited state lifetime measurements an Oriel model 79111 pulsed nitrogen laser (337 nm) was used. Spectra were fully corrected for the instrumental response. For

Received: March 19, 2014
Revised: June 26, 2014
Published: June 27, 2014

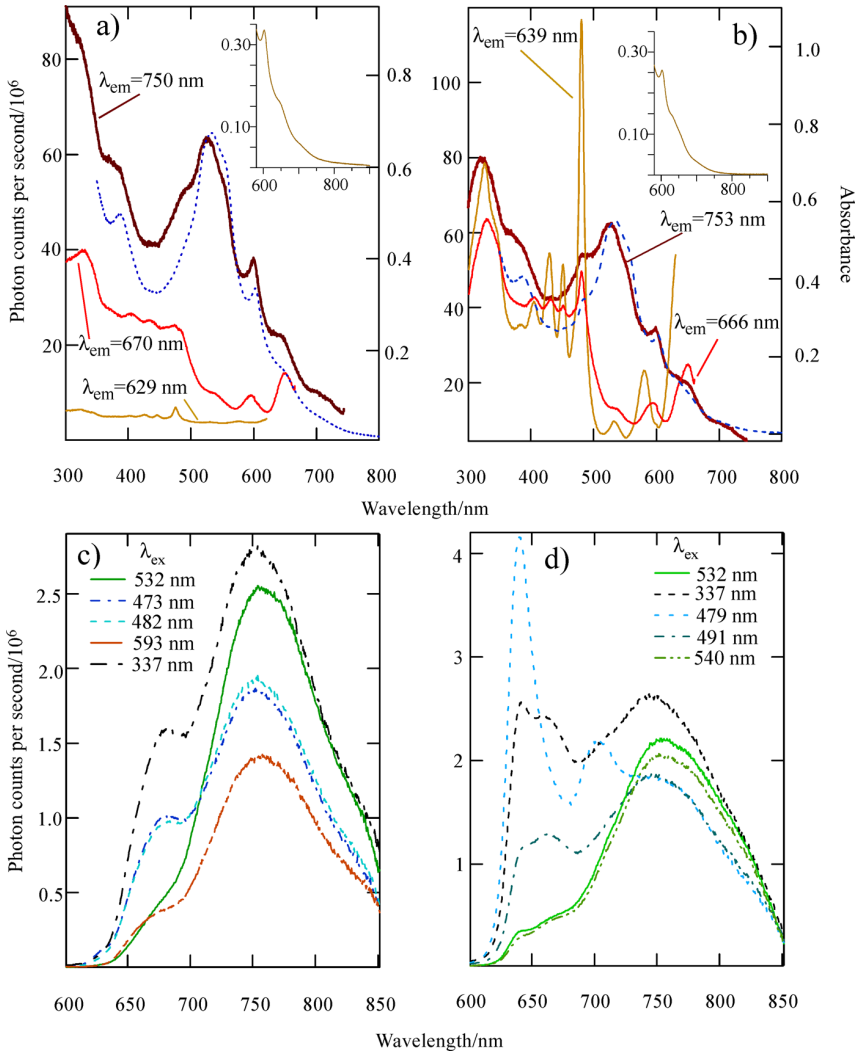

Figure 1. Absorption and selective excitation and fluorescence spectra of C132 GQDs at room temperature. (a) Selective excitation spectra as monitored at various emission wavelengths λ_{em} together with the absorption spectrum (dashed line) in heptane. The inset shows the absorption spectrum in 600−900 nm region. (b) As in (a) but for toluene. (c) Selectively excited fluorescence spectra for various excitation wavelengths λ_{ex} in heptane. (d) As in (c) but for toluene. The absorption spectra were measured in a 5 cm cuvette. All spectra were corrected for the instrumental response.

temperatures below 77 K a Janis/Sumitomo SHI-4.5 closed-cycle refrigerator was employed.

Theory. The geometry of the GQDs was first optimized in the S_0 electronic ground state based on density-functional theory (DFT). Electronic transitions were calculated in the optimized S_0 geometry based on linear response time-dependent density functional theory (TD-DFT), followed by a TD-DFT geometry optimization in the excited electronic S_1 state. All these calculations were done with the Gaussian 09 program suite,[19] consistently at the same level of theory with the Becke three-parameter Lee−Yang−Parr hybrid functional (B3LYP) and 6-31G* basis set. This choice of functional and basis set was previously found to give results in good agreement with available experimental data.[20] Visualizations of molecular geometry and orbitals were done with GaussView, version 5.[21] All optimizations were done without any symmetry constraints. We note that the resulting optimized S_0 and S_1 geometries are not perfectly planar. Absorption spectra were simulated based on the nuclear-ensemble approach.[22] For this purpose the Newton-X program[23] interfaced with Gaussian 09 was used. One-thousand geometries were sampled using a Wigner distribution. The first 20 excitations were calculated for each geometry. For the generation of the simulated spectrum each transition was convoluted with a Gaussian broadening of 0.035 eV. Because of the sampling of different ground state geometries, the spectra calculated within the nuclear ensemble approach are slightly red-shifted compared with the electronic transitions calculated for the optimized ground state geometries. All calculations in this work were done for C132 GQDs dissolved in toluene. The solvent was included based on the polarizable continuum model as implemented in Gaussian 09. Additional side groups on the GQDs were neglected, as those are largely not involved in the lowest optical excitations.

3. RESULTS AND DISCUSSION

Figure 1 shows absorption and selective excitation and fluorescence spectra of the C132 GQDs in heptane and toluene. The most pronounced feature in the absorption

dx.doi.org/10.1021/jp502753a | J. Phys. Chem. A 2014, 118, 5189−5195

spectra (dashed lines and insets) is centered around 535 nm in both solvents. On the basis of quantum chemistry calculations (see Methods for details), this feature can be assigned to the bright $S_0 \rightarrow S_3$ and $S_0 \rightarrow S_4$ transitions in the C132 GQDs (cf. Figure 2 and Tables S1 and S2 in the Supporting Information).

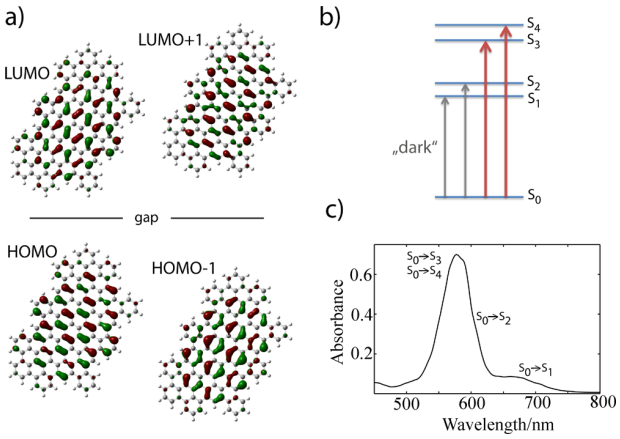

Figure 2. (a) Frontier orbitals of the graphene quantum dot that dominate the lowest optical transitions from the electronic ground state S_0. (b) Illustration of the four lowest optical transitions. The transitions $S_0 \rightarrow S_1$ and $S_0 \rightarrow S_2$ are optically almost dark with oscillator strengths of only 0.0003 and 0.0756, respectively. (c) Long-wavelength range of simulated absorption spectrum computed using the nuclear-ensemble approach, partly taking into account electron–vibrational coupling.

Figure 2 summarizes the computed results for the C132 GQDs in toluene (see Methods for details of the calculations). The four lowest transitions from the S_0 ground state are almost exclusively dominated by the four frontier orbitals shown. The degeneracy of the lowest bright transitions and of the frontier orbitals is lifted because of the absence of symmetry of the C132 GQD. However, we still find that the two lowest singlet excitations $S_0 \rightarrow S_1$ and $S_0 \rightarrow S_2$ are optically almost dark, as was found in a previous calculation[20,24] for higher symmetry GQDs and in other low-dimensional carbon structures, i.e., carbon nanotubes.[25] The oscillator strength we find for the lowest excitation (for the vertical electronic excitation) is about 2 orders of magnitude smaller than the one extracted from the experimental data in Figure 1 (see discussion below). In order to resolve this apparent discrepancy, Figure 2c shows the absorption spectrum obtained using the nuclear-ensemble approach, taking into account coupling of electronic states to the vibrational modes in the quantum dot's ground state. Our calculations only partially include electron–vibrational coupling in the sense that because of the ground-state sampling in the nuclear ensemble approach, spectral contributions for different (nonoptimized) ground state geometries are included in the shown spectra. We note that here we do not analyze the vibrational modes and vibronic progression in the spectra in detail.

Visible is an overall small red-shift of the computed spectrum (peak maximum at 577 nm) compared to the measurements in Figure 1 (peak maximum at 535 nm). However, more importantly, the two low-energy transitions (shoulders) corresponding to the two nominally "dark" electronic transitions are also visible in the calculated spectrum. We note that the absorption feature clearly visible in the experimental spectrum of Figure 1a and Figure 1b at about 600 nm is only visible as a small shoulder on the low-energy side of the main absorption feature in the calculated spectrum due to the finite phenomenological broadening that was employed in the simulation. This result illustrates that because of electron–vibrational coupling, the nominally "dark" low-energy electronic transitions significantly borrow some oscillator strength from the nominally "bright" higher-lying transitions. The main absorption feature in the spectrum in Figure 2c stems from the $S_0 \rightarrow S_3$ and $S_0 \rightarrow S_4$ transitions with oscillator strengths $f = 3.497$ and $f = 1.521$, respectively, for the vertical electronic transitions. To better reproduce the measured spectrum also for wavelengths smaller than 500 nm, electronic transitions higher in energy would have to be included in the calculations. In the present calculations, transitions from S_0 into S_5 to S_{20} only carry low oscillator strengths. A list of the lowest 20 singlet transitions including oscillator strengths is given in the Supporting Information. For completeness, also a list of the lowest 40 triplet excitations is included in the supplement.

The inset in Figure 1 illustrates that the first absorption band with a noticeable oscillator strength is observed between 700 and 750 nm. From ref 12 it follows that the molar extinction coefficient at around 530 nm is 100 000 M^{-1} cm^{-1}, and thus, the extinction coefficient at 720 nm is ~7000 M^{-1} cm^{-1}. Assuming a width of this transition of ~1700 cm^{-1} (as estimated from the fluorescence spectra in Figure 1c and Figure 1d, we calculate an oscillator strength of $f \approx 0.03$ using eq 1.

$$f = (4.3 \times 10^{-9}) \int \varepsilon(\bar{\nu})\, \mathrm{d}\bar{\nu} \tag{1}$$

From the value of the oscillator strength we estimate an excited state lifetime of ~130 ns, employing eq 2 where n is the refractive index and g_a and g_b are the degeneracy of the excited and ground state, respectively.[26]

$$\tau_{\mathrm{rad}} = (1.5 \times 10^{4}) \frac{{\lambda_{\mathrm{ba}}}^2}{n[(n^2 + 2)/3]^2} \frac{g_b}{g_a} \frac{1}{f} \tag{2}$$

Room temperature fluorescence spectra of the C132 GQDs in heptane and toluene as excited at various wavelengths are summarized in Figures 1c and 1d.

It is apparent that the main emission band associated with the 530 nm absorption feature is centered at ~750 nm. Two other fluorescence features appear around 630–640 nm and 660–670 nm. The intensity of these features is strongly dependent on the excitation wavelength, and they can be, to some degree, selectively excited. This behavior is strong evidence for different chemical species. We stress here that in fluorescence and excitation spectra minority species may be grossly overemphasized because of variations in quantum efficiency. Hence, impurities at a low percentage levels may still appear as dominant features.

The finding from the selective fluorescence spectra are corroborated by the photoluminescence excitation spectra shown in Figure 1a and Figure 1b as detected at various wavelengths for the C132 GQDs in heptane and toluene. When the emission is detected at 750 nm, the excitation spectrum is a good match of the absorption spectrum; naturally there are some variations due to the partial selectivity in the excitation spectra as the effects of heterogeneity are overcome to some degree. We note here that we have also measured excitation spectra with the wavelength detected around 825 nm where a

dx.doi.org/10.1021/jp502753a | J. Phys. Chem. A 2014, 118, 5189–5195

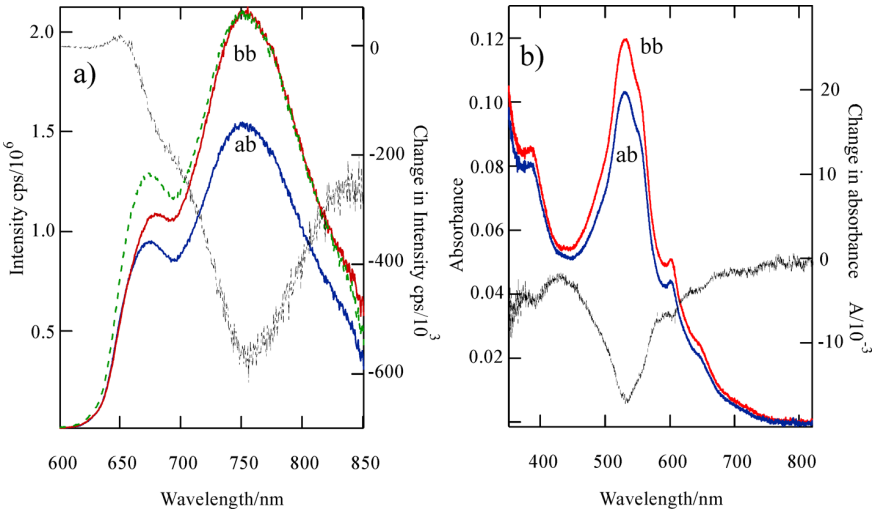

Figure 3. Selective bleaching experiment. The (a) fluorescence excited at 337 nm and (b) absorption spectra were measured in heptane before (bb) and after (ab) bleaching in dichloromethane. The dashed line in (a) shows the bleached spectrum renormalized to the 750 nm peak of the unbleached spectrum. The dash−dotted lines in (a) and (b) show the difference spectra (spectrum after bleaching minus spectrum before bleaching).

shoulder is observed in the emission spectra. These spectra are within the experimental accuracy the same as for the 750 nm detection wavelength. In the excitation spectra of the emitters at 629 or 639 nm well pronounced vibrational progressions are observed in the excitation spectra with the vibrational frequency significantly reduced for the higher singlet state at around 480 nm. When the emission is observed at 666 (toluene) or 670 nm (heptane), vibrational progressions are also observed but the transitions appear to be much broader and the electronic origin at around 480 nm carries less intensity. These spectra imply again that the emissions at 629 or 639 and at 670 or 666 nm in toluene and heptane, respectively, are likely due to other species. We note that these transitions appear to be more intense in toluene than in heptane. It appears that there is excitation energy transfer to the 750 nm emitter and that this process is more efficient in heptane than in toluene. In particular, the 639 nm emitter in toluene is much more intense than the 630 nm emitter in heptane. It is possible that there is some molecular association between the impurities (see also the discussion about the heavy atom effect below) and the C132 GQDs and that this association is more pronounced in the case of heptane, in particular for the 639 nm emitter. Possibly, toluene provides some screening effect reducing the energy transfer rate. The idea of energy transfer is corroborated by the observation of a significantly higher intensity of the 639 nm emitter and a reduced 750 nm emission in a 5-fold diluted toluene sample upon excitation at 480 nm (see Supporting Information) because energy transfer can be expected to be strongly concentration dependent. This concentration effect also excludes the explanation of the ∼630 and ∼670 nm emitters being due to H-aggregates. Likewise, J-aggregates, as a possible explanation of the 750 nm emission, can be excluded because this emission is perfectly correlated with the main absorption feature at 530 nm and independent of concentration.

Both the 629 or 639 nm and the 666 or 670 nm emissions carry very little excitation intensity in the 530 nm absorption band; the latter is the main feature of the absorption spectrum. This observation has been interpreted previously by a different branching ratio of the singlet states to the excited states that emit at around 670 and 750 nm.

To provide further evidence that 670 nm (and 630 nm) emission peaks are not due to the main species, C132 GQDs, we conducted photobleaching experiments. The fluorescence was measured in heptane before bleaching. The heptane was then evaporated, and the C132 GQDs were taken up in dichloromethane (dcm). This suspension was then exposed in a 1 cm cuvette to 12 mW of 532 nm light for 3600 s. Subsequently the dcm was evaporated at room temperature, the dry dots were taken up in heptane, and the fluorescence was remeasured. It clearly follows from Figure 3a that the 670 nm emission bleaches at a lower rate than the 750 nm emission; i.e., the bleaching is wavelength selective, indicating strongly that the 670 nm emission is due to an impurity. If the 670 nm emission were intrinsic fluorescence from the C132 GQDs, we would expect that the 532 nm bleaching led to a uniform decrease of the intensity across the emission spectrum.

We note here that the result illustrated in Figure 3a was reproduced several times. As is illustrated in Figure 3b, we have also measured the absorption spectrum before and after bleaching, and it appears that most (absorption) features down to 500 nm are due to the C132 GQDs. However, below 450 nm there is a contribution to the absorption spectrum that bleaches at a slightly lower rate. This is consistent with the observation that excitation wavelengths below 480 nm strongly select the 670 or 666 nm and the 639 or 629 nm emissions for toluene and heptane, respectively. Assuming that the ∼630 and ∼670 nm emissions are due to the C132 GQDs, it would be possible to explain the selective photochemistry by proposing that the photochemical reaction of the C132 GQDs yields a species where the emission of the 670 nm is favored because of a higher population of this state in the relaxation pathway. However, this is an unlikely explanation, since the main features of the absorption and emission spectra remain unchanged.

As previously reported,[12] the 750 nm emission exhibits a very strong external heavy atom effect.[27] We have reinvestigated this effect by adding 1,2-dibromoethane to heptane and toluene solutions. Results are summarized in Table 1, and emission

dx.doi.org/10.1021/jp502753a | J. Phys. Chem. A 2014, 118, 5189−5195

Table 1. External Heavy Atom Effect by Dibromoethane in the 750 nm Fluorescence of C132 GQDs in Heptane and Toluene[a]

toluene			heptane		
X	I(755 nm)	I_0/I(755 nm)	X	I(755 nm)	I_0/I(755 nm)
0.08	0.93	1.1	0.075	0.41	2.4
0.17	0.8	1.3	0.145	0.16	6.3
0.38	0.48	2.1	0.3	0.06	17
0.57	0.25	4	0.55	0.03	33

[a]X denotes the mole fraction. The intensities are normalized to the intensity at $X = 0$, I_0.

spectra are shown in the Supporting Information (Figure S1). Upon addition of 1,2-dibromoethane, the shape of the luminescence spectra stays approximately the same with a minor wavelength shift due to the change in the dielectric constant of the solvent mixture.

Interestingly, the heptane suspension is subject to a significantly stronger heavy atom effect than the toluene suspension as a function of the mole fraction of 1,2-dibromoethane. Stern–Volmer plots of I_0/I against the quencher concentration reveal a sizable superlinearity; this is possibly due to a contribution by static quenching caused by the molecular association of the 1,2-dibromoethane with the C132 GQDs. We note here that the quencher concentration is very high and perfect linearity in a Stern–Volmer plot cannot be expected. The significantly higher quenching effect may be due to the lower viscosity of heptane in comparison with toluene and/or a higher molecular association of the quencher with the GQDs. It is also possible that the singlet–triplet spacing varies between heptane and toluene because of the dielectric constant, resulting in a larger heavy atom effect for heptane. Importantly, we cannot exclude that the toluene shields the GQDs, dynamically or statically, to a certain extent. This latter explanation is consistent with the observation that the ~630 and ~670 nm species appear to be subject to

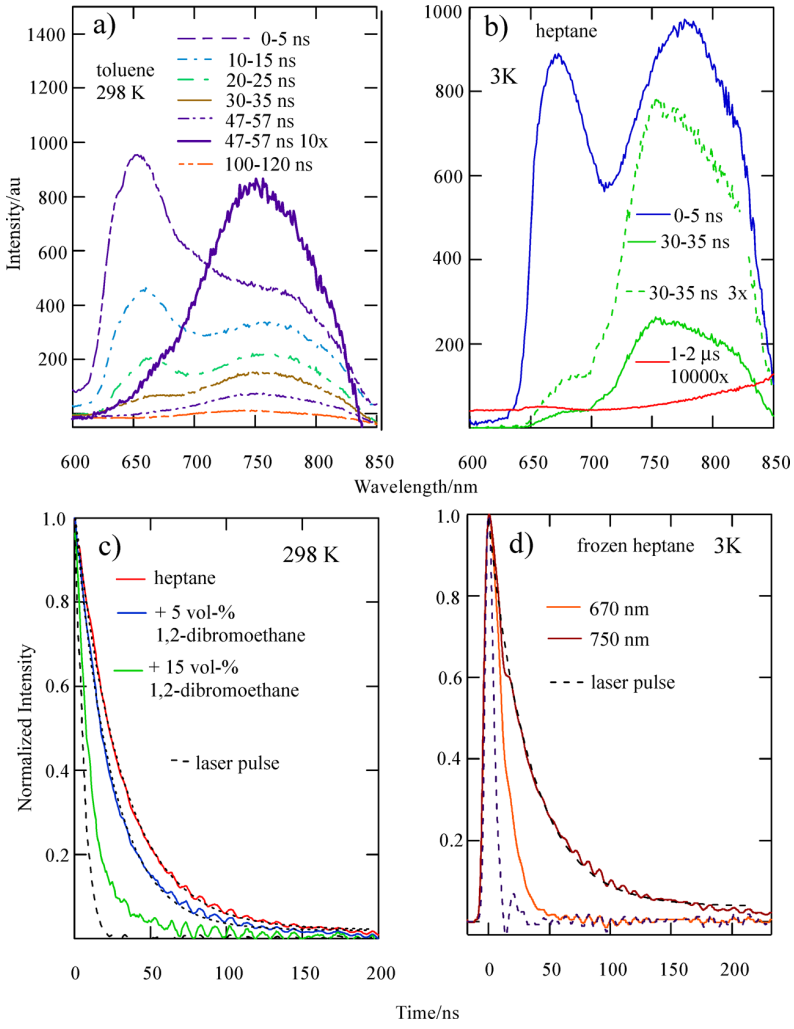

Figure 4. Time-resolved (TR) fluorescence spectra and excited state lifetime measurements of the graphene quantum dots with pulsed 337 nm N_2 laser excitation. (a) and (b) show TR spectra in toluene at 298 K and frozen heptane at 3 K, respectively. The time gate at which the emission was observed and magnification multipliers are indicated. (c) shows lifetime measurements of the graphene quantum dots for a heptane suspension and for heptane suspensions to which 5 and 15 vol % 1,2-dibromoethane were added. In (d) the decay is shown for the 750 and 670 nm emission in frozen heptane at 3 K. The dashed line in (c) and (d) shows the N_2 laser pulse.

dx.doi.org/10.1021/jp502753a | J. Phys. Chem. A 2014, 118, 5189–5195

significantly faster excited-state energy transfer to the C132 GQDs in heptane compared to toluene (see above).

The observed heavy atom effect indicates that the C132 GQDs must have a triplet state not far below the 750 nm emitting state, consistent with the decreased singlet−triplet energy spacing due to the large conjugation size and the reduced exchange interaction.[20] In agreement with this statement we note that the DFT calculations (see Supporting Information) predict a S_1−T_1 splitting of ∼3300 cm^{-1} in toluene.

The heavy atom effect is again in contradiction with the initial assignment of the 670 and 750 nm emissions to intrinsic $S_1 \rightarrow S_0$ and $T_1 \rightarrow S_0$ transitions by Mueller et al.[12] The (external) heavy atom effect strongly enhances the internal system conversion (ISC) $S_1 \rightarrow T_1$; i.e., quenching of the S_1 state and an increase in $T_1 \rightarrow S_0$ intensity are usually observed.[27] Hence, with the energy level assignment given in ref 12 a massive drop of the 670 nm emission with an increase of the 750 nm emission would be expected; however, this is not the case and the heavy atom effect quenches the 750 nm emission to a much greater extent than the 670 (630, 640) nm emissions. This indicates again that the 670 (630, 640) nm transitions are not the S_1 state of the C132 GQDs but indeed due to other species. The quenching of the 750 nm emission is consistent with it being due to the $S_1 \rightarrow S_0$ transition, and the quenching is based on the ISC $S_1 \rightarrow T_1$. If the 750 nm emission would be the (lowest-excited) T_1 state, in addition to a massive increase in its population, the radiative deactivation rate to the S_0 ground state would be increased and the 750 nm emission would be strongly enhanced by the ISC. The opposite is observed.

Figure 4 shows measurements of time-resolved emission spectra (TRS) and excited state lifetimes, respectively, upon excitation of the GQDs at 337 nm with a pulsed N_2 laser. The TRS displayed in Figure 4 a and Figure 4b confirm that the 750 nm emission decays on the 30 ns time scale, in contrast to the ∼630 and ∼670 nm emissions that decay on the 10 ns time scale. From these spectra and lifetime measurements it follows that there may be a minor component at 825 nm that displays a longer lifetime (approximately 200 ns). This is possibly due to the triplet state.

At room temperature, the lifetime of the 750 nm photoluminescence is 31 ns in heptane. In comparison a slight increase of the lifetime to 34 ns is observed in frozen heptane at 3 K. In comparison, the 670 nm emitter (impurity) has a significantly shorter lifetime. The measured lifetimes are summarized in Table 2.

Table 2. Summary of Measured Excited State Lifetimes at Room Temperature

solvent	emission wavelength, nm	lifetime, ns
toluene	640	10 ± 3
toluene	743	26 ± 2
heptane	670	8 ± 3
heptane	750	31 ± 2

From the lifetime and the calculated oscillator strength we estimate a relatively high quantum efficiency of ∼0.2 for the 750 nm emission.

The relatively long excited state lifetime of the graphene quantum dots is consistent with the oscillator strength observed in the absorption spectrum. The quantum chemical calculations as discussed above clearly confirm that the lowest excited singlet states are "near-dark states", i.e., singlet states with very low oscillator strengths.

The electronic oscillator strength we computed for S_1 in emission (f = 0.0003) is the same as in absorption and much lower than found in the measurements. However, also in emission, borrowing of oscillator strength from higher-lying transitions through electron-vibrational coupling is likely to occur in the real system. This mechanism was demonstrated to have a pronounced effect on our simulated absorption spectrum in Figure 2c.

In our measurements, we have been unable to observe a transient on the microsecond time scale between 750 and 800 nm as has been reported previously. We conclude that this reported observation may have been due to the phosphorescence of an impurity.

The remaining question is the origin of the ∼630 and 670 nm emissions; above we have been able to rule out J- and H-aggregates. It is possible that these emitters are C132 GQDs with some structural defects or different symmetry. However, it would be surprising that minor structural or symmetry changes would lead to vastly different behavior, in particular to spectra that are somewhat reminiscent of polycyclic hydrocarbons with well-defined vibrational progressions. More likely explanations for these emitters include fragments of the C132 GQDS; it is also possible that these species are oxidized GQDs. However, for the latter we would expect similar broad spectroscopic features as for the main C132 GQDs.[12,13] Further work would be needed to identify the chemical properties of these impurities; however, we note here again that impurities at very low concentration can have a significant impact on photoluminescence and excitation.

4. CONCLUSIONS

A range of spectroscopic experiments, including selective fluorescence and excitation spectra, time-resolved spectra, external heavy atom experiments, and wavelength selective bleaching experiments, were undertaken on C132 GQDs at room and low temperatures. In particular, the wavelength selective photobleaching yields strong evidence for the identification of the intrinsic emission of the C132 GQDs at 750 nm and shows that it is safe to assign emitters at around 670 and 640 nm to chemically different species. The spectra of these impurities appear to be quite intense in the fluorescence and excitation spectra because of their higher quantum efficiency and narrower features with well-defined vibrational progressions. Thus, it is possible to identify the intrinsic features of the C132 GQDs: the main absorption and emission feature are centered around 530 and 750 nm, respectively, and the two transitions have a very similar overall line shape. From a comparison of the absorption spectrum and the emission spectrum it follows that the $S_0 \rightarrow S_1$ electronic origin is around 720−730 nm and the main intensity component must be of vibrational nature in agreement with quantum chemical nuclear ensemble calculations. The relatively long lifetime of 30 ns and the relatively low oscillator strength of the transition are in qualitative accord with the quantum chemical calculations that indicate near-dark low-lying singlet states. Furthermore, the singlet state at 750 nm gets quenched upon the addition of heavy atom solvents in agreement with expectations.

dx.doi.org/10.1021/jp502753a | J. Phys. Chem. A 2014, 118, 5189−5195

■ ASSOCIATED CONTENT

Supporting Information

Full author list for refs 8 9, and19, vertical excitation energies for the first 20 singlet states, vertical excitation energies for the first 40 triplet states, spectra showing the observed heavy atom effect, and photoluminescence spectrum for diluted sample. This material is available free of charge via the Internet at http://pubs.acs.org.

■ AUTHOR INFORMATION

Corresponding Author

*E-mail: h.riesen@adfa.edu.au.

Author Contributions

The manuscript was written through contributions of all authors. All authors have given approval to the final version of the manuscript.

Notes

The authors declare no competing financial interest.

■ ACKNOWLEDGMENTS

We thank Professor Liang-shi Li, Indiana University, Bloomington, IN, for providing us with graphene quantum dots. The Paderborn group acknowledges financial support from the DFG (Grant GRK 1464) and a grant for computing time at PC^2 Paderborn Center for Parallel Computing. C.W. is grateful for his Ph.D. scholarship from the Friedrich-Ebert-Stiftung.

■ REFERENCES

(1) Kroto, H. W.; Heath, J. R.; O'Brien, S. C.; Curl, R. F.; Smalley, R. E. C-60 Buckminsterfullerene. *Nature* **1985**, *318*, 162−163.

(2) Boehm, H. P. The First Observation of Carbon Nanotubes. *Carbon* **1997**, *35*, 581−584.

(3) Geim, A. K. Graphene: Status and Prospects. *Science* **2009**, *324*, 1530−1534.

(4) Güçlü, A. D.; Potasz, P.; Hawrylak, P. Excitonic Absorption in Gate-Controlled Graphene Quantum Dots. *Phys. Rev. B* **2010**, *82*, 155445.

(5) Mochalin, V. N.; Shenderova, O.; Ho, D.; Gogotsi, Y. The Properties and Applications of Nanodiamonds. *Nat. Nanotechnol.* **2012**, *7*, 11−23.

(6) Doherty, M. W.; Manson, N. B.; Delaney, P.; Jelezko, F.; Wrachtrup, J.; Hollenberg, L. C. L. The Nitrogen-Vacancy Colour Centre in Diamond. *Phys. Rep.* **2013**, *528*, 1−45.

(7) Geim, A. K.; Novoselov, K. S. The Rise of Graphene. *Nat. Mater.* **2007**, 183−191.

(8) Novoselov, K. S.; Morozov, S. V.; Mohinddin, T. M. G.; Ponomarenko, L. A.; Elias, D. C.; Yang, R.; Barbolina, I. I.; Blake, P.; Booth, T. J.; Jiang, D.; et al. Electronic Properties of Graphene. *Phys. Status Solidi B* **2007**, *244*, 4106−4111.

(9) Wang, J. T.-W.; Ball, J. M.; Barea, E. M.; Abate, A.; Alexander-Webber, J. A.; Huang, J.; Saliba, M.; Mora-Sero, I.; Bisquert, J.; Snaith, H. J.; et al. Low-Temperature Processed Electron Collection Layers of Graphene/TiO_2Nanocomposites in Thin Film Perovskite Solar Cells. *Nano Lett.* **2014**, *14*, 724−730.

(10) Filter, R.; Farhat, M.; Steglich, M.; Alaee, R.; Rockstuhl, C.; Lederer, F. Tunable Graphene Antennas for Selective Enhancement of THz-Emission. *Opt. Express* **2013**, *21*, 3737−3745.

(11) Gierz, I.; Petersen, J. C.; Mitrano, M.; Cacho, C.; Turcu, I. C. E.; Springate, E.; Stohr, A.; Kohler, A.; Starke, U.; Cavalleri, A. Snapshots of Non-Equilibrium Dirac Carrier Distributions in Graphene. *Nat. Mater.* **2013**, *12*, 1119−1124.

(12) Mueller, M. L.; Yan, X.; McGuire, J. A.; Li, L. S. Triplet States and Electronic Relaxation in Photoexcited Graphene Quantum Dots. *Nano Lett.* **2010**, *10*, 2679−2682.

(13) Li, L. S.; Yan, X. Colloidal Graphene Quantum Dots. *J. Phys. Chem. Lett.* **2010**, 2572−2576.

(14) Yan, X.; Cui, X.; Li, B. S.; Li, L. S. Large, Solution-Processable Graphene Quantum Dots as Light Absorbers for Photovoltaics. *Nano Lett.* **2010**, *10*, 1869−1873.

(15) Yan, X.; Cui, X.; Li, L. S. Synthesis of Large, Stable Colloidal Graphene Quantum Dots with Tunable Size. *J. Am. Chem. Soc.* **2010**, *132*, 5944−5945.

(16) Yan, X.; Li, L. S. Solution-Chemistry Approach to Graphene Nanostructures. *J. Mater. Chem.* **2011**, *21*, 3295−3300.

(17) Zhang, Z. P.; Zhang, J.; Chen, N.; Qu, L. T. Graphene Quantum Dots: An Emerging Material for Energy-Related Applications and Beyond. *Energy Environ. Sci.* **2012**, *5*, 8869−8890.

(18) Li, L.; Wu, G.; Yang, G.; Peng, J.; Zhao, J.; Zhu, J.-J. Focusing on Luminescent Graphene Quantum Dots: Current Status and Future Perspectives. *Nanoscale* **2013**, *5*, 4015−4039.

(19) Frisch, M. J.; Trucks, G. W.; Schlegel, H. B.; Scuseria, G. E.; Robb, M. A.; Cheeseman, J. R.; Scalmani, G.; Barone, V.; Mennucci, B.; Petersson, G. A.; et al. *Gaussian 09*, revision B.01; Gaussian, Inc.: Wallingford, CT, 2009.

(20) Schumacher, S. Photophysics of Graphene Quantum Dots: Insights from Electronic Structure Calculations. *Phys. Rev. B* **2011**, *83*, 081417.

(21) Dennington, R.; Keith, T.; Millam, J. *GaussView*, version 5; Semichem Inc.: Shawnee Mission, KS, 2009.

(22) Crespo-Otero, R.; Barbatti, M. Spectrum Simulation and Decomposition with Nuclear Ensemble: Formal Derivation and Application to Benzene, Furan and 2-Phenylfuran. *Theor. Chem. Acc.* **2012**, *131*, 1237.

(23) Barbatti, M.; Granucci, G.; Persico, M.; Ruckenbauer, M.; Vazdar, M.; Eckert-Maksic, M.; Lischka, H. The On-the-Fly Surface-Hopping Program System NEWTON-X: Application to ab Initio Simulation of the Nonadiabatic Photodynamics of Benchmark Systems. *J. Photochem. Photobiol., A* **2007**, *190*, 228−240.

(24) Ozfidan, I.; Korkusinski, M.; Güçlü, A. D.; McGuire, J. A.; Hawrylak, P. Microscopic Theory of Optical Properties of Colloidal Graphene Quantum Dots. *Phys. Rev. B* **2014**, *89*, 085310.

(25) Kilina, S.; Tretiak, S.; Doorn, S. K.; Luo, Z.; Papadimitrakopoulos, F.; Piryatinski, A.; Saxena, A.; Bishop, A. R. Cross-Polarized Excitons in Carbon Nanotubes. *Proc. Natl. Acad. Sci. U.S.A.* **2008**, *105*, 6797−6802.

(26) Solomon, E. I., Lever, A. B. P., Eds. *Inorganic Electronic Structure and Spectroscopy*; Wiley-Interscience: Hoboken, NJ, 2006; Vol. *I*.

(27) McGlynn, S. P.; Azumi, T.; Kinoshita, M. *Molecular Spectroscopy of the Triplet State*; Prentice-Hall: Englewood Cliffs, NJ, 1969; p xiii, 434 pp.

■ NOTE ADDED AFTER ASAP PUBLICATION

This article posted ASAP on July 8, 2014. The reference numbers in the following locations have been revised: Methods section, paragraph 2; Results and Discussion section, paragraph 2, sentence 4, and paragraph 12, sentence 2. The correct version posted July 17, 2014.

Supporting Information

On the Optical Spectroscopy of Graphene Quantum Dots: the Case of C132.

Hans Riesen[a], Christian Wiebeler[b], and Stefan Schumacher[b]*

[a]School of Physical, Environmental and Mathematical Sciences

UNSW Australia, ADFA, Canberra Australian Capital Territory 2600, Australia

[b]Department of Physics and Center for Optoelectronics and Photonics Paderborn (CeOPP)

University of Paderborn

Warburger Str. 100

33098 Paderborn, Germany

Full Author List for References 8, 9 and 19

(8) Novoselov, K. S.; Morozov, S. V.; Mohinddin, T. M. G.; Ponomarenko, L. A.; Elias, D. C.; Yang, R.; Barbolina, I. I.; Blake, P.; Booth, T. J.; Jiang, D.; Giesbers, J.; Hill, E. W.; Geim, A. K., Electronic properties of graphene. *Phys Status Solidi B* **2007**, *244* (11), 4106-4111.

(9) Wang, J. T.-W.; Ball, J. M.; Barea, E. M.; Abate, A.; Alexander-Webber, J. A.; Huang, J.; Saliba, M.; Mora-Sero, I.; Bisquert, J.; Snaith, H. J.; Nicholas, R. J., Low-Temperature Processed Electron Collection Layers of Graphene/TiO2Nanocomposites in Thin Film Perovskite Solar Cells. *Nano Lett* **2014**, *14* (2), 724-730.

(19) Frisch, M. J.; Trucks, G. W.; Schlegel, H. B.; Scuseria, G. E.; Robb, M. A.; Cheeseman, J. R.; Scalmani, G.; Barone, V.; Mennucci, B.; Petersson, G. A.; Nakatsuji, H.; Caricato, M.; Li, X.; Hratchian, H. P.; Izmaylov, A. F.; Bloino, J.; Zheng, G.; Sonnenberg, J. L.; Hada, M.; Ehara, M.; Toyota, K.; Fukuda, R.; Hasegawa, J.; Ishida, M.; Nakajima, T.; Honda, Y.; Kitao, O.; Nakai, H.; Vreven, T.; Montgomery, Jr., J. A.; Peralta, J. E.; Ogliaro, F.; Bearpark, M.; Heyd, J. J.; Brothers, E.; Kudin, K. N.; Staroverov, V. N.; Kobayashi, R.; Normand, J.; Raghavachari, K.; Rendell, A.; Burant, J. C.; Iyengar, S. S.; Tomasi, J.; Cossi, M.; Rega, N.; Millam, J. M.; Klene, M.; Knox, J. E.; Cross, J. B.; Bakken, V.; Adamo, C.; Jaramillo, J.; Gomperts, R.; Stratmann, R. E.; Yazyev, O.; Austin, A. J.; Cammi, R.; Pomelli, C.; Ochterski, J. W.; Martin, R. L.; Morokuma, K.; Zakrzewski, V. G.; Voth, G. A.; Salvador, P.; Dannenberg, J. J.; Dapprich, S.; Daniels, A. D.; Farkas, Ö.; Foresman, J. B.; Ortiz, J. V.; Cioslowski, J.; Fox, D. J. *Gaussian 09, Revision B.01*, Gaussian, Inc., Wallingford CT, **2009**.

Table S1: Excitation wavelengths in nm and oscillator strengths for the first 20 singlet states. The values were obtained using B3LYP/6-31G* for the optimized ground state geometry. Toluene was taken into account as solvent by using the polarizable continuum model. Note that the two brightest excitations are found for state 3 and 4 and that the higher-lying excitations (5-20) only show low oscillator strengths.

Singlet States		
State	**Wavelength/nm**	**Osc. Strength**
1	645.86	0.0003
2	627.00	0.0756
3	565.78	3.4972
4	541.87	1.5210
5	528.56	0.0023
6	504.02	0.0073
7	493.89	0.0001
8	486.59	0.0016
9	466.81	0.0000
10	466.69	0.0006
11	460.36	0.0010
12	449.27	0.0044
13	440.32	0.1310
14	436.95	0.0089
15	429.96	0.0002
16	426.69	0.0595
17	422.28	0.0064
18	419.92	0.0000
19	414.50	0.0590
20	414.09	0.0020

Table S2: Wavelengths in nm for the first 40 triplet states. The values were obtained using the same methodology as for the calculation of the singlet excitations, i.e. using B3LYP/6-31G* for vertical excitation energies taking Toluene into account as solvent in a polarizable continuum model. All transitions from the singlet ground state to the triplet states are optically forbidden such that the calculated oscillator strengths are zero.

	Triplet States		
State	**Wavelength/nm**	**State**	**Wavelength/nm**
1	819.81	**21**	448.71
2	671.19	**22**	448.50
3	668.73	**23**	441.33
4	658.80	**24**	437.77
5	638.76	**25**	436.05
6	588.49	**26**	428.01
7	551.10	**27**	427.28
8	538.26	**28**	423.56
9	537.02	**29**	422.77
10	521.96	**30**	419.22
11	511.80	**31**	414.55
12	497.81	**32**	413.12
13	487.99	**33**	412.17
14	481.14	**34**	411.01
15	469.32	**35**	405.78
16	468.22	**36**	404.72
17	467.88	**37**	403.45
18	460.63	**38**	401.70
19	458.20	**39**	400.46
20	452.74	**40**	398.07

5.4 Molecular Orbitals & Spectrum Decomposition

Similarly to the investigation in reference [54], the frontier MOs are classified into inner- and outer-shell and their energetic ordering is investigated, see figure 5.2. This leads to the following statements:

- The HOMO-1 and HOMO are nearly degenerate and can be classified as inner-shell
- The same holds for LUMO and LUMO+1
- HOMO-2 and LUMO-2 belong to the class of outer-shell
- The electronic gap is 2.34 eV
- Considering the first absorption maximum, the optical gap is about 2.24 eV, which depends on the applied broadening
- The energy of both gaps is similar

To sum these findings up, the results are either comparable to the previously reported investigations, i.e. energetic ordering and structure of the frontier orbitals, or show the expected trend, i.e. electronic and optical gap for the intermediately sized C132 compared to the other two GQDs investigated in reference [54]. The fact that in contrast to the previously reported calculations, no symmetry constraints were applied does, therefore, not influence these observations.

In order to further analyze the spectrum, the contributions of the different electronic states can be investigated analogous to the discussion in reference [53]. As can be seen in figure 5.3, the lowest energy shoulder is not only caused by the absorption of S_1, but also by the absorption of S_2. Parts of the absorption of S_2 and of S_3 result in the second shoulder. The source of the absorption around the maximum is traced back to the absorption of three excited states: S_3, S_4, and S_5. Finally, the remainder of the absorption originates from the higher-lying and mainly dark states, which have been grouped in two groups each consisting of several excited electronic states. For the sake of comparison, also the oscillator strengths from a VEA calculation using the optimized S_0 geometry are shown as sticks. To conclude, the approach of decomposing a total spectrum into the contributions from adiabatic states allows a more detailed understanding compared to an assignment based on the comparison with results from VEA.

To further improve the understanding of the spectra of GQDs, a spectrum simulation based on the quantum mechanical FCA could be employed. However, due to the size of the investigated molecule, such a calculation is computationally not feasible for C132. In chapter 6, smaller two dimensional conjugated systems will, therefore, be investigated.

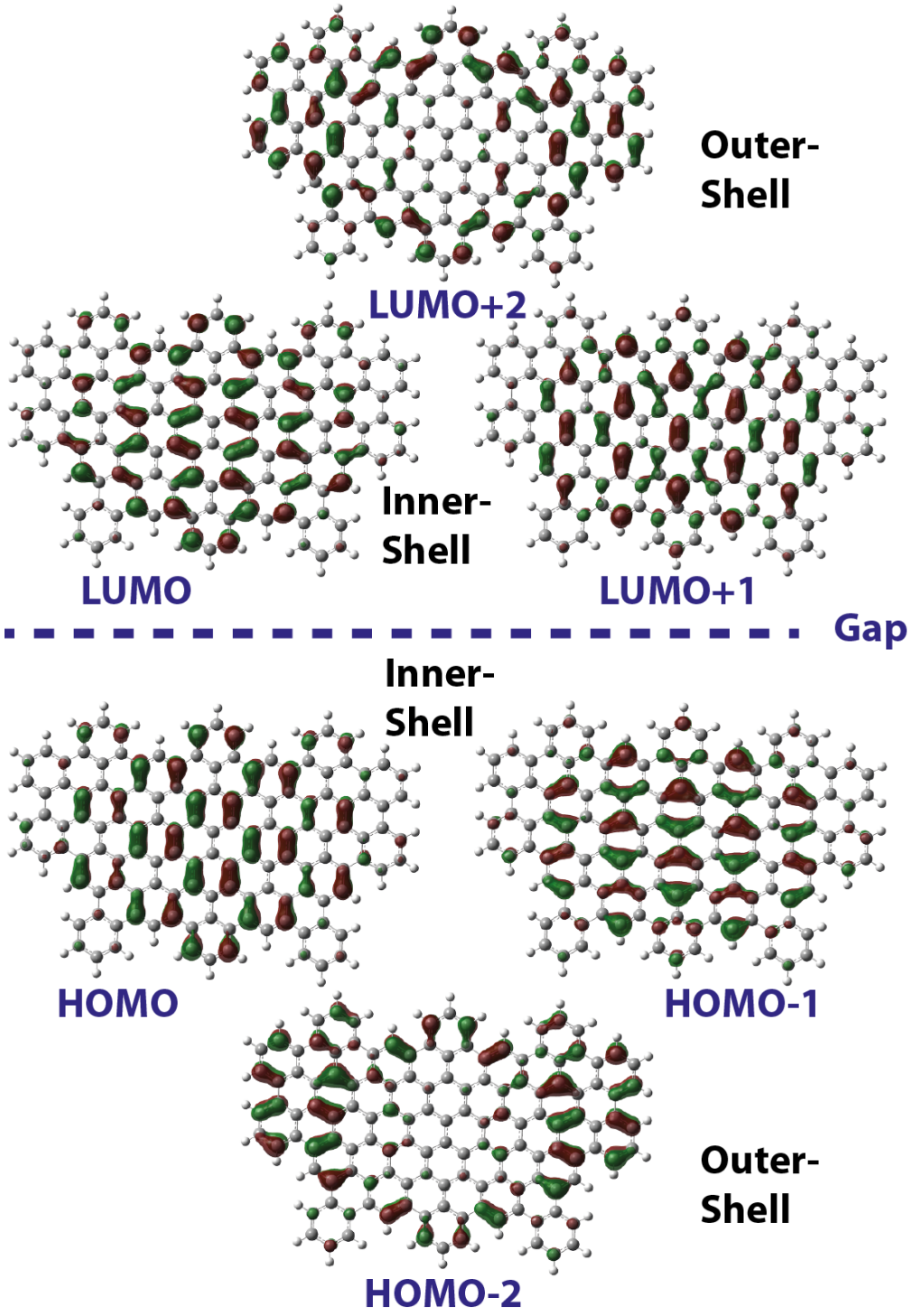

Figure 5.2: Frontier MOs of C132. The carbon atoms are represented in dark grey and the hydrogen atoms in light grey. The MOs can be classified into two shells: inner (HOMO-1, HOMO, LUMO, and LUMO+1) and outer (HOMO-2 and LUMO+2).

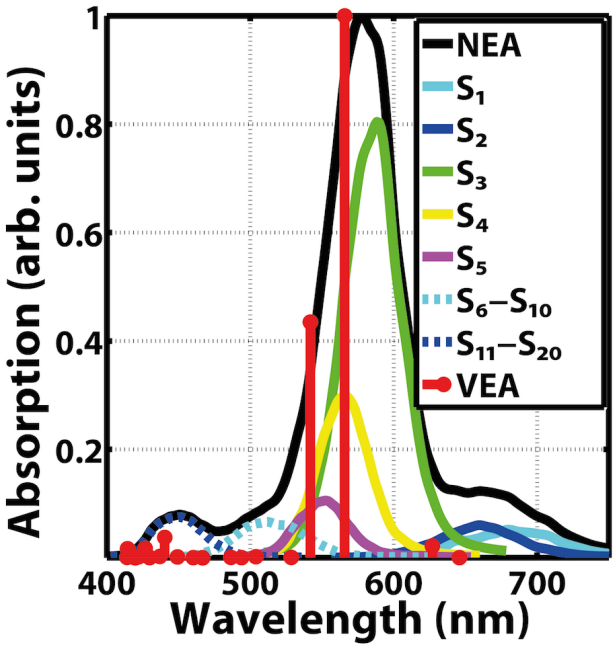

Figure 5.3: Simulated spectrum and contributions of the electronic states towards the total spectrum. The oscillator strengths obtained from the corresponding calculation using VEA are also shown as sticks in red. The first shoulder is caused by absorption of S_1 and S_2. The latter also contributes to the second shoulder together with S_3.

6 Medium-Sized Two Dimensional Conjugated Systems: Perylene Derivatives

> There is no point in undertaking a problem if the methodology and means for solving it are not available: It is important to feel that a problem is ripe for solution.
>
> *(Martin Karplus[55])*

As graphene can be seen as a two dimensional analogue of one dimensional conjugated polymers, extended perylenes can be seen as a two dimensional analogue of one dimensional oligomers. The conjugated system in this case extends in two directions with similar but finite lengths, giving rise to special electronic and optical properties of this particular class of polycyclic aromatic hydrocarbons. Derivatives of perylene are promising for organic electronics, because they show for example strong luminescence.[56] Furthermore, they might be used in OPV.[57] In order to design such molecules for a specific application, their properties have to be understood on a molecular level. This chapter starts with the description of the quantum mechanical FCP and a discussion of vibronically allowed transitions. The included paper deals with the electronic and optical properties of perylene derivatives that have been synthesized and investigated in experiment.[3] After this, the influence of the DFT functional and basis set on the FC spectrum is discussed. Furthermore, the results obtained for a perylene derivative obtained with VEA, NEA and FCA are compared. For the latter, the influence of a different broadening and of the Herzberg-Teller approximation (HTA) is also investigated. The chapter ends with the calculation of the fluorescence spectrum using FCA.

6.1 Quantum Mechanical Description of the Franck-Condon Principle

As it was mentioned in the previous chapter, the FCP can be stated as:[49] "Nuclei preserve their dynamical state during an electronic transition." This can be rephrased in a quantum mechanical description:[49] "The nuclear wave function remains unchanged during an electronic transition."

A depiction of the quantum mechanical FCP and its influence on an absorption spectrum are shown in figure 6.1. The vibrational state that mostly resembles the vibrational

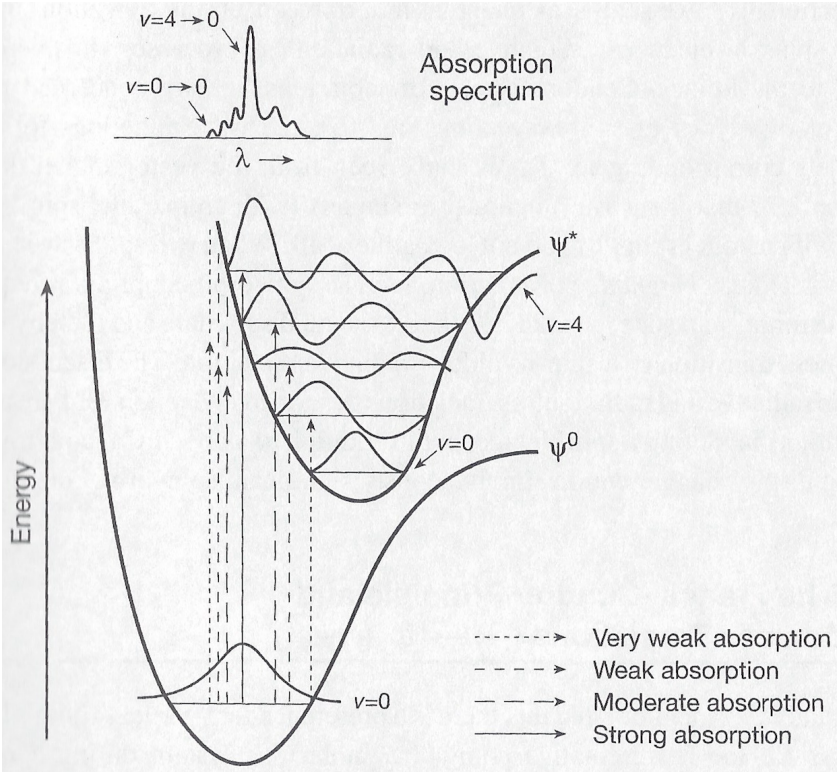

Figure 6.1: Illustration of the FCP taken from reference [50]. The absorption of a molecule in its ground vibrational state of S_0 is the stronger, the higher the resemblance between this vibrational state and the vibrational state of the excited state is. Therefore, a vibronic structure of the electronic transition can be seen in the absorption spectrum.

state of S_0 is a state with a peak immediately above the equilibrium geometry of S_0. It has to be mentioned that even the classical description, i.e. VEA, often yields similar energy levels as the quantum mechanical description.[49]

In order to describe the FCP in quantitative terms, the electronic dipole transition moment between the ground vibronic state $|\varepsilon_n \nu_{nk}\rangle$ and the upper vibronic state $|\varepsilon_{n'} \nu_{n'k'}\rangle$ has to be analyzed. This will be done following the description found in reference [49].

The electric dipole moment in a molecule depends on the positions and charges of the electrons, $\boldsymbol{r}_i$ and $-e$, and on the positions and charges of the nuclei, $\boldsymbol{R}_I$ and $Z_I e$, respectively:

$$\boldsymbol{\mu} = -e \sum_i \boldsymbol{r}_i + e \sum_I Z_I \boldsymbol{R}_I = \boldsymbol{\mu}_e + \boldsymbol{\mu}_N \tag{6.1}$$

The BOA leads to a separation of the wave function into an electronic and a nuclear part and the electronic wave function does only depend parametrically on the positions of the nuclei. So the vibronic state $|\varepsilon_n \nu_{nk}\rangle$ can be written as the wave function $\Psi_\varepsilon(\boldsymbol{r}; \boldsymbol{R})\Psi_\nu(\boldsymbol{R})$, where $\boldsymbol{r}$ and $\boldsymbol{R}$ denote the collective electronic and nuclear coordinates,

respectively. Following this notation, the excited vibronic state $|\varepsilon_{n'}\nu_{n'k'}\rangle$ is written $\Psi_{\varepsilon'}(\boldsymbol{r};\boldsymbol{R})\Psi_{\nu'}(\boldsymbol{R})$

After this considerations, the electronic dipole transition moment can be calculated:

$$\langle\varepsilon_{n'}\nu_{n'k'}|\boldsymbol{\mu}|\varepsilon_n\nu_{nk}\rangle = \int \Psi^*_{\varepsilon'}(\boldsymbol{r};\boldsymbol{R})\Psi^*_{\nu'}(\boldsymbol{R})[\boldsymbol{\mu}_e+\boldsymbol{\mu}_N]\Psi_\varepsilon(\boldsymbol{r};\boldsymbol{R})\Psi_\nu(\boldsymbol{R})\mathrm{d}\boldsymbol{r}\mathrm{d}\boldsymbol{R} \tag{6.2}$$

$$= \int \Psi^*_{\nu'}(\boldsymbol{R})\left[\int \Psi^*_{\varepsilon'}(\boldsymbol{r};\boldsymbol{R})\boldsymbol{\mu}_e\Psi_\varepsilon(\boldsymbol{r};\boldsymbol{R})\mathrm{d}\boldsymbol{r}\right]\Psi_\nu(\boldsymbol{R})\mathrm{d}\boldsymbol{R} \tag{6.3}$$

$$+ \int \Psi^*_{\nu'}(\boldsymbol{R})\boldsymbol{\mu}_N\left[\int \Psi^*_{\varepsilon'}(\boldsymbol{r};\boldsymbol{R})\Psi_\varepsilon(\boldsymbol{r};\boldsymbol{R})\mathrm{d}\boldsymbol{r}\right]\Psi_\nu(\boldsymbol{R})\mathrm{d}\boldsymbol{R}$$

Due to the orthogonality of the electronic states for fixed $\boldsymbol{R}$, the last term vanishes. Now in a first approximation, the integral over the electron coordinates is independent of the positions of nuclei as long as they are close to the equilibrium. Therefore, the expression can be approximated by a constant $\boldsymbol{\mu}_{\varepsilon'\varepsilon}$. Furthermore, the overlap integral between the two vibrational states in their respective electronic state can be defined as:

$$S(\nu_{n'k'},\nu_{nk}) = \int \Psi^*_{\nu'}(\boldsymbol{R})\Psi_\nu(\boldsymbol{R})\mathrm{d}\boldsymbol{R} \tag{6.4}$$

So the overall electronic dipole transition moment is:

$$\langle\varepsilon_{n'}\nu_{n'k'}|\boldsymbol{\mu}|\varepsilon_n\nu_{nk}\rangle = \boldsymbol{\mu}_{\varepsilon'\varepsilon}\int \Psi^*_{\nu'}(\boldsymbol{R})\Psi_\nu(\boldsymbol{R})\mathrm{d}\boldsymbol{R} = \boldsymbol{\mu}_{\varepsilon'\varepsilon}S(\nu_{n'k'},\nu_{nk}) \tag{6.5}$$

As discussed qualitatively before, the electronic dipole transition moment is largest between vibrational states that have the greatest overlap. In general, significant values for the overlap integral are not obtained for a single vibrational state ν', but for a progression of vibrational states. This causes a series of vibrational transitions that can be seen in the absorption spectrum and is called a progression of transitions. In addition, the FC factors are defined as $|S(\nu',\nu)|^2$ and the relative intensities of the absorption lines are proportional to them, because they are proportional to the square of the electronic dipole transition moment, see the discussion in chapter 5.

Taking equation 6.5 as a starting point, expressions for the calculation of FC spectra can be derived.[58] Furthermore, this approach, i.e. FCA, can be generalized by expanding $\boldsymbol{\mu}_{\varepsilon'\varepsilon}$ as a Taylor series in the normal coordinates around a reference state, so that the electronic transition dipole moment is not constant anymore:[58]

$$\boldsymbol{\mu}_{\varepsilon'\varepsilon}(Q') \approx \boldsymbol{\mu}_{\varepsilon'\varepsilon}(Q'_{eq}) + \sum_{k=1}^{N}\left(\frac{\partial\boldsymbol{\mu}_{\varepsilon'\varepsilon}}{\partial Q'_k}\right)_{eq} Q'_k + \ldots \tag{6.6}$$

In this expression, the normal coordinates Q' of the final state and its equilibrium geometry Q'_{eq} are taken into account. The zeroth order term corresponds to the FCA as it was derived before. This approximation yields in general good results for allowed transitions. The consideration of a variation of the dipole moment during an electronic transition is necessary for weakly allowed or forbidden transitions. To achieve this,

the linear term in the expansion can be considered, giving rise to the HTA. Further information concerning the numerical implementation that is used for the calculation of vibronic spectra will not be discussed in the text, but can be found in reference [58].

Considering all FC factors for transitions from a given state ν_{nk} to the electronic state n', the following sum rule can be derived:

$$\begin{aligned}\sum_{\nu'} |S(\nu_{n'k'}, \nu_{nk})|^2 &= S^*(\nu_{n'k'}, \nu_{nk}) S(\nu_{n'k'}, \nu_{nk}) = \sum_{k'} \left(\langle \nu_{n'k'} \,|\, \nu_{nk} \rangle\right)^* \langle \nu_{n'k'} \,|\, \nu_{nk} \rangle \\ &= \sum_{k'} \langle \nu_{nk} \,|\, \nu_{n'k'} \rangle \langle \nu_{n'k'} \,|\, \nu_{nk} \rangle = \langle \nu_{nk} | \sum_{k'} |\nu_{n'k'}\rangle \langle \nu_{n'k'} \,|\, \nu_{nk} \rangle \\ &= \langle \nu_{nk} \,|\, \nu_{nk} \rangle = 1\end{aligned} \tag{6.7}$$

Apart from rewriting the expression, only the orthonormality of the vibrational states and the closure relation have been used. This equation defines an analytic limit for the calculation of FC spectra. Therefore, the convergence of the calculations towards this limit can be determined to assess the accuracy of the spectrum simulation, for which only a limited number of integrals and a limited number of vibrational excitations are used. An analogous expression exists for the HTA, so that even for this approximation the convergence can be determined easily as well.[58]

6.2 Vibronically Allowed Transitions

The dark transitions that have been found in the absorption spectrum of C132, as it was discussed in chapter 5, can become visible in the absorption spectrum by intensity borrowing. This can be understood in the framework of the quantum mechanical FCP according to reference [49].

The electronic Hamiltonian depends on nuclear coordinates and can be expressed using a Taylor expansion with respect to displacements along the normal coordinates:

$$H = H^{(0)} + \sum_i \left(\frac{\partial H}{\partial Q_i}\right) Q_i + \dots \tag{6.8}$$

The eigenfunctions of the unperturbed Hamiltonian $H^{(0)}$ are denoted ψ_ε with energies E_ε. The eigenstates are mixed due to the presence of the additional terms. The perturbed wave function belonging to the electronic eigenfunction $\psi_{\varepsilon'}$ can be written as:

$$\psi = \psi_{\varepsilon'} + \sum_{\varepsilon \neq \varepsilon'} c_\varepsilon \psi_\varepsilon \qquad \text{with} \qquad c_\varepsilon = \frac{\langle \varepsilon_n \,|\, \sum_i (\partial H / \partial Q_i)_0 \,|\, \varepsilon_{n'} \rangle \, Q_i}{E_{\varepsilon'} - E_\varepsilon} \tag{6.9}$$

The absorption from the lower unperturbed electronic state ε'' to the upper perturbed electronic state ε' is now investigated. The electronic dipole transition moment can be written as:

$$\boldsymbol{\mu}_{\varepsilon',\varepsilon''} = \langle \varepsilon_{n'} \,|\, \boldsymbol{\mu} \,|\, \varepsilon_{n''} \rangle + \sum_{n \neq n'} c_{\varepsilon}^{*} \langle \varepsilon_{n} \,|\, \boldsymbol{\mu} \,|\, \varepsilon_{n''} \rangle \tag{6.10}$$

The first matrix element is zero for a forbidden transition, so:

$$\boldsymbol{\mu}_{\varepsilon',\varepsilon''} = \sum_{n \neq n'} c_{\varepsilon}^{*} \langle \varepsilon_{n} \,|\, \boldsymbol{\mu} \,|\, \varepsilon_{n''} \rangle \tag{6.11}$$

To conclude, the transition from ε'' to ε' can borrow intensity from the allowed transitions between ε'' and ε, when the perturbation can mix the states ε' and ε as can be seen in the definition of the coefficients c_{ε}. This explains the visibility of the two nominally dark states in the experimental spectrum of C132.

6.3 "Polycyclic Aromatic Hydrocarbons Obtained by Lateral Core Extension of Mesogenic Perylenes: Absorption and Optoelectronic Properties"

This paper has been published in "Chemistry - A European Journal" and reports the synthesis, experimental characterization and quantum chemical investigation of extended perylene derivatives. The main findings of our theoretical investigations are:

1. The red-shift of the low-energy absorption of the imides compared to the esters can be traced back to the more planar structure of the perylene core for the former series.

2. The extension of the core does not lead to a red-shift of absorption, owing to the fact that the NTOs involved in the transitions stay in principle the same upon extension.

3. The first absorption band in the UV increases relative to the visible absorption with larger size of the molecule. The HONTOs describing this absorption are located at the extended parts and the LUNTOs at the perylene core, explaining this finding.

4. In order to identify all the absorption peaks found in experiment, the calculation of absorption spectra using VEA is not sufficient and FCA has to be employed.

In the sections 6.4 to 6.7, the calculation of FC spectra for one of the molecules will be studied in more detail.

ChemPubSoc Europe

DOI: 10.1002/chem.201403287

CHEMISTRY
A European Journal
Communication

Electroluminescence

Polycyclic Aromatic Hydrocarbons Obtained by Lateral Core Extension of Mesogenic Perylenes: Absorption and Optoelectronic Properties

Joachim Vollbrecht,[a, b] Harald Bock,[b] Christian Wiebeler,[a] Stefan Schumacher,[a] and Heinz Kitzerow*[a]

Abstract: Bilaterally extended perylenes were synthesized, characterized, and used to create organic light-emitting devices. A detailed investigation of the electronic and optical properties, and a comparison of perylene derivatives and compounds with unilaterally and bilaterally extended aromatic cores, reveal unexpected changes of the absorption spectrum, which are in agreement with simulations based on DFT.

Polycyclic aromatic hydrocarbons are very promising materials for organic electronics. For example, perylene and its derivatives have been extensively studied because it shows a very strong luminescence with quantum yields exceeding 99%.[1] Also, the series of -rylenes is well known[2] and is useful for electroluminescence and photovoltaics.[3] Likewise, circular polyaromatic cores (coronene, hexabenzocoronene, and their symmetric extensions) have been extensively studied.[4] Lateral flexible chains attached to a polycyclic aromatic core may yield discotic liquid crystals, which form columnar mesophases.[5–10] The latter can show a large charge carrier mobility, similar to smectic mesophases of calamitic liquid crystals (containing rodlike molecules).[11–12] Charge-carrier mobilities exceeding 0.1 $cm^2V^{-1}s^{-1}$ have been reported for both columnar and smectic liquid crystals.[5–12] In addition to advantageous semiconducting properties, many polycyclic hydrocarbons show a very high quantum yield of luminescence, which makes them perfect candidates for fabricating not only conducting but also luminescent layers in organic light-emitting diodes (OLEDs). During the search for efficient emitters with tailored chromaticity, many different compounds consisting of disklike aromatic molecules have been synthesized. The wavelengths of absorption and luminescence increase typically with increasing size of the aromatic core,[13] but also depend on the lateral substituents. Moreover, the formation of J and H aggregates may cause blue- and redshifts in absorption, respectively,[14] whereas the formation of dimers in the excited state (excimers) can cause a huge redshift of the luminescence.[15] In contrast to the size effects in planar polycyclic aromatic systems,[2–4] the behavior of the corresponding twisted[16,17] or curved structures[18] is much more sophisticated and less predictable. Therefore, experimental and theoretical investigations into polycyclic hydrocarbons with sterically demanding side groups are needed.

Herein, we describe the synthesis of polyaromatic hydrocarbons obtained by systematic lateral extension of a perylene core; their application as emitter materials for OLEDs; and compare the absorption spectra of derivatives containing a perylene, a unilaterally extended perylene core, and a bilaterally extended perylene core. The experimental spectra have been compared with quantum chemical calculations based on DFT.

In particular, asymmetric lateral extensions of the perylene core through the addition of naphthalene units and subsequent cyclization have been studied. The corresponding lateral extension of perylene on one side has been reported previously.[19] Here, the perylene core is extended on both sides. A comparison of different members of this series reveals a continuous change of the chromaticity of the absorption and luminescence to shorter wavelengths with increasing size of the aromatic core of the molecules. This surprising behavior is in stark contrast to other homologuous series of aromatic compounds. Quantum chemical calculations show that this change is caused by the intramolecular tension of the nonplanar molecules.

We report the synthesis of an extended perylene with two [4]helicene fragments. Perylene-3,4,9,10-tetracarboxylic tetraethylester (**2**) was used as a starting material because of its high solubility and easy synthesis from the commercially available perylene-3,4,9,10-tetracarboxylic dianhydride (**1**).[20] The bromination of perylene–tetraesters, such as **2**, is known to yield a mixture of 1,6-dibromo, 1,7-dibromo, 1-bromo, and non-brominated products,[21] which can be separated by column chromatography. The dibrominated products had the highest polarity and were subsequently isolated (6:1 1,6-dibromo/1,7-dibromo). Naphthalene-1-boronic acid was used as a counterpart for a Suzuki cross-coupling with **4** as the product. Cyclization of **4** induced by irradiation in the presence of oxygen took place to yield ester **5**. After saponification of **5**,

[a] J. Vollbrecht, C. Wiebeler, Prof. S. Schumacher, Prof. H. Kitzerow
Center for Optoelectronics and Photonics Paderborn
Universität Paderborn
Warburger Strasse 100, 33098 Paderborn (Germany)
E-mail: heinz.kitzerow@upb.de

[b] J. Vollbrecht, Dr. H. Bock
Centre de Recherche Paul Pascal (CRPP), CNRS
Universite Bordeaux, 33600 Pessac (France)

Supporting information for this article is available on the WWW under http://dx.doi.org/10.1002/chem.201403287.

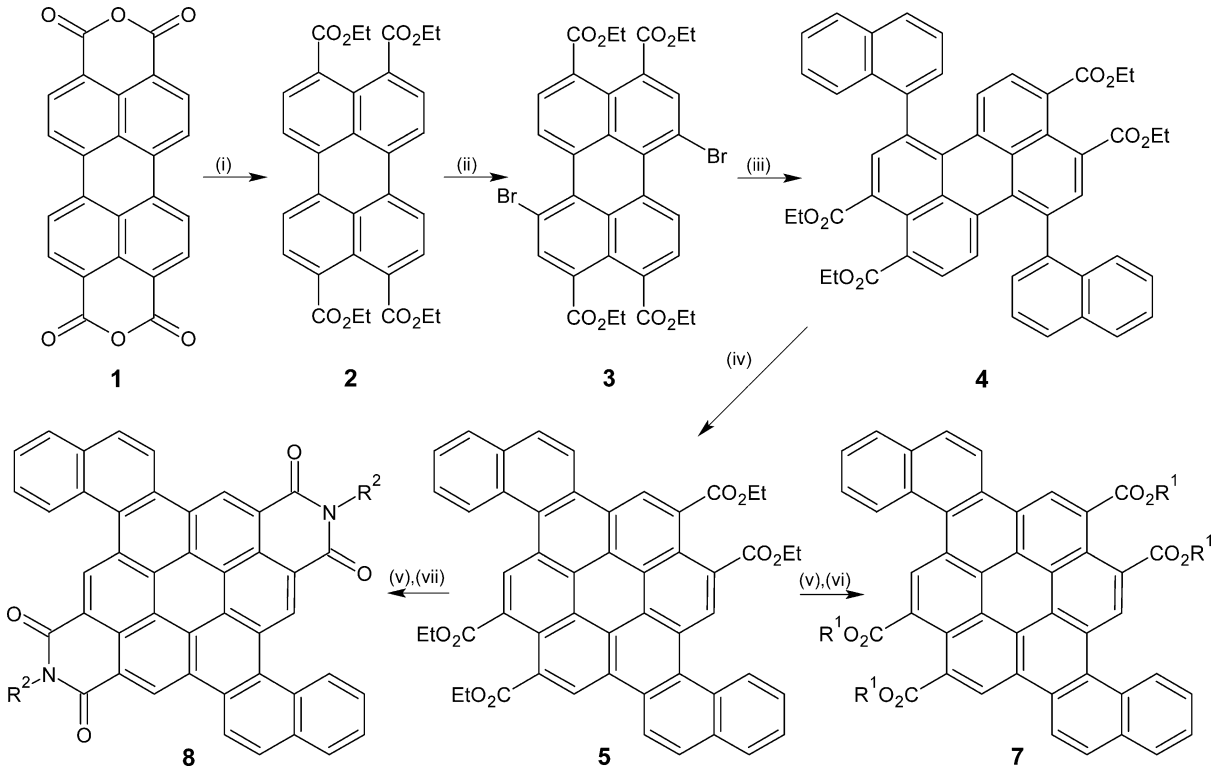

Scheme 1. Synthesis of esters **7** and bisimide **8**: i) EtBr, EtOH/THF (1:1), 1,5-diazabicyclo[5.4.0]undec-5-ene (DBU), 25 °C, 24 h, 77%; ii) Br_2, K_2CO_3, CH_2Cl_2, 25 °C, 48 h, 73%; iii) naphthalene-1-boronic acid, Na_2CO_3 (aq.), $[Pd(PPh_3)_4]$, toluene/H_2O/EtOH (50:17:7), 80 °C, 24 h, 86%; iv) I_2, light, toluene, 111 °C, 3 h, 59%; v) KOH, MeOH, 170 °C, 4 h, 98%; vi) R^1Br, R^1OH, CH_3CN, DBU, 60 °C, 24 h, 14–35%; vii) 6-undecylamine, imidazole, 180 °C, 5 h, 97%.

which yielded dianhydride **6** as the product, different compounds with a dinaphthocoronene core were synthesized, namely, three different tetraesters **7** and one bisimide **8** (R^1: -butyl (**10**), -2-ethylhexyl (**11**), -2-butyloctyl (**12**); R^2: -6-undecyl (**13**); Scheme 1 and Scheme 2). Additional information and analytical data can be found in the Supporting Information.

The low solubility of dianhydride **6** makes the synthesis of new ester compounds a challenge (see the Supporting Information). The phase transitions of the newly synthesized compounds were characterized by polarized light microscopy and differential scanning calorimetry (Table 1). Only the compounds with longer side chains undergo phase transitions from the crystalline to the isotropic phase within an applicable range.

As expected, the absorption spectra of the ester compounds show similar peaks, whereas the spectrum of the bisimide shows a redshift (Figure 1 a). The photoluminescence spectra

Table 1. Overview and phase transitions of the synthesized compounds determined by differential scanning calorimetry and polarized light microscopy.

	R	M [g mol^{-1}]	Yield [%]	$T_{crys\rightarrow iso}$ [°C]	$T_{iso\rightarrow crys}$ [°C]
5	-ethyl	788.84	28.7	>300	>300
10	-butyl	901.05	9.9	>300	>300
11	-2-ethylhexyl	1125.48	8.5	227.6	218.1
12	-2-butyloctyl	1349.90	3.9	163.5	147.5
13	-6-undecyl	947.21	27.1	>300	>300

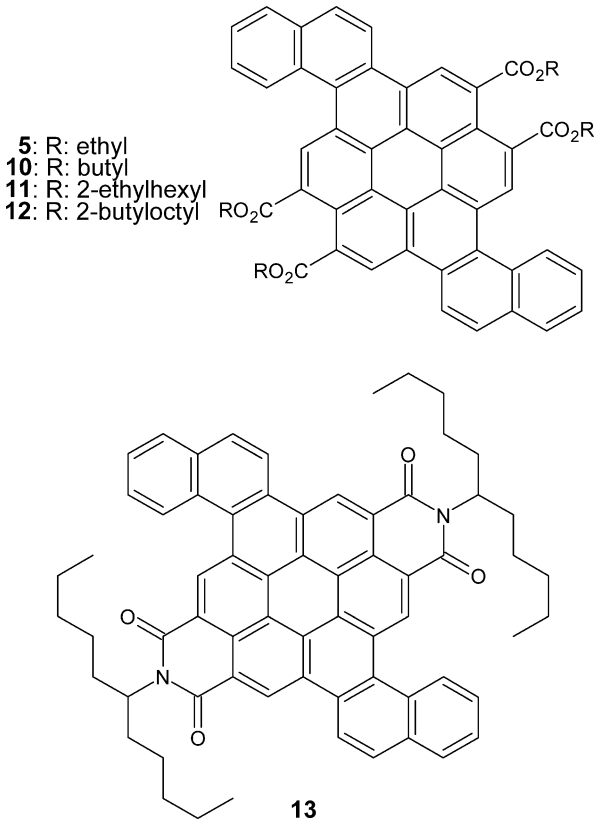

Scheme 2. Molecular structures of the synthesized esters: tetraethylester **5**, tetrabutylester **10**, tetrakis(2-ethylhexyl) ester **11**, tetrakis(2-butyloctyl)ester **12**, and bisimde **13**.

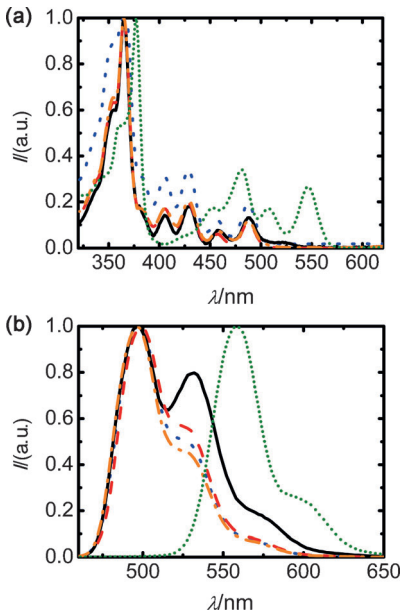

Figure 1. a) UV/Vis absorption and b) photoluminescence spectra (excited wavelength (λ_{exc}) = 350 nm) of **5** (black solid line), **10** (red dashed line), **11** (blue dotted line), **12** (orange dash-dotted line), and **13** (green dotted line) in $CHCl_3$.

show an identical main peak (λ_1 = 498 nm) for the ester compounds. The spectrum of the bisimide is redshifted by 60 nm in comparison to the other compounds (Figure 1 b).

Cyclic voltammetry (CV) and square-wave voltammetry (SQW) were performed to determine the energy of the LUMO (Table 2). The values for the HOMO are accessible ($E_{HOMO} = E_{LUMO} - \Delta E_{gap}$), for which ΔE_{gap} can be obtained from the absorption band with the longest wavelength (Figure 1 a). Due to the low solubility of **5**, no CV or SQW measurements were performed for this compound.

Table 2. Electronic properties determined by CV, SQW, and UV/Vis spectroscopy (see the Supporting Information for more details).

	E_{LUMO} [eV]	E_{LUMO+1} [eV]	ΔE_{gap} [eV]	E_{HOMO} [eV]
10	−3.29	−3.04	2.46	−5.75
11	−3.28	−3.03	2.46	−5.74
12	−3.29	−3.01	2.46	−5.75
13	−3.72	−3.52	2.18	−5.90

The ester compounds have similar values for the LUMO (−3.29 eV), LUMO + 1 (−3.03 eV), and HOMO (−5.74 eV) levels. As expected, the length of the alkyl chains does not change the electronic properties of the ester compounds. The bisimide has significantly lower values for the LUMO (−3.72 eV) and LUMO + 1 (−3.52 eV); this makes it a stronger electron acceptor than the ester compounds.

In the second step, all compounds were tested as potential emitter materials for OLEDs. Therefore, OLEDs with a single organic layer were assembled and characterized. Glass substrates, coated with indium tin oxide (ITO) serving as an anode material, were cleaned by plasma treatment and sonication in deionized water and organic solvents. If possible, the organic layers were deposited by thermal vapor deposition (TVD) in vacuo ($p = 5 \times 10^{-7}$ mbar) with a layer thickness of d_{org} = 30–50 nm. If TVD was not a viable approach, the compounds were spin-coated (SC) as a solution in $CHCl_3$ onto the substrates. An aluminum layer served as the cathode. It was deposited on the organic layer by TVD in vacuo ($p = 5 \times 10^{-5}$ mbar) with a typical layer thickness of d_{Al} = 80 nm (Figure 2 a). Subsequently, the OLEDs were tempered for 60 min at 80 °C. The electroluminescent and electro-optical behavior of the assembled OLEDs was studied.

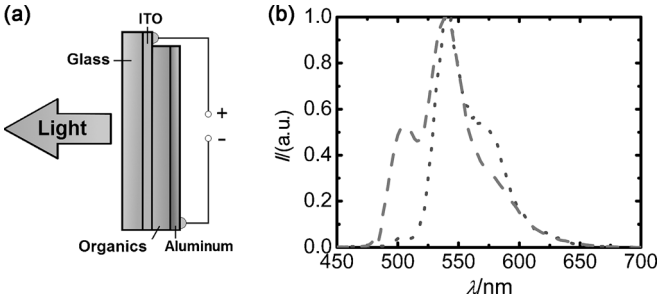

Figure 2. a) Schematic illustration of a single-layer OLED. b) Electroluminescence of single-layer OLEDs with **10** (dashed line) and **11** (dotted line).

Due to its high sublimation temperature and low solubility, compound **5** is not a feasible emitter material because it cannot be deposited either by TVD or by SC. The electroluminescence peaks are redshifted relative to the photoluminescence peaks (Figures 1 b and 2 b). This can be explained by the formation of excimers[15] in thin films, which tend to increase the wavelengths of the spectra (see the Supporting Information).

Furthermore, the signal-to-noise ratio of the electroluminescence spectra and the electro-optical measurements indicate that **10** and **11** show the best results as emitter materials (Figure 2 b and Figure 3). The performance of **13** is substandard; this can be attributed to its low solubility and high sublimation temperature, which results in poor or no deposits of thin films on substrates by SC and TVD, respectively. The results for **12** are only based on a small number of devices due to the low quantity of synthesized substance. The electro-optical measurements demonstrate that all manufactured OLEDs show typical diode behavior and the luminance increases with increasing voltage. OLEDs based on **12** and **13** had only very low luminance, which prevented its absolute measurement. A direct comparison of **11**-based OLEDs fabricated by TVD (Figure 3 a) and SC (Figure 3 b) underlines the higher quality of thin films deposited by TVD.

Compounds with shorter side chains exhibit lower solubility as well as higher melting and sublimation temperatures. Consequently, compound **5** shows no possible application as an emitter, compound **10** shows promising results as an emitter for SC as a deposition method, and **11** shows the best results with both deposition techniques. In principle, compound **12**

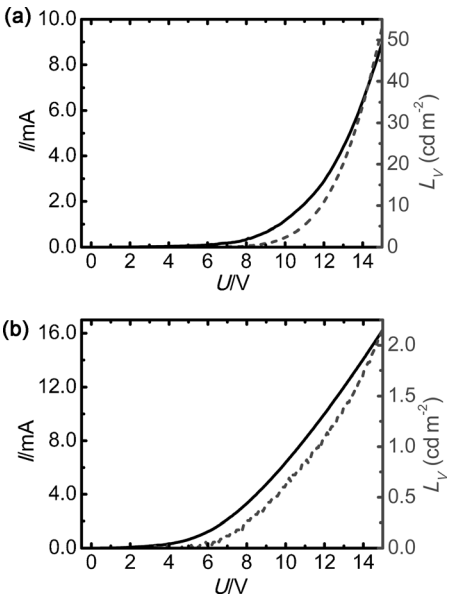

Figure 3. Current–voltage (solid line) and absolute luminance (dashed line) characteristics of OLEDs with **11** as an emitter layer deposited by a) TVD and b) SC. Threshold voltages of $U_{th} = 6.0$ and 3.9 V were used for a) and b), respectively. The measurements were conducted under a nitrogen atmosphere.

can also be expected to show good results, but the small amount of substance inhibited a detailed investigation. Compound **13**, although containing side chains with a comparable length to those of compounds **11** and **12**, only serves as a mediocre emitter when obtained by using SC, because there are only two side chains attached to the core, whereas the ester compounds have four side chains. At some point, further increasing the length of the side chains would start to increase the melting and sublimation temperatures.

The bilaterally extended perylene core was compared with the unilaterally and unaltered perylene cores, especially focusing on their electronic and optical properties. For this purpose, UV/Vis absorption spectra of esters and imides with three different aromatic cores were selected (Scheme 3). Esters **2**, **11**, and **15** were dissolved in $CHCl_3$. The absorption spectra show that all compounds have almost identical peaks in the wavelength region of $\lambda = 375$–525 nm (Figure 4). However, the intensity of the peaks appearing at longer wavelengths decreases significantly with extension of the core. Furthermore, the intensity of peaks in the wavelength region of $\lambda = 325$–375 nm increases with core extension. In particular, compound **2**, with an unaltered perylene core, has no peaks in this wavelength region, whereas compound **11**, with a bilaterally extended perylene core, has its main peak in this region (Figure 4a).

Bisimide **13** was dissolved in toluene to measure the UV/Vis absorption spectrum, whereas the spectra of compounds **14** and **16** where reported in the literature.[19,22] The spectra of **14** and 3,4,9,10-perylenetetracarboxylic diimide are very similar.[23] The absorption of imides is generally redshifted in comparison with the respective esters. Within the groups of imide compounds, we observe the same trends of changing absorption with increasing size of the aromatic core as in the group of ester compounds (see above).

In systematic studies of other polyaromatic series, an extension of the aromatic system is known to lead to a smaller band gap, and thus, to a bathochromic shift.[13] Surprisingly, this shift is missing in the two series **2**, **11**, and **15** (Figure 4a) and **13**, **14**, and **16** (Figure 4b). In addition, the absorption cross sections change dramatically within each series (**2**, **11**, and **15** and **13**, **14**, and **16**). The energy levels of the different compounds were also compared. Data for compounds **2** and **14**–**16** were obtained from the literature.[19,20,24,25] It is important to note that the band gap between the E_{HOMO} and E_{LUMO} for com-

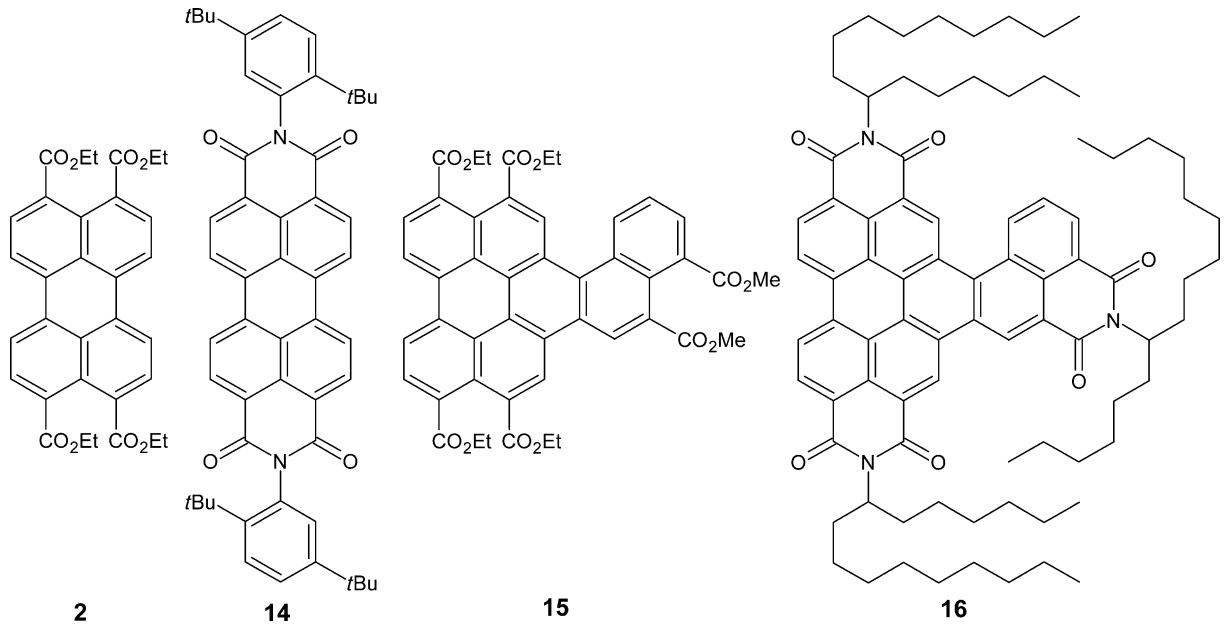

Scheme 3. Molecular structures of perylene and unilaterally extended perylene esters (**2**, **15**) and imides (**14**, **16**).

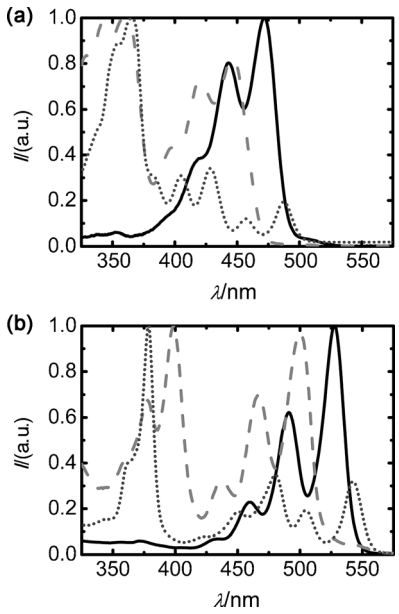

Figure 4. UV/Vis absorption spectra of a) esters **2** (solid line), **11** (dotted line), and **15** (dashed line) in $CHCl_3$, and b) imides **13** (dotted line) and **14** (solid line) in toluene and **16** (dashed line) in $CHCl_2$.

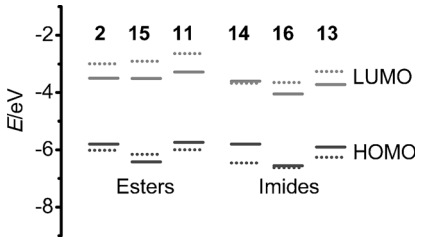

Figure 5. Experimentally (solid line) and theoretically (dotted line) obtained energy levels of esters **2**, **15**, and **11** and of imides **14**, **16**, and **13**.

pounds **11** and **13** was obtained by measuring the absorption edge with the highest wavelength (Figure 5).

For a more in-depth interpretation of the experimental results discussed above, we calculated optimized ground-state geometries and vertical electronic excitations for all compounds of the two series studied. The calculations are based on DFT and time-dependent density functional theory (TD-DFT), respectively, at the PBE0/6-311G(d,p) level. For computations of the vibronic spectra, PBE0/6-31G(d) was employed. All calculations presented herein were performed by using the Gaussian 09 software package.[26] Visualization of molecular structures and orbitals was achieved by using GaussView.[27] Details of the methodology are given in the Supporting Information. Natural transition orbitals (NTOs)[28] are used as the main tool to analyze the character of the electronic transitions.

The redshift of the imides, relative to the corresponding esters, found experimentally can be understood by inspection of the optimized molecular structures. As depicted in Figure 6, the perylene core of **2** is slightly bent compared with the more planar core of **14**. The planarity of the latter enables a more extended conjugation between electronic π bonds, and therefore, the fundamental absorption is found at longer wavelengths. Visualizations of optimized geometries of the remaining four molecular structures of the series are included in the Supporting Information.

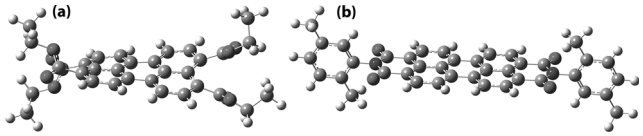

Figure 6. Molecular structures of a) ester **2** and b) imide **14**. The perylene core in a) is slightly bent and planar in b). The more planar core structure is accompanied by an improved electronic conjugation and gives rise to a red-shift of the fundamental absorption edge.

All peaks found experimentally can be attributed to the corresponding features found in our calculated vibronic spectra. The absence of a bathochromic shift found in the experiments is related to the conformation of the larger molecules. In the calculations, we find that the outermost naphthalene rings are bent out of the plane of the coronene core (cf. Figure S4 in the Supporting Information). Thus, one of the conditions for optimal aromaticity, that is, planarity of the conjugated system, is not given. Therefore, the NTOs involved in the long-wavelength excitations remain about the same (Figure 7a and b); the extension of the conjugated system is not increased with increasing molecular size.

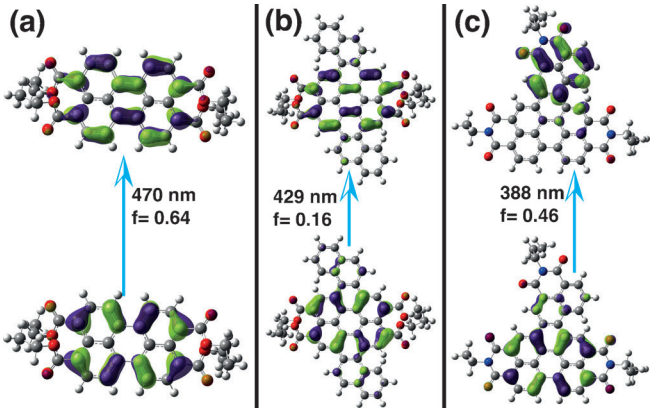

Figure 7. NTOs for long-wavelength excitations of a) **2** and b) **11**, and c) for an excitation at shorter wavelength of **16**. Clearly, the orbitals involved in the long-wavelength transitions are similar for the smaller (a) and larger (b) molecules. Furthermore, the shorter-wavelength transition shows significant charge-transfer character from the core to the naphthalene unit or vice versa. The oscillator strength of these transitions increases with increasing size of the molecules in the series.

A second trend observed in the measured absorption spectra is a change in the relative intensities of long- and short-wavelength absorption bands with increasing aromatic core size. This change is sufficiently pronounced enough to shift the perceived color of the different substances in solution for molecules with larger cores. Inspection of the NTOs involved in the transitions at shorter wavelengths shows that these transitions have a strong charge-transfer character from the outer

parts of the molecules to the inner core (cf. Figure 7c). This also explains the absence of the corresponding short-wavelength peaks for the smallest ester (**2**) and imide (**14**). For the bilaterally extended molecules, **11** and **13**, a stronger absorption feature is found at short wavelengths than those for the unilaterally extended ones (**15** and **16**). The additional naphthalene unit in the bilaterally extended system leads to a second contribution to the observed CT excitations, and consequently, increased oscillator strength, as confirmed by the calculations. We note that one needs to be careful with quantitative analysis of the CT excitations found within our TD-DFT calculations. However, for these excitations, very good agreement with the experimentally observed spectral features and trends is also found.

In conclusion, we synthesized and characterized electroluminescent organic semiconductors derived from perylene compounds by lateral extension of the conjugated molecular cores. The surprising lack of a redshift of the absorption with increasing conjugated core size could be explained by nonplanarity of the extended cores, which resulted in similar NTOs in the same long-wavelength regime for the selected cores. The increasing absorption in the UV range, on the other hand, could be attributed to charge-transfer effects between the outer and inner parts of the extended cores. The observed dominance of short-wavelength peaks changed the subjective color perception accordingly. The compounds synthesized were suitable for fabricating OLEDs.

Acknowledgements

We thank the German Research Foundation (DFG: GRK 1464) and Friedrich-Ebert-Stiftung for financial support, PC^2 for computing time, S. Keuker-Baumann for differential scanning calorimetry, Dr. A. Neuba for cyclic and square-wave voltammetry, and Dr. H. Egold for helping to analyze the NMR spectra.

Keywords: absorption · density functional calculations · electroluminescence · perylenes · semiconductors

[1] S. R. Forrest, *Chem. Rev.* **1997**, *97*, 1793.
[2] H. Langhals in *Fundamentals of Picoscience* (Eds.: K. D. Sattler), CRC, Boca Raton, **2014**, chapter 37.
[3] L. Schmidt-Mende, A. Fechtenkötter, K. Müllen, E. Moons, R. H. Friend, J. D. MacKenzie, *Science* **2001**, *293*, 1119.
[4] W. Pisula, X. Feng, K. Müllen, *Chem. Mater.* **2011**, *23*, 554 – 567.
[5] R. J. Bushby, K. Kawata, *Liquid Crystals* **2011**, *38*, 1415 – 1426.
[6] S. Laschat, A. Baro, N. Steinke, F. Giesselmann, C. Hägele, G. Scalia, R. Judele, E. Kapatsina, S. Sauer, A. Schreivogel, M. Tosoni, *Angew. Chem.* **2007**, *119*, 4916 – 4973; *Angew. Chem. Int. Ed.* **2007**, *46*, 4832 – 4887.
[7] T. Christ, B. Glüsen, A. Greiner, A. Kettner, R. Sander, V. Stümpflen, V. Tsukruk, J. H. Wendorff, *Adv. Mat.* **1997**, *9*, 219.
[8] D. Adam, P. Schuhmacher, J. Simmerer, L. Häussling, K. Siemensmeyer, K. H. Etzbach, H. Ringsdorf, D. Haarer, *Nature* **1994**, *371*, 141 – 143.
[9] A. M. van de Craats, J. M. Warman, A. Fechtenkötter, J. D. Brand, M. A. Harbison, K. Müllen, *Adv. Mater.* **1999**, *11*, 1469 – 1472.
[10] W. Pisula, M. Zorn, J. Y. Chang, K. Müllen, R. Zentel, *Macromol. Rapid Commun.* **2009**, *30*, 1179 – 1202.
[11] M. Funahashi, J. Hanna, *Adv. Mater.* **2005**, *17*, 594 – 598.
[12] M. O'Neill, S. M. Kelly, *Adv. Mater.* **2011**, *23*, 566 – 584.
[13] N. G. Pschirer, C. Kohl, F. Nolde, J. Qu, K. Müllen, *Angew. Chem.* **2006**, *118*, 1429 – 1432; *Angew. Chem. Int. Ed.* **2006**, *45*, 1401 – 1404.
[14] F. C. Spano, *Acc. Chem. Res.* **2010**, *43*, 429 – 439.
[15] B. Stevens, M. I. Ban, *Trans. Faraday Soc.* **1964**, *60*, 1515.
[16] Y.-H. Tian, G. Park, M. Kertesz, *Chem. Mater.* **2008**, *20*, 3266 – 3277.
[17] A. Pradhan, P. Dechambenoit, H. Bock, F. Durola, *J. Org. Chem.* **2013**, *78*, 2266 – 2274.
[18] J. Li, Y. Liu, Y. Qian, L. Li, L. Xie, J. Shang, T. Yu, M. Yi, W. Huang, *Phys. Chem. Chem. Phys.* **2013**, *15*, 12694.
[19] J. Kelber, M.-F. Achard, F. Durola, H. Bock, *Angew. Chem.* **2012**, *124*, 5290 – 5293; *Angew. Chem. Int. Ed.* **2012**, *51*, 5200 – 5203.
[20] I. Seguy, P. Jolinat, P. Destruel, R. Mamy, H. Allouchi, C. Courseille, M. Cotrait, H. Bock, *ChemPhysChem* **2001**, *2*, 448 – 452.
[21] Z. Yuan, Y. Xiao, Z. Li, X. Qian, *Org. Lett.* **2009**, *11*, 2808 – 2811.
[22] W. E. Ford, P. V. Kamat, *J. Phys. Chem.* **1987**, *91*, 6373 – 6380.
[23] M. Oltean, A. Calborean, G. Mile, M. Vidrighin, M. Iosin, L. Leopold, D. Maniu, N. Leopold, V. Chiş, *Spectrochim. Acta Mol.* **2012**, *97*, 703 – 710.
[24] C. M. Fischer, M. Burhard, S. Roth, K. V. Klitzing, *Europhys. Lett.* **1994**, *28*, 129 – 134.
[25] T. Oekermann, D. Schlettwein, *J. Appl. Electrochem.* **1997**, *27*, 1172 – 1178.
[26] Gaussian 09, Revision D.01, M. J. Frisch, G. W. Trucks, H. B. Schlegel, G. E. Scuseria, M. A. Robb, J. R. Cheeseman, G. Scalmani, V. Barone, B. Mennucci, G. A. Petersson, H. Nakatsuji, M. Caricato, X. Li, H. P. Hratchian, A. F. Izmaylov, J. Bloino, G. Zheng, J. L. Sonnenberg, M. Hada, M. Ehara, K. Toyota, R. Fukuda, J. Hasegawa, M. Ishida, T. Nakajima, Y. Honda, O. Kitao, H. Nakai, T. Vreven, J. A. Montgomery, Jr., J. E. Peralta, F. Ogliaro, M. Bearpark, J. J. Heyd, E. Brothers, K. N. Kudin, V. N. Staroverov, R. Kobayashi, J. Normand, K. Raghavachari, A. Rendell, J. C. Burant, S. S. Iyengar, J. Tomasi, M. Cossi, N. Rega, J. M. Millam, M. Klene, J. E. Knox, J. B. Cross, V. Bakken, C. Adamo, J. Jaramillo, R. Gomperts, R. E. Stratmann, O. Yazyev, A. J. Austin, R. Cammi, C. Pomelli, J. W. Ochterski, R. L. Martin, K. Morokuma, V. G. Zakrzewski, G. A. Voth, P. Salvador, J. J. Dannenberg, S. Dapprich, A. D. Daniels, Ö. Farkas, J. B. Foresman, J. V. Ortiz, J. Cioslowski, D. J. Fox, Gaussian Inc., Wallingford CT. **2009**.
[27] R. Dennington, T. Keith, J. Millam, *GaussView Version 5.0.9*, Semichem Inc. Shawnee Mission KS **2009**.
[28] R. L. Martin, *J. Chem. Phys.* **2003**, *118*, 4775 – 4777.

Received: April 28, 2014
Published online on August 5, 2014

CHEMISTRY
A European Journal

Supporting Information

Polycyclic Aromatic Hydrocarbons Obtained by Lateral Core Extension of Mesogenic Perylenes: Absorption and Optoelectronic Properties

Joachim Vollbrecht,[a, b] Harald Bock,[b] Christian Wiebeler,[a] Stefan Schumacher,[a] and Heinz Kitzerow*[a]

chem_201403287_sm_miscellaneous_information.pdf

Table of Contents

Theoretical Modeling

Methods

To understand the molecular properties and spectral trends found in experiments, DFT-based electronic structure calculations were performed. The structures of the esters **2**, **11**, and **15** and of the imides **13**, **14**, and **16** were optimized using the PBE0 [2, 3] functional and 6-311G(d,p) basis set. Calculations of vibrational frequencies confirmed that the structures found were stable minima. Optical absorption spectra were calculated using time-dependent DFT (TD-DFT) with the same basis set and functional.

Energies of the frontier molecular orbitals were also investigated. For this purpose, the optimized structures were used as structures for single point calculations with additional diffuse functions, i.e. using the 6-311+G(d,p) basis set to ensure better convergence of the molecular orbital energies [4]. All quantum chemical computations were done using Gaussian 09 [5]. Molecular structures and orbitals were visualized with GaussView [6].

For the calculation of vibrationally resolved spectra employing the Franck-Condon principle the size of the molecules and the basis set were reduced to allow efficient numerical calculation of vibrational frequencies for excited states. For this purpose all side chains were replaced by hydrogen atoms. Furthermore, for PDI the substituents at the nitrogen atoms were replaced by hydrogen atoms as well. To further speed up the calculations, 6-31G(d) was used as basis set. Only small shifts in the vertical electronic spectra are observed with this methodology in comparison to the previously described approach, justifying these simplifications. Finally, the calculation of vibrationally resolved spectra was done employing the methodology described in [7] using 8 Classes and an integral threshold of 10^{10}. The spectra are calculated in the range of 17400 cm^{-1} to 30200 cm^{-1} with a resolution of 10 cm^{-1} and a broadening of 200 cm^{-1} for half width at half maximum. The results obtained for PDI are in good agreement with previously published spectra [8]. However, our choice of cut-off paramters also allows an efficient calculation of vibrationally resolved spectra for larger molecules without significantly affecting accuracy.

Molecular Structures

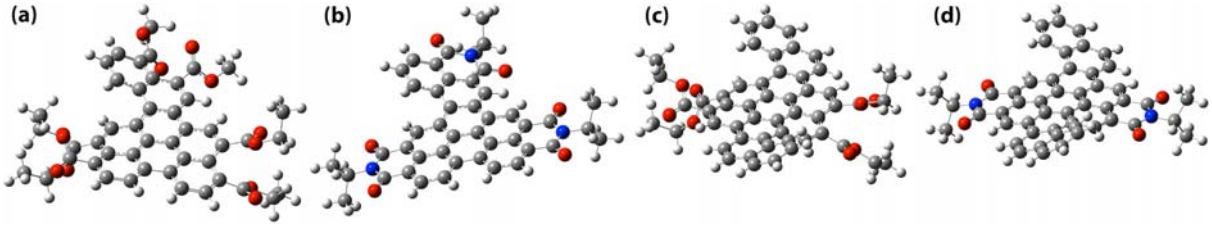

Figure IV: Optimized molecular structures of the unilaterally extended (a) ester **15** and (b) imide **16** and of the bilaterally extended (c) ester **11** and (d) imide **13**.

The optimized molecular structures of the small ester **2** and imide **14** are shown in Fig. 6 of the main text. There it was found that the imide is more planar than the ester. This trend can also be observed for the larger molecules. Furthermore, all the naphthalene units used for the extension of the cores are bent out off the plane of the corresponding core.

Electronic and Vibrationally Resolved Spectra

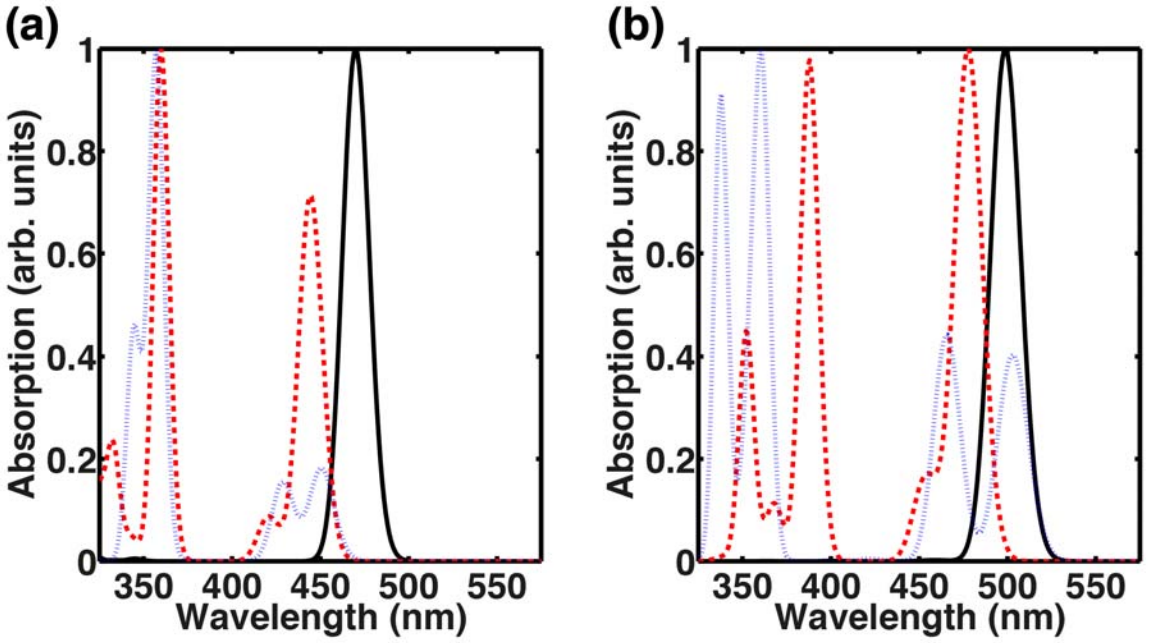

Figure V: Calculated UV-vis absorption spectra of (a) esters **2** (black, solid line), **11** (blue, dotted line) and **15** (red, dashed line) and of (b) imides **13** (blue, dotted line), **14** (black, solid line) and **16** (red, dashed line). All spectra are normalized to their maximum value.

As seen in Figure V, the calculations show that the absorption of the imides is red-shifted compared to the corresponding esters. Furthermore, the intensity of the peaks in the region of higher wavelengths decreases and the intensity of the peaks for lower wavelengths increases. All these trends are also observed experimentally.

Comparing the results of our calculations with the measured spectra, it is evident that more peaks are found for larger wavelengths than are obtained by our calculations. In the following we identify vibrational coupling as the cause of these additional peaks. For this purpose, we investigated the excitation into the first excited state, S_1, for the structures of **2** and **14** and the excitations into the first and second excited singlet state, S_1 and S_2, for the molecules **11**, **15**, **13**, and **16**. Contributions of higher excited states are not included in the computation of vibrationally resolved spectra. As is shown in Figure VI, the vibronic spectra show the extra vibrational replica that are missing in the calculation of vertical electronic excitation spectra only. All the peaks found in experiment can be attributed to the corresponding spectral features found in our calculations.

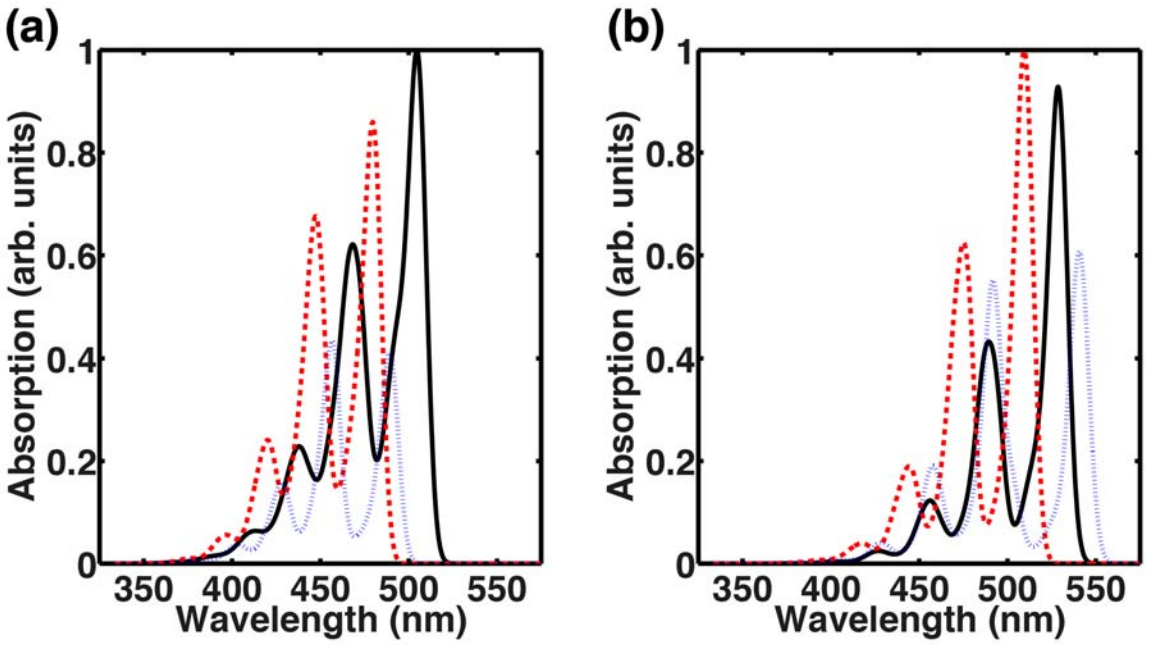

Figure VI: Calculated vibrationally resolved electronic spectra of (a) esters **2** (black, solid line), **11** (blue, dotted line) and **15** (red, dashed line) and of (b) imides **13** (blue, dotted line), **14** (black, solid line) and **16** (red, dashed line). Only the first excited state is included for **2** and **14** and the first and second excited states for **11**, **15**, **13**, and **16.** Each spectrum is normalized to the maximum value in the respective vertical excitation spectrum.

Natural Transition Orbitals

In Figure 7 of the main text NTOs [9] for three different electronic excitations are shown as representative examples. All the peaks visible in the spectra are unambiguously related to a single electronic transition. The electronic transition shown in Figure 7 (a) corresponds to the spectral feature in Figure V (a) for molecule **2**. The resonance at about 430 nm of **11** corresponds to the electronic transition in Figure 7 (b). The electronic transition in Figure 7 (c) corresponds to the resonance of **16** at about 390 nm.

Additional NTOs not included in the main text are shown in Figure VII. In panels (a) and (b), the nature of the long-wavelength excitations of the imides is shown where the orbitals are mainly localized at the core. In addition, the characteristic feature of the transitions at shorter wavelengths, i.e. charge-transfer character of the excitation, is also found for the esters as depicted in part (c). We note that all the transitions shown here can be characterized with one pair of NTOs only. For the bilaterally extended molecules, for the high-energy transitions, two sets of NTOs have to be invoked to give a good account of their nature.

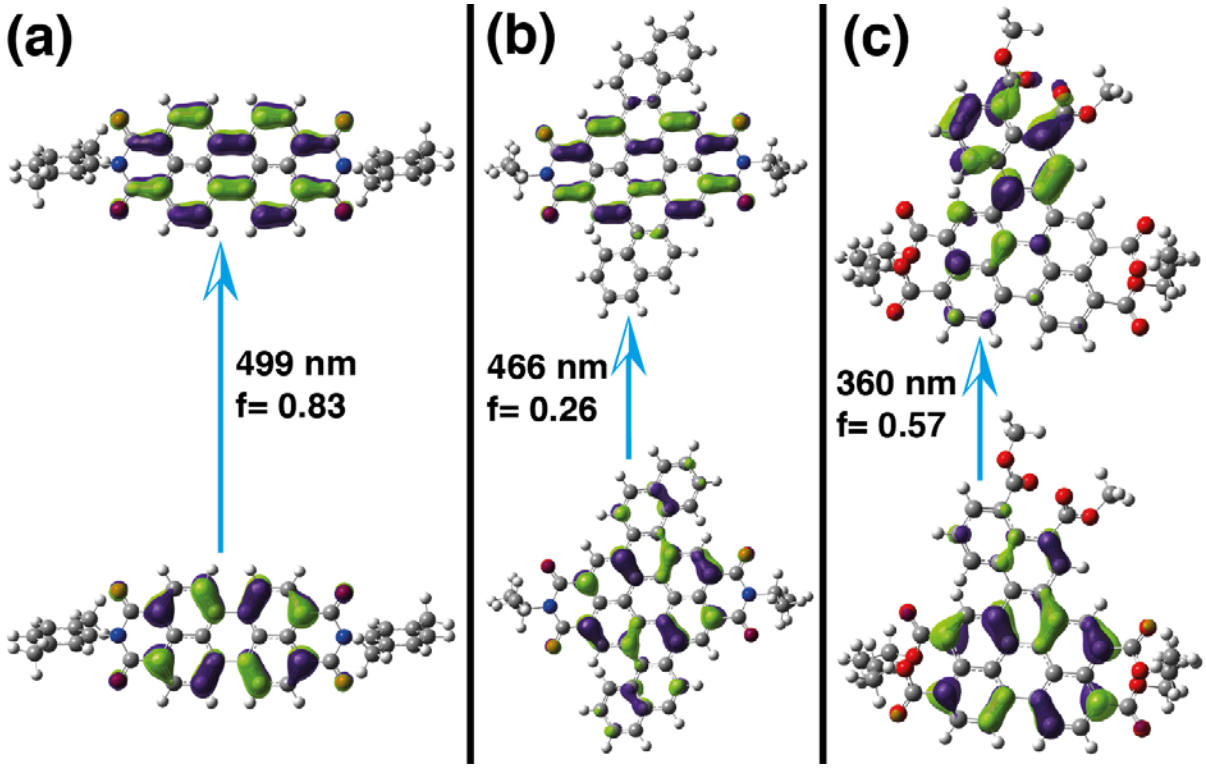

Figure VII: Natural Transition Orbitals for long-wavelength excitations of (a) **14** and (b) **13** and (c) for a transition at short wavelength for **15**.

References

[1] Z. Yuan, Y. Xiao, Z. Li, X. Qian: "Efficient Synthesis of Regioisomerically Pure Bis(trifluoromethyl)-Substituted 3,4,9,10-Perylene Tetracarboxylic Bis(benzimidazole)" Org. Lett. **2009**, *11(13)*, 2808-2811.

[2] J. P. Perdew, K. Burke, and M. Ernzerhof: "Generalized Gradient Approximation Made Simple", Phys. Rev. Lett. **77**, 3865-3868 (1996).

[3] C. Adamo and V. Barone: "Toward reliable density functional methods without adjustable parameters: The PBE0 model", J. Chem. Phys. **110**, 6158-6170 (1999).

[4] J.-H. Chen, L.-M. He, and R. L. Wang: "Connection of DFT Molecular Orbital Eigenvalues with the Observable Oxidation Potentials/Oxidation Energies", J. Phys. Chem. A **117**, 5132-5139 (2013).

[5] M. J. Frisch, G. W. Trucks, H. B. Schlegel, G. E. Scuseria, M. A. Robb, J. R. Cheeseman, G. Scalmani, V. Barone, B. Mennucci, G. A. Petersson, H. Nakatsuji, M. Caricato, X. Li, H. P. Hratchian, A. F. Izmaylov, J. Bloino, G. Zheng, J. L. Sonnenberg, M. Hada, M. Ehara, K. Toyota, R. Fukuda, J. Hasegawa, M. Ishida, T. Nakajima, Y. Honda, O. Kitao, H. Nakai, T. Vreven, J. A. Montgomery, Jr., J. E. Peralta, F. Ogliaro, M. Bearpark, J. J. Heyd, E. Brothers, K. N. Kudin, V. N. Staroverov, R. Kobayashi, J. Normand, K. Raghavachari, A. Rendell, J. C. Burant, S. S. Iyengar, J. Tomasi, M. Cossi, N. Rega, J. M. Millam, M. Klene, J. E. Knox, J. B. Cross, V. Bakken, C. Adamo, J. Jaramillo, R. Gomperts, R. E. Stratmann, O. Yazyev, A. J. Austin, R. Cammi, C. Pomelli, J. W. Ochterski, R. L. Martin, K. Morokuma, V. G. Zakrzewski, G. A. Voth, P. Salvador, J. J. Dannenberg, S. Dapprich, A. D. Daniels, Ö. Farkas, J. B. Foresman, J. V. Ortiz, J. Cioslowski and D. J. Fox, *Gaussian 09 Revision D.01*, Gaussian Inc. Wallingford CT 2009.

[6] R. Dennington, T. Keith, and J. Millam, *GaussView Version 5.0.9*, Semichem Inc. Shawnee Mission KS 2009.

[7] V. Barone, J. Bloino, M. Biczysko, and F. Santoro: “Fully Integrated Approach to Compute Vibrationally Resolved Optical Spectra: From Small Molecules to Macrosystems”, J. Chem. Theory Comput. **5**, 540-554 (2009).

[8] M. Oltean, A. Calborean, G. Mile, M. Vidrighin, M. Iosin, L. Leopold, D. Maniu, N. Leopold, and V. Chiş: „Absorption spectra of PTCDI: A combined UV–Vis and TD-DFT study“ Spectrochimica Acta A **97**, 703–710 (2012).

[9] R. L. Martin: “Natural transition orbitals”, J. Chem. Phys. 118, 4775-4777 (2003).

6.4 Influence of Functional and Basis Set on Vibronic Spectra

In comparison to spectra based on VEA, vibronic spectra that are obtained from FCA are seldom reported. Therefore, it is of interest to investigate the influence of the chosen functional and basis set. For this purpose, the smallest ester, molecule **2** in the article, will be investigated. The functionals used were B3LYP[59,60] and PBE0,[61,62] commonly used functionals for organic molecules, yielding for example convincing results regarding spectrum calculation using VEA for DAEs.[21] Furthermore, CAM-B3LYP,[63] a long-range corrected hybrid functional employing a variable fraction of exact exchange, was used. The basis sets utilized were 6-31G* and 6-31+G*.

Comparing the results for the two basis sets, see figure 6.2, it can be seen that the inclusion of diffuse functions leads to a small red-shift, i.e. about 0.08 eV, of the absorption, which holds for VEA and FCA. A similar trend has been observed for DAEs.[21] Therefore, basis sets with diffuse functions should also be employed for vibronic calculations, if computationally feasible.

The investigation of the results obtained for the different functionals shows that the trends found for VEA also translate directly in trends for FCA, see figure 6.2. In addition, there is a red-shift of the absorption maximum, when going from VEA to FCA. This shift is more pronounced for CAM-B3LYP, 0.31 eV, than for B3LYP and PBE0, both about 0.22 eV.

In order to investigate the influence of basis set and functional on the vibronic progression, the presentation of the spectra shown in figure 6.3 can be analyzed. The position of the vibronic peaks relative to the energy of the first absorption maximum does neither depend on the basis set nor on the functional and is therefore similar for all methods used. Furthermore, the height of these peaks increases the more exact exchange is used in the functional.

To sum things up, PBE0 and B3LYP have proven their accuracy for the calculation of vertical excitation spectra, the position of the vibronic peaks relative to the 0-0 transition does not depend on the functional, and CAM-B3LYP yields the best results for vibronic spectra, if the absolute position and height of the peaks are considered. These findings are in agreement with recent publications that investigate the accuracy of vibronic spectrum calculations in dependence of the functional used.[23,64] Due to this, the discussion in the following two sections concerning vibronic spectra will rely on CAM-B3LYP/6-31+G* as quantum chemical method.

6.5 Approximations for Spectrum Calculation & Properties of Vibronic Spectra

The FCP has been discussed in classical, semiclassical, and quantum mechanical interpretation. Each of these interpretations corresponds to a method for spectrum simulation. In all approximations, the molecule is in its corresponding ground state. The classical interpretation leads to VEA: geometry optimization with subsequent calculation of the vertical transition energies and oscillator strengths. The semiclassical one takes into

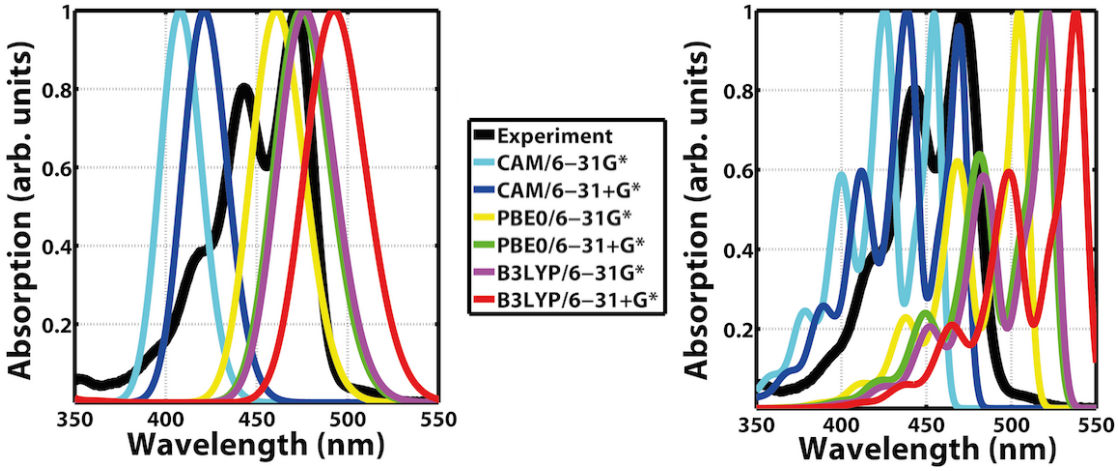

Figure 6.2: Absorption spectra of molecule **2** that is shown as inset in figure 6.3 calculated within VEA (left) and employing FCA (right). Shown are the results for three functionals and two basis sets. The larger basis set, i.e. 6-31+G*, yields spectra that are slightly shifted to lower energies. More pronounced is the influence of the functional: For VEA the best result is obtained with PBE0, whereas for FCA CAM-B3LYP gives the spectrum that is closest to experiment.

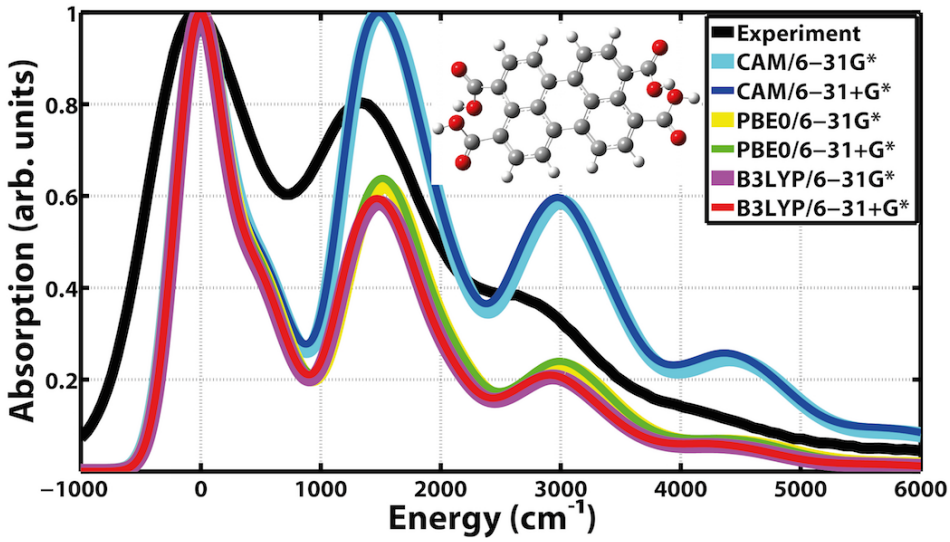

Figure 6.3: Absorption calculated with FCA in dependence of cm^{-1} for molecule **2** that is shown as inset. Energies are relative to the energy of the first absorption maximum. This plot allows an easier analysis of the vibronic progression. The absorption of the vibronic replica increases with the fraction of exact exchange that is used in the functional. The energies of the peaks relative to the corresponding maximum does neither depend on the functional nor on the basis.

account the sampling of the ground state geometries due to the zero-point vibrational motion and NEA is based on this idea. Finally, the full quantum mechanical interpretation, where the overlap between the vibrational states is considered yields vibronic spectra based on FCA.

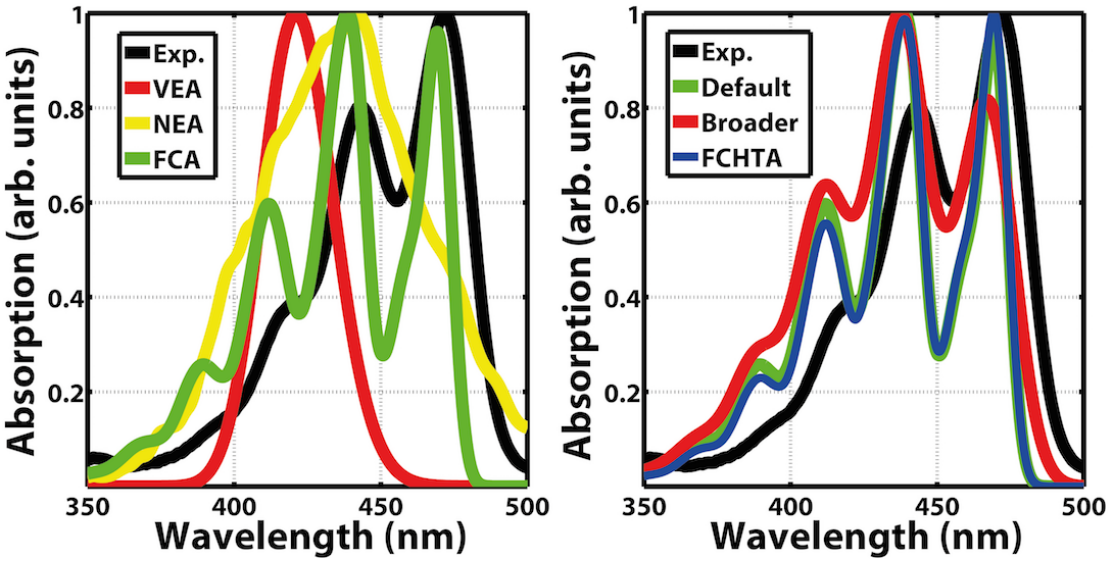

Figure 6.4: Absorption spectra of molecule **2** calculated with CAM-B3LYP/6-31+G* employing different approximations: VEA, NEA, and FCA (left). The changes found when going from VEA to NEA show the right tendency, but FCA yields much more convincing results. For FCA, absorption spectra calculated with higher broadening or with the inclusion of HTA for the same molecule are also shown (right). Higher broadening leads to an increase in intensity of the vibronic replica and the inclusion of HTA in addition to FCA, i.e. FCHTA, has only a minor influence on the spectrum.

As can be seen on the left in figure 6.4, the spectrum from VEA shows only one peak and no finer structure. Therefore, this widely used method may, depending on the functional employed, give reliable results for the optical gap, but fails to describe the structure of the spectrum. Using NEA results in shoulders of the absorption peaks for lower and higher wavelengths compared to the absorption maximum. Such a structure is, however, not observed in experiment for higher wavelengths. Nonetheless, the structure for lower wavelengths is a significant improvement. Note that this method does not reproduce vibronic progression, which is the cause of the additional peaks.[52,53] To properly reproduce this peaks, vibronic spectra employing FCA have to be calculated, leading to convincing agreement with experiment.

On the right in figure 6.4, the influences of the employed broadening and the use of the HTA are shown. The higher broadening leads to a structure of the absorption spectrum that more strongly resembles the experimental one. However, the peaks of the vibronic transitions relative to the first peak are now higher than before. Not only considering the FCA but also taking into account the HTA does not change the spectrum much. As

it is discussed in section 6.1, this had to be expected, because the investigated electronic transition is an allowed and bright one.

6.6 Analysis of the Involved Vibrational Modes

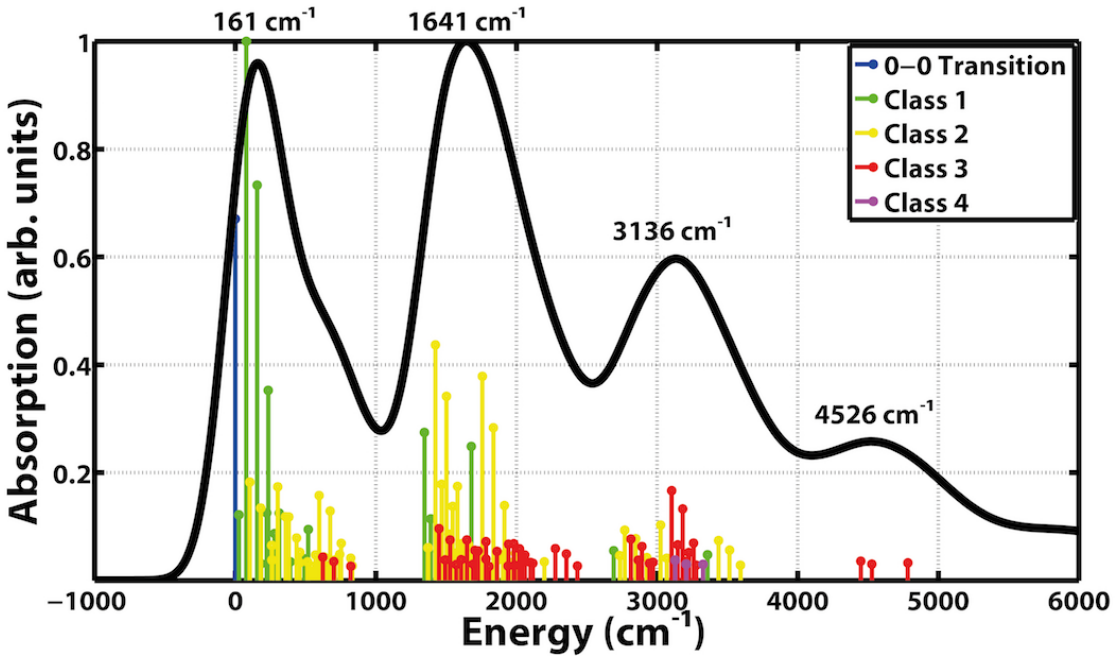

Figure 6.5: Vibronic spectrum of molecule **2** using CAM-B3LYP/6-31+G* shown in black. Energies are relative to the 0-0 transition. The energies of the maxima are shown as insets. Individual vibronic transitions with an intensity higher than 0.1% compared to the analytic limit are shown as sticks. They are divided into classes of simultaneously excited modes. Note that up to 10^{10} integrals are calculated for each class above class 2 and the first 8 classes have been considered in the calculation. The spectrum progression towards the analytic limit is 98.25 %.

Having calculated the vibronic spectrum, the results can be further analyzed. The maxima of the corresponding peaks are listed at the top of figure 6.5. The differences between neighboring peaks are: 1480 cm^{-1}, 1495 cm^{-1}, 1390 cm^{-1}. Note that the maximum of the last peak is shifted to lower energies due to the fact that it only appears as a shoulder. Therefore, the energy of the vibronic progression is about 1480 cm^{-1}. In the following the vibronic transitions that are arranged in four groups will be further investigated.

The first peak is mainly caused by the 0-0 transition and transitions that correspond to excitations of the 5th vibrational mode, see table 6.1. Due to this, the latter are transitions of class 1 meaning that only one vibrational mode is excited. The involved

$\Delta E(\mathrm{cm}^{-1})$	rel. Intensity	Final State	Class
	Peak 1		
78.28	1.00	$\|5^1\rangle$	1
156.55	0.73	$\|5^2\rangle$	1
0.00	0.67	$\|0\rangle$	0-0
234.83	0.35	$\|5^3\rangle$	1
	Peak 2		
1424.08	0.44	$\|90^1;5^1\rangle$	2
1757.54	0.38	$\|110^1;5^3\rangle$	2
1502.36	0.34	$\|90^1;5^2\rangle$	2
1835.82	0.28	$\|110^1;5^2\rangle$	2
1345.80	0.27	$\|90^1\rangle$	1
1679.26	0.25	$\|110^1\rangle$	1
	Peak 3		
3103.34	0.17	$\|110^1;90^1;5^1\rangle$	3
3181.62	0.13	$\|110^1;90^1;5^2\rangle$	3
3025.07	0.10	$\|110^1;90^1\rangle$	2
	Peak 4		
4449.15	0.04	$\|110^1;90^2;5^1\rangle$	3
4782.61	0.03	$\|110^2;90^1;5^1\rangle$	3
4527.43	0.03	$\|110^1;90^2;5^2\rangle$	3

Table 6.1: Listing of the most important vibronic transitions. The energy is given relative to the 0-0 transition and the intensity of each line is relative to the maximum intensity. The final state is written as a ket consisting of the excited vibrational modes separated by semicolons and the number of corresponding quanta in a specific excited mode as superscript. The results are discussed in the text.

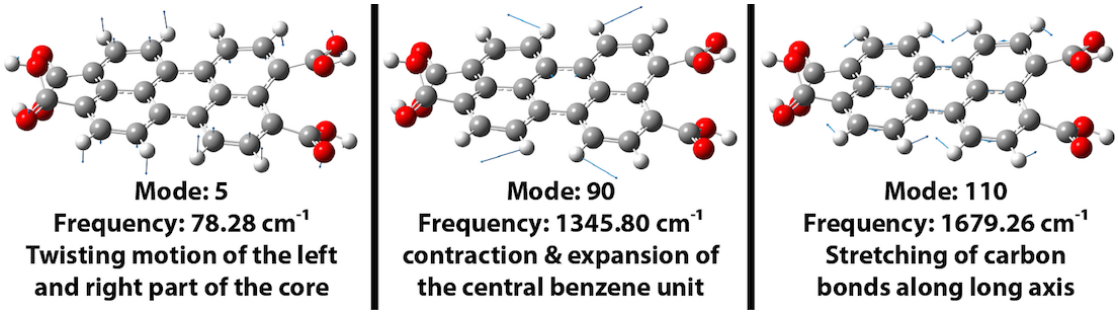

Figure 6.6: The three vibrational modes that are involved in the most important vibronic transitions as listed in table 6.1. Refer to the text for further information.

vibrational mode is depicted in figure 6.6: a twisting motion between the left and right part of the perylene core.

The second peak is dominated by four vibronic transitions of class 2 and two transitions of class 1. The latter correspond to excitations of the 90th and 110th mode, respectively. The former are a combination of excitations of the 5th mode with the 90th or 110th mode. Mode 90 is a vibration that leads to a "breathing motion", i.e. contraction and expansion, of the central benzene unit. The vibrations of mode 110 mainly include a stretching motion of the carbon bonds that are oriented along the long molecular axis, i.e. from left to right.

The vibronic peaks of the third peak are relatively weak. So only the three brightest transitions are considered. The two brightest transitions belong to class 3 and involve the simultaneous excitation of the three vibrational modes discussed before. The third transition is an excitation of the modes 90 and 110 only and belongs to class 2. Finally, only three vibronic transitions of class 3 are reported for the fourth peak, which only appears as a shoulder of the third one. They also involve the simultaneous excitations of the vibrational modes 5, 90, and 110.

Overall, large FC factors are obtained for excitations of the modes 5, 90, 110. The vibronic transitions are grouped according to the number of excitations of the 90th and 110th mode causing the four peaks found in the spectrum. The fine structure is mainly determined by additional excitations of mode 5. The results are in agreement with a previous analysis of the vibronic spectrum of a molecule that consists also of a perylene core.[65]

6.7 Fluorescence Spectrum Employing Franck-Condon Approximation

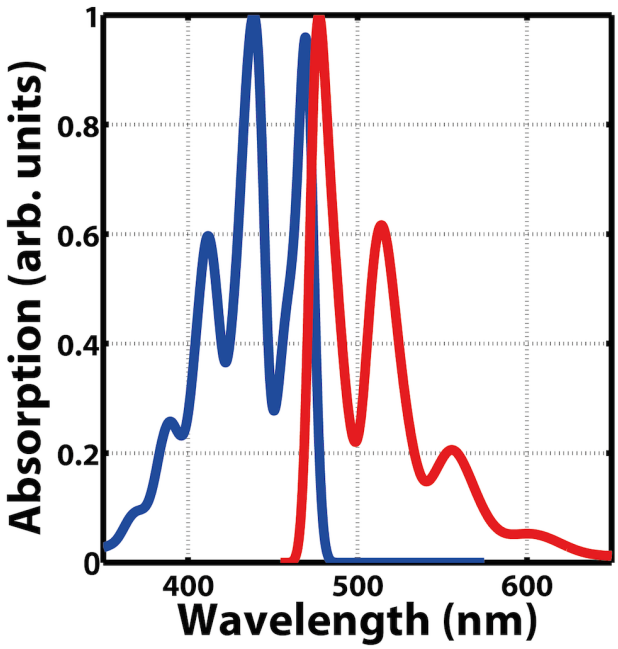

Figure 6.7: Absorption (blue) and fluorescence (red) spectra calculated with FCA for molecule **2** employing CAM-B3LYP/6-31+G*. The overlap between absorption and fluorescence is an indication, that the equilibrium structures of S_0 and S_1 are similar.

In order to determine fluorescence spectra employing FCA, it is assumed that the molecule is in the ground vibrational state S_1 according to Kasha's rule.[17] This leads to a progression of vibronic peaks towards lower energies. Additionally, the 0-0 transition in emission is shifted to lower energy compared to the 0-0 transition in absorption, as can be seen in 6.7.

For the molecule investigated, there is an overlap between the vibronic 0-0 bands of absorption and fluorescence and the two first vibrational bands are the strongest. This is the case, when the equilibrium geometries of both electronic states are similar. Therefore, the bonding situation does not change much upon excitation and the minima of the PESs are only slightly displaced. This is typical for large conjugated systems, where the excitation of a single electron from a π to a π^* MO has only a small impact on the molecular structure, because the remaining π electrons are still in their original bonding orbitals. Similar findings have also been reported for anthracene, another rigid aromatic hydrocarbon.[50]

7 Switching between two Conjugated Systems: CMTE

> The test of all knowledge is experiment. Experiment is the sole judge of scientific "truth".
>
> *(Richard P. Feynman[66])*

Photochromic molecules possess a conjugated system of electrons as it was the case for the molecules before. However in addition, the size of the conjugated system can be switched via isomerization between two stable forms of the molecule, inducing a change in the electronic and optical properties. This makes photochromic molecules highly interesting for potential applications like optical switches and memories.[67,68] Therefore, this chapter and the next one are dedicated to a certain class of photochromic molecules: diarylethenes, DAEs as introduced before. In this chapter the most important properties of this class of molecules will be explained and a molecule that will be used in experiments in Paderborn is used for exemplification. The chapter begins with the introduction of CMTE and of important properties of photochromic DAEs. Additional properties of CMTE have been reported in the paper that is included in this chapter.[4] Then, TSH, i.e. the method used for NA-AIMD, is validated by comparison with wave function-based calculations. After that, the results of NEA and FCA for spectrum simulation of this molecule are discussed. Initial condition generation for cycloreversion and cyclization reaction mimicking the experimental excitation completes this chapter.

7.1 CMTE and Important Properties of Photochromic Diarylethenes

First of all, photochromism is a light-induced transformation between two isomers of a molecule in at least one direction via light irradiation and the two forms are having different absorption spectra.[69,70] An example for such a class of materials are DAEs that have been first synthesized by M. Irie and his coworkers.[71] An overview of the current state of research concerning DAEs can be, e.g., obtained by reading reviews of Irie and coworkers.[72,73] As a particular example the DAE derivative cis-1,2-dicyano-1,2-bis(2,4,5-trimethyl-3-thienyl)ethene, abbr. CMTE, will be studied, which shows efficient light-induced electrocyclic photochromic isomerization between open and closed form (OF and CF, respectively) both in solution and film, see Scheme 1 of article [4] that is included in this chapter.[74,75] The corresponding light-induced change in the refractive index provides a promising mechanism to all-optically tune the resonance frequencies in

SiO2 microdisks with embedded colloidal nanocrystals as recently demonstrated with a different class of organic molecules.[76] Pictures from the switching of CMTE between OF and CF and the structure of the experimental setup are shown in figure 7.1.

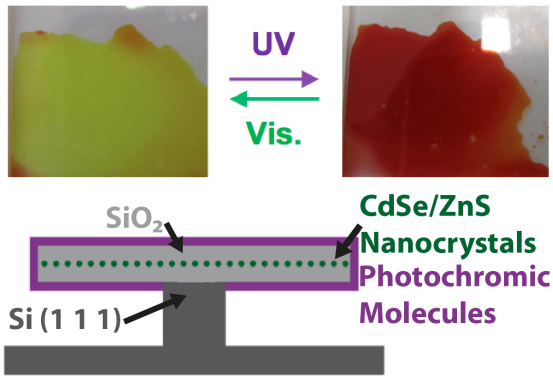

Figure 7.1: Switching between OF and CF in a film of CMTE and a scheme of the potential application.

The first investigations in Paderborn concerning DAEs using quantum chemical calculations have been made in my master's thesis to understand some properties of this class of molecules. For more details and information regarding the methodology used please refer to my master's thesis[21] or the corresponding article.[4] The key properties[67] of DAEs are discussed in the following using CMTE for exemplification.

1. **Thermal Stability:** To show that there are two stable isomers of a DAE, the PES of S_0 along the distance between the reactive carbon atoms can be calculated. As can be seen in figure 6 of reference [4] that is reproduced in this chapter,[4] both forms have about the same energy assuring thermal stability.

   The strongest influence on the energy of both isomers is due to the aryl units. These units are aromatic in the OF and for the CF the aromaticity is lost, see scheme 1 of the corresponding article.[4] Using thiophene, both isomers have about the same energy and if the two thiophene rings are replaced, e.g., by benzene, the OF would be much lower in energy.[68] Therefore, the CF would not be thermally stable. To conclude, for having two stable isomers, it is important to use aryl units with low aromatic stabilization energy.

2. **Difference in Absorption Spectra:** The absorption spectra for both isomers were calculated. For the determination of the absorption spectrum of the OF, best agreement with experiment is obtained using RI-CC2 and taking into account two molecular conformations, see figure 1 of reference [4] included in this chapter. The calculation of the absorption spectrum of the CF is straightforward and not only the wave function-based approach, but also DFT-based calculations using PBE0[61,62] yield good agreement with experiment, see figure 2 of reference [4] included in this chapter.

Based on the results of these calculations, further examinations can be made, e.g., determining the perceived color, see figure 3 of reference [4] included in this chapter. Furthermore, considering the planned application it is important to estimate the change of the frequency-dependent refractive index, because this change determines the shift of the resonance frequencies in the microdisk resonator. To achieve this, a Lorentz-oscillator model was employed using the transition energies and oscillator strengths obtained from the spectrum calculations. This approach yields good agreement between theory and experiment for the frequency dependence of the refractive index of both isomers, see figure 5 of reference [4] included in this chapter.

To sum up, there is a pronounced difference in the absorption of both isomers due to the peak at about 530 nm. It is absent in the OF for both conformers, but it is dominating the absorption in the visible part of the CF. This results in distinct electronic and optical properties of the CF compared to the OF.

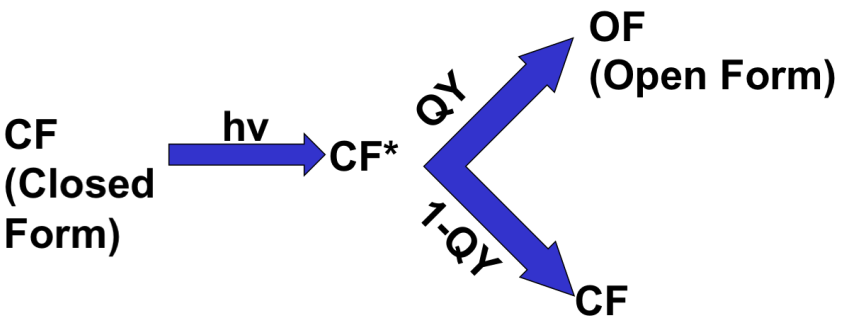

Figure 7.2: Scheme for explaining the QY as it is defined for the cycloreversion reaction of DAEs. It is the probability that a molecule of the CF undergoes the photochemical reaction successfully and therefore transforms into the OF after a photon with a wavelength in the visible range of the electromagnetic spectrum has been absorbed.

3. **Quantum Yield (QY):** The definition of QY as it is used in this context is explained in Figure 7.2 and it is the probability that the CF will isomerize to the OF after excitation to S_1. It is stated that "[a]lthough the QY is one of the most important properties in various applications, it is also the most difficult property to predict before a molecule is actually synthesized."[77]

   So far, the QYs have been explained by static calculations, i.e., investigations of PESs.[77,78] It is known that the isomerization between OF and CF proceeds via relaxation through a CI,[79,80] which is in this case a geometry where the energies of S_0 and S_1 are degenerate.[81] Calculations of the nonadiabatic dynamics near this CI for DAEs have been done previously only on a semiempirical level using the Molecular Mechanics Valence Bond model.[82]

   The first NA-AIMD simulations investigating the cycloreversion reaction of a DAE using TSH[83] are presented in the article reproduced in this chapter and allow the determination of the QY.[4] The result is in good agreement with experiment and

clarifies why its value is relatively low for CMTE.[4] In principle, this approach can be extended to study the photocyclization reaction of the molecule. However, this is more complex due to the involvement of several excited states is most likely.

4. **Reaction Times:** Having calculated trajectories for the NA-AIMD of the cycloreversion reaction starting with the excited CF, with subsequent relaxation through the CI, and reaching the minimum of S_0 corresponding to the OF, also the reaction times can be determined. However, no experimental value of the reaction time has been found for the reaction of this molecule and therefore the quality of this theoretical estimation ca not be assessed.

5. **Fatigue Resistance:** To investigate this property based on quantum chemical calculations, also NA-AIMD can be used in principle. However, for fatigue resistant molecules, e.g. CMTE, the probability for side-product formation, which is the cause of fatigue, is rather low. So, many trajectories would have to be calculated, to see the formation of these products. Generally, the NA-AIMD as employed for CMTE is not biased towards a specific photochemical reaction, but allows the exploration of all possible reaction paths.

To sum up, the first two properties, i.e. thermal stability and difference in absorption spectra, can be determined using static calculation.[4,21] The QY of the cycloreversion reaction was also calculated using TSH[4] and an extension to the photocyclization reaction is possible. Finally, this approach also allows to estimate reaction times and explore possible reaction mechanisms that might lead to fatigue.

7.2 "Optical Spectrum, Perceived Color, Refractive index, and Nonadiabatic Dynamics of the Photochromic Diarylethene CMTE"

This article has been published in the journal "Physical Chemistry Chemical Physics" and is a case study of key properties for CMTE that will be used for the functionalization of microdisk resonators in the research group of professor Cedrik Meier, University Paderborn. The related presentation of our poster at DFT2013 in Durham, UK, was awarded one of four poster prizes at the conference. It is the first article that uses NA-AIMD to investigate the cycloreversion reaction of DAEs. Note that animations of trajectories for the four presented categories have been published as Electronic Supporting Information online.

An assessment of the reliability of the method used for the TSH and further investigations regarding spectrum simulation and initial condition generation for mimicking experimental conditions of the excitation, will be shown in the sections 7.3 to 7.5, supplementing the published study of CMTE.

PCCP

PAPER

View Article Online
View Journal | View Issue

Cite this: *Phys. Chem. Chem. Phys.*, 2014, **16**, 14531

Optical spectrum, perceived color, refractive index, and non-adiabatic dynamics of the photochromic diarylethene CMTE†

Christian Wiebeler, Christina A. Bader, Cedrik Meier and Stefan Schumacher*

Received 28th December 2013,
Accepted 11th March 2014

DOI: 10.1039/c3cp55490b

www.rsc.org/pccp

Photochromism allows for reversible light-induced conversion of a molecular species into a different form with significantly altered optical properties. One promising compound that excels with high fatigue resistance and shows its photochromic functionality both in solution and in molecular solid films is the diarylethene derivative CMTE. Here we present a comprehensive study of its photophysical properties with density-functional theory based methods and benchmark the results against higher-level quantum-chemical approaches and experiments. In addition to static properties such as optical absorption, perceived color, and refractive index, we also investigate reaction dynamics based on non-adiabatic *ab initio* molecular dynamics. This gives detailed insight into the molecules' ultrafast reaction dynamics and enables us to extract reaction time scales and quantum yields for the observed electrocyclic reaction following photoexcitation.

I. Introduction

Functionalization with molecular materials poses a promising route towards the design of novel optoelectronic and photonic devices.[1,2] Light-controlled, reversible molecular mechanisms add to the list of properties typically available in materials used in optical systems. One such molecular mechanism is photochromism, which is defined as a reversible transformation of a single chemical species between two forms with different absorption spectra. This transformation is induced in one or two directions *via* light irradiation.[3,4] Among the different photochromic materials that can reversibly and optically be switched between both of their forms, diarylethenes excel with high fatigue resistance, thermal stability, and relatively high quantum yields.[5–7] One particular diarylethene derivative that shows its photochromic functionality even in solid films is *cis*-1,2-dicyano-1,2-bis(2,4,5-trimethyl-3-thienyl)ethene (CMTE) (*cf.* Scheme 1).[5,8] This makes it a promising candidate to be used in future solid-state/molecular photonic hybrid structures.[9,10]

Using diarylethenes as the active component in a light controlled dielectric environment, both absorptive and dispersive parts of the dielectric function play an important role.[11] Most studies, however, focus on the optical absorption; only little information is available on the dispersive behavior of the dielectric response. Experimental studies also include investigations of the reaction dynamics of certain diarylethene derivatives with ultrafast spectroscopic techniques and determination of reaction quantum yields.[12–14] Theoretical work is mostly focused on the fundamental understanding of the chemical reaction mechanism underlying the photochromism.[15–17] Detailed *ab initio* calculations of the reaction dynamics of diarylethenes were not reported.

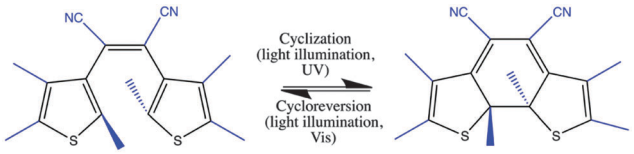

Scheme 1 Diarylethene derivative CMTE. Shown are open (left) and closed (right) ring form. The essential part for a normal-type diarylethene is shown in black, the side groups of CMTE in blue. Cyclization and cycloreversion by illumination with light are indicated.

In this article we present a comprehensive study of the photophysics of the diarylethene derivative CMTE. This includes the optical absorption spectra, perceived color, frequency dependent refractive index, and the reaction dynamics following photoexcitation. The latter gives us direct access to reaction timescales and quantum yields, which are typically difficult to access theoretically. We benchmark our results against higher-level quantum chemical methods and experiments. The convincing

Physics Department and Center for Optoelectronics and Photonics Paderborn (CeOPP), Universität Paderborn, Warburger Strasse 100, 33098 Paderborn, Germany. E-mail: stefan.schumacher@uni-paderborn.de

† Electronic supplementary information (ESI) available: Calculated spectra of the parallel and antiparallel conformers of the open ring form and of the closed ring form, tabulated values for the determination of color, tabulated values for static polarizability, trajectories of categories 2 and 4, and videos of the molecular dynamics. DOI: 10.1039/c3cp55490b

agreement we find highlights the potential of density-functional theory (DFT) based non-adiabatic *ab initio* molecular dynamics for the future design of more efficient photochromic compounds.

II. Methods

A. Experiment

For the absorption measurements CMTE (TCI, Japan) was dissolved in acetonitrile and stirred at room temperature for 24 h by weight percentage of 0.02 wt%, corresponding to a concentration of 0.0005 M. To minimize the solvent effect in determination of the refractive index, toluene was used with the same concentration. The measurements were performed using a quartz cuvette with a width of 1 cm. All data were normalized to a spectrum of the empty cuvette as a reference. The photochromic reaction was induced by continuous wavelength irradiation with Xe lamp light (150 W). Interference filters with central wavelengths of 546 nm and 405 nm and bandwidths of 10 nm were used. The setup for measurements of the extinction spectra consisted of a Xe light source, four off-axis parabolic mirrors, a grating monochromator (600 grooves per mm, blaze wavelength 400 nm), and a charge coupled device as a detector.

B. Theory

Geometry optimization and spectra. The ground state structures of the two isomers were optimized using density-functional theory (DFT)[18] with the PBE0[19,20] functional and the def2-SVP basis set.[21] The structures found are stable minima as proven by vibrational frequency analysis. The excitation energies were calculated with time-dependent DFT (TDDFT)[22] using the same functional and basis set. These were compared with calculations of excitation energies using the Tamm–Dancoff approximation (TDA)[23] and simplified Tamm–Dancoff approximation (sTDA).[24] To further assess the accuracy of TDDFT, TDA, and sTDA, respectively, excitation energies were also calculated using a wavefunction-based method. To this end, open and closed ring structures were optimized with CC2[25] using the resolution-of-the-identity implementation (RI-CC2)[26–29] in Turbomole[30] in combination with the def-TZVPP basis set[31] and the corresponding auxiliary basis set. The vertical excitation energies were then calculated with RI-CC2 using the def2-TZVPPD basis set[32] with the corresponding auxiliary basis set. All these calculations were done with Turbomole 6.5.[30] Basis set convergence and influence of solvent on the electronic excitation spectra for the DFT calculations were checked with a larger basis set and the polarizable continuum model with acetonitrile as solvent using the Gaussian 09 software package[33] and PBE0 functional. The deviations were found to be small, so the smaller basis set was used and no solvent was included in all production runs using Turbomole. Molecular structures were visualized using GaussView.[34]

Potential energy surfaces. Potential energy surfaces were calculated using the Gaussian09 suite[33] following the ideas of Masunov and co-workers.[35,36] The def-SVP basis set was used with the PBE0 functional. To account for the diradical character near the transition state, the PES for the ground state was calculated using unrestricted DFT with broken symmetry guess, *i.e.*, keyword guess = (mix, always) was used in Gaussian. The scan was performed varying the distance between the two reactive carbon atoms. The vertical excitation energies were then calculated with restricted TDDFT using TDA, starting from the structures of the relaxed ground state scan.

Non-adiabatic *ab initio* molecular dynamics. The non-adiabatic *ab initio* molecular dynamics for the cycloreversion, *i.e.*, ring opening reaction, was calculated along the lines given in ref. 37. The basis set and functional used were the same as for the static calculations, def2-SVP and PBE0, respectively. To generate a swarm of trajectories for the dynamical calculations with different initial conditions, the ground state of the rather rigid closed ring isomer was sampled using Born–Oppenheimer molecular dynamics. A timestep size of 50 a.u. was used and the ground state trajectory was calculated for a total of 4000 steps ($\sim$4.84 ps). To ensure thermal equilibration, a Nosé–Hoover thermostat with a temperature of 300 K and a response time of 500 a.u. was used. Finally, 100 structures with corresponding nuclear velocities were randomly chosen to calculate the non-adiabatic *ab initio* molecular dynamics starting in the first excited singlet state based on Trajectory Surface Hopping.[38] TDDFT in Tamm–Dancoff approximation was used with a timestep of 40 a.u. and a total of 1000 timesteps (corresponding to $\sim$0.97 ps). The initial conditions sampled from a canonical ensemble are then evolved in a microcanonical ensemble for the non-adiabatic dynamics – no thermostat was used. The implementation of the non-adiabatic dynamics calculations is based on linear response time-dependent density-functional theory.[39] Further details are given in ref. 37 and 40. Only the non-adiabatic coupling between the first excited state and the ground state is included which can be easily justified here with the significant energy separation to higher-lying excited states as long as the system is found in the first excited state (*cf.* Fig. 7 and 8; Fig. S4 and S5, ESI†). Methodological problems using TDDFT in the vicinity of the conical intersection[41] of ground and first excited states are alleviated using TDA.[42] Finally, we note that in order to perform the calculations with the SMP-version of Turbomole 6.5, the parallelization described in ref. 43 needs to be used.

III. Results and Discussion

A. Spectra of open and closed ring forms

Absorption spectra of CMTE measured in solution of open and closed ring forms are shown in Fig. 1 and 2, respectively. Conversion between the two forms is achieved by illumination with light in the visible or the UV spectral range, respectively, *cf.* Scheme 1. We compare the measured spectra with spectra for the two forms computed with a number of different theoretical methods. For proper calculation of the spectrum of the open ring form, two stable conformers have to be considered.[8] It is to be expected (very similar total energies are found for the two conformers) that the concentration for both conformers is about

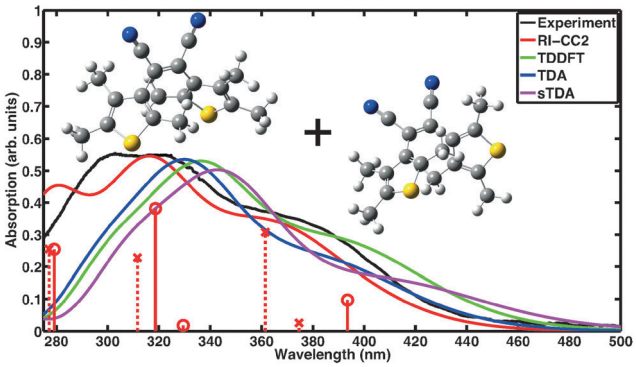

Fig. 1 Absorption spectrum of the open ring form of CMTE. The spectrum was measured in acetonitrile. Computed spectra are shown for different theoretical methods. These include both stable conformers in equal proportion. For RI-CC2 the transitions belonging to the antiparallel and parallel conformers are included as solid sticks with circles and dashed sticks with crosses, respectively. Due to the broken electronic conjugation of the inner ring in the open ring form, there is only negligible absorption in the visible range. Each spectrum is normalized to the corresponding maximum for the closed ring isomer in Fig. 2.

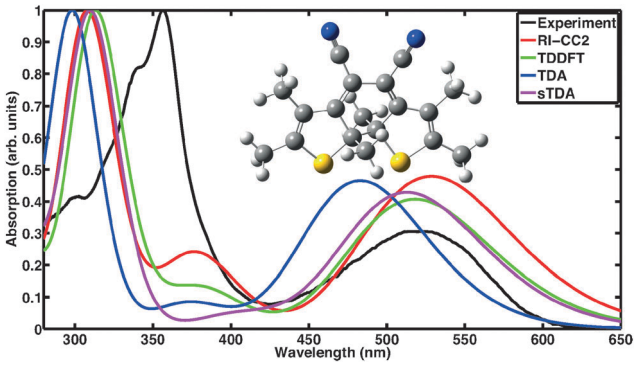

Fig. 2 Absorption spectrum of the closed ring form. Shown are the absorption measured in acetonitrile and theoretical data obtained with different methods. In contrast to the open ring form in Fig. 1, the lowest absorption feature lies here well within the visible range. Each spectrum is normalized to its maximum value.

the same such that their contributions are equally weighted in the calculated spectra. This way, a convincing agreement with the measured data is obtained with the wavefunction based RI-CC2 calculations. We note that the corresponding values of the D1 diagnostics[44] are sufficiently small (0.0658 and 0.0652 for the antiparallel and the parallel conformer, respectively) such that reliable results are obtained. We note that the spectra of antiparallel and parallel conformer individually do not agree as well with experiment as the averaged spectrum (*cf.* the sticks in Fig. 1 showing the contributions of both conformers separately and Fig. S1 and S2 of the ESI†). For the DFT-based calculations, we use the same approach. Inclusion of the two conformers still improves the overall result, however, in TDDFT the spectra are more similar for the two conformers such that the experimentally observed double-peak structure of the spectrum at shorter wavelength is not quite as well reproduced. The closed ring form of CMTE is rather rigid and only one stable ground state conformer exists. The spectra are shown in Fig. 2. Characteristic of the closed ring form of diarylethenes is the absorption at higher wavelength compared to the open ring form. This is found in all calculations and the excitation energies are in good agreement with the measurement. The high-energy peak found in experiment at approximately 350 nm is modeled less accurately. The D1 diagnostics here yields a value of 0.0948. Overall, we can conclude that the results of RI-CC2 and DFT-based methods are very similar for the closed ring form, but the (computationally much more expensive) wavefunction-based method yields a slightly improved absorption spectrum for the open ring form. This improvement is mostly found in the UV region, whereas the absorption in the visible region is rather similar.

B. Estimation of perceived color

A significant difference in the optical absorption of open and closed ring forms of CMTE in the visible spectral range is found above. This difference also determines the physiologically perceived difference in color of the two forms. To estimate the color from the optical absorption, this has to be translated into wavelength-dependent transmission or reflectance. To this end, we normalize the calculated absorption, $\alpha(\lambda)$, in the interval 380–780 nm. As successfully used in previous work,[45] from this the "inverse spectrum" can be calculated as a measure of the reflectance following the idea of Beck:[46]

$$\beta(\lambda) = 1 - \alpha(\lambda). \quad (1)$$

Now normalized values for the CIE Tristimulus values can be calculated as:[47]

$$X_n = \int_{380\ \mathrm{nm}}^{780\ \mathrm{nm}} S(\lambda)\bar{x}(\lambda)\mathrm{d}\lambda. \quad (2)$$

In this equation $S(\lambda)$ is the spectral power distribution of the illuminant. To simulate daylight conditions, the D_{65} standard illuminant is used. $\bar{x}(\lambda)$ is one of the three color matching functions (CMF) for which the CIE 1931 standard is used. Analogous equations are defined for Y_n and Z_n with the corresponding CMF, $\tilde{y}$ and $\tilde{z}$. Data for these quantities are for example tabulated online[48] and can be found in ref. 47. The tristimulus values are now obtained as:

$$X = k\int_{380\ \mathrm{nm}}^{780\ \mathrm{nm}} \beta(\lambda)S(\lambda)\bar{x}(\lambda)\mathrm{d}\lambda, \quad (3)$$

with $k = 100/Y_n$. The other two values, Y and Z, are calculated analogously. If needed, the tristimulus values obtained can be transformed into other color spaces, *e.g.*, chromaticity coordinates or CIE ($L^*a^*b^*$)-space (*cf.* Table S1 of the ESI†). For the latter, the following equations can be used as long as $\frac{X}{X_n}$, $\frac{Y}{Y_n}$, and $\frac{Z}{Z_n}$ are larger than 0.01:[47]

$$L^* = 116\left(\frac{Y}{Y_n}\right)^{1/3} - 16, \quad (4)$$

$$a^* = 500\left[\left(\frac{X}{X_n}\right)^{1/3} - \left(\frac{Y}{Y_n}\right)^{1/3}\right], \quad (5)$$

$$b^* = 200\left[\left(\frac{Y}{Y_n}\right)^{1/3} - \left(\frac{Z}{Z_n}\right)^{1/3}\right]. \quad (6)$$

The colors that we determined as described above are shown in Fig. 3 for experiment and the different theoretical methods used. Pictures of CMTE in solution in open and closed ring form are shown in Fig. 4. The difference in color compared to the colors estimated in Fig. 3 is partly due to the different ambient illumination under laboratory conditions. We note that according to the ΔE-values given in the ESI,† for the open ring form CC2 yields the best results and for the closed ring form sTDA and TDDFT. This is consistent with the absorption spectra of open and closed ring form in the visible range.

C. Dielectric function and refractive index

The absorption spectra discussed thus far (Fig. 1 and 2) only contain direct information about the imaginary part of the molecules' dielectric response. However, a thorough analysis of the optical properties and changes thereof in the different forms of the photochromic molecules should also include the dispersive part of the dielectric function. For the system under study, the spectral range of interest is in the visible region, where the biggest change of optical properties is found with the photochromic conversion process. As this spectral range contains resonances related to electronic excitations, care has to be taken in constructing the dielectric response. The resonant contribution to the dielectric response can be given as:

$$\varepsilon_r(\omega) = 1 + \sum_{j=1}^{N} \chi_j'(\omega) + i\chi_j''(\omega), \quad (7)$$

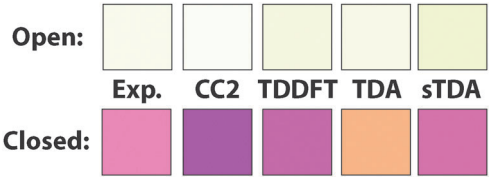

Fig. 3 Perceived colors of open and closed ring isomers as determined from the absorption spectra under daylight conditions. Colors are obtained from experiment and the different theoretical methods used.

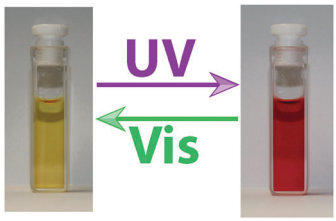

Fig. 4 Pictures of CMTE in solution in open (left) and closed (right) ring forms. The difference in color perception compared with Fig. 3 is partly due to the different ambient light laboratory conditions under which the pictures were taken.

with the real and imaginary parts:

$$\chi_j'(\omega) = \chi_{0j}\frac{{\omega_{0j}}^2 - \omega^2}{({\omega_{0j}}^2 - \omega^2)^2 + (\omega\Delta\omega_j)^2},$$
$$\chi_j''(\omega) = -\chi_{0j}\frac{\omega\Delta\omega_j}{({\omega_{0j}}^2 - \omega^2)^2 + (\omega\Delta\omega_j)^2}, \quad (8)$$

of the dielectric response. From the measured extinction data, we determine the absorption coefficient taking into account the cuvette thickness and the molecular concentration used. Then we fit the absorption data using a Lorentz oscillator model for $\varepsilon_r(\omega)$ with multiple oscillators:

$$\alpha(\omega) = -\frac{2\mathrm{Im}\left(\sqrt{\varepsilon_r(\omega)}\right)\omega}{c_0}. \quad (9)$$

Using the resulting fitting parameters (widths, amplitudes, and spectral position) of each Lorentzian the resonant contribution to the (real) refractive index $\Delta n(\omega)$ is computed:

$$\Delta n = \mathrm{Re}\left(\sqrt{\varepsilon_r(\omega)}\right). \quad (10)$$

For the open form, good agreement between the fit and the experimental data was obtained using four model oscillators. For the closed form of the molecule, five oscillators were required. From the theoretical side, the resonant part of the dielectric function can be constructed directly based on eqn (8) using the computed oscillator strengths χ_{0j} and resonance energies ω_{0j}. Here, all the computed 20 transitions are included with a common broadening to reproduce the experimental absorption spectrum. A common prefactor was included to obtain the correct absolute values for the concentration used in the experiment. In addition to the resonant contribution discussed above, the refractive index also contains a contribution from the static polarizability of the system, both from the solvent and from the molecules of interest. In a first approximation, here we add a constant offset to the dielectric function such that $n(\omega \to 0) \approx 1.54$ for the closed ring form is obtained, which is in good agreement with previous work.[49] Results are shown in Fig. 5. A significant change of the refractive index is found in the visible spectral range upon photo-induced

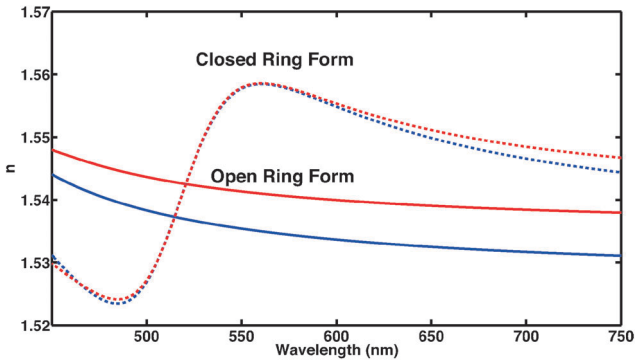

Fig. 5 Frequency-dependent refractive index of CMTE in the visible spectral range. Clearly visible is the significant difference of open and closed ring form in the spectral range shown both for experiment (blue) and theory (red).

isomerization between open and closed ring forms. Comparing the experimental data with the computed results, the main difference lies in the slight offset for the open ring form. We note that this is consistent with the difference in the absorption spectra in the UV spectral range comparing experiment and theory in Fig. 1. In a more sophisticated approach, computed data can also be used for the static part of the dielectric function using the Lorentz–Lorenz equation

$$\frac{\varepsilon_{r_0}-1}{\varepsilon_{r_0}+2}=\frac{\rho N_A}{3\varepsilon_0 M}\alpha. \quad (11)$$

Here, ε_{r_0} denotes the static relative electric permittivity. On the right-hand side, ρ is the density of the substance, N_A Avogadro's number, ε_0 the vacuum permittivity, and M the molar mass. To be applicable to molecules in a solvent, also the solvent contribution has to be taken into account and the Lorentz–Lorenz equation for a two-component system has to be used.[50] In the ESI,† we have tabulated our computed values for the diarylethenes' contribution to the static polarizability α and give a brief discussion of the accuracy of different quantum chemical methods for obtaining this quantity.

D. Reaction mechanism and non-adiabatic *ab initio* molecular dynamics

Apart from the molecular equilibrium properties discussed above, insight on an entirely different level can be obtained from an investigation of the actual reaction mechanism leading to photochromic conversion upon light irradiation. In addition to the equilibrium properties, important quantities that characterize the reaction are for example the reaction quantum yield and reaction timescales. Both are typically difficult to access, experimentally and theoretically.

Here we focus on a detailed analysis of the cycloreversion reaction, leading from the closed ring form to the open ring form. A qualitative feeling for the reaction can be obtained from the potential energy surfaces along a reactive coordinate, *i.e.*, the interatomic distance of the two reactive carbon atoms of the central conjugated ring of CMTE. The computed result is shown in Fig. 6

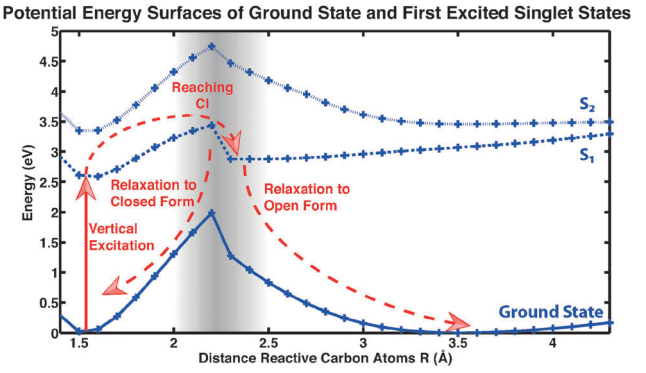

Fig. 6 Potential energy surfaces of CMTE. Shown are ground state and excited states S_1 (dashed) and S_2 (dotted). The lines are included as a guide to the eye. For a successful cycloreversion after vertical excitation (photoexcitation) a potential barrier has to be overcome in the S_1 state to reach the conical intersection (CI). For more details see discussion in the text.

and the different reaction pathways after illumination of the closed-ring form with visible light are indicated. After vertical excitation into the first excited state S_1, the system arrives in a pronounced minimum in energy on the S_1 surface. In order for the cycloreversion reaction to occur, the system now has to reach the conical intersection between S_0 and S_1 at about 2.1 Å. For this, the potential energy barrier of about 0.8 eV has to be overcome. Otherwise, the molecule relaxes back to the former ground state through a different non-radiative relaxation channel (in experiment also radiative decay can occur), preventing a successful cycloreversion. We note that for methodological reasons (*cf.* Methods section above), the data in Fig. 6 in the vicinity of the conical intersection (grey-shaded area) have to be treated with care.

In the following we present a detailed analysis of the cycloreversion reaction based on non-adiabatic *ab initio* molecular dynamics calculations. We note that in contrast to the largely simplified one-dimensional picture of the potential energy surface in Fig. 6, which gives only a rough picture of the expected reaction, in these calculations the reaction takes place on the very complex and high-dimensional potential energy surface including all the dynamical degrees of freedom. We have computed 100 trajectories starting from slightly different initial conditions in the S_1 state (see details in the Methods section above). The trajectories we find can be grouped into four different categories.

The first category consists of eleven trajectories that underwent a successful cycloreversion. A representative example of such a trajectory is shown in Fig. 7. The minimum in the first excitation energy from the ground state is found in each trajectory at a distance between the two reactive carbon atoms at about 2 Å. This is consistent with the PES shown in Fig. 6. This minimum was reached in the calculations within 150–500 fs, followed by successful ring opening.

Ten trajectories belong to the second category. These reached the conical intersection at about 2 Å but subsequently relaxed back to the closed ring form in the ground state (see Fig. S4 of the ESI†). The time needed to reach the conical intersection in these cases is about the same as in the first category. The distance for the minimum energy of the first excitation tends to be about 0.03 Å lower than in the first category. The minimum of the first excitation energy we find is about 0.2 eV or smaller.

The third category consists of 26 trajectories. For these the system "hopped" back into the ground state even though the conical intersection was still far away. This process is mediated by vibronic coupling.[40] Analyzing the data of these trajectories it is found that apart from one exception, the minimal value of the first excitation energy is bigger than 0.8 eV. The distance between the reactive carbon atoms does not exceed 1.87 Å for all trajectories except the trajectory with an energy separation lower than 0.8 eV. So for this category, the trajectories seem to be trapped in a minimum of the first excited state that prevents the molecules from reaching the conical intersection and consequently does not lead to ring opening. In Fig. 8 we show one of the trajectories of this third category as an example of the reaction dynamics.

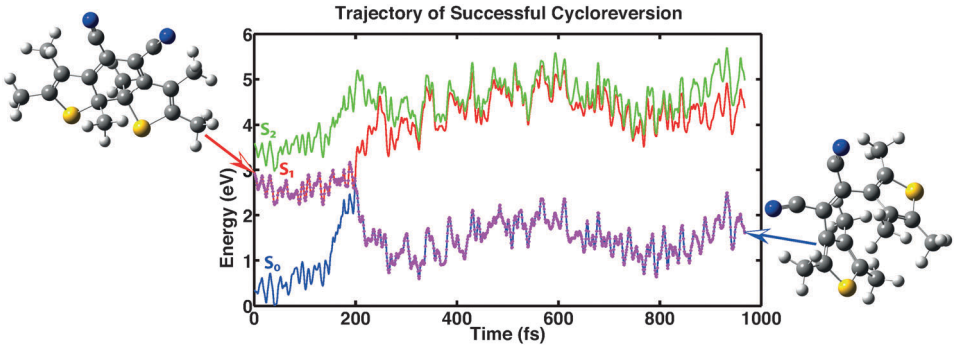

Fig. 7 Example showing a successful cycloreversion reaction. The trajectory shown is representative of 11 of the computed 100 trajectories.

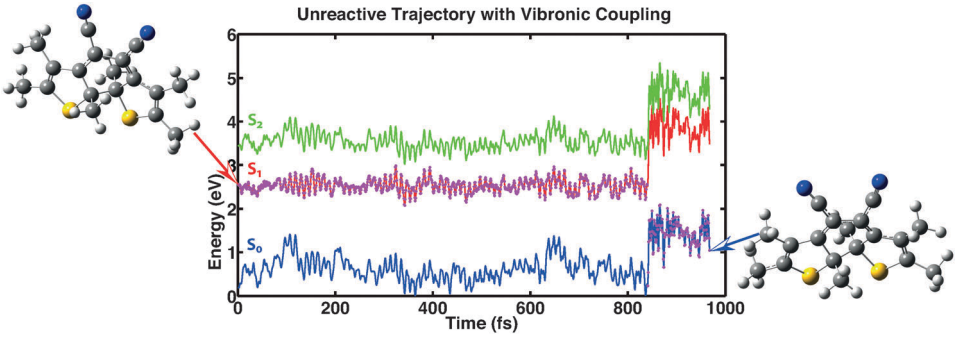

Fig. 8 Example showing one out of 26 trajectories for which the molecule relaxed back into the ground state without actually reaching the conical intersection. This process is mediated by vibronic coupling.

Finally, the fourth category consists of 53 trajectories that did not reach the ground state within the time of simulation (see Fig. S5 of the ESI†). Only seven trajectories reach a distance between the reactive carbon atoms of 1.9 Å or larger, and the minimum in the first excitation energy is bigger than 0.5 eV. So it is to be expected that these trajectories do not reach the conical intersection but are trapped in a minimum of the first excited state similar to the third category. Continuation of these trajectories for another 2000 time steps in the dynamics led to 24 trajectories that jumped back into the ground state, but none of these underwent successful cycloreversion.

Videos showing the computed time-evolution of the molecular geometries for the four types of different trajectories discussed are available online in the ESI.†

After analysis of all the data, it appears to be plausible to assume that the trajectories of the third and fourth category will not undergo successful cycloreversion. So the quantum yield for cycloreversion we determine by our simulations is 0.11. This is in good agreement with previous values found experimentally, *i.e.* 0.07 ± 0.02 and 0.12 ± 0.02 respectively.[8]

We note that in contrast to the non-adiabatic *ab initio* molecular dynamics of the cycloreversion, for the dynamics of the cyclization process, more than just the first excited singlet state may have to be included. In the spectrum of the open form, Fig. 1, it is clearly visible that the lowest excitation energy is only a shoulder on a higher-lying excitation. Therefore, irradiation with UV light will result in population of multiple excited singlet states. However, in the current implementation of the trajectory surface hopping in Turbomole as employed here, analytic non-adiabatic coupling (NAC) vectors are only available between the ground and the first excited state. The calculation of analytic NAC-vectors between excited states has already been described theoretically[51] and an extension of the present approach to also include these is to be expected in the future. We further note that Newton-X[52] interfaced with Turbomole already offers the possibility to calculate non-adiabatic dynamics on any excited state using TDDFT. However, to the best of our knowledge the combination with TDA we used here to improve the description of the potential energy surfaces of ground and first excited singlet states near the conical intersection[53] is currently not supported. We further note that in our calculations each single trajectory requires 1000 ground state DFT calculations with subsequent calculation of excitation energies using TDA. To reduce computational cost in future studies of larger systems usage of sTDA instead of TDA may also be a viable option.

IV. Conclusion

We have investigated different facets of the photochromic diarylethene derivative CMTE. We have shown that optical absorption related to electronic excitations, perceived color, frequency dependent refractive index, and reaction quantum yields and time scales can be successfully computed (and predicted) using density-functional theory based quantum-chemical approaches.

The computed results compare well with experimental data. For example, from our non-adiabatic *ab initio* molecular dynamics calculations, we confirm that the cycloreversion quantum yield of CMTE is about 11%. For the future it would be worthwhile to build upon these first results and theoretically study the influence of different substituents to improve on the quantum yield without the need to actually synthesize all the molecules studied. Furthermore, with its proven photochromic capabilities also in solid films, CMTE would be a promising compound to be used in future solid-state/molecular hybrid structures utilizing the light-induced change in the molecular material's dielectric response for optical applications.[11]

Conflicts of interest

The authors declare no competing financial interest.

Acknowledgements

We are grateful for fruitful discussions with Prof. Martin J. Paterson, Heriot-Watt University, Edinburgh, UK. We acknowledge financial support from the DFG (GRK 1464) and a grant for computing time at PC^2 Paderborn Center for Parallel Computing. C.W. is grateful for his PhD-scholarship from the Friedrich-Ebert-Stiftung. We thank the Turbomole Support team for providing helpful information on the implementation of the TSH-algorithm.

References

1 A. Bianco, S. Perissinotto, M. Garbugli, G. Lanzani and C. Bertarelli, *Laser Photonics Rev.*, 2011, **5**, 711–736.
2 D. Nau, R. P. Bertram, K. Buse, T. Zentgraf, J. Kuhl, S. G. Tikhodeev, N. A. Gippius and H. Giessen, *Appl. Phys. B: Lasers Opt.*, 2006, **82**, 543–547.
3 *Photochromism*, ed. G. H. Brown, John Wiley & Sons, 1971, vol. III.
4 *Photochromism: Molecules and Systems*, ed. H. Dürr and H. Bouas-Laurent, Elsevier, 2003.
5 *New Frontiers in Photochromism*, ed. M. Irie, Y. Yokoyama and T. Seki, Springer, Japan, 2013.
6 M. Irie, *Proc. Jpn. Acad., Ser. B*, 2010, **86**, 472–483.
7 M. Irie, *Chem. Rev.*, 2000, **100**, 1685–1716.
8 A. Spangenberg, J. A. P. Perez, A. Patra, J. Piard, A. Brosseau, R. Métivier and K. Nakatani, *Photochem. Photobiol. Sci.*, 2010, **9**, 188–193.
9 H. Jean-Ruel, R. R. Cooney, M. Gao, C. Lu, M. A. Kochman, C. A. Morrison and R. J. D. Miller, *J. Phys. Chem. A*, 2011, **115**, 13158–13168.
10 S. Kobatake, H. Hasegawa and K. Miyamura, *Cryst. Growth Des.*, 2011, **11**, 1223–1229.
11 K. A. Piegdon, M. Lexow, G. Grundmeier, H.-S. Kitzerow, K. Pärschke, D. Mergel, D. Reuter, A. D. Wieck and C. Meier, *Opt. Express*, 2012, **20**, 6060–6067.
12 Y. Tatsumi, J. Kita, W. Uchida, K. Ogata, S. Nakamura and K. Uchida, *J. Phys. Chem. A*, 2012, **116**, 10973–10979.
13 Y. Ishibashi, T. Umesato, S. Kobatake, M. Irie and H. Miyasaka, *J. Phys. Chem. C*, 2012, **116**, 4862–4869.
14 H. Jean-Ruel, M. Gao, M. A. Kochman, C. Lu, L. C. Liu, R. R. Cooney, C. A. Morrison and R. J. D. Miller, *J. Phys. Chem. B*, 2013, **117**, 15894–15902.
15 M. Boggio-Pasqua, M. Ravaglia, M. J. Bearpark, M. Garavelli and M. A. Robb, *J. Phys. Chem. A*, 2003, **107**, 11139–11152.
16 S. Nakamura, K. Uchida and M. Hatakeyama, *Molecules*, 2013, **18**, 5091–5103.
17 A. Perrier, S. Aloïse, M. Olivucci and D. Jacquemin, *J. Phys. Chem. Lett.*, 2013, **4**, 2190–2196.
18 M. Häser and R. Ahlrichs, *J. Comput. Chem.*, 1989, **10**, 104–111.
19 J. P. Perdew, K. Burke and M. Ernzerhof, *Phys. Rev. Lett.*, 1996, **77**, 3865–3868.
20 C. Adamo and V. Barone, *J. Chem. Phys.*, 1999, **110**, 6158–6170.
21 A. Schäfer, H. Horn and R. Ahlrichs, *J. Chem. Phys.*, 1992, **97**, 2571–2577.
22 F. Furche and R. Ahlrichs, *J. Chem. Phys.*, 2002, **117**, 7433–7447.
23 S. Hirata and M. Head-Gordon, *Chem. Phys. Lett.*, 1999, **314**, 291–299.
24 S. Grimme, *J. Chem. Phys.*, 2013, **138**, 244104.
25 O. Christiansen, H. Koch and P. Jørgensen, *Chem. Phys. Lett.*, 1995, **243**, 409–418.
26 C. Hättig and F. Weigend, *J. Chem. Phys.*, 2000, **113**, 5154–5161.
27 C. Hättig and A. Köhn, *J. Chem. Phys.*, 2002, **117**, 6939–6951.
28 C. Hättig, *J. Chem. Phys.*, 2003, **118**, 7751–7761.
29 C. Hättig, A. Hellweg and A. Köhn, *Phys. Chem. Chem. Phys.*, 2006, **8**, 1159–1169.
30 *TURBOMOLE V6.5 2013, a development of University of Karlsruhe and Forschungszentrum Karlsruhe GmbH, 1989-2007, TURBOMOLE GmbH, since 2007, available from* http://www.turbomole.com.
31 F. Weigend, M. Häser, H. Patzelt and R. Ahlrichs, *Chem. Phys. Lett.*, 1998, **294**, 143–152.
32 D. Rappoport and F. Furche, *J. Chem. Phys.*, 2010, **133**, 134105.
33 M. J. Frisch, G. W. Trucks, H. B. Schlegel, G. E. Scuseria, M. A. Robb, J. R. Cheeseman, G. Scalmani, V. Barone, B. Mennucci, G. A. Petersson, H. Nakatsuji, M. Caricato, X. Li, H. P. Hratchian, A. F. Izmaylov, J. Bloino, G. Zheng, J. L. Sonnenberg, M. Hada, M. Ehara, K. Toyota, R. Fukuda, J. Hasegawa, M. Ishida, T. Nakajima, Y. Honda, O. Kitao, H. Nakai, T. Vreven, J. A. Montgomery Jr., J. E. Peralta, F. Ogliaro, M. Bearpark, J. J. Heyd, E. Brothers, K. N. Kudin, V. N. Staroverov, R. Kobayashi, J. Normand, K. Raghavachari, A. Rendell, J. C. Burant, S. S. Iyengar, J. Tomasi, M. Cossi, N. Rega, J. M. Millam, M. Klene, J. E. Knox, J. B. Cross, V. Bakken, C. Adamo, J. Jaramillo, R. Gomperts, R. E. Stratmann, O. Yazyev, A. J. Austin, R. Cammi, C. Pomelli, J. W. Ochterski, R. L. Martin, K. Morokuma, V. G. Zakrzewski,

G. A. Voth, P. Salvador, J. J. Dannenberg, S. Dapprich, A. D. Daniels, Ö. Farkas, J. B. Foresman, J. V. Ortiz, J. Cioslowski and D. J. Fox, *Gaussian 09 Revision D.01*, Gaussian Inc., Wallingford, CT, 2009.

34 R. Dennington, T. Keith and J. Millam, *GaussView Version 5.0.9*, Semichem Inc., Shawnee Mission, KS, 2009.

35 I. Mikhailov and A. E. Masunov, Theoretical Photochemistry of the Photochromic Molecules Based on Density Functional Theory Methods, in *Computational Science – ICCS 2009*, ed. G. Allen, J. Nabrzyski, E. Seidel, G. D. van Albada, J. Dongarra and P. M. A. Sloot, Springer-Verlag, Berlin, Heidelberg, 2009, vol. 5545, pp. 169–178.

36 P. D. Patel and A. E. Masunov, *J. Phys. Chem. C*, 2011, **115**, 10292–10297.

37 E. Tapavicza, A. M. Meyer and F. Furche, *Phys. Chem. Chem. Phys.*, 2011, **13**, 20986–20998.

38 J. C. Tully, *J. Chem. Phys.*, 1990, **93**, 1061–1071.

39 E. Tapavicza, I. Tavernelli and U. Röthlisberger, *Phys. Rev. Lett.*, 2007, **98**, 023001.

40 E. Tapavicza, G. D. Bellchambers, J. C. Vincent and F. Furche, *Phys. Chem. Chem. Phys.*, 2013, **15**, 18336–18348.

41 B. G. Levine, C. Ko, J. Quenneville and T. J. Martnez, *Mol. Phys.*, 2006, **104**, 1039–1051.

42 E. Tapavicza, I. Tavernelli, U. Röthlisberger, C. Filippi and M. E. Casida, *J. Chem. Phys.*, 2008, **129**, 124108.

43 C. Van Wüllen, *J. Comput. Chem.*, 2011, **32**, 1195–1201.

44 A. Köhn and C. Hättig, *J. Chem. Phys.*, 2003, **119**, 5021–5036.

45 C. Adamo and D. Jacquemin, *Chem. Soc. Rev.*, 2013, **42**, 845–856.

46 M. E. Beck, *Int. J. Quantum Chem.*, 2005, **101**, 683–689.

47 G. Wyszecki and W. S. Stiles, *Color Science: Concepts and Methods, Quantitative Data and Formulae*, John Wiley & Sons, 2000.

48 www.cie.co.at.

49 A. Spangenberg, R. Métivier, R. Yasukuni, K. Shibata, A. Brosseau, J. Grand, J. Aubard, P. Yu, T. Asahi and K. Nakatani, *Phys. Chem. Chem. Phys.*, 2013, **15**, 9670–9678.

50 G. Callierotti, A. Bianco, C. Castiglioni, C. Bertarelli and G. Zerbi, *J. Phys. Chem. A*, 2008, **112**, 7473–7480.

51 I. Tavernelli, B. F. E. Curchod, A. Laktionov and U. Röthlisberger, *J. Chem. Phys.*, 2010, **133**, 194104.

52 M. Barbatti, M. Ruckenbauer, F. Plasser, J. Pittner, G. Granucci, M. Persico and H. Lischka, *WIREs: Comput. Mol. Sci.*, 2014, **4**, 26–33.

53 S. L. Li, A. V. Marenich, X. Xu and D. G. Truhlar, *J. Phys. Chem. Lett.*, 2014, **5**, 322–328.

Supplement: Optical spectrum, perceived color, refractive index, and non-adiabatic dynamics of the photochromic diarylethene CMTE

Christian Wiebeler,[1] Christina A. Bader,[1] Cedrik Meier,[1] and Stefan Schumacher[1]

[1]*Physics Department and Center for Optoelectronics and Photonics Paderborn (CeOPP), Universität Paderborn, Warburger Strasse 100, 33098 Paderborn, Germany*

(Dated: December 28, 2013)

I. SUPPLEMENT

A. Spectra of open and closed ring forms

As discussed in the main article, the spectra of the open ring form was calculated as average of two conformers. For one conformer the thiophene rings are oriented approximately antiparallel to each other and for the other one they are oriented approximately parallel. Similar trends for basis set convergence and influence of solvent are found among all DFT-based methods, therefore only the corresponding spectra calculated with TDDFT are shown here. For all DFT calculations PBE0 was used as functional. The RI-CC2 and TDDFT calculations with def2-SVP basis set were done using Turbomole,[1] the other calculations shown in this section using Gaussian 09.[2]

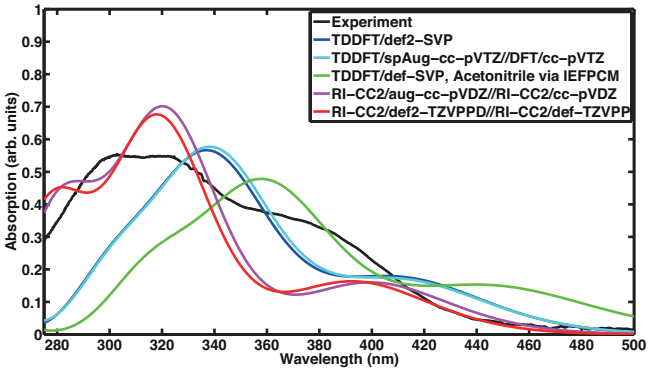

FIG. S1: Absorption spectrum of the antiparallel conformer of the open ring form of CMTE. Computed spectra are shown for different theoretical methods. All spectra are normalized to the respective maximum of the closed ring isomer.

For the antiparallel conformer, the absorption at about 410 nm is similar for all methods shown, see FIG. S1. However, the absorption at about 320 nm is red-shifted compared to the results of the wavefunction-based method. Furthermore, the high-energy shoulder of the absorption is more pronounced with the latter method.

For the parallel conformer, the absorption at 370 nm is more distinct for the RI-CC2 results than for the TDDFT one, see FIG. S2. Furthermore, the absorption is again more pronounced in the low wavelength region with the former method.

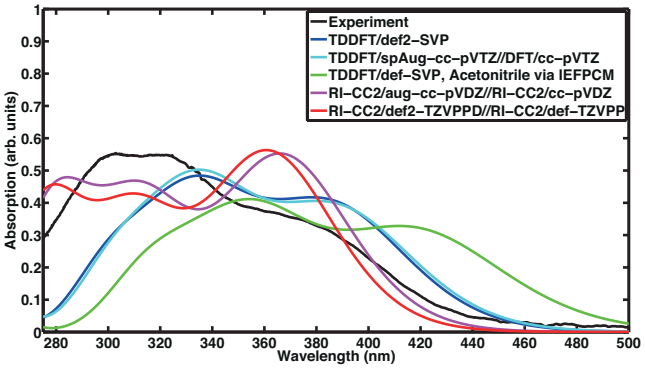

FIG. S2: Absorption spectrum of the parallel conformer of the open ring form of CMTE. Computed spectra are shown for different theoretical methods. All spectra are normalized to the respective maximum of the closed ring isomer.

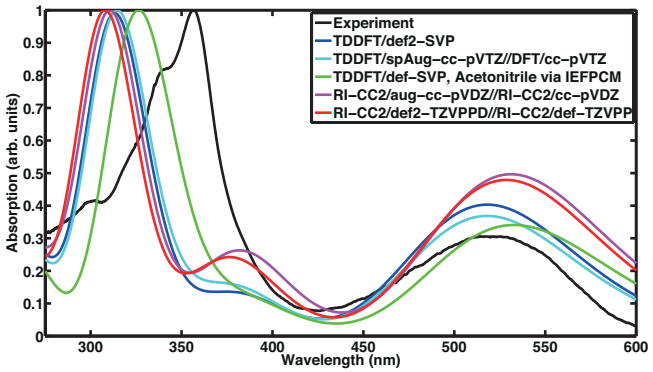

FIG. S3: Absorption spectrum of the closed ring form. Shown are the spectra calculated with different theoretical methods. All spectra are normalized to the respective maximum value.

The absorption of the closed ring isomer is similar for both methods, see FIG. S3. Especially the peaks with higher absorption are quite similar. There is only a slight deviation in the shape of the absorption between the two peaks.

Overall, it can be seen that the inclusion of solvent effects leads to small red-shifts of the absorption. However the quality of the absorption spectra is in general not improved. Furthermore, the results for the DFT-based method seem to be nearly converged, even for the smaller def2-SVP basis set. For the wavefunction-based method

the spectrum calculated with aug-cc-pVDZ seems to already yield reliable results, that do not change much, if a larger basis set is used.

B. Estimation of perceived color

Following the description for the estimation of perceived color, the results are first given in CIE tristimulus values. These values can be transformed in different color spaces. The values for two color spaces are therefore given in TABLE S1.

C. Dielectric function and refractive index

For the determination of the static polarizability with PBE0 and RI-MP2, first the structures were optimized using the cc-pVDZ and cc-pVTZ basis sets.[4,5] For the RI-MP2 calculations the corresponding auxiliary basis sets[6] were used. For the calculations of the static polarizability, the augmented versions of the previously mentioned basis sets were used. RI-MP2 is used as a reference for the DFT calculation.[7] The calculations described in this section were done using Turbomole.[1] The static polarizabilities are tabulated in TABLE S2. Both methods show that the polarizability of parallel and antiparallel conformer is similar and that the closed ring form is the structure with the highest polarizability.

D. Reaction mechanism and non-adiabatic ab initio molecular dynamics

In the main article only the trajectories for two categories are shown. The remaining trajectories can be found in FIG. S4 and FIG. S5. Furthermore, animations for trajectories of all four categories can be found online.

[1] *TURBOMOLE V6.5 2013, a development of University of Karlsruhe and Forschungszentrum Karlsruhe GmbH, 1989-2007, TURBOMOLE GmbH, since 2007, available from* `http://www.turbomole.com`.

[2] M. J. Frisch, G. W. Trucks, H. B. Schlegel, G. E. Scuseria, M. A. Robb, J. R. Cheeseman, G. Scalmani, V. Barone, B. Mennucci, G. A. Petersson, H. Nakatsuji, M. Caricato, X. Li, H. P. Hratchian, A. F. Izmaylov, J. Bloino, G. Zheng, J. L. Sonnenberg, M. Hada, M. Ehara, K. Toyota, R. Fukuda, J. Hasegawa, M. Ishida, T. Nakajima, Y. Honda, O. Kitao, H. Nakai, T. Vreven, J. A. Montgomery, Jr., J. E. Peralta, F. Ogliaro, M. Bearpark, J. J. Heyd, E. Brothers, K. N. Kudin, V. N. Staroverov, R. Kobayashi, J. Normand, K. Raghavachari, A. Rendell, J. C. Burant, S. S. Iyengar, J. Tomasi, M. Cossi, N. Rega, J. M. Millam, M. Klene, J. E. Knox, J. B. Cross, V. Bakken, C. Adamo, J. Jaramillo, R. Gomperts, R. E. Stratmann, O. Yazyev, A. J. Austin, R. Cammi, C. Pomelli, J. W. Ochterski, R. L. Martin, K. Morokuma, V. G. Zakrzewski, G. A. Voth, P. Salvador, J. J. Dannenberg, S. Dapprich, A. D. Daniels, Ö. Farkas, J. B. Foresman, J. V. Ortiz, J. Cioslowski and D. J. Fox, *Gaussian 09 Revision D.01*, Gaussian Inc. Wallingford CT 2009.

[3] G. Wyszecki and W. S. Stiles, *Color Science: Concepts and Methods, Quantitative Data and Formulae*, John Wiley & Sons, 2000.

[4] T. H. Dunning, *J. Chem. Phys.*, 1989, **90**, 1007–1023.

[5] R. A. Kendall, T. H. Dunning and R. J. Harrison, *J. Chem. Phys.*, 1992, **96**, 6796–6806.

[6] F. Weigend, A. Köhn and C. Hättig, *J. Chem. Phys.*, 2002, **116**, 3175–3183.

[7] D. H. Friese, N. O. C. Winter, P. Balzerowski, R. Schwan and C. Hättig, *J. Chem. Phys.*, 2012, **136**, 174106.

TABLE S1: Tabulated values for the perceived colors of open and closed ring isomers as determined from the absorption spectra for daylight conditions. The last column shows the distance between the coordinates of $(L^*a^*b^*)$-values based on calculated absorption spectra to the $(L^*a^*b^*)$-values calculated from the corresponding measured absorption spectrum. This difference is proportional to the deviation in color perception.[3]

	X	Y	Z	x	y	L^*	a^*	b^*	**ΔE**
Open									
Exp.	88.09	93.71	91.12	0.3228	0.3433	97.51	-1.78	7.23	
CC2	93.36	99.84	100.40	0.3180	0.3401	99.94	-2.70	5.23	3.28
TDDFT	90.46	99.33	85.28	0.3289	0.3611	99.74	-7.05	15.19	9.80
TDA	91.76	99.60	92.14	0.3237	0.3513	99.85	-5.15	10.55	5.27
sTDA	88.29	98.16	73.44	0.3397	0.3777	99.29	-9.05	23.36	17.78
Closed									
Exp.	67.69	46.67	61.78	0.3843	0.2650	73.98	58.68	-10.45	
CC2	51.84	28.15	76.35	0.3316	0.1800	60.02	80.84	-46.62	44.66
TDDFT	58.44	34.45	68.44	0.3623	0.2135	65.32	74.67	-31.12	27.54
TDA	73.46	63.71	33.63	0.4301	0.3730	83.82	28.62	36.90	56.93
sTDA	61.05	38.08	61.74	0.3795	0.2367	68.08	68.99	-20.58	15.61

TABLE S2: Static polarizabilities calculated for the three stable structures of CMTE. Further information about the methodology are given in the text.

	PBE0/pVDZ	**PBE0/pVTZ**	**RI-MP2/pVDZ**	**RI-MP2/pVTZ**
Closed	282.30	278.56	278.25	272.99
Parallel	272.47	269.05	266.81	261.98
Antiparallel	271.70	268.37	266.37	261.62

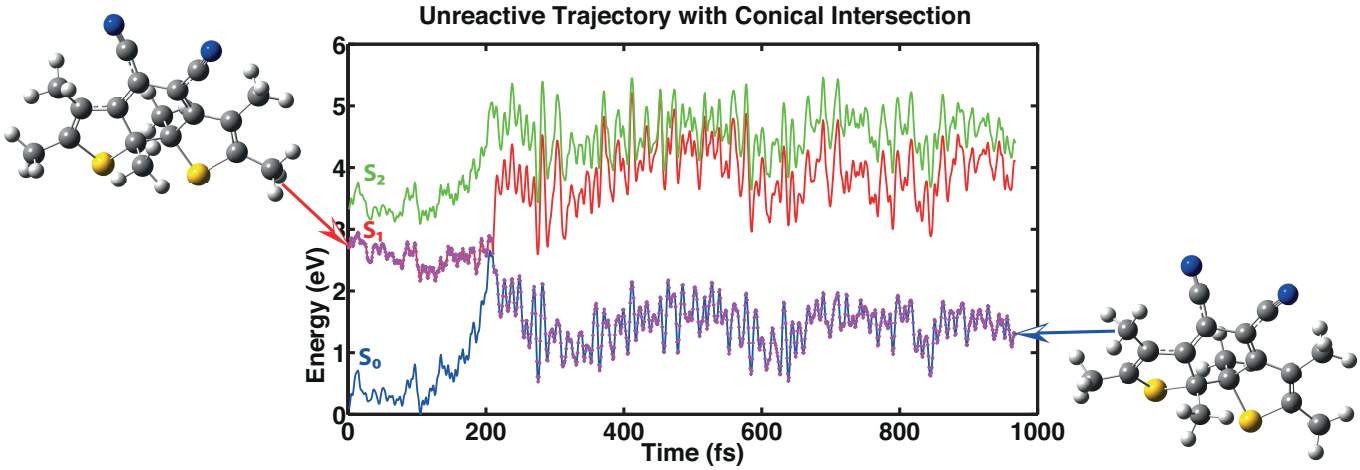

FIG. S4: Example showing an unsuccessful cycloreversion reaction after the trajectory reached the Conical Intersection. The trajectory shown is representative for 9 of the computed 100 trajectories.

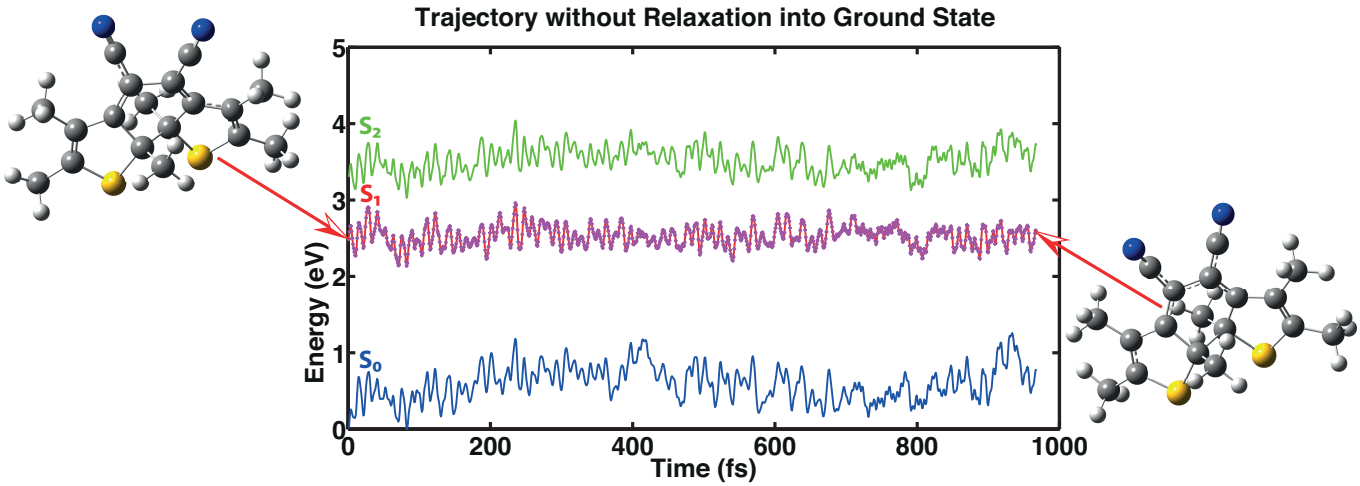

FIG. S5: Example showing one out of 53 trajectories for which the molecule is trapped in the first excited singlet state and does not reach the conical intersection.

7.3 Validation of Nonadiabatic Dynamics for Cycloreversion Reaction

To assess the reliability of the NA-AIMD results and further analyze the outcome, more investigations will be presented. Concerning the size of the time step, it has been checked that the total population (almost) exactly stays 1 during the entire time of evolution, proving the stability of the used time step. In addition, we simulated trajectories using only a quarter of the original time step yielding in principle the same results for the dynamics apart from the statistical hopping events. To check the accuracy of the quantum chemical method employed, i.e. PBE0/def2-SVP using TDDFT in Tamm-Dancoff approximation (TDA), single point RI-CC2 calculations have been done for the two exemplary trajectories that reached the CI. The geometries were taken from every fifth time step of the TSH trajectories and 60 calculations per trajectory were done such that both trajectories have passed the CI.

For the trajectory of category I, see left part of figure 7.3, the energies of S_0 calculated with RI-CC2 (red) and TDDFT (blue) are rather similar and in particular show the same trends. The same is true for the energies of S_1. Only in the region near the CI, a slightly more pronounced deviations is found.

For the trajectory of category II, see right part of figure 7.3, similar results are obtained as for the trajectory of category I. However, the differences near the CI are more evident. This is consistent with the high values in the corresponding D1 diagnostics[84] for RI-CC2 calculations based on geometries taken from the trajectory of category II shown in figure 7.4. Due to the high values of the D1 diagnostics near the CI for a time around 200 fs, the excitation energies calculated with RI-CC2 have to be treated with care. However, apart from the region near the CI and in particular for the optimized geometries of OF and CF the D1 diagnostics are below 0.15. Therefore, the corresponding RI-CC2 results can be considered to be reliable.[84]

Finally, it might be interesting to investigate, if the fact that trajectories have passed through the CI can be related to some geometrical properties at the beginning of the dynamics. For this purpose, we investigated for example the dependence from the distance between the reactive carbon atoms and from the difference of two dihedral angles, where each dihedral angle has been defined analogously as in a previous investigation concerning a molecule that consists of the same reactive system.[85] Therefore, the two dihedral angles are made of the 6 carbon atoms of the cyclohexadiene unit. The reactive carbon atoms are numbered with 1 and 6. The first dihedral angle is the one defined by the carbon atoms 1 to 4 and the other one is formed by the carbon atoms 3 to 6. Analyzing the data with some geometrical values of the initial configurations as indicators, it is not possible to predict whether a trajectory will reach the CI due to the lack of correlation, i.e. clustering of the trajectories marked in green in one area, see figure 7.5.

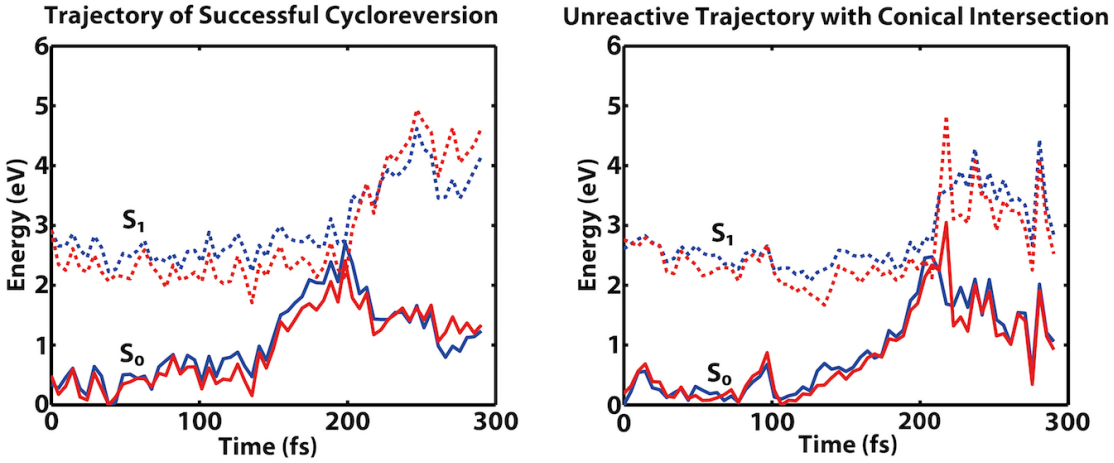

Figure 7.3: Comparison of the potential energies of S_0 and S_1 along two trajectories calculated using TDDFT (blue) and RI-CC2 (red) for the exemplary trajectory of categories I (left) and category II (right). The energies are similar and the largest deviations are found near the CI.

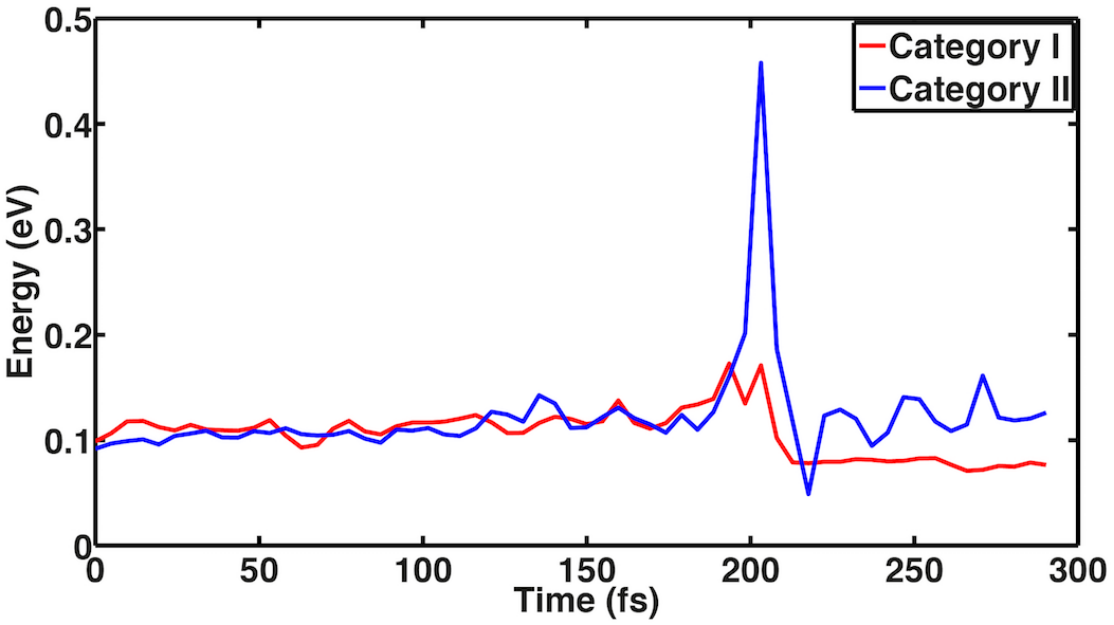

Figure 7.4: D1 diagnostics for the CC2 calculations belonging to the two trajectories shown in figure 7.3. Values larger than 0.15 indicate that the results might be unreliable and for both trajectories this is only the case near the CI.

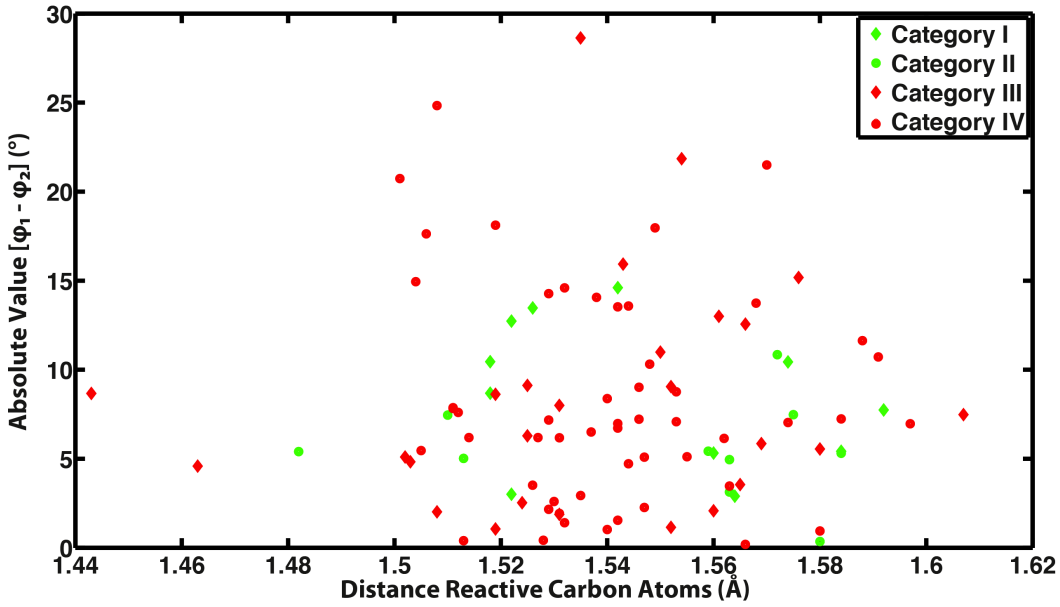

Figure 7.5: Distribution of initial configurations depending on the distance between the reactive carbon atoms and on the difference of two dihedral angles. Shown in green are trajectories that relax to S_0 via the CI (Categories I and II) and in red trajectories for which this is not the case (Categories III and IV). No grouping of the green trajectories can be found and therefore no correlation between a geometric parameter and the possibility to reach the CI can be established.

7.4 Advanced Methods for the Spectrum Simulation of CMTE

So far, the best theoretical method to calculate the absorption spectrum of OF and CF is RI-CC2. Furthermore, in reference [4] only calculations employing VEA have been discussed. The main differences of TDDFT calculations compared to the measured spectra are found in the structure of the absorption of the OF and in the position of the second absorption maximum for the CF. For the latter, even RI-CC2 as method of reference does not yield good results. In the following, the spectra resulting from VEA, NEA, and FCA will be discussed based on CAM-B3LYP/def2-SVP. The functional was chosen due to its accuracy regarding calculation of vibronic spectra, as demonstrated in chapter 6. For NEA 1000 geometries per isomer and conformer were sampled.

The broad absorption found for the OF is not reproduced within VEA, see figure 7.6. Instead, two distinct absorption maxima with nearly similar intensities are found. There is no bright transition in between and the first absorption maximum is too high. The spectrum obtained from NEA alleviates these shortcomings: the absorption is now broader and is similar to the results of RI-CC2 for VEA. To calculate the absorption spectrum employing FCA, the first five excited states of both conformers are investigated. Due to the large displacements of the optimized geometries of the excited states compared to the S_0 geometry and the occurrence of imaginary frequencies after optimization of

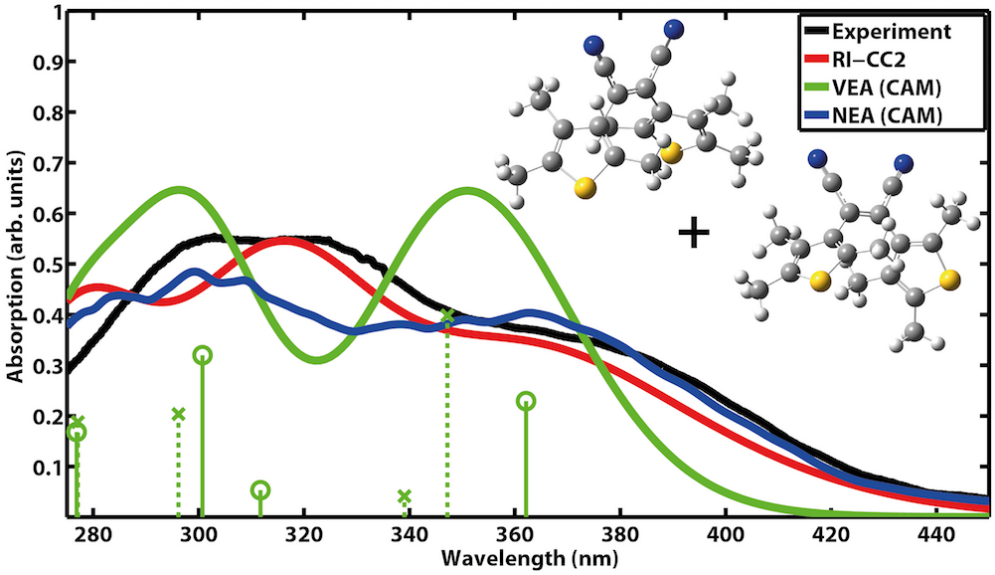

Figure 7.6: Absorption spectra of the OF of CMTE. The experimental spectrum was measured in acetonitrile. Computed spectra are shown for different theoretical methods, see legend. All calculations include both stable conformers in equal proportion. For the TDDFT calculation employing VEA, transitions belonging to the antiparallel and parallel conformers are included as solid sticks with circles and dashed sticks with crosses, respectively. Each spectrum is normalized to the corresponding maximum of the spectrum for the CF in figure 7.7.

the corresponding excited state, the calculation of absorption spectra using FCA was not successful.

The two absorption peaks of the CF calculated with TDDFT in VEA are blue-shifted compared to the experiment, see figure 7.7. The structure of the absorption is in principle better described as with RI-CC2, due to the fact that for the latter the absorption of S_2 is much too weak. Employing NEA the spectrum is red-shifted and the structure remains about the same. Therefore, the agreement with experiment is improved and the trend found is promising for spectrum simulation using FCA. For this purpose, optimizations of the first five excited states with subsequent frequency calculations were performed. The optimizations of the fourth and fifth excited state did not yield minima but geometries with multiple imaginary frequencies. The optimized and stable structures belonging to the first, second, and third excited state are shown in figure 7.8. The structures are rather similar compared to the optimized geometry of S_0, nonetheless the overlap integrals between the ground vibrational states of S_0 and excited states S_1 and S_3 are too small. Due to this, only the vibronic spectrum of S_2 could be calculated. The result is also shown in figure 7.7: the energy of the absorption maximum is in agreement with experiment and a shoulder is reproduced.

Overall, the difficulties encountered for the vibronic spectrum calculation of the CF are

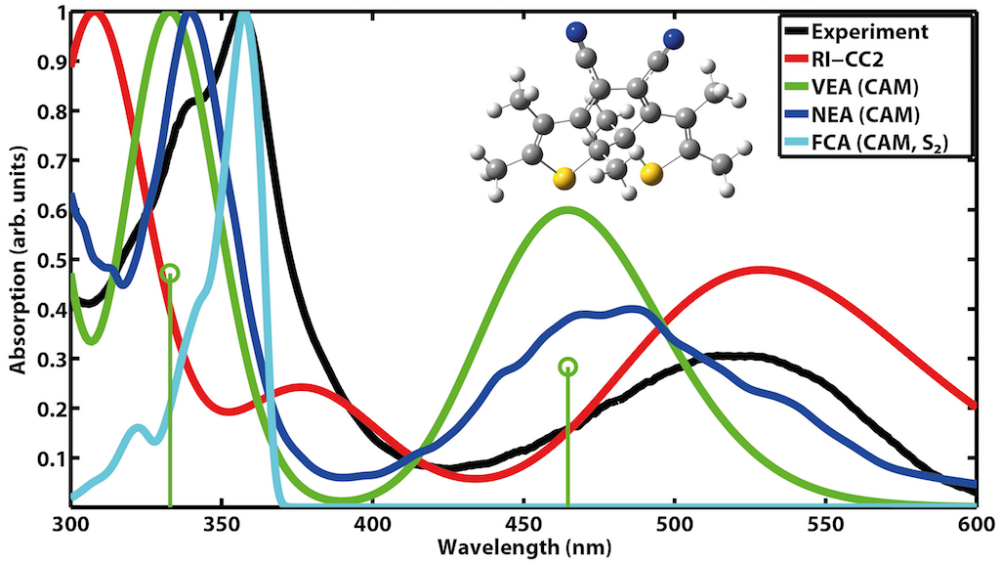

Figure 7.7: Absorption spectra of the CF. Shown are the absorption measured in acetonitrile and theoretical spectra obtained with different methods, see legend. Each spectrum is normalized to its maximum value and the molecular structure is shown as inset. NEA leads to shifts in the absorption spectrum that shows the right tendency when comparing with the corresponding VEA result. The calculation of the vibronic spectrum for the CF only succeded for S_2 explaining the second peak found in experiment, but the method failed for the calculation with further excited states.

not surprising. In reference [86] similar findings have been reported. Even severe is the case regarding calculation of vibronic spectra of the OF due to the much larger involved displacements. Further developments are, therefore, needed to correctly describe the absorption of both isomers.

7.5 Mimicking Experimental Conditions of Excitations

A spectrum simulation based on NEA can be taken as a starting point for NA-AIMD simulations via generation of appropriate initial conditions. To achieve this, energy windows are defined for excitations of CF and OF mimicking the experimental conditions, see figure 7.9, and transitions are weighted with their corresponding oscillator strength. The chosen parameters lead to 79 accepted initial conditions of the CF all starting in S_1. For the antiparallel conformer of OF, 80 initial conditions are accepted: 57 in S_1, 22 in S_2, and 1 in S_3. Finally, 67 initial conditions are accepted for the parallel conformer: 27 in S_1 and 40 in S_2. Overall, already these results give insights regarding the excited states that play a role in the photochemical reaction of both isomers. For example, the cyclization reaction might proceed via S_1, which is a rather dark state but which is excited for both conformers of OF.

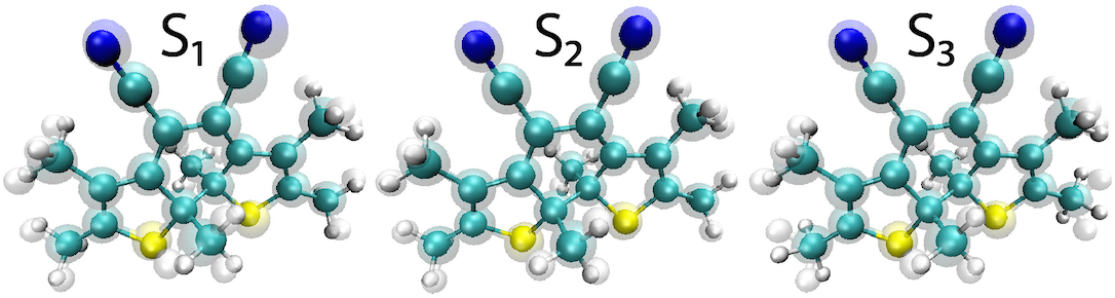

Figure 7.8: Superposition of optimized geometries of excited states (solid balls & sticks) and of S_0 (transparent balls & sticks) geometries visualized using VMD.[87] Shown are the optimized geometries of S_1 (left), S_2 (middle), and S_3 (right) compared to the corresponding geometry of S_0. Differences in geometries are mainly found near the methyl groups. Due to these differences, only the FCA-calculation for the transition to S_2 succeeded.

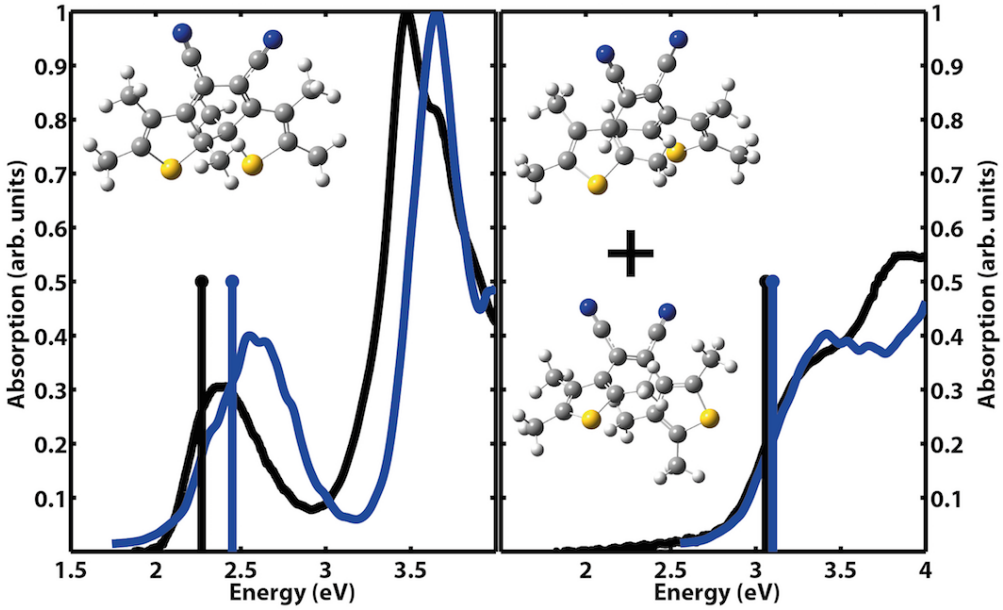

Figure 7.9: Absorption spectra of CF (left) and OF (right) measured in acetonitrile (black) and calculated employing NEA (blue). The black sticks indicate the experimental excitation energies for the switching between both states. The blue sticks designate the middle of the energy window used for the acceptance of initial conditions. The width of it was chosen to be 0.02 eV and 0.05 eV for the CF and OF, respectively. It is chosen this way, because sufficient but not too many initial conditions were accepted.

8 Switching of Conjugated Systems: Cycloreversion Reaction of Diarylethenes

> C'est par la logique qu'on démontre, c'est par l'intuition qu'on invente. Savoir critiquer est bon, savoir créer est mieux.
>
> *(Henri Poincaré[88])*

Photochromic DAEs consist of two aryl groups that are connected via an ethene bridge. There are two stable isomers for this kind of molecules: CF and OF. In the former isomer, the conjugated system extends over the whole molecule and in the latter one the conjugated systems of the aryl units are isolated from each other, see the scheme at the beginning of reference [5] that is included in this chapter. As discussed in chapter 7, it is planned to use DAEs to all-optically shift the resonance frequency of inorganic microdisk resonators.[4,76] In order to understand the switching between OF and CF of photochromic DAEs, the reaction involved in the isomerization has to be investigated in more detail. First of all, the class of reaction is identified, giving insights into the reaction mechanism based on chemical knowledge. In addition, the dynamics of the reaction can be understood by using nonadiabatic dynamics simulations. This approach allows to understand the fundamental differences in the cycloreversion reaction of two prototypical DAEs, which is discussed in the included paper.[5] Furthermore, TSH can be used to understand the cycloreversion reaction of experimentally relevant DAEs and to study the effect of substituents. These two topics, therefore, conclude the chapter.

8.1 Electrocyclic Reactions and Woodward-Hoffmann Rules

In organic chemistry there are three main types of reactions: ionic reactions, radical reactions and pericyclic reactions.[89–91]

In ionic reactions electrons move from an electron-rich atom towards an electron-deficient one. Intermediates of these reactions are cations and anions, that might react in further steps. Most organic reactions are of this type. As an example the dissociation of a carbon-chlorine bond is shown in figure 8.1. In this case, the chlorine atom, which has a much higher electronegativity, takes away one of the electrons of the carbon atom, which participated in the chemical bond. This process of bond cleavage is called heterolytic.[90] Ionic reactions involve pairs of electrons moving in one direction.[89]

The opposite of heterolytic bond cleavage is the homolytic one. This is the case for the second kind of reactions: radical reactions. First of all, it has to be explained that

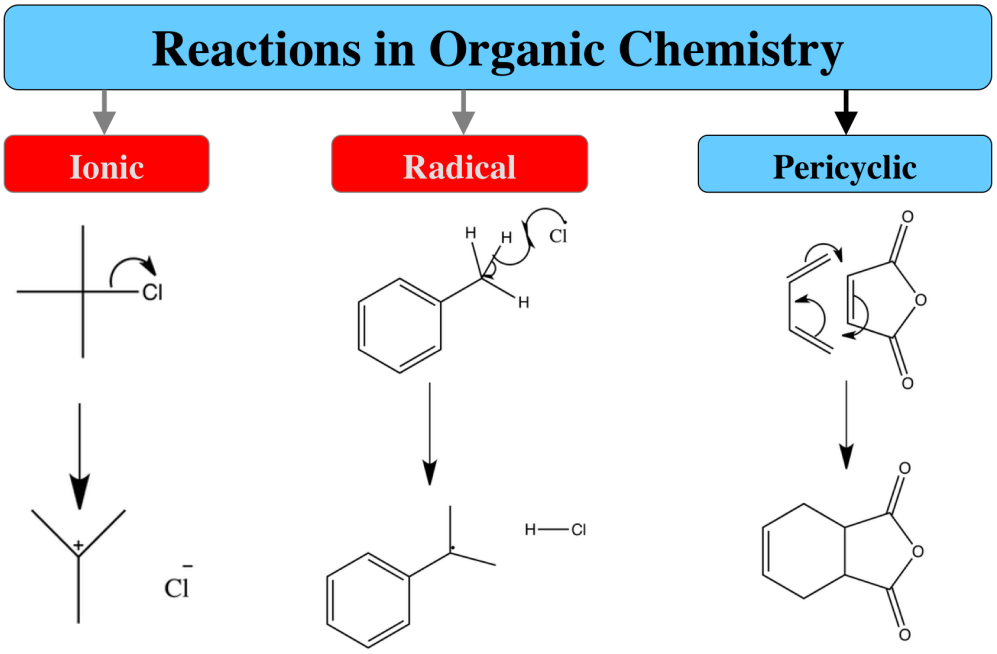

Figure 8.1: Illustration of the three main types of reactions in organic chemistry: ionic, radical, and pericyclic. The photochemical reaction of DAEs belongs to the category of percicyclic reactions.

a radical is a molecule with at least one unpaired electron, giving rise to high reactivity. In figure 8.1 the radical chlorine atom is marked by a dot, indicating the unpaired electron. This unpaired electron reacts with an electron of a hydrogen atom, leading to the formation of HCl. However, the electron of the H-atom was originally involved in a chemical bond with a carbon atom, therefore a homolytic bond cleavage has occured, leaving behind a radical carbon atom. This carbon atom is now highly reactive and can react with further molecules.[90] Radical reactions involve the correlated movement of single electrons.[89]

The third type of reactions are pericyclic reactions. In this type, there are no negative and positive charges. Furthermore, there are no intermediates at all and pericyclic reaction are concerted. In figure 8.1 the most famous pericyclic reaction is shown: the Diels-Alder reaction. The photochemical reaction of DAEs belongs to this third class and therefore it will be analyzed in more detail in the following. Pericyclic reactions involve electrons moving round a circle and can be described as the movement of electron pairs or of single electrons.[89]

The category of pericyclic reactions can be further divided into four subcategories: cycloadditions, sigmatropic rearrangements, group transfer reactions, and pericyclic reactions. Each subcategory is characterized by the number of reacting molecules and the number of π or σ bonds that are broken or formed. This allows the distinction of one kind of reaction from the others. However, all of these reactions have in common that the electrons move round a circle. In the following, the four subcategories will be

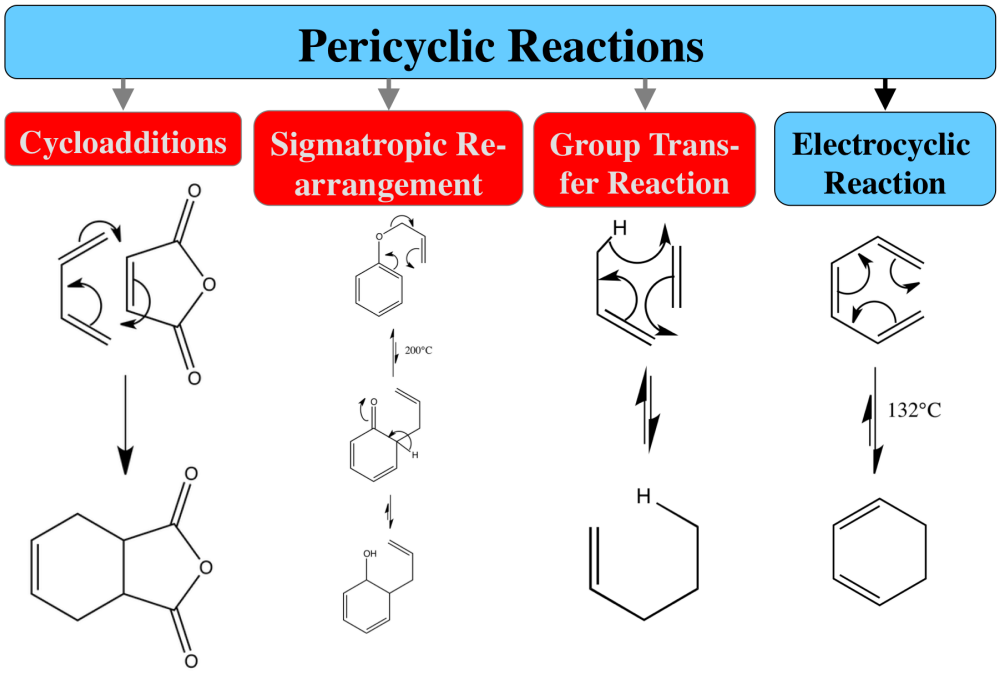

Figure 8.2: Scheme to illustrate the four kinds of pericyclic reactions: Cycloaddition, Sigmatropic Rearrangements, Group Transfer Reactions and Electrocyclic Reactions. The photochemical reaction of DAEs is part of the subcategory of electrocyclic reactions.

discussed based on a discussion given in reference [89].

In general, the most important class of pericyclic reactions are cycloadditions. In these bimolecular reactions a diene reacts with a dienophile and an example can be found in figure 8.2. In the course of such a reaction, two new σ bonds are formed from two former π bonds. Normally, this reaction proceeds in such a way that one ring is formed, because the two formed σ bonds are more stable than the two broken π bonds.

Sigmatropic rearrangements are unimolecular reactions and in total no bonds are broken or formed, but a σ bond is moved. An example for such a reaction is the first step in the Claisen rearrangement as can be seen in figure 8.2. Apart from the movement of the σ bond also the π bonds have to rearrange, in order to accommodate the newly formed bond.

Bimolecular group transfer reactions resemble both previously discussed subcategories of pericyclic reaction, see figure 8.2. They are similar to sigmatropic rearrangements, since a σ bond moves as it is for example the case for the drawn hydrogen bond. However, during the course of the reaction a π bond is replaced by a σ bond. In addition, the lower part of the drawn reaction resembles a cycloaddition, but the second π bond of the diene is now replaced by a σ bond in the upper part of the molecule.

The fourth subcategory are unimolecular electrocyclic reactions. Similar to group transfer reactions a new σ bond is formed and a π bond is broken during an electrocyclic

reaction. Therefore, the form with the closed ring is in general more stable. As an example the isomerization of hexatriene to cyclohexadiene is shown in figure 8.2. This system also constitutes the reactive core of DAEs, so this class of photochromic molecules undergoes electrocyclic reaction during the photoisomerization.

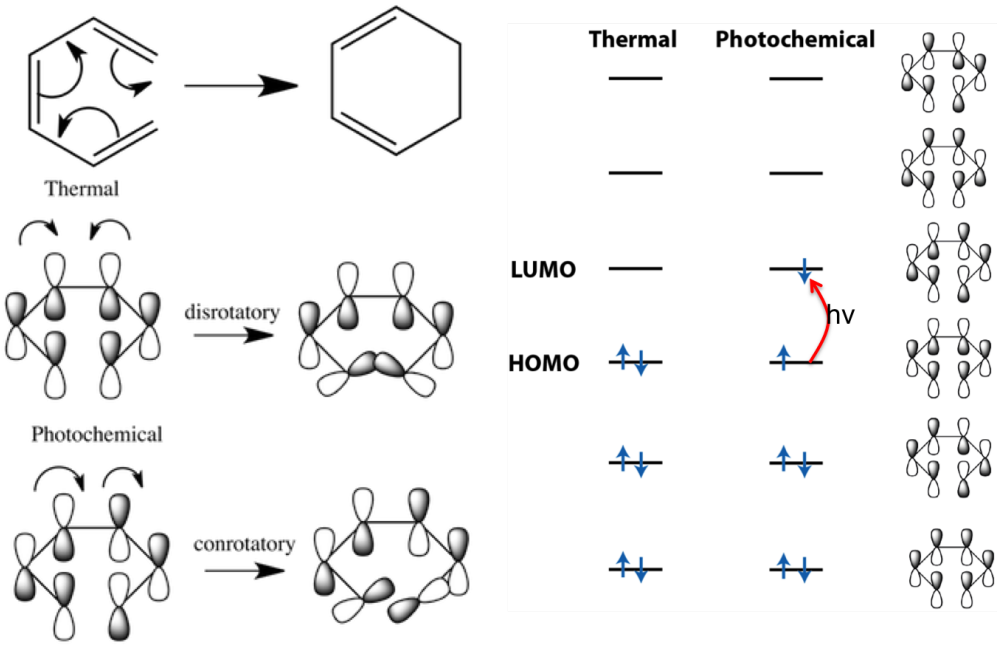

Figure 8.3: Scheme to explain the pericyclic reaction that is involved in the isomerization of hexatriene to cyclohexadiene. The reaction is depicted in the upper left part. The frontier MOs are shown on the right. For the thermal reaction, the HOMO has to be considered (middle left) and for the photochemical reaction (bottom left) the LUMO.

In order to better understand the reaction that is taking part during the isomerization between OF and CF of DAEs, the frontier orbitals of the hexatriene-cyclohexadiene system can be analyzed, see figure 8.3. Starting with a level scheme for the system of six π electrons, the MOs for all six energy levels can be drawn by taking into account that the energy of a MO increases with the number of nodes between neighboring atomic orbitals. So for the MO with the lowest energy, all atomic p orbitals have to be oriented in the same way. For the orbital with the second lowest energy, a node can be found in the middle of the molecule, where the atomic p orbitals change their orientation. The other MOs are constructed analogously. This approach allows to determine the structure of the frontier MOs that are involved in the chemical reactions.

For the thermal reaction, the HOMO has to be considered. To form a new σ bond between the two carbon atoms at the ends of the molecule, the atomic orbitals have to rotate in different directions, see figure 8.3. This leads to a bonding interaction between the p orbitals of those two atoms and in the end the ring is closed. Therefore, the reaction proceeds in a disrotatory fashion.[92]

In order to understand the photochemical reaction, the LUMO has to be considered, because an electron has been excited into this orbital after the absorption of a photon with energy $h\nu$. Now, the atomic orbitals have to rotate in the same direction for bonding interaction between the two atomic orbitals, see figure 8.3. So, the reaction is happening in a conrotatory fashion.[92]

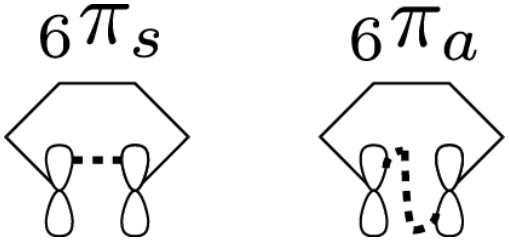

Figure 8.4: Scheme to visualize the supra- (left) and antarafacial (right) reaction mechanisms as needed for the analysis of the reaction employing the photochemical Woodward-Hoffmann rule.

Another approach to describe the reaction is based on the Woodward-Hoffmann rule for photochemical reactions.[93] This rule can be stated in the following way: "A pericyclic change in the first electronically excited state is symmetry-allowed when the total number of $(4q+2)_s$ and $(4r)_a$ components is even."[89] In the expressions given q and r have to be integers. The index s means that only components reacting suprafacial have to be considered, whereas the index a indicates that components reacting antarafacial have to be taken into account. In the case at hand, only one component is involved and it consists of six electrons.

For a suprafacial reaction, as depicted on the left of figure 8.4, the total number of the relevant components equals one, i.e. one component with 6 electrons reacting suprafacial. Therefore the reaction is photochemically not allowed. On the right of figure 8.4 the antarafacial reaction is illustrated. In this case, a component having six electrons reacts antarafacial, so it does not enter in the counting of the relevant components. Therefore, the total number of the relevant components equals zero and the antarafacial reaction is allowed, leading to a conrotatory reaction.

Investigation of the frontier orbitals of the molecule at hand and analysis of the reaction using the photochemical Woodward-Hoffmann rule, yield the same results. However, the former approach is more intuitive, whereas the latter is more general and can be more easily applied to complex reactions.

To sum things up, electrocyclic reactions are always allowed and the way they are happening can be understood with the considerations done above. Therefore, the photochemical reaction occuring during the isomerization of DAEs is an electrocyclic one. It happens in conrotatory fashion, which can be derived by analyzing the structure of the LUMO or by applying the Woodward-Hoffmann rule for photochemical reactions to the isomerization at hand. However, considerations like these can only state if a reaction is symmetry allowed and they can not be used to derive how efficient a reaction is, i.e. how large the QY is and how fast the reaction takes place. To address these issues, advanced computational methods that allow the determination of reaction dynamics

have to be used. Such Methods are: Multiconfiguration Time-Dependent Hartree,[94] Ab Initio Multiple Spawning,,[95] Ehrenfest dynamics,[96] and TSH.[83] The latter is used in the NA-AIMD simulations employing Tully's fewest switches algorithm (TFSA) and linear-response time-dependent DFT (LR-TDDFT). The theoretical background of this method will be given in chapter 9.

8.2 "Quantum Yields and Reaction Times of Photochromic Diarylethenes: Nonadiabatic Ab Initio Molecular Dynamics for Normal- and Inverse-Type"

This article has been published in "The Journal of Physical Chemistry A" and investigates the differences in the cycloreversion reaction for normal- and inverse-type DAEs. For this purpose, not only static calculations have been employed as done before,[77,78,97] but also NA-AIMD have been used, allowing the estimation of QYs and reaction times. The whole paper is solely based on results and discussions of our own calculations. In the paper reproduced in this chapter, two prototypical molecules have been investigated. Only the dynamics reveal the fundamental differences in the cycloreversion reaction of N- and I-type DAEs. Note that animations of the NA-AIMD of four typical trajectories have been published as Electronic Supporting Information. Investigations of the cycloreversion reaction for experimentally relevant DAEs will be given in the final sections 8.3 and 8.4 of this chapter.

THE JOURNAL OF PHYSICAL CHEMISTRY A

Article

pubs.acs.org/JPCA

Quantum Yields and Reaction Times of Photochromic Diarylethenes: Nonadiabatic Ab Initio Molecular Dynamics for Normal- and Inverse-Type

Christian Wiebeler[†] and Stefan Schumacher*[,†]

[†]Physics Department and Center for Optoelectronics and Photonics Paderborn (CeOPP), Universität Paderborn, Warburger Strasse 100, 33098 Paderborn, Germany

Supporting Information

ABSTRACT: Photochromism is a light-induced molecular process that is likely to find its way into future optoelectronic devices. In further optimization of photochromic materials, light-induced conversion efficiencies as well as reaction times can usually only be determined once a new molecule was synthesized. Here we use nonadiabatic ab initio molecular dynamics to study the electrocyclic reaction of diarylethenes, comparing normal- and inverse-type systems. Our study highlights that reaction quantum yields can be successfully predicted in accord with experimental findings. In particular, we find that inverse-type diarylethenes show a significantly higher reaction quantum yield and cycloreversion on times typically as short as 100 fs.

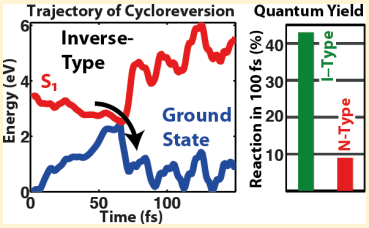

I. INTRODUCTION

In photochromic molecular materials, illumination with light leads to a reversible transformation of a single chemical species between two forms with different optical properties. The transformation is induced all-optically, in one or two directions.[1] This type of light-induced functionality is typically not found in materials used in photonic systems. Integration of photochromic molecules therefore poses a promising route to the design of novel optoelectronic and photonic devices.[2,3] Photochromic spiropyrans were for example used to functionalize single-walled carbon nanotubes,[4] and azobenzene-based polyelectrolytes were incorporated into tunable semiconductor microresonator structures.[5] Among the different photochromic materials that can reversibly and optically be switched between both of their forms, diarylethenes excel with high fatigue resistance, thermal stability, and high quantum yields.[6,7] Showing their photochromic functionality even in solid films, diarylethenes are promising to be used in solid-state photonic hybrid structures.[8,9] Potential applications include optical memories[10] and multifunctional all-optical switches.[7,11,12]

For diarylethenes it was noted that they can be further divided into two subcategories: (i) normal-type diarylethenes in which the ethylene bridge is connected on both sides to a carbon atom of the thiophene ring that is in the 3-position; (ii) inverse-type diarylethenes in which the ethylene bridge is connected to a carbon atom in the 2-position. The two structures are depicted in Scheme 1. Normal-type (N-type) and inverse-type (I-type) diarylethenes have many of their favorable properties in common, e.g., the same reactive center. However, there are also three main differences. The closed form of N-type diarylethene absorbs light at lower energies than the I-type, which is attributed to the larger conjugation of π-electrons in the former case.[7] For the open forms the situation is reversed.[13] And third and most importantly for prospective applications, the quantum yield of the cycloreversion of I-type was recently found to be significantly higher than for the N-type.[14,15]

Scheme 1. Illustration of the Two Diarylethenes under Study, Normal-Type (Top) and Inverse-Type (Bottom)[a]

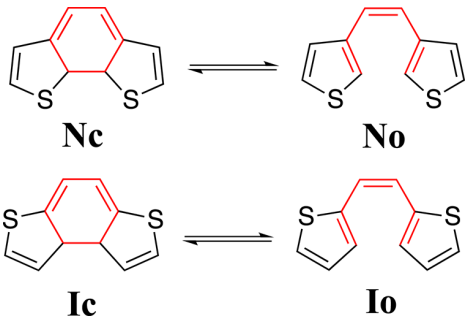

[a]Shown are closed (left) and open (right) ring forms as denoted by the labels. The reactive centers are highlighted, and the photoinduced conversion between open- and closed-ring forms is indicated.

Following photoexcitation of a diarylethene molecule from its thermally stable closed-ring form, the system can undergo an electrocyclic reaction, leading to opening of the central reactive ring (cf. Scheme 1). The electrocyclic photoisomerization of diarylethenes is analogous to the photoisomerization from 1,3-cyclohexadiene (CHD) to 1,3,5-hexatriene (HT). This is shown in Scheme 1. Only the center of the molecule, the CHD/HT-system that is colored in red, is actively involved in the reaction. We note that this center is a well-known textbook

Received: June 25, 2014
Revised: August 19, 2014
Published: August 20, 2014

dx.doi.org/10.1021/jp506316w | J. Phys. Chem. A 2014, 118, 7816−7823

example for electrocyclic reactions.[16,17] Therefore, the reaction leading to the isomerization is a photochemical 6 electron reaction happening in a conrotatory fashion, as dictated by the Woodward−Hoffmann rules.[18] Upon absorption of visible light, the molecule is in the first excited singlet state. Relaxation leads to a conical intersection between this state and the ground state, leading to an ultrafast reaction and radiationless decay to one of the two stable ground-state structures. For this photochemical isomerization the conical intersection plays a fundamental role.[19]

So far, theoretical studies of the reaction mechanisms of diarylethenes were based on calculated potential energy surfaces with emphasis on N-type forms.[15,20,21] Dynamical studies were limited to the molecular mechanics valence bond method.[22] Generally, only very little work is available on I-type diarylethenes with a notably increasing interest in the past year, both experimentally[23−25] and theoretically.[13,14] Ab initio nonadiabatic dynamics on related systems, e.g., azobenzene[26−28] and stilbene,[29] were calculated. Studies of ab initio nonadiabatic dynamics for diarylethenes were only reported for one specific diarylethene compound.[30] The focus of the present study is on the comparison of qualitative differences in the dynamics of prototypical inverse- and normal-type diarylethenes.

To optimize photochromic materials further, it is crucial to understand the achievable reaction quantum yields and reaction time scales. However, these quantities typically only become accessible after a given substance has been synthesized. From a theoretical point of view, predicting reaction quantum yields involving excited electronic states usually poses a formidable task. Experimentally, reaction time scales are only accessible with advanced spectroscopic techniques. However, these will play an increasingly important role in miniaturized applications in which photochromic functionality is implemented with a few molecules only.[31,32] In this case, the actual molecular reaction times are not overshadowed by the slow overall response of a large molecular ensemble.

In this article, we theoretically investigate the reaction mechanisms in I- and N-type diarylethenes. Our ab initio calculations of the cycloreversion reaction dynamics are based on nonadiabatic trajectory surface hopping (TSH). We demonstrate that this approach gives us direct access to both reaction quantum yields and reaction time scales.

II. METHODS

A. Ground-State Optimization and Vertical Excitation Energies. Optimization of the ground-state structures of the two isomers was carried out using density-functional theory (DFT)[33] with the def2-SVP basis set[34] and the PBE0[35,36] functional. Vibrational frequency analysis confirmed that the structures found are stable minima. Employing the same basis set and the same functional, the excitation energies were calculated with time-dependent DFT (TDDFT)[37] and within the Tamm−Dancoff approximation.[38] To test for convergence regarding the basis set, the same calculaions were repeated using aug-cc-pVTZ[39,40] as the basis set. Furthermore, the excitation energies were also calculated using wave function-based methods allowing benchmarking of the DFT-based results. For this purpose, the open- and closed-ring structures were optimized with RI-CC2[41−45] using the implementation in Turbomole[46] and employing the aug-cc-pVDZ basis set with the corresponding auxiliary basis set[47] and default frozen orbitals. The same basis sets and frozen orbitals were then used to calculate the vertical excitation energies with RI-CC2 and RI-ADC(2).[48−50] Convergence regarding the basis set was again tested by doing the same calculations with the aug-cc-pVTZ basis set. All these calculations were done with Turbomole 6.5.[46]

B. Nonadiabatic Dynamics of the Cycloreversion Reaction. The nonadiabatic ab initio molecular dynamics was calculated following the protocol described in ref 51. As in the static calculations, def2-SVP and PBE0 were used as basis set and functional, respectively. Sampling of the ground state for the rigid closed ring isomers was done using Born−Oppenheimer molecular dynamics. This allows the generation of a swarm of trajectories for the dynamical calculations with different initial conditions. The ground-state trajectories were calculated for a total of 5000 steps with a time step size of 50 au, such that the simulation time was about ∼4.84 ps. A Nosé−Hoover thermostat with a temperature of 300 K and a response time of 500 au was used to simulate the dynamics in the ground state at room temperature. To calculate the nonadiabatic ab initio molecular dynamics starting in the first excited singlet state based on trajectory surface hopping,[52] 100 structures with corresponding nuclear velocities were randomly chosen. A time step of 40 au and a total of 1000 time steps (∼0.97 ps) were used and the TD-DFT in Tamm−Dancoff approximation was employed. The initial conditions sampled from a canonical ensemble were then evolved in the microcanonical ensemble for the nonadiabatic dynamics. No thermostat was used for the nonadiabatic dynamics and furthermore no decoherence is included in these gas phase calculations. The latter might be of importance for systems with slower reaction times or in the case of coupling with a bath.[53] Further details of the implementation of the nonadiabatic dynamics calculations can be found in refs 51 and 54. It is based on linear response time-dependent density-functional theory.[55] TDA alleviates methodological problems[56] of TD-DFT in the vicinity of the conical intersections between ground and first excited state.[57,58] All the nonadiabatic dynamics calculations were done with the parallelization described in ref 59 using the SMP-version of Turbomole 6.5.

The visualization of molecular structures was realized using GaussView.[60]

C. Potential Energy Surfaces. Potential energy surfaces were calculated using the def2-SVP basis set and the PBE0 functional. The scan coordinate was the distance between the two reactive carbon atoms. The structures of the relaxed ground-state scan were used to calculate the vertical excitation energies with TDA. A second relaxed scan was done optimizing the energy of the first excited state employing TDA. To assess the accuracy of the calculated potential energy surfaces, the same kind of calculations was done using a wave function-based method, i.e., RI-CC2 for ground-state optimization with subsequent calculation of vertical excitation energies and optimization of the first excited state. For all wave function-based calculations aug-cc-pVDZ was used as basis set.

III. RESULTS AND DISCUSSION

A. Ground-State Optimization and Vertical Excitation Energies. As a starting point, the stable open- and closed-ring isomers of both types of molecules are optimized and the vertical excitation energies are calculated. This allows the assessment of the accuracy of the basis set and method used in the dynamics and potential energy surface calculations. Results are summarized in Table 1. The results for all TDDFT

dx.doi.org/10.1021/jp506316w | J. Phys. Chem. A 2014, 118, 7816−7823

Table 1. Computed Excitation Energies for Normal- (N) and Inverse-Type (I) Diarylethenes in Their Respective Closed- and Open-Ring Forms As Indicated by the Corresponding Labels Introduced in Scheme 1[a]

	PBE0/SVP (TDA)	PBE0/ aug-cc-pVTZ (TDA)	PBE0/ SVP	PBE0/ aug-cc-pVTZ	ADC(2)/ aug-cc-pVDZ	ADC(2)/ aug-cc-pVTZ	CC2/ aug-cc-pVDZ	CC2/ aug-cc-pVTZ	experiment (N-type: 1 from 61 I-type: 2 from 23)
					N_C				
S_1	3.07	3.00	2.83	2.79	2.85	2.86	2.89	2.90	2.46
S_2	3.81	3.77	3.77	3.74	3.78	3.82	3.76	3.80	
					N_O				
S_1	4.15	4.04	3.97	3.88	4.27	4.34	4.34	4.36	4.09
S_2	4.83	4.77	4.81	4.75	4.95	5.02	4.94	5.02	
					I_C				
S_1	3.47	3.37	3.32	3.23	3.42	3.40	3.43	3.42	2.87
S_2	4.38	4.13	4.35	4.11	4.30	4.35	4.27	4.31	
					I_O				
S_1	3.86	3.77	3.63	3.57	3.82	3.83	3.83	3.85	3.89
S_2	4.70	4.62	4.68	4.61	4.86	4.93	4.86	4.93	

[a]All energies are given in eV. Note that the structures for the diarylethene molecules used in the experiment are different from the structures of the two model diarylethenes; see Supporting Information for the corresponding structures.

calculations are found to be very similar. The smaller basis set, i.e., def2-SVP, leads to small deviations compared to calculations with larger basis sets. However, the error is, apart from one case, not larger than 0.11 eV. Furthermore, the excitation energies obtained with TDA are in general in better agreement with the RI-CC2 calculations than the TDDFT excitation energies. However, the differences between TDDFT and TDA are rather small compared to the accuracy of the DFT-based methods of about 0.2 eV. We note that the latter might be reversed depending on the chosen functional, e.g., using CAM-B3LYP instead of PBE0. We further note that the excitation energies with RI-ADC(2) are in good agreement with RI-CC2, making the more economic RI-ADC(2) method a good candidate for future calculations of low lying excitation energies of larger diarylethenes. In addition, we find it to be sufficient to use the aug-cc-pVDZ basis set for the wave function-based methods. Qualitative trends are correctly reproduced by all the methods used; i.e., the closed-ring form absorbs at lower energy than the open-ring form, the closed-ring form of I-type absorbs at higher energy than the corresponding form of N-type and the open-ring form of I-type absorbs at lower energy than the open-ring form of N-type.

B. Nonadiabatic Dynamics of the Cycloreversion Reaction. In the following, we will investigate the details of the cycloreversion reaction based on ab initio calculations of the nonadiabatic system dynamics (technical details are given in the Methods). In a first step, we sample the molecules' ground states in the closed-ring form and generate 100 initial conditions in the first excited S_1 state of each molecule. Then we compute the systems' time evolution for a swarm of 100 trajectories. In a second step, we extract the quantum yield of the cycloreversion reaction from a statistical evaluation of the computed trajectories.

The main result is shown in Figure 1 for both normal- and inverse-type diarylethenes. It is clearly visible that the quantum yield for I-type diarylethenes with 77% is significantly higher than for N-type diarylethenes with only 55%. To obtain deeper insight into the dynamics of the reaction, one can divide the trajectories in two classes. The first class consists of trajectories that reacted within the first 100 fs, and the second class consists of the remaining trajectories showing slower reactions. For the I-type diarylethene 50% of trajectories belong to the first class,

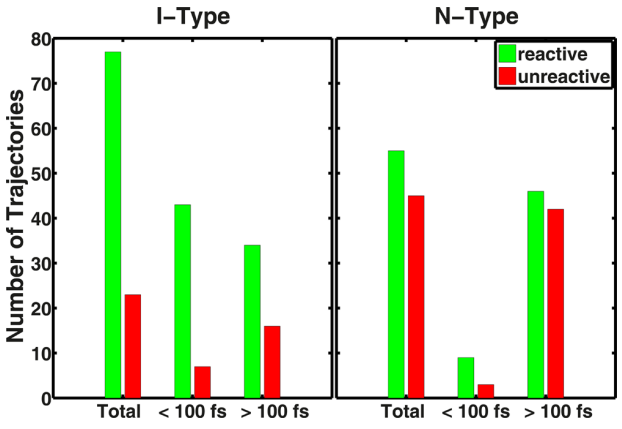

Figure 1. Quantum yield of photoinduced cycloreversion of normal- (N) and inverse-type (I) diarylethenes. The statistics is based on a total of 100 computed trajectories for each type. Given is the total number of trajectories that successfully lead to cycloreversion after relaxation into the S_0 ground state. Out of these trajectories, for I-type a large number already shows a reaction on a very short time scale of only 100 fs. For N-type, the reaction is considerably slower, along with a significantly reduced cycloreversion quantum yield.

whereas only 12% of trajectories reacted within 100 fs for the N-type diarylethene.

In addition to the quantum yields, also the excited-state lifetimes can be obtained using single exponential fits. Using the calculated data, it is possible to determine not only the lifetime for all trajectories but also the lifetimes for reactive and unreactive trajectories as well. The corresponding lifetimes for the CHD/HT-system were reported previously[51] and following the approach described there, we obtain the lifetimes for N- and I-type diarylethenes as listed in Table 2. According to these data the quantum yield for the CHD/HT-system is larger than for the N-type model diarylethene and smaller than for the I-type model diarylethene. The lifetimes for both model diarylethenes are larger, which may be attributed to the thiophene rings that are attached to the CHD backbone. Therefore, it is to be expected that the excited-state lifetime of the larger diarylethene used in experiment[62] is even higher than for the model systems studied here.

dx.doi.org/10.1021/jp506316w | J. Phys. Chem. A 2014, 118, 7816−7823

Table 2. Quantum Yields (%) and Excited-State Lifetimes (ps) for the CHD/HT System, for a Diarylethene Studied in the Experiment and for N- and I-Type Diarylethenes[a]

	QY	τ_{total}	$\tau_{reactive}$	$\tau_{unreactive}$
CHD/HT (Theory[51])	62	0.058	0.043	0.082
N-Type	55	0.28	0.21	0.36
I-Type	77	0.18	0.15	0.30
DAE (Exp.[62])	7.5	1.3		

[a]The lifetimes are obtained by single exponential fits up to the time when 90% of the trajectories have decayed to the ground state. In addition to the lifetime averaged over all trajectories, values are also reported separately for reactive and unreactive trajectories.

A more detailed picture of the reaction can be obtained by looking at the computed trajectories individually. In Figures 2 and 3 we show representative examples of successful cycloreversion reactions for I- and N-type diarylethenes, respectively. Shown are the initial and final molecular geometries together with the time evolution of the energies of the lowest molecular states. Initially, the molecules are in the first excited electronic state and in the ground state after successful cycloreversion, as indicated in the figures. For inverse-type diarylethenes we find that 50% of trajectories reach the ground state within 100 fs. A reaction dynamics this fast we can attribute to the specific topology of the potential energy landscape in the first excited state, which drives the molecule efficiently to the conical intersection (further discussion of the potential energy surfaces is given below). This is also evidenced in Figure 2 in the rapid lowering in energy of the first excited state during the time evolution at early times. For this kind of trajectory we find that the quantum yield for the desired cycloreversion is as high as 86%. In contrast, for trajectories reaching the ground state at times larger than 100 fs, the quantum yield is found to be only 68%. In these cases that show a slower reaction dynamics, the molecule is not driven as efficiently toward the conical intersection between first excited state and ground state as for the fast reaction. All trajectories were found to be in the ground state after 500 fs. Only 23% did not show the desired cycloreversion reaction such that the final geometry was the closed-ring form again. For N-type diarylethenes we only find 12 trajectories that show a reaction within the first 100 fs. The cycloreversion quantum yield for this kind of trajectory is rather high with about 75%. The remaining 88 trajectories reached the ground state at times later than 100 fs, with a reduced quantum yield of about 52%. Four trajectories did not reach the ground state within the total time of the simulation. Inspecting the trajectory in Figure 3, we do not find a pronounced reduction of the energy of the first excited state during the time evolution. In contrast, after a first relaxation in the first excited state, for the N-type diarylethene an energetic barrier has to be overcome to reach the conical intersection leading to the ground state. Therefore, the normal-type molecule is not driven efficiently toward the conical intersection, explaining the lower quantum yield and higher reaction time compared to I-type molecules. This different behavior might be attributed to the different topography of the conical intersections involved[63,64] that have an impact on the effectiveness of photochemical reactions[65] and excited-state lifetimes.[66]

In Figures 4 and 5, we show additional examples of computed trajectories. Figure 4 shows an example of one of the 50 trajectories for I-type diarylethenes that do not react within the first 100 fs. In this case, the I-type molecule is not driven as efficiently toward the conical intersection as is the case for the trajectory shown in Figure 2. Figure 5 shows one of the 12 trajectories for N-type diarylethene that reacts within the first 100 fs. Even in this case, a small energy barrier has to be overcome to reach the conical intersection, which is the same as for the trajectory shown in Figure 3. Both trajectories pass through the conical intersection and relax back to the initial closed-ring ground-state structure.

Videos showing the computed time-evolution of the molecular geometries for these four different types of trajectories are available online as Supporting Information.

On a more technical note, we find that as long as the molecule is in the first excited state, this state is significantly lower in energy than the second excited state. After the jump into the electronic ground state, however, both of the excited-state energies come very close and sometimes are even almost degenerate. We believe that this does not significantly influence the computed dynamics as it only occurs when the system is in the ground state, which is always very well separated from the excited states. We would further like to note that the

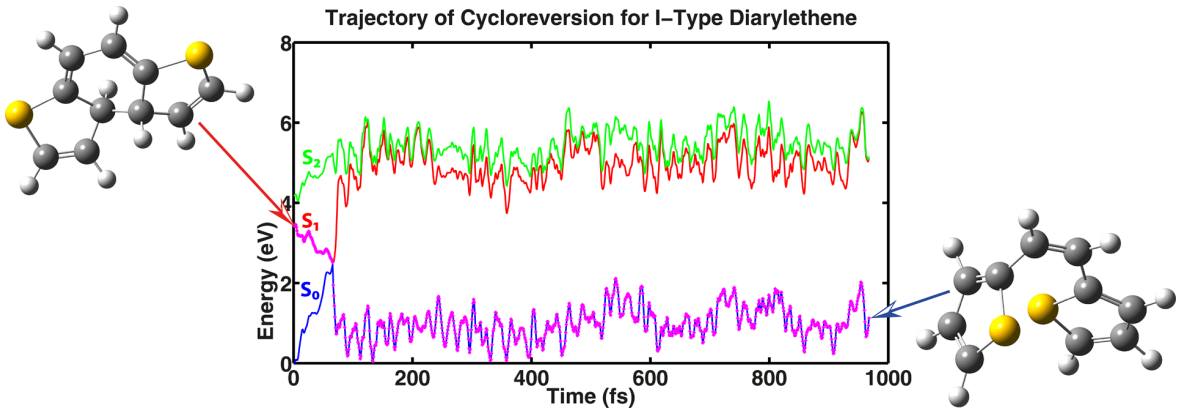

Figure 2. Typical trajectory showing successful cycloreversion for the inverse-type diarylethene (representative of 77% trajectories). Shown is one of the 43 computed trajectories for which the system reacted within a very short time span of only 100 fs. Depicted are the respective energies of S_0, S_1, and S_2 states during the time evolution. After the system passes the conical intersection of S_0 and S_1, the energy separation between S_0 and S_1 significantly increases (compared to the initial separation at $t = 0$), indicative of the cycloreversion reaction. This is confirmed by the initial (closed-ring form) and final (open-ring form) molecular geometries.

dx.doi.org/10.1021/jp506316w | J. Phys. Chem. A 2014, 118, 7816−7823

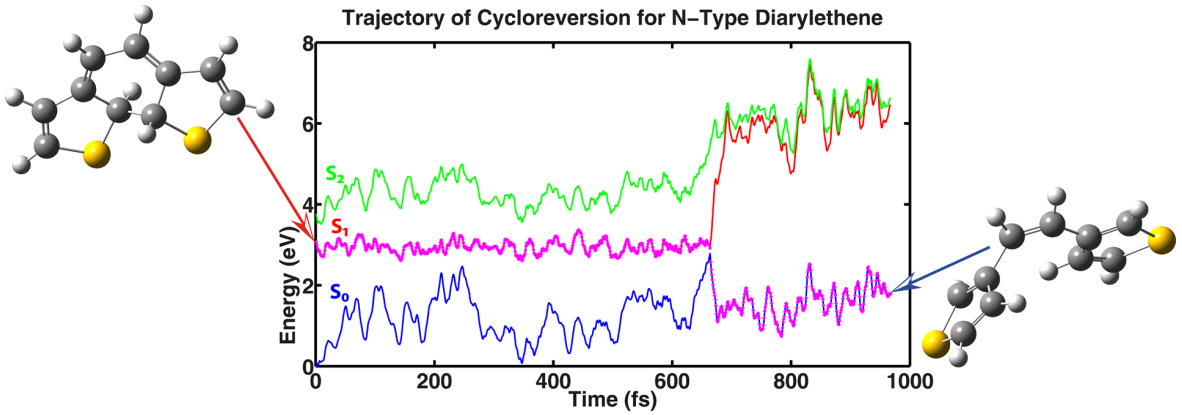

Figure 3. Typical trajectory for successful cycloreversion of the normal-type diarylethene (representative of 55% of trajectories). Here, the typical reaction is significantly slower than for the inverse-type shown in Figure 2.

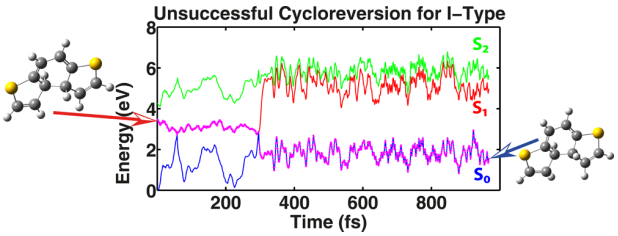

Figure 4. Trajectory for I-type diarylethene that does not reach the ground state within the first 100 fs. The system passes a conical intersection for the first time without relaxing into the ground state. After a while, it reaches the conical intersection for the second time and relaxes back into the closed form, such that no cycloreversion is observed.

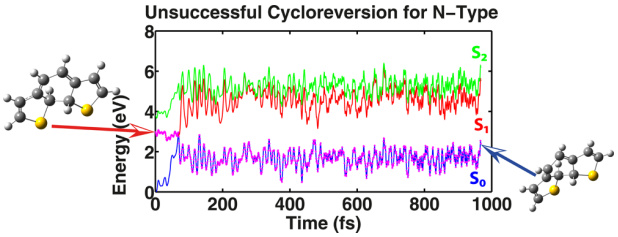

Figure 5. Trajectory for N-type diarylethene that reaches the ground state within 100 fs, not leading to cycloreversion.

semiclassical theoretical approach employed here naturally does not include the true quantized nature of vibrational modes. As a result, the computed reaction time scales are expected to be slightly too fast and the computed excited-state lifetimes underestimated.[51] We note that alternative methods that treat the motion of nuclei more rigorously are Ab Initio Multiple Spawning[67] and Multiconfiguration time-dependent Hartree (MCTDH).[68]

Ultrafast dynamics of the photochemical reactions of diarylethenes were previously investigated in a number of experimental studies (e.g., chapter 12 in ref 6) using, e.g., transient absorption spectroscopy[8,62,69] and femtosecond electron crystallography.[70] Our findings on the reaction dynamics of diarylethenes as discussed above are in accord with previous experimental findings and demonstrate the capabilities of the theoretical approach employed here.

C. Potential Energy Surfaces. To further deepen our understanding of the different dynamics found in N- and I-type diarylethenes, it is instructive to compare the potential energy surfaces for the ground and first excited states. A corresponding relaxed ground-state potential energy surface scan of the energies for varying distance of the two reactive carbon atoms is shown in Figure 6. As expected, we find two almost equally

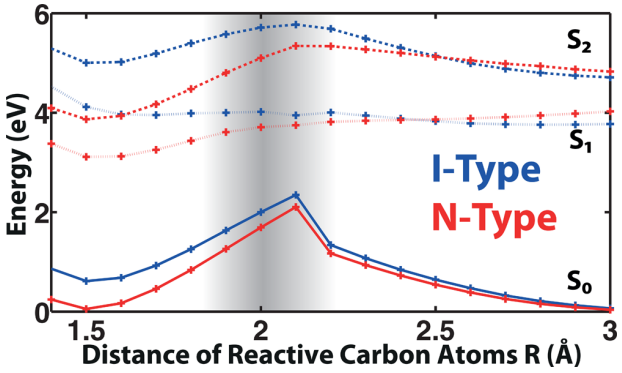

Figure 6. Potential energy surfaces of the normal- (red) and inverse-type (blue) diarylethenes obtained by optimizing the ground-state geometry for varying distances between the reactive carbon atoms. Shown are ground S_0 (solid) and excited S_1 (dotted) and S_2 (dashed) states. Clearly visible is the different topology of the S_1 PES for normal- and inverse-type at $R < 2.1$ Å. To reach the conical intersection between S_0 and S_1 at $R \approx 2.1$ Å in the cycloreversion reaction, for the normal-type diarylethene a potential barrier has to be overcome in the S_1 state. This barrier is absent for the inverse-type diaryethene, leading to a significantly faster and more effcient cycloreversion.

stable ground-state geometries. Vertically exciting the systems from the closed ring form (from the minimum of the ground-state PES at small R) to the first excited state, we find that for the N-type diarylethene a barrier in energy of about 0.6 eV has to be overcome to reach the conical intersection at $R \approx 2.1$ Å. In contrast, there is only a very small energy barrier in the first excited state for the I-type diarylethene such that the ring-opening reaction is (mostly) "downhill" and thus very efficient.

The same qualitative properties of the potential energy surfaces are also found by using RI-CC2 for geometry optimization and calculation of vertical excitation energies, see Figure S3 in the Supporting Information. The good

dx.doi.org/10.1021/jp506316w | J. Phys. Chem. A 2014, 118, 7816–7823

agreement between RI-CC2 and DFT calculation is rather encouraging for using the computationally much cheaper DFT approach.

To obtain a better understanding of the involved PES, we also calculated scans with DFT and RI-CC2 optimizing the first excited state; see Figure 7 and Figure S4 in the Supporting Information. These scans show that even for the optimized S_1 geometries, there is still a barrier for the cycloreversion reaction of N-Type diarylethenes and that the reaction for I-Type molecules proceeds without a barrier. Again, qualitative agreement between DFT and RI-CC2 is found.

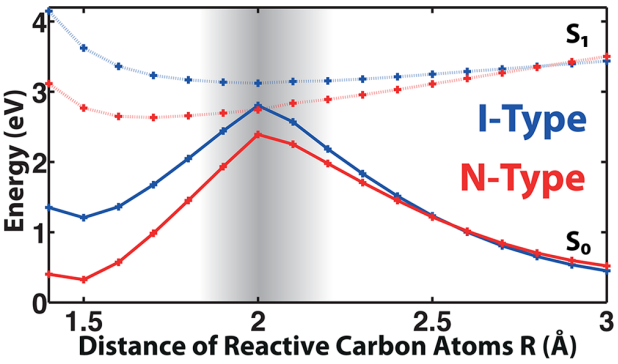

Figure 7. (TD-)DFT calculation of potential energy surfaces obtained by optimizing the first excited state employing TDA. Theses calculations confirm the presence of a potential energy barrier for the normal-type and no barrier for the inverse-type diarylethene when approaching the conical intersection in the S_1 state. The reference energy is the same as for the potential energy surface shown in Figure 6.

We note that in the area shaded in gray in Figures 6 and 7 and in Figures S3 and S4 of the Supporting Information in the vicinity of the conical intersection, our results for the PES based on time-dependent DFT and RI-CC2, respectively, have to be treated with care. Furthermore, the geometry of the conical intersection is a distorted structure[14] such that a PES relaxed on the ground state with vertical excitation energies will not yield this geometry.

The absence of an energy barrier for I-type diarylethenes was already reported before, on the basis of a higher-level quantum chemical approach for a slightly different molecule of this class.[15] We would further like to emphasize that although the difference in reaction efficiencies of I- and N-type can be expected from the PES shown, extraction and prediction of actual numbers for the reaction quantum yields and reaction times is only possible from the full nonadiabatic dynamics calculations as reported here. The actual reaction then takes place on a much more complex, multidimensional PES including all the nuclear degrees of freedom in the system.

IV. CONCLUSION

In this article we report on nonadiabatic ab initio molecular dynamics calculations for the cycloreversion reaction of diarylethenes. We demonstrate that the method employed (trajectory surface hopping based on linear-response time-dependent DFT) is able to reproduce the different dynamics found for N- and I-type diarylethenes. The simulations give detailed insight into the dynamics of the reaction investigated. In particular, reaction quantum yields and reaction times can be extracted that are usually very hard to predict theoretically.

Inspired by these first calculations, there are many future directions that can be addressed. One promising aspect is to study the effect of substitutions at the reactive carbon atoms for N-[71] and I-type[23] diarylethenes for further optimization. Also, detailed studies of the cyclization reaction would be of interest. Apart from its value to the specific field, the present study also constitutes a prime example of the capabilities of high-level available methods in predicting reaction quantum yields and time scales for medium-sized molecular systems.

■ ASSOCIATED CONTENT

Supporting Information

Chemical structures of the diarylethenes studied in experiment used as reference for the excitation energies and for the ultrafast dynamics, a table summarizing the results of Figure 1, videos of the molecular dynamics for the trajectories shown in the text, potential energy surfaces calculated employing RI-CC2 with optimization of the ground and first excited state, respectively, and geometries of the PES obtained by optmizing the first excited state employing TDA. This material is available free of charge via the Internet at http://pubs.acs.org

■ AUTHOR INFORMATION

Corresponding Author

*S. Schumacher. E-mail: stefan.schumacher@uni-paderborn.de.

Notes

The authors declare no competing financial interest.

■ ACKNOWLEDGMENTS

C.W. is grateful for his full PhD-scholarship from the Friedrich-Ebert-Stiftung. We further thank the Turbomole Support team for providing helpful information on the implementation of the TSH-algorithm. We are grateful for fruitful discussions with Prof. Martin J. Paterson, Heriot-Watt University, Edinburgh, UK. Finally, we acknowledge financial support from the DFG (GRK 1464) and a grant for computing time at PC^2 Paderborn Center for Parallel Computing.

■ REFERENCES

(1) Dürr, H., Bouas-Laurent, H., Eds. *Photochromism: Molecules and Systems*; Elsevier: Amsterdam, 2003.

(2) Bianco, A.; Perissinotto, S.; Garbugli, M.; Lanzani, G.; Bertarelli, C. Control of Optical Properties Through Photochromism: a Promising Approach to Photonics. *Laser Photonics Rev.* **2011**, *5*, 711−736.

(3) Nau, D.; Bertram, R. P.; Buse, K.; Zentgraf, T.; Kuhl, J.; Tikhodeev, S. G.; Gippius, N. A.; Giessen, H. Optical Switching in Metallic Photonic Crystal Slabs with Photoaddressable Polymers. *Appl. Phys. B: Laser Opt.* **2006**, *82*, 543−547.

(4) Malic, E.; Weber, C.; Richter, M.; Atalla, V.; Klamroth, T.; Saalfrank, P.; Reich, S.; Knorr, A. Microscopic Model of the Optical Absorption of Carbon Nanotubes Functionalized with Molecular Spiropyran Photoswitches. *Phys. Rev. Lett.* **2011**, *106*, 097401.

(5) Piegdon, K. A.; Lexow, M.; Grundmeier, G.; Kitzerow, H.-S.; Pärschke, K.; Mergel, D.; Reuter, D.; Wieck, A. D.; Meier, C. All-optical Tunability of Microdisk Lasers via Photo-adressable Polyelectrolyte Functionalization. *Opt. Express* **2012**, *20*, 6060−6067.

(6) Irie, M., Yokoyama, Y., Seki, T., Eds. *New Frontiers in Photochromism*; Springer: Tokyo, Japan, 2013.

(7) Irie, M. Diarylethenes for Memories and Switches. *Chem. Rev.* **2000**, *100*, 1685−1716.

(8) Jean-Ruel, H.; Cooney, R. R.; Gao, M.; Lu, C.; Kochman, M. A.; Morrison, C. A.; Miller, R. J. D. Femtosecond Dynamics of the Ring Closing Process of Diarylethene: A Case Study of Electrocyclic

Reactions in Photochromic Single Crystals. *J. Phys. Chem. A* **2011**, *115*, 13158−13168.
(9) Kobatake, S.; Hasegawa, H.; Miyamura, K. High-Convertible Photochromism of a Diarylethene Single Crystal Accompanying the Crystal Shape Deformation. *Cryst. Growth Des.* **2011**, *11*, 1223−1229.
(10) Fukaminato, T.; Kobatake, S.; Kawai, T.; Irie, M. Three-dimensional Erasable Optical Memory using a Photochromic Diarylethene Single Crystal as the Recording Medium. *Proc. Jpn. Acad., Ser. B* **2001**, *77*, 30−35.
(11) Liu, Y.; Lagrost, C.; Costuas, K.; Tchouar, N.; Le Bozec, H.; Rigaut, S. A Multifunctional Organometallic Switch with Carbon-rich Ruthenium and Diarylethene Units. *Chem. Commun.* **2008**, 6117−6119.
(12) Seefeldt, B.; Altenhöner, K.; Tosic, O.; Geisler, T.; Sauer, M.; Mattay, J. Kinetic Studies on Visible-light-switchable Photochromic Fluorophores Based on Diarylethenes. *Photochem. Photobiol. Sci.* **2011**, *10*, 1488−1495.
(13) Aloïse, S.; Sliwa, M.; Buntinx, G.; Delbaere, S.; Perrier, A.; Maurel, F.; Jacquemin, D.; Takeshita, M. Do Inverse Dithienylethenes Behave as Normal Ones? A Joint Spectroscopic and Theoretical Investigation. *Phys. Chem. Chem. Phys.* **2013**, *15*, 6226−6234.
(14) Perrier, A.; Aloïse, S.; Olivucci, M.; Jacquemin, D. Inverse versus Normal Dithienylethenes: Computational Investigation of the Photocyclization Reaction. *J. Phys. Chem. Lett.* **2013**, *4*, 2190−2196.
(15) Nakamura, S.; Uchida, K.; Hatakeyama, M. Potential Energy Surfaces and Quantum Yields for Photochromic Diarylethene Reactions. *Molecules* **2013**, *18*, 5091−5103.
(16) Clayden, J.; Greeves, N.; Warren, S.; Wothers, P. *Organic Chemistry*; Oxford University Press: Oxford, U.K., 2001.
(17) Fleming, I. *Pericyclic Reactions*; Oxford Chemistry Primers; Oxford University Press: Oxford, U.K., 1998.
(18) Woodward, R. B.; Hoffmann, R. The Conservation of Orbital Symmetry. *Angew. Chem., Int. Ed.* **1969**, *8*, 781−853.
(19) Levine, B. G.; Martínez, T. J. Isomerization Through Conical Intersections. *Annu. Rev. Phys. Chem.* **2007**, *58*, 613−634.
(20) Ern, J.; Bens, A. T.; Martin, H.-D.; Mukamel, S.; Tretiak, S.; Tsyganenko, K.; Kuldova, K.; Trommsdorff, H. P.; Kryschi, C. Reaction Dynamics of a Photochromic Fluorescing Dithienylethene. *J. Phys. Chem. A* **2001**, *105*, 1741−1749.
(21) Asano, Y.; Murakami, A.; Kobayashi, T.; Goldberg, A.; Guillaumont, D.; Yabushita, S.; Irie, M.; Nakamura, S. Theoretical Study on the Photochromic Cycloreversion Reactions of Dithienylethenes; on the Role of the Conical Intersections. *J. Am. Chem. Soc.* **2004**, *126*, 12112−12120.
(22) Boggio-Pasqua, M.; Ravaglia, M.; Bearpark, M. J.; Garavelli, M.; Robb, M. A. Can Diarylethene Photochromism Be Explained by a Reaction Path Alone? A CASSCF Study with Model MMVB Dynamics. *J. Phys. Chem. A* **2003**, *107*, 11139−11152.
(23) Tatsumi, Y.; Kita, J.; Uchida, W.; Ogata, K.; Nakamura, S.; Uchida, K. Photochromism of 1,2-Bis(2-thienyl)perfluorocyclopentene Derivatives: Substituent Effect on the Reactive Carbon Atoms. *J. Phys. Chem. A* **2012**, *116*, 10973−10979.
(24) Yuan, K.; Boixel, J.; Le Bozec, H.; Boucekkine, A.; Doucet, H.; Guerchais, V.; Jacquemin, D. Perfluorocyclohexene Bridges in Inverse DiArylEthenes: Synthesis Through Pd-catalysed C-H Bond Activation, Experimental and Theoretical Studies on Their Photoreactivity. *Chem. Commun.* **2013**, *49*, 7896−7898.
(25) Kudernac, T.; Kobayashi, T.; Uyama, A.; Uchida, K.; Nakamura, S.; Feringa, B. L. Tuning the Temperature Dependence for Switching in Dithienylethene Photochromic Switches. *J. Phys. Chem. A* **2013**, *117*, 8222−8229.
(26) Schultz, T.; Quenneville, J.; Levine, B.; Toniolo, A.; Martínez, T. J.; Lochbrunner, S.; Schmitt, M.; Shaffer, J. P.; Zgierski, M. Z.; Stolow, A. Mechanism and Dynamics of Azobenzene Photoisomerization. *J. Am. Chem. Soc.* **2003**, *125*, 8098−8099.
(27) Böckmann, M.; Doltsinis, N. L.; Marx, D. Unraveling a Chemically Enhanced Photoswitch: Bridged Azobenzene. *Angew. Chem., Int. Ed.* **2010**, *49*, 3382−3384.
(28) Böckmann, M.; Doltsinis, N. L.; Marx, D. Nonadiabatic Hybrid Quantum Molecular Mechanic Simulations of Azobenzene Photoswitching in Bulk Liquid Environment. *J. Phys. Chem. A* **2010**, *114*, 745−754.
(29) Toniolo, A.; Levine, B.; Thompson, A.; Quenneville, J.; Ben-Nun, M.; Owens, J.; Olsen, S.; Manohar, L.; Martínez, T. J. Photochemistry from First Principles and Direct Dynamics. *Computational Methods in Photochemistry* **2005**, 167−234.
(30) Wiebeler, C.; Bader, C. A.; Meier, C.; Schumacher, S. Optical spectrum, perceived color, refractive index, and non-adiabatic dynamics of the photochromic diarylethene CMTE. *Phys. Chem. Chem. Phys.* **2014**, *16*, 14531−14538.
(31) Snegir, S. V.; Marchenko, A. A.; Yu, P.; Maurel, F.; Kapitanchuk, O. L.; Mazerat, S.; Lepeltier, M.; Léaustic, A.; Lacaze, E. STM Observation of Open- and Closed-Ring Forms of Functionalized Diarylethene Molecules Self-Assembled on a Au(111) Surface. *J. Phys. Chem. Lett.* **2011**, *2*, 2433−2436.
(32) Tsuboi, Y.; Shimizu, R.; Shoji, T.; Kitamura, N. Near-Infrared Continous-Wave Light Driving a Two-Photon Photochromic Reaction with the Assistance of Localized Surface Plasmon. *J. Am. Chem. Soc.* **2009**, *131*, 12623−12627.
(33) Häser, M.; Ahlrichs, R. Improvements on the Direct SCF Method. *J. Comput. Chem.* **1989**, *10*, 104−111.
(34) Schäfer, A.; Horn, H.; Ahlrichs, R. Fully Optimized Contracted Gaussian Basis Sets for Atoms Li to Kr. *J. Chem. Phys.* **1992**, *97*, 2571−2577.
(35) Perdew, J. P.; Burke, K.; Ernzerhof, M. Generalized Gradient Approximation Made Simple. *Phys. Rev. Lett.* **1996**, *77*, 3865−3868.
(36) Adamo, C.; Barone, V. Toward Reliable Density Functional Methods without Adjustable Parameters: The PBE0Model. *J. Chem. Phys.* **1999**, *110*, 6158−6170.
(37) Furche, F.; Ahlrichs, R. Adiabatic Time-dependent Density Functional Methods for Excited State Properties. *J. Chem. Phys.* **2002**, *117*, 7433−7447.
(38) Hirata, S.; Head-Gordon, M. Time-dependent Density Functional Theory within the Tamm-Dancoff Approximation. *Chem. Phys. Lett.* **1999**, *314*, 291−299.
(39) Dunning, T. H. Gaussian Basis Sets for Use in Correlated Molecular Calculations. I. The Atoms Boron Through Neon and Hydrogen. *J. Chem. Phys.* **1989**, *90*, 1007−1023.
(40) Kendall, R. A.; Dunning, T. H.; Harrison, R. J. Electron Affinities of the First-row Atoms Revisited. Systematic Basis Sets and Wave Functions. *J. Chem. Phys.* **1992**, *96*, 6796−6806.
(41) Christiansen, O.; Koch, H.; Jørgensen, P. The Second-order Approximate Coupled Cluster Singles and Doubles Model CC2. *Chem. Phys. Lett.* **1995**, *243*, 409−418.
(42) Hättig, C.; Weigend, F. CC2 Excitation Energy Calculations on Large Molecules Using the Resolution of the Identity Approximation. *J. Chem. Phys.* **2000**, *113*, 5154−5161.
(43) Hättig, C.; Köhn, A. Transition Moments and Excited-state First-order Properties in the Coupled Cluster model CC2 Using the Resolution-of-the-Identity Approximation. *J. Chem. Phys.* **2002**, *117*, 6939−6951.
(44) Hättig, C. Geometry Optimizations with the Coupled-Cluster Model CC2 Using the Resolution-of-the-Identity Approximation. *J. Chem. Phys.* **2003**, *118*, 7751−7761.
(45) Hättig, C.; Hellweg, A.; Köhn, A. Distributed Memory Parallel Implementation of Energies and Gradients for Second-order Møller-Plesset Perturbation Theory with the Resolution-of-the-Identity Approximation. *Phys. Chem. Chem. Phys.* **2006**, *8*, 1159−1169.
(46) *TURBOMOLE* V6.5 2013, a development of University of Karlsruhe and Forschungszentrum Karlsruhe GmbH, 1989−2007, TURBOMOLE GmbH, since 2007, available from http://www.turbomole.com.
(47) Weigend, F.; Köhn, A.; Hättig, C. Efficient Use of the Correlation Consistent Basis Sets in Resolution of the Identity MP2 Calculations. *J. Chem. Phys.* **2002**, *116*, 3175−3183.

(48) Schirmer, J. Beyond the Random-phase Approximation: A new Approximation Scheme for the Polarization Propagator. *Phys. Rev. A* **1982**, *26*, 2395−2416.
(49) Trofimov, A. B.; Schirmer, J. An Efficient Polarization Propagator Approach to Valence Electron Excitation Spectra. *J. Phys. B: At., Mol. Opt. Phys.* **1995**, *28*, 2299−2324.
(50) Hättig, C. Structure Optimizations for Excited States with Correlated Second-Order Methods: CC2 and ADC(2). *Adv. Quantum Chem.* **2005**, *50*, 37−60.
(51) Tapavicza, E.; Meyer, A. M.; Furche, F. Unravelling the Details of Vitamin D Photosynthesis by Non-adiabatic Molecular Dynamics Simulations. *Phys. Chem. Chem. Phys.* **2011**, *13*, 20986−20998.
(52) Tully, J. C. Molecular Dynamics with Electronic Transitions. *J. Chem. Phys.* **1990**, *93*, 1061−1071.
(53) Jaeger, H. M.; Fischer, S.; Prezhdo, O. V. Decoherence-induced Surface Hopping. *J. Chem. Phys.* **2012**, *137*, 22A545.
(54) Tapavicza, E.; Bellchambers, G. D.; Vincent, J. C.; Furche, F. Ab Initio Non-adiabatic Molecular Dynamics. *Phys. Chem. Chem. Phys.* **2013**, *15*, 18336−18348.
(55) Tapavicza, E.; Tavernelli, I.; Röthlisberger, U. Trajectory Surface Hopping within Linear Response Time-Dependent Density-Functional Theory. *Phys. Rev. Lett.* **2007**, *98*, 023001.
(56) Levine, B. G.; Ko, C.; Quenneville, J.; Martínez, T. J. Conical Intersections and Double Excitations in Time-dependent Density Functional Theory. *Mol. Phys.* **2006**, *104*, 1039−1051.
(57) Tapavicza, E.; Tavernelli, I.; Röthlisberger, U.; Filippi, C.; Casida, M. E. Mixed Time-dependent Density-functional Theory/Classical Trajectory Surface Hopping Study of Oxirane Photochemistry. *J. Chem. Phys.* **2008**, *129*, 124108.
(58) Li, S. L.; Marenich, A. V.; Xu, X.; Truhlar, D. G. Configuration Interaction-Corrected Tamm-Dancoff Approximation: A Time-Dependent Density Functional Method with the Correct Dimensionality of Conical Intersections. *J. Phys. Chem. Lett.* **2014**, *5*, 322−328.
(59) Van Wüllen, C. Shared-Memory Parallelization of the TURBOMOLE Programs AOFORCE, ESCF, and EGRAD: How to Quickly Parallelize Legacy Code. *J. Comput. Chem.* **2011**, *32*, 1195−1201.
(60) Dennington, R.; Keith, T.; Millam, J. *GaussView* Version 5.0.9; Semichem Inc.: Shawnee Mission, KS, 2009.
(61) Kobatake, S.; Yamada, T.; Uchida, K.; Kato, N.; Irie, M. Photochromism of 1,2-Bis(2,5-dimethyl-3-thienyl)-perfluorocyclopentene in a Single Crystalline Phase. *J. Am. Chem. Soc.* **1999**, *121*, 2380−2386.
(62) Ishibashi, Y.; Mukaida, M.; Falkenström, M.; Miyasaka, H.; Kobatake, S.; Irie, M. One- and multi-photon cycloreversion reaction dynamics of diarylethene derivative with asymmetrical structure, as revealed by ultrafast laser spectroscopy. *Phys. Chem. Chem. Phys.* **2009**, *11*, 2640−2648.
(63) Atchity, G. J.; Xantheas, S. S.; Ruedenberg, K. Potential Energy Surfaces Near Intersections. *J. Chem. Phys.* **1991**, *95*, 1862−1876.
(64) Yarkony, D. R. Nuclear Dynamics Near Conical Intersections in the Adiabatic Representation: I. The Effects of Local Topography on Interstate Transitions. *J. Chem. Phys.* **2001**, *114*, 2601−2613.
(65) Ben-Nun, M.; Molnar, F.; Schulten, K.; Martínez, T. J. The Role of Intersection Topography in Bond Selectivity of cis-trans Photoisomerization. *Proc. Natl. Acad. Sc. U. S. A.* **2002**, *99*, 1769−1773.
(66) Lee, A. M. D.; Coe, J. D.; Ho, M.-L.; Lee, S.-J.; Ullrich, S.; Cheng, B.-M.; Zgierski, M. Z.; Chen, I.-C.; Martínez, T. J.; Stolow, A. Substituent Effects on Dynamics at Conical Intersections: α,β-Enones. *J. Phys. Chem. A* **2007**, *111*, 11948−11960.
(67) Ben-Nun, M.; Quenneville, J.; Martnez, T. J. Ab Initio Multiple Spawning: Photochemistry from First Principles Quantum Molecular Dynamics. *J. Phys. Chem. A* **2000**, *104*, 5161−5175.
(68) Beck, M. H.; Jäckle, A.; Worth, G. A.; Meyer, H.-D. The Multiconfiguration Time-dependent Hartree (MCTDH) Method: a Highly Efficient Algorithm for Propagating Wavepackets. *Phys. Rep.* **2000**, *324*, 1−105.
(69) Ishibashi, Y.; Umesato, T.; Kobatake, S.; Irie, M.; Miyasaka, H. Femtosecond Laser Photolysis Studies on Temperature Dependence of Cyclization and Cycloreversion Reactions of a Photochromic Diarylethene Derivative. *J. Phys. Chem. C* **2012**, *116*, 4862−4869.
(70) Jean-Ruel, H.; Gao, M.; Kochman, M. A.; Lu, C.; Liu, L. C.; Cooney, R. R.; Morrison, C. A.; Miller, R. J. D. Ring-Closing Reaction in Diarylethene Captured by Femtosecond Electron Crystallography. *J. Phys. Chem. B* **2013**, *117*, 15894−15902.
(71) Morimitsu, K.; Kobatake, S.; Irie, M. Control of Cycloreversion Quantum Yields of Diarylethenes by Introduction of Substituents at the Reactive Carbons. *Mol. Cryst. Liq. Cryst.* **2005**, *431*, 151−154.

Supporting Information: Quantum Yields and Reaction Times of Photochromic Diarylethenes: Nonadiabatic Ab Initio Molecular Dynamics for Normal- and Inverse-Type

Christian Wiebeler[1] and Stefan Schumacher[1]

[1]*Physics Department and Center for Optoelectronics and Photonics Paderborn (CeOPP), Universität Paderborn, Warburger Strasse 100, 33098 Paderborn, Germany*

(Dated: August 25, 2014)

I. SUPPORTING INFORMATION

A. Structures of the Experimental Relevant Diarylethenes

The experimental excitation energies that are shown in TABLE I have been obtained for two small diarylethene molecules with similar structures, see FIG. S1. The N-type molecule has been investigated in reference 1 and the I-Type molecule in reference 2. Both measurements were done in hexane solution.

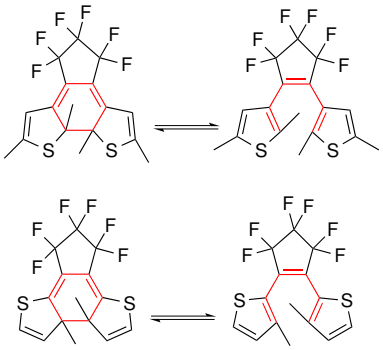

FIG. S1: Illustration of normal[1] and inverse[2]-type diarylethenes that have been chosen as experimental reference for the excitation energies. The reactive centers are highlighted and the photoinduced conversion between open and closed ring forms is indicated.

The ultrafast dynamics of the cycloreversion of several diarylethene molecules has been investigated in experiment.[3] The structure of one molecule studied is shown in FIG. S2.[4] The reported cycloreversion quantum yield is 0.075 and the time constant associated with the lifetime of the excited state is 1.3 ps. The measurements were done in n-hexane. Note that the molecule is significantly larger than the model diarylethene molecules studied here and that the quantum yield is rather low. The reaction for this molecule is expected to be slower than for our model diarylethenes.

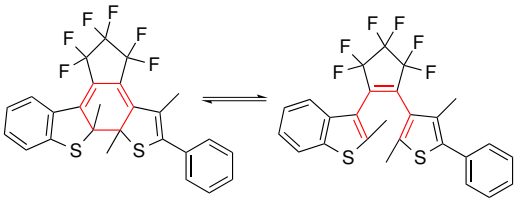

FIG. S2: Illustration of the diarylethene molecule for which ultrafast dynamics was investigated in experiment.[4]

B. Quantum Yields of the Cycloreversion Reactions

The data presented in FIG. 1 of the main text are given in TABLE S1.

TABLE S1: Reactive and unreactive trajectories for normal- (N) and inverse- (I) type diarylethenes given for trajectories that reacted faster or slower than 100 fs respectively and all trajectories. Reactive trajectories lead to formation of the open ring isomer and unreactive trajectories do not undergo chemical reaction and therefore return to the closed ring structure.

	Reactive	Unreactive	Number of Traj.
N-Type			
Total	55	45	100
< 100 fs	9	3	12
> 100 fs	46	42	88
I-Type			
Total	77	23	100
< 100 fs	43	7	50
> 100 fs	34	16	50

C. Potential Energy Surfaces Calculated Using CC2

In order to assess the accuracy of the used (TD-)DFT calculations in Tamm-Dancoff approximation, we have also calculated the PES shown in FIG. 6 and FIG. 7 employing RI-CC2, see FIG. S3 and FIG. S4. Further details of the calculations can be found in the methods section of the main article. Note that no converged geometries have been found for the optimizations along the first ex-

cited state for N- and I-type diarylethenes for a distance of 2.1 $\mathring{A}$ and for I-type for a distance of 1.5 $\mathring{A}$. However, in total, good agreement between both approaches is obtained.

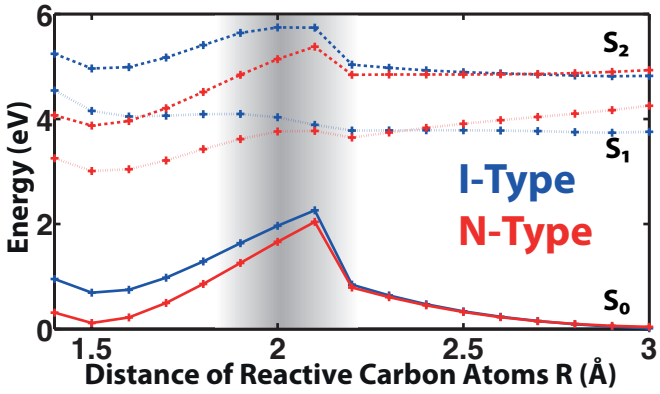

FIG. S3: RI-CC2-calculation of Potential Energy Surfaces obtained optimizing the ground state along the distance between the reactive carbon atoms. We find very good agreement of the RI-CC2 results with the DFT results shown in FIG. 6. In particular the RI-CC2 calculations confirm the presence of a potential energy barrier for the normal-type and nearly no barrier for the inverse-type diarylethene when approaching the conical intersection in the S_1 state.

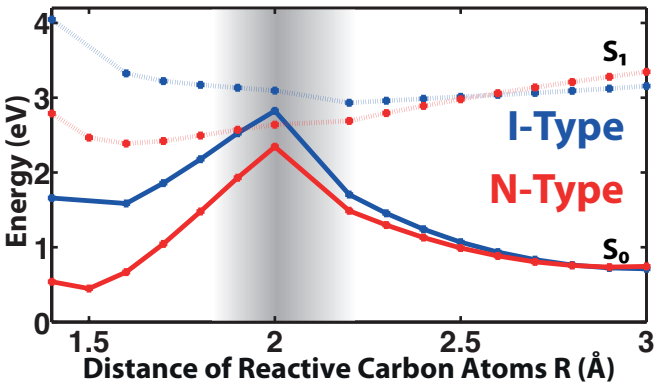

FIG. S4: RI-CC2-calculation of Potential Energy Surfaces obtained optimizing the first excited state. We find qualitative agreement of the RI-CC2 results with the DFT results shown in FIG. 7, i.e., barrier for cycloreversion of N-type diarylethene and no barrier for cycloreversion of I-type. The reference energy is the same as for the potential energy surface shown in FIG. S3.

D. Geometries of First Excited State PES Scan

The geometries in xyz-format of the PES Scan obtained using (TD-)DFT relaxed for the first excited state are given in the following for N- and I-type diarylethenes:

```
20
N–Type, R = 1.4 angstroms
C  0.704324  2.267136  −0.069530
H  1.245170  3.204900  −0.219866
C  −0.704403  2.267093  0.069749
H  −1.245261  3.204804  0.220160
C  −1.402957  1.059405  0.021262
C  −0.607000  −0.176000  −0.349000
C  −2.741354  0.755997  0.381070
S  −1.716944  −1.609604  −0.053031
C  −3.044434  −0.582182  0.401986
H  −3.460840  1.524040  0.674027
H  −3.995854  −1.035142  0.681743
C  1.402903  1.059458  −0.021189
C  0.607000  −0.176000  0.349000
C  2.741303  0.756134  −0.380972
S  1.717024  −1.609519  0.052908
C  3.044447  −0.582021  −0.402006
H  3.460768  1.524170  −0.673876
H  3.995868  −1.034964  −0.681807
H  0.399686  −0.175787  1.435623
H  −0.399694  −0.175698  −1.435626

20
N–Type, R = 1.5 angstroms
C  0.702392  2.251288  −0.083819
H  1.237448  3.188203  −0.259850
C  −0.702473  2.251287  0.084089
H  −1.237621  3.188180  0.260167
C  −1.407291  1.045599  0.041599
C  −0.652000  −0.192000  −0.371000
C  −2.719572  0.751095  0.503698
S  −1.758273  −1.603888  −0.068182
C  −3.032058  −0.581242  0.531686
H  −3.399677  1.522039  0.872390
H  −3.955180  −1.034658  0.893061
C  1.407245  1.045630  −0.041559
C  0.652000  −0.192000  0.371000
C  2.719604  0.751226  −0.503583
S  1.758317  −1.603849  0.068092
C  3.032090  −0.581110  −0.531708
H  3.399652  1.522260  −0.872271
H  3.955221  −1.034448  −0.893108
H  0.405442  −0.189342  1.447334
H  −0.405442  −0.189275  −1.447335

20
N–Type, R = 1.6 angstroms
C  0.700051  2.230562  −0.097828
H  1.229668  3.166562  −0.295694
C  −0.700090  2.230523  0.097937
H  −1.229713  3.166486  0.295912
```

H −1.149813 −2.535442 −0.439560
C 0.680678 −1.584797 0.153998
H 1.145275 −2.537571 0.434270
C 1.521112 −0.450038 0.060880
C 1.297000 0.766000 −0.648000
S 3.056178 −0.376998 0.899748
C 2.344296 1.695071 −0.474248
C 3.356075 1.227567 0.328976
H 4.275960 1.740279 0.610139
C −1.523120 −0.448127 −0.062367
C −1.297000 0.766000 0.649000
S −3.058362 −0.371077 −0.900616
C −2.342800 1.697163 0.477203
C −3.355567 1.232930 −0.326684
H −4.274691 1.747709 −0.606670
H −2.366114 2.679400 0.952223
H 2.369403 2.678203 −0.947342
H −0.475686 0.874488 1.357424
H 0.476015 0.877242 −1.356385

20
I−Type, R = 3.0 angstroms

C −0.679743 −1.538425 −0.167353
H −1.132607 −2.494312 −0.457917
C 0.679281 −1.538747 0.166779
H 1.131890 −2.494974 0.456595
C 1.539453 −0.417338 0.082678
C 1.359000 0.799000 −0.634000
S 3.073779 −0.387974 0.929260
C 2.432656 1.694971 −0.461851
C 3.426944 1.200587 0.349939
H 4.359467 1.687978 0.634679
C −1.539660 −0.416870 −0.082448
C −1.359000 0.799000 0.635000
S −3.074002 −0.386726 −0.928963
C −2.432551 1.695212 0.463479
C −3.426935 1.201492 −0.348615
H −4.359399 1.689186 −0.633009
H −2.489227 2.675094 0.940642
H 2.489454 2.675165 −0.938377
H −0.526530 0.943505 1.324302
H 0.526542 0.944084 −1.323193

[1] Kobatake, S.; Yamada, T.; Uchida, K.; Kato, N.; Irie, M. *J. Am. Chem. Soc.* **1999**, *121*, 2380–2386.
[2] Tatsumi, Y.; Kita, J.; Uchida, W.; Ogata, K.; Nakamura, S.; Uchida, K. *J. Phys. Chem. A* **2012**, *116*, 10973–10979.
[3] Irie, M., Yokoyama, Y., Seki, T., Eds. *New Frontiers in Photochromism*; Springer Japan, 2013.
[4] Ishibashi, Y.; Mukaida, M.; Falkenström, M.; Miyasaka, H.; Kobatake, S.; Irie, M. *Phys. Chem. Chem. Phys.* **2009**, *11*, 2640–2648.

8.3 Results of Nonadiabatic Dynamics for Experimentally Relevant Molecules

The methodology used for the NA-AIMD simulations of the prototypical normal- and inverse-type DAEs can also be applied to larger, experimentally relevant molecules. One such molecule is CMTE and results concerning this molecule will also be included in this section, even though they have already been presented in the chapter 7. Another experimentally-relevant molecule is 1-(2-methyl-3-benzothienyl)-2-(2,4dimethyl-5-phenyl-3-thienyl)-perfluorocyclopentene (BPT) and its structure is shown in figure 8.5 in magenta. In an investigation of this molecule, not only the QY of the cycloreversion reaction was determined, but also the reaction time. The experiments were done in n-hexane as solvent and employed ultrafast laser spectroscopy.[98]

To estimate the QYs of the cycloreversion reaction of the corresponding DAE, PESs can be analyzed. For this purpose, the simplest approach is the optimization of the S_0 geometry for a fixed distance between the reactive carbon atoms and subsequent calculation of the excitation energy using TDA. The results are shown on the left in figure 8.5. The PESs of the three normal-type molecules are similar to each other, i.e. for all three PESs there is a barrier in S_1 separating the initial geometry of the CF from the CI. Closer inspection shows, that the barrier increases in the following order: N-Type, CMTE, BPT. Increasing barrier height should lead to lower QYs, so it is expected that the QY of N-Type is the highest and decreases for the other molecules.

A more sophisticated approach for the calculation of the PESs is based on the optimization of the geometry of S_1 employing TDA. Even though, TDA is used to alleviate problems of TDDFT close to CIs,[99,100] it was not possible to obtain converged results for two geometries of BPT with fixed distances of the reactive carbon atoms that are close to the CI. Nonetheless, the results are sufficient to interpret them. Due to the fact that the reference energy for each molecule is the optimized S_0 CF, the energies for each molecule can be compared for both types of optimization. Therefore, it has to be noted that the S_0 energy of these calculations is shifted upward and the energy of S_1 is lowered leading to a smaller gap between the energies. Furthermore, the barrier between the initial geometry of the CF and the CI on the S_1 is now smaller, but the trends between the heights remain the same among the three normal-type molecules. So the estimation of the trends for the QYs is the same as derived from the optimization of S_0 geometry with subsequent calculation of vertical excitation energies.

As has been shown in the previous discussion, it is possible to estimate trends between QYs using PESs and this was done in former combined computational and experimental studies.[77,78] Actual number, however, cannot be obtained by this approach. In order to predict it, NA-AIMD has to be used and this was done for the four DAEs presented employing the same methodology as used in the included paper.[5] The QY for CMTE is in good agreement to the experimental values.[74] The QY for BPT is in the right ball park, but it is a bit too low. In addition to the estimation of the QYs of the cycloreversion reaction, also the reaction times can be calculated. The only experimental value regarding this quantity for the four molecules has been reported for BPT.[98] Again,

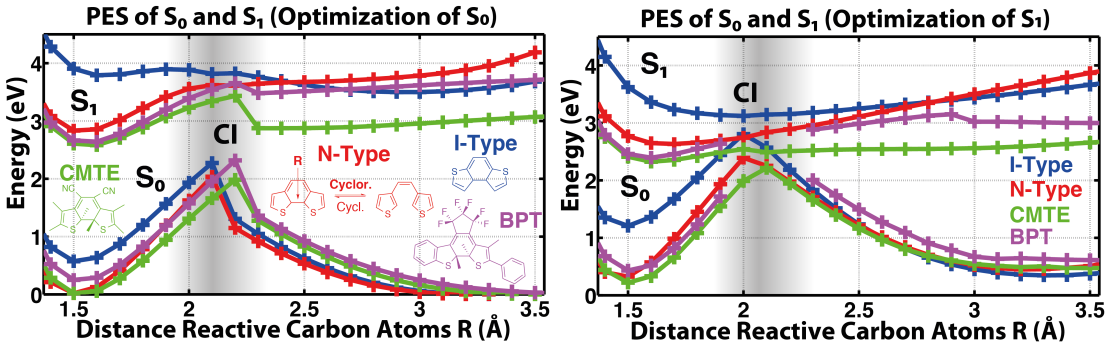

Figure 8.5: PESs plotted for four DAEs. Shown as insets are the color coded molecular structures of the investigated DAEs (left) and their names (right). The PESs on the left were calculated optimizing the geometry of S_0 and calculating the vertical excitation energy; the PESs on the right were calculated optimizing the geometry of S_1. In both cases, the distance between the reactive carbon atoms was fixed. Furthermore, def2-SVP was used as basis and PBE0 as functional. For the calculation of excited states TDA was employed. The main characteristics of the PES relevant for the cycloreversion reaction are the same and do not depend on the way the PESs are calculated. The I-type DAE can reach the CI of the S_1 state without a barrier and the height of the barriers for the remainder increases from N-type over CMTE to BPT.

From NA-AIMD

	QY (%)	τ_{total} (ps)	$\tau_{reactive}$ (ps)	$\tau_{unreactive}$ (ps)
I-Type	77	0.18	0.15	0.30
N-Type	55	0.28	0.21	0.36
CMTE	11	1.3	Too few reactive trajectories	
BPT	3	2.3	Too few reactive trajectories	

From Experiment

	QY (%)	τ_{total} (ps)	Publication
CMTE	12 and 7, respectively	-	Spangenberg et al. Photochem. Photobiol. Sci. **9**, 188-193 (2010)
BPT	7.5	1.3	Ishibashi et al. PCCP **11**, 2640-2648 (2009)

Figure 8.6: Summary of QYs and reaction times for the four DAEs investigated (top) and values obtained from experiment (bottom). The computational methodology is described in [5] and the reaction times were obtained from exponential fits. The trends estimated from the barrier heights of the S_1 state found for both types of PES calculations carry over to the QYs. Furthermore, the reaction time increases with molecular size and it is faster if the involved PES is more favorable for reaching the CI.

the value obtained from NA-AIMD is in the right ball park, but it is too high.

The deviations from the experimental values might be explainable with the fact that the calculations were done without taking into account any solvent effect, whereas the measurements were performed in n-hexane solution. The solvent might stabilize the state near the CI. This would decrease the barrier and therefore the reaction would be more likely and would proceed faster. Overall, these results are promising and the application of this kind of calculations to further DAEs is a reasonable next step. For example the effect of substitution at the reactive carbon atoms can be investigated and the corresponding results will be discussed in section 8.4.

8.4 Effect of Substitution on the Cycloreversion Reaction

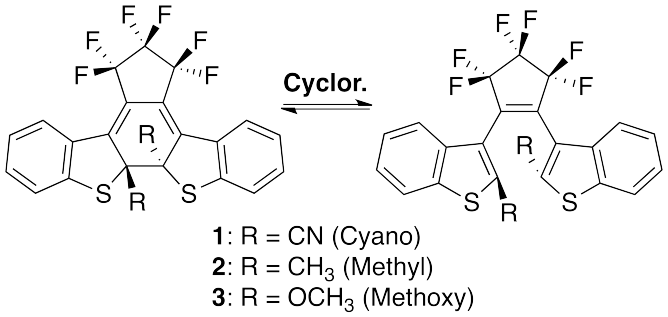

Figure 8.7: Three DAEs with different substituents at the reactive carbon atoms. The cyano group, i.e. CN, is an electron-withdrawing group, the methyl group, i.e. CH_3, is a weakly electron-donating group, and the methoxy group, i.e. OCH_3, is an electron-donating group.

The influence of substituents at the reactive carbon atoms on the cycloreversion reaction of DAEs has been studied extensively in experiment.[101] Three molecules investigated are shown in figure 8.7 and the results regarding QYs and absorption maxima of the CF obtained from experimental measurements and from DFT-based quantum chemical calculations using TDA for excited state calculations are summarized in table 8.1.

The QY and absorption maximum for the DAE with cyano groups are in agreement with experimental findings. Having methyl groups as substituents, the shift of the absorption maximum is correctly described. However, the QY is now much too low. Finally for the DAE with methoxy groups as substituents, the QY is again in good agreement with experiment, but the maximum of absorption in the visible range is quite far off. Therefore, even the trend found in experiment for the absorption maxima is not reproduced by the theoretical calculations.

In order to better understand the QYs estimated from NA-AIMD, the PESs are shown in figure 8.8 for optimizations of the S_0 geometry. The barrier for the cycloreversion reaction in the first excited singlet state has about the same height for the DAEs with methyl and methoxy groups. This explains the similar QYs. However, this barrier is

Molecule	QY (Exp.[101])	QY (Theo.)	λ/nm (Exp.[101])	λ/nm (Theo.)
1:	0.59	0.69	496	486
2:	0.35	0.03	517	507
3:	0.03	0.02	547	485

Table 8.1: QYs and absorption maxima in the visible range for the three substituted DAEs. Both quantities were determined experimentally and based on quantum chemical calculations using TDA and def2-SVP/PBE0. Comparing the data between experiment and calculations, it has to be noted that good agreement is obtained for molecule **1**. The shift in absorption between **1** and **2** is correctly described, whereas the QY of **2** is much too low. Finally, the QYs for **3** are similar, but the absorption energies differ the strongest for this molecule.

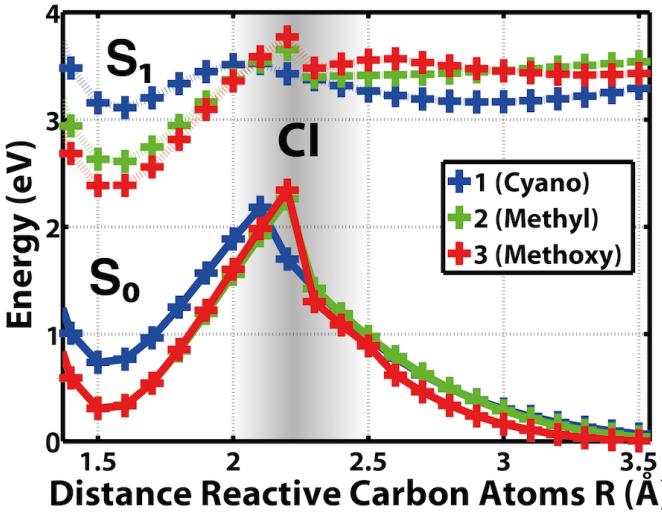

Figure 8.8: PESs of the three substituted DAEs obtained optimizing the S_0 geometry followed by calculation of vertical excitation energies employing TDA and PBE0/def2-SVP. The barrier for the cycloreversion reaction of molecule **1** is the smallest leading to the largest QY. The barriers of molecules **2** and **3** are similar giving an explanation why the QYs of both are calculated to be about the same.

significantly smaller for the DAE with cyano groups. This justifies that the QY for this molecule is much larger than for the other two molecules.

Overall, it can be said that NA-AIMD as it was used in this chapter is a valuable method for the estimation of QYs and reaction times. In future studies it might be interesting to use this method to complement experiments. For example, in a recent study the temperature dependence of the cycloreversion reaction was investigated[102] and might be verifiable using NA-AIMD. Furthermore, recent studies investigate the dynamics of the photocyclization reaction using ultrafast transient absorption spectroscopy and femtosecond electron crystallography.[103,104] However, to investigate this direction of the reaction, the methodology used in this chapter, i.e. TSH with Turbomole, must be most likely extended to include nonadiabatic couplings (NAC) between excited states.

9 Ultrafast Dynamics of Charge Separation in Conjugated Oligomers

> Was wir vor den griechischen Philosophen voraus haben, ist, dass wir unendlich besser wissen, als Sokrates es wusste, dass wir, gerade in Beziehung auf das, was wir wissen möchten, Nichts wissen. Wir ersteigen einen Berg, auf der Spitze angelangt, sieht der umfassendere Blick immer neue Berge sich erheben, die anfänglich dem Auge nicht sichtbar waren.
>
> *(Justus von Liebig[105])*

The molecule studied in the present chapter is an oligomer based on PCPDT-BT consisting of a CPDT unit capped by two BT units. As mentioned in chapter 4, one of the promising applications for conjugated polymers is OPV. For this application, not only the static properties are of importance, but also the dynamic ones, i.e. the photophysics upon excitation. To investigate this, NA-AIMD, which has been used to understand the photochemistry of DAEs in chapters 7 and 8, can be employed for the photophysics of these larger systems. After a discussion of NA-AIMD employing TSH with TFSA, the static electronic and optical properties will be discussed in the article that is included in this chapter.[6] Then, the motivation for investigating the ultrafast dynamics will be explained in more detail and first results obtained employing TSH for a uni- and bimolecular system will be presented.

9.1 Trajectory-based Nonadiabatic Dynamics

The considerations in the following are based on reference [106]. In order to formally derive TSH, the time-dependent Schrödinger equation is taken as starting point:

$$\left(i\hbar\frac{\partial}{\partial t} - H\right)\Psi(\boldsymbol{r}, \boldsymbol{R}, t) = 0 \tag{9.1}$$

The Hamiltonian can be divided into nuclear kinetic energy and electronic Hamiltonian. Therefore, the latter also includes the Coulomb interaction between nuclei:

$$H = T_N + H_e \tag{9.2}$$

The molecular wave function is now written using a Born-Oppenheimer expansion:

$$\Psi(\boldsymbol{r}, \boldsymbol{R}, t) = \sum_j \chi_j(\boldsymbol{R}, t)\Phi_j(\boldsymbol{r}; \boldsymbol{R}) \tag{9.3}$$

The sum runs over all electronic states, the electronic wave function Φ_j is a function of the electronic coordinates $\boldsymbol{r}$ and depends parametrically on the nuclear coordinates $\boldsymbol{R}$. The nuclear wave function χ_j is a function of $\boldsymbol{R}$ and time t. Furthermore, the electronic wave functions are orthonormal. Using this expansion in the Hamiltonian, multiplying by Φ_k^*, and integrating over the electronic coordinates yields:

$$i\hbar\frac{\partial\chi_k}{\partial t} + \frac{1}{2}\hbar^2\nabla_M^2\chi_k + \sum_j\left(-H_{kj} + i\hbar\boldsymbol{F}_{kj}\cdot\hat{\boldsymbol{v}} + \frac{1}{2}\hbar^2 G_{kj}\right)\chi_j = 0 \tag{9.4}$$

In this equation, the following definitions are employed:

$$\nabla_M^2 = \sum_m^{N_{at}}\frac{\nabla_m^2}{M_m} = -\frac{2}{\hbar^2}T_n \tag{9.5}$$

$$H_{kj}(\boldsymbol{R}) = \langle\Phi_k|H_e|\Phi_j\rangle_{\boldsymbol{r}} \tag{9.6}$$

$$G_{kj} = (\boldsymbol{R}) = \langle\Phi_k|\nabla_M^2|\Phi_j\rangle_{\boldsymbol{r}} \tag{9.7}$$

The index m runs over all N_{at} nuclei. For atom m the velocity operator and nonadiabatic coupling vector (NACV) are defined as:

$$\hat{\boldsymbol{v}}_m = -i\hbar\frac{\nabla_m}{M_m} \tag{9.8}$$

$$\boldsymbol{F}_{kj}^m(\boldsymbol{R}) = \langle\Phi_k|\nabla_m|\Phi_m\rangle_{\boldsymbol{r}} \tag{9.9}$$

So far, no approximation has been used. In order to solve equation 9.4, PES, nuclear wave functions and coupling terms have to be determined beforehand for the whole configuration space for a limited number of states j.[106] This leads to quantum mechanical wave packet propagation methods like Multiconfiguration Time-Dependent Hartree.[94] For the Ab Initio Multiple Spawning method[95] the "saddle point" approximation is assumed:

$$\langle\chi_k|O_{kj}(\boldsymbol{R})|\chi_l\rangle \approx \langle\chi_k|\chi_l\rangle\, O_{kj}(\boldsymbol{R}^c) = \langle\chi_k|\chi_l\rangle\, O_{kj}^c \tag{9.10}$$

In this equation, $\boldsymbol{R}^c$ denotes a single set of coordinates. Neglecting all terms that are proportional to $\hbar^2$ in equation 9.4 leads to the independent trajectory approximation. Furthermore, the nuclear wave function χ_k describing the wave packet around each trajectory $\boldsymbol{R}^c$ is approximated using the trivial factorization:

$$\chi_k(\boldsymbol{R}, \boldsymbol{R}^c, t) = c_k(t)\zeta(\boldsymbol{R} - \boldsymbol{R}^c) \qquad \text{with} \qquad \langle\zeta_k|\zeta_k\rangle_{\boldsymbol{R}} = 1 \tag{9.11}$$

$\zeta(\boldsymbol{R} - \boldsymbol{R}^c)$ is a peaked function centered at each trajectory $\boldsymbol{R}^c$ of the swarm. Using these approximations in equation 9.4, multiplying by ζ_k^* and integrating over the nuclear coordinates, yields:

$$i\hbar\frac{\mathrm{d}c_k}{\mathrm{d}t} + \sum_j[-\langle\zeta_k|H_{kj}|\zeta_j\rangle_{\boldsymbol{R}} + i\hbar\langle\zeta_k|\boldsymbol{F}_{kj}\cdot\hat{\boldsymbol{v}}|\zeta_j\rangle_{\boldsymbol{R}}]c_j = 0 \tag{9.12}$$

The final equation for the quantum amplitudes is obtained by three additional approximations. First, the velocity operator is replaced by the velocity function. Second, the saddle point approximation (see equation 9.10) is employed. Third, motivated by the fact that the amplitudes cannot be transferred between different $\boldsymbol{R}^c$ trajectories, the overlap between the nuclear wave functions is assumed to be:

$$\langle\zeta_k|\zeta_l\rangle_{\boldsymbol{R}} = 1 \tag{9.13}$$

Therefore, the equation of motion for the quantum amplitudes is:

$$i\hbar\frac{\mathrm{d}c_k}{\mathrm{d}t} + \sum_j[-H_{kj}^c + i\hbar\boldsymbol{F}_{kj}^c\cdot\boldsymbol{v}^c]c_j = 0 \tag{9.14}$$

Using the Ehrenfest theorem, the motion of nucleus m is determined by Newton's law:

$$\frac{\mathrm{d}\langle\Psi|\hat{\boldsymbol{P}}_m|\Psi\rangle_{\boldsymbol{rR}}}{\mathrm{d}t} + \langle\Psi|\nabla_m H_e|\Psi\rangle_{\boldsymbol{rR}} = 0 \tag{9.15}$$

Employing the Born-Oppenheimer expansion (equation 9.3), the factorization of equation 9.11, the approximation for the overlap between nuclear wave function (equation 9.13) and the saddle point approximation (equation 9.10), the force on m is:

$$\mathcal{F}_m^c = -\langle\Psi|\nabla_m H_e|\Psi\rangle_{\boldsymbol{rR}} \approx -\sum_{kj} c_k^* c_j \langle\Phi_k^c|\nabla_m H_e|\Phi_j^c\rangle_{\boldsymbol{r}} \tag{9.16}$$

Therefore, the coordinates $\boldsymbol{R}^c$ can be determined from a classical trajectory using Newton's equation of motion for each nucleus m:

$$\frac{\mathrm{d}^2\boldsymbol{R}_m^c}{\mathrm{d}t^2} - \frac{\mathcal{F}_m^c}{M_m} = 0 \tag{9.17}$$

The equations 9.17 and 9.14 for forces obtained from equation 9.16 are the working equations of the Ehrenfest method.[96,107] In this method, the evolution of each initial point is determined by a single independent trajectory that is driven by an average PES involving several electronic states. Due to this, the computational cost in comparison to TSH is relatively low. However, if the wave packet splits between two adiabatic states and leaves the region of strong adiabatic coupling, the single trajectory will also move on an average surface. The main alternative to overcome this problem is TSH. Central idea

of this method is that the trajectories are always only driven by a single adiabatic PES and that the correct distribution among the states is achieved by allowing trajectories to change the surface on which they are moving. The method will be discussed in more detail in section 9.2. A further discussion regarding the underlying assumptions of this derivation and the wrong asymptotic behavior of the Ehrenfest method can be found in reference [106].

9.2 Trajectory Surface Hopping & Tully's Fewest Switches Algorithm

Using the adiabatic representation, the Hamiltonian is diagonal and can be written as $H_{kj} = V_k \delta_{kj}$. In TSH, the force on the nucleus m is caused by a single PES l:

$$\mathcal{F}_m^c = -\nabla_m V_l^c \tag{9.18}$$

The redefined force enters in equation 9.17 and together the two equations determine the dynamics of the trajectories. Simultaneously, the quantum amplitudes for each state are integrated according to equation 9.14. This allows the evaluation of transition probabilities between two electronic states and a stochastic algorithm is used to determine if a surface hop occurs.

Due to the classical treatment of the nuclear degrees of freedom, no expression for the hopping probability can be explicitly derived. Therefore, a variety of hopping algorithms has been proposed.[108] One of the most popular choices is TFSA that was suggested by Tully.[83] Central idea of the algorithm is that the quantum-classical self-consistency is maintained with the minimum number of hopping events. The minimum of possible hopping events ensures that the trajectories do not evolve on an average of the relevant PESs leading to a mean field description similar to the Ehrenfest method.[108] The quantum-classical self-consistency can be defined as:[106]

$$f_k(t) \equiv \frac{N_k(t)}{N_T} = \frac{1}{N_T} \sum_n^{N_T} |c_k^{(n)}|^2 \equiv \bar{a}_{kk}(t) \tag{9.19}$$

The classical quantity is the fraction of trajectories in state k to the total number of the trajectories that is found on the left of the equation. The quantum mechanical quantity is the average of the square of the absolute value of the quantum amplitude $|c_k|^2$ of state k. In order to arrive at an expression for the hopping probability, the density matrix elements are defined as $\rho_{kl} = c_k c_l^*$ and equation 9.14 is rewritten using this definition. The hopping probability in TFSA is therefore:[106]

$$P_{l\to k} = \frac{\text{Population increment in } k \text{ due to flux from } l \text{ during } \Delta t}{\text{Population of } l} \tag{9.20}$$

$$= \max\left[0, \frac{2\Delta t}{\rho_{ll}} (\hbar^{-1} \mathrm{Im}(\rho_{kl}) H_{lk}^c - \mathrm{Re}(\rho_{kl}) \boldsymbol{F}_{kl}^c \cdot \boldsymbol{v}^c\right] \tag{9.21}$$

In order to test if a hopping event from state l to state k takes place, a random number $r_t \in [0, 1]$ is generated and it takes place if:

$$\sum_{n=1}^{k-1} P_{l\to n} < r_t \geq \sum_{n=1}^{k} P_{l\to n}(t) \tag{9.22}$$

Energy conservation is ensured by velocity adjustment, which is described in more detail in reference [108]. More information regarding the motivation for the hopping algorithm can be found in the original paper [83].

9.3 Calculation of Nonadiabatic Couplings

In order to propagate the quantum amplitudes in time according to equation 9.14 and to determine the hopping probability given in equation 9.21, the NACs can be calculated explicitly via electronic structure calculations. In principle there are two ways to do so: analytical and numerical.

For the analytical approach, the expression given in equation 9.9 has to be evaluated. This approach is in general superior to the numerical one, due to its better accuracy and numerical stability.[109] However, the explicit evaluation of NACV is not a standard task for electronic structure calculations. Therefore, implementations of it are only available for a relatively small number of methods.

If NACVs are not available, the nonadiabatic coupling element (NACME) σ_{kj} can be approximated. It is defined as:[110]

$$\sigma_{kj} = \boldsymbol{F}^c_{kj} \cdot \boldsymbol{v}^c = \left\langle \Phi_k \middle| \frac{\partial}{\partial t} \Phi_l \right\rangle \tag{9.23}$$

Approximating it by numerical differences for different times the following expressions can be derived:[111]

$$\sigma_{kl}\left(t - \frac{3}{2}\Delta t\right) \approx \frac{1}{2\Delta t}[\langle \Phi_k(t - 2\Delta t)|\Phi_l(t - \Delta t)\rangle - \langle \Phi_k(t - \Delta t)|\Phi_l(t - 2\Delta t)\rangle] \tag{9.24}$$

$$\sigma_{kl}\left(t - \frac{1}{2}\Delta t\right) \approx \frac{1}{2\Delta t}[\langle \Phi_k(t - \Delta t)|\Phi_l(t)\rangle - \langle \Phi_k(t)|\Phi_l(t - \Delta t)\rangle] \tag{9.25}$$

Linear extrapolation yields:

$$\sigma_{kl}(t) \approx \frac{1}{2}\left[3\sigma_{kl}\left(t - \frac{1}{2}\Delta t\right) - \sigma_{kl}\left(t - \frac{3}{2}\Delta t\right)\right] \tag{9.26}$$

This equation allows the calculation of NACMEs between subsequent time steps. It can be used for every electronic structure method, if a configuration interaction representation of the electronic wave function can be constructed.[106] The method for the calculation of NACs based on this approach will be denoted OVL.

9.4 The TSH Algorithm

Having derived the equations of motion for TSH, defined an algorithm for the surface hopping, and explained how to calculate the NACs in sections 9.1, 9.2, and 9.3, respectively, the whole algorithm of TSH-based dynamics can be stated as follows:

1. **Generation of Initial Conditions:** The starting point of a trajectory is defined by nuclear coordinates and velocities as well as quantum amplitudes. For the TSH calculations presented in this work, S_0 is the state of reference for the sampling. The sampling is either based on snapshots from Born-Oppenheimer molecular dynamics (BOMD) or on a Wigner-distribution. In the BOMD simulations, the motion of the nuclei is treated classically and as long as the energy in each degree of freedom is larger than the zero-point energy both approaches should yield comparable results.[106]

2. **Dynamics:** The steps described in the following explain how a single time step for a specific trajectory is executed. For a certain trajectory, they have to be repeated until the endpoint, e.g. final time, is reached. This procedure is then repeated for a swarm of trajectories to take into account the stochastic nature of the algorithm.

   a) **Electronic Structure Calculation:** For the dynamics the following quantities have to be determined by standard electronic structure calculations, i.e. for a fixed nuclear geometry: energies, gradients, and NACs. The choice of the method for electronic structure calculation mainly determines the reliability and computational effort of the TSH calculations. For small molecules, Multireference Configuration Interaction can be used and with CASSCF up to about 20 atoms can be treated.[106] For even larger systems, semiempirical methods, e.g. OM2/MRCI,[108] or DFT-based methods, e.g. LR-TDDFT,[112] can be employed. Comparisons regarding the performance of these methods for electronic structure calculation for TSH-based dynamics can be found in references [113] and [114]. In both articles, the ultrafast relaxation of 9H-Adenine is investigated.

   b) **Calculation of TSH-related Quantities:** In addition to the classical time propagation as described in step 2.d) that is known from BOMD, also the quantum amplitudes have to be propagated in time and the hopping probability has to be computed for TSH. For the former, a unitary propagator can be employed. Often, a smaller time step is used for this task compared to the time step for the classical time propagation. The corresponding expressions for the calculation of NACs have been discussed in section 9.3.

   c) **Hopping Algorithm:** For a successful surface hop, two conditions have to be met: the generated random number must fulfill equation 9.22 and the velocity of the system in the direction of the NACV has to be sufficient to ensure conservation of total energy.[108] If this is the case, the velocity will be adjusted to compensate the change in the electronic energy and the active PES for the dynamics is changed.

d) **Classical Time Propagation:** The coordinates and velocities of the nuclei are determined at the next time using equation 9.17 and the force is obtained from the selected PES according to equation 9.18. This step is equivalent to the time propagation in classical BOMD. In principle, a standard algorithm for solving the equation of motion can be used. However, in order to calculate the NACs, positions and velocities have to be computed at the same time. Due to this, the leap-frog algorithm cannot be used for example, but the velocity-Verlet algorithm is a viable choice.

The physical interpretation of the TSH algorithm is discussed in figure 9.1 and concludes this section.

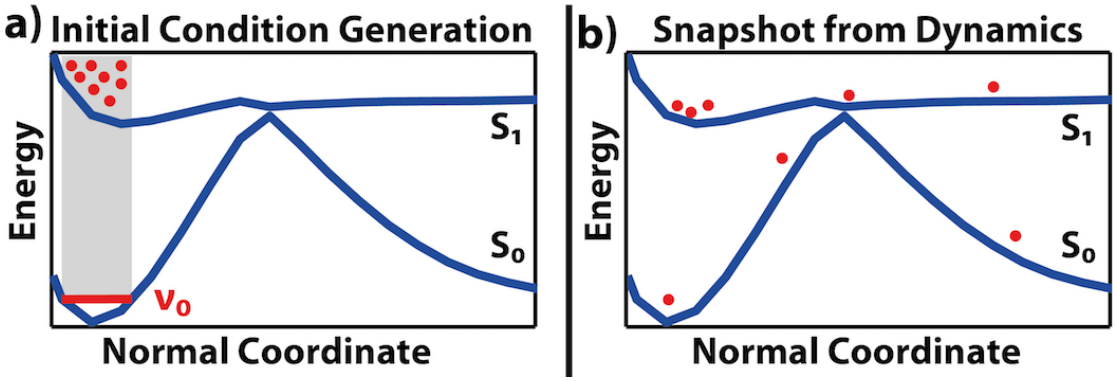

Figure 9.1: Illustration to explain the principle of TSH. Each trajectory at a certain time is represented by a red dot. At the beginning of the dynamics shown in a), a Wigner-distribution of S_0 is used to select appropriate initial conditions. This means that for a given normal coordinate the values that can be reached via the zero-point vibrational motion can be chosen. So the dynamics will be starting in the FC region of the excited state and the initial conditions can be weighted by the oscillator strength of the corresponding transition. In b), a possible situation at some point in time of the TSH-based dynamics is shown. Some trajectories might be trapped in the region of the initial excitation. Other trajectories might be in the area of the CI with strong NAC, where the probability for hopping events is the highest. There can be trajectories that have passed the CI without relaxation and if relaxation has taken place, these trajectories can either relax to the initial S_0 geometry or reach a different minimum on the S_0 PES. Overall, the distribution of the trajectories is supposed to reflect the nuclear wave packet distribution and account for the quantum effect of wave packet splitting at CIs.

9.5 TSH using Linear-Response Time-Dependent DFT

For TSH-based dynamics of larger systems, LR-TDDFT can be employed due to its low computational cost compared to MRCI and CASSCF. Reference [115] contains an

overview of the implementation for quantities that are needed for TSH, i.e. energies, gradients, and NACs. The analytical calculation of the NACVs has been described recently[116] and is implemented in Turbomole.[117] So far, only couplings between S_0 and an excited state are included in the implementation that is described in more detail in the references [85] and [118]. Therefore, using Turbomole no couplings between excited states can be evaluated. Nonetheless, we have used this implementation for the TSH-based dynamics for the cycloreversion reaction of DAEs.[4,5]

For the investigation of the charge separation in D-A conjugated materials, the NACs between excited states have to be considered. In order to achieve this, Turbomole or Gaussian 09 is interfaced with Newton-X.[109] The electronic structure calculation apart from the calculation of the NACs is done by one of the former programs and the latter is used for the calculation of NACs, TSH-related quantities, the execution of the hopping algorithm and the classical time propagation. Regarding the calculation of TSH-related quantities, not only the numerical approach based on the overlap of electronic wave functions (OVL), but also the method of local diabatization (LD) that avoids the explicit calculation of NACs is used.[119]

For OVL, the wave function is written as a formal Configuration Interaction with Single excitations wave function:[114]

$$|\Phi_n\rangle = \sum_{ia} \sqrt{\frac{\epsilon_a - \epsilon_i}{E_n}} X_{ia}^n \, |\phi_{ia}\rangle \tag{9.27}$$

The expression $|\phi_{ia}\rangle$ is a Slater determinant that corresponds to an excitation from Kohn-Sham orbital i to Kohn-Sham orbital a. The orbital energies are ε_i and ε_a and E_n is the excitation energy for state n. X_{ia}^n is the corresponding linear-response pseudo-eigenvector. The wave function is constructed in such a way that the NACs are computed within an approach equivalent to the TDA.[114] Such an approach is necessary due to the fact that the wave function overlaps have to be determined for the NACs, but in DFT actual wave functions are not calculated.

Information for calculating the two kinds of TSH-based dynamics are given in chapter 10. Details of the actual calculations are given in the corresponding articles for the cycloreversion reaction of DAEs[4,5] and in sections 9.8 and 9.9 regarding the dynamics of charge separation.

9.6 "Charge Photogeneration in Donor-Acceptor Conjugated Materials: Influence of Excess Excitation Energy and Chain Length"

This paper has been published in the "Journal of the American Chemical Society". Transient absorption spectroscopy is used to investigate the different dynamics upon photoexcitation of a film made of polymer or oligomer to understand the influence of chain length. Furthermore, the dynamics observed for different excitation energies are investigated. In our contribution, we explain the experimental findings with static quantum chemical calculations. In a next step, TSH will be employed to investigate the ultrafast photophysics of charge separation. Therefore, an explanation of NA-AIMD has been given in the first five sections of this chapter and the following three sections explain the aim of the NA-AIMD investigation and first results obtained for uni- and bimolecular systems are discussed. Note that the oligomer in the article is named CPDT-BT, but it consists of two BT units and therefore the abbreviation used in the remainder of the text for this molecule is CPDT-BBT.

JACS
JOURNAL OF THE AMERICAN CHEMICAL SOCIETY

Article

pubs.acs.org/JACS

Charge Photogeneration in Donor−Acceptor Conjugated Materials: Influence of Excess Excitation Energy and Chain Length

Raphael Tautz,[†] Enrico Da Como,*[,‡] Christian Wiebeler,[§] Giancarlo Soavi,[∥] Ines Dumsch,[⊥] Nils Fröhlich,[⊥] Giulia Grancini,[#] Sybille Allard,[⊥] Ullrich Scherf,[⊥] Giulio Cerullo,[∥] Stefan Schumacher,[§] and Jochen Feldmann[†]

[†]Photonics and Optoelectronics Group, Department of Physics and CeNS, Ludwig-Maximilians-Universität München, Amalienstr. 54, 80799 Munich, Germany

[‡]Department of Physics, University of Bath, Claverton Down, Bath BA2 7AY, United Kingdom

[§]Physics Department and Center for Optoelectronics and Photonics Paderborn (CeOPP), Universität Paderborn, Warburger Strasse 100, 33098 Paderborn, Germany

[∥]IFN-CNR, Dipartimento di Fisica, Politecnico di Milano, Piazza L. da Vinci 32, 20133 Milano, Italy

[⊥]Macromolecular Chemistry Group and Institute for Polymer Technology, Bergische Universität Wuppertal, Gaussstr. 20, 42119 Wuppertal, Germany

[#]Center for Nano Science and Technology@PoliMi, Istituto Italiano di Tecnologia, Via Giovanni Pascoli 70/3, 20133 Milano, Italy

Supporting Information

ABSTRACT: We investigate the role of excess excitation energy on the nature of photoexcitations in donor−acceptor π-conjugated materials. We compare the polymer poly(2,6-(4,4-bis(2-ethylhexyl)-4H-cyclopenta[1,2-*b*;3,4-*b*′]dithiophene)-4,7-benzo[2,1,3]thiadiazole) (PCPDTBT) and a short oligomer with identical constituents at different excitation wavelengths, from the near-infrared up to the ultraviolet spectral region. Ultrafast spectroscopic measurements clearly show an increased polaron pair yield for higher excess energies directly after photoexcitation when compared to the exciton population. This effect, already observable in the polymer, is even more pronounced for the shorter oligomer. Supported by quantum chemical simulations, we show that excitation in high-energy states generates electron and hole wave functions with reduced overlap, which likely act as precursors for the polaron pairs. Interestingly, in the oligomer we observe a lifetime of polaron pairs which is one order of magnitude longer. We suggest that this behavior results from the intermolecular nature of polaron pairs in oligomers. The study excludes the presence of carrier multiplication in these materials and highlights new aspects in the photophysics of donor−acceptor small molecules when compared to polymers. The former are identified as promising materials for efficient organic photovoltaics.

1. INTRODUCTION

The photogeneration of charge carriers in organic semiconducting materials remains a fascinating topic which involves several studies spanning more than two decades of research.[1−15] While being of fundamental relevance, it is also a topic of interest for the application of these materials in photovoltaics.[16−18] The general question of what are the primary photoexcitations in organic semiconductors cannot be answered without a detailed study of the molecular structure of the materials and the excess energy with which an excited state is generated.[19−21] Experiments on both disordered conjugated polymers and well-ordered small molecule single crystals have shown that a certain amount of charge carriers is generated upon photoexcitation.[22,23] However, how this occurs and to what extent is sometimes very difficult to address in a reliable and accurate way.

The initial picture that the primary photoexcitations in disordered conjugated polymers are free polarons has been disproved by a number of ultrafast spectroscopy experiments,[3,24] clearly pointing out that strongly bound Frenkel excitons are first generated as the majority of photoexcitations. Several experiments based on pump−probe spectroscopy in the visible, infrared, and terahertz spectral range have confirmed this picture.[8,25,26] In parallel with these studies there has been a growing interest in the detection and identification of loosely bound charge carrier pairs or polaron pairs.[6,27,28] These are believed to be the secondary species generated upon light absorption, since the low-dielectric constant of organic materials does not allow for charges to escape from the mutual Coulomb attraction even at room temperature.[29,30] The interest in polaron pairs recently has risen again, because of the application of conjugated polymers in bulk-heterojunction photovoltaics. Since polaron pairs exhibit a lower binding energy with respect to Frenkel excitons,[31] they might split into free polarons by exploiting heterojunctions with smaller energy offsets. This represents a substantial advantage in optimizing the available photovoltage in solar cells.[32]

Recently, a new class of π-conjugated semiconducting materials has been introduced exhibiting unique performances

Received: September 25, 2012
Published: February 25, 2013

   dx.doi.org/10.1021/ja309252a | J. Am. Chem. Soc. 2013, 135, 4282−4290

in photovoltaic applications and in bipolar charge transport.[33−35] Their advantageous properties originate in the molecular structure, which can be tailored to provide the desired optoelectronic properties.[17,34,36] In these materials, two moieties with different electron affinity alternate along the molecular backbone, and the electronic coupling between them generates new electronic states, resulting in a narrow optical bandgap compared to widely used homopolymers and consequently better absorption in the red and near-infrared (NIR). Furthermore, our recent studies,[17] and from others,[37−39] showed that their chemical structure favors the formation of weakly bound polaron pairs, in absence of fullerenes or other electron-accepting compounds.

Two important classes of donor−acceptor copolymer have emerged with outstanding performances in photovoltaic blends: poly(thienothiophene benzodithiophene)[34] copolymers (PTB-type) and poly(cyclopentadithiophene benzothiadiazole)[40] copolymers (PCPDTBT-type). Ultrafast generation of polaron pairs has been reported for both systems, even in the absence of fullerene acceptors.[37,39] By performing a femtosecond absorption study in the infrared spectral range for a series of PCPDTBT copolymers, we have recently quantified the overall amount of polaron pairs formed from the initial photoexcitations.[17] Remarkably, this amount can be of the order of 24% and shows a strong dependence on the chemical structure of the polymer and the on-chain topology, i.e., the separation between the donor and acceptor moieties. These findings, together with the recent interest in donor−acceptor small-molecule-based organic photovoltaics,[41,42] prompted us to compare the photogeneration of charges in PCPDTBT and the respective oligomer.

Here, we present broadband femtosecond absorption spectroscopy of the polymer PCPDTBT and the oligomer CPDTBT. The broadband probe light allows us to monitor several excited species, excitons, and polaron pairs and to perform relative comparisons on their population. We address the role of photoexcitation excess energy in determining the nature of the primarily generated species, showing that a larger fraction results in polaron pairs as the excitation wavelength is tuned toward the blue part of the absorption spectrum. Supported by quantum chemical calculations, we show that excitation in high-energy states generates electron and hole wave functions with reduced overlap, which likely act as precursors for polaron pairs. Interestingly, we observe that the recombination lifetime of polaron pairs in the oligomer is 1 order of magnitude longer than the recombination lifetime in the polymer, suggesting that the oligomers and, in general, small-molecule donor−acceptor materials are systems capable of generating weakly bound long-lived polaron pairs that can be separated at suitable heterojunctions in solar cells.

2. EXPERIMENTAL AND COMPUTATIONAL METHODS

2.1. Material Synthesis. Reagents and dry solvents were purchased from Aldrich, ABCR Chemicals, or VWR International and were used without further purification. ^{1}H and ^{13}C NMR spectra were recorded on a Bruker Avance 400, chemical shifts are given in ppm. UV−vis and photoluminescence (PL) spectra were recorded with a Jasco V-670 and a Varian Cary Eclipse, respectively. Molecular weights of the polymer were determined by gel permeation chromatography analysis with polystyrene calibration. For mass spectrometry, a Fisons Instruments Sectorfield mass spectrometer VG instrument ZAB 2-SE-FDP at the MPI for Polymer Research (Mainz, Germany) was used.

PCPDTBT and CPDTBT are both generated in Stille-type cross-coupling reactions. The polymer PCPDTBT (M_n = 19 000 g/mol, M_w = 26 000 g/mol) was synthesized from 4,7-dibromobenzo[2,1,3]-thiadiazole and 2,6-bis(tributylstannyl)-4,4-bis(2-ethylhexyl)-4H-cyclopenta[2,1-*b*:3,4-*b*′]dithiophene according to a published procedure.[43] The PCPDTBT sample of this study shows long-wavelength absorption maxima at 730 and 747 nm in chloroform solution and as thin film, respectively; the solution emission maximum is observed at 786 nm (excitation wavelength 400 nm). The average number of repeat units in the polymer is 35 and 48 based on M_n and M_w estimations, respectively. 4-Bromo-7-methylbenzo[2,1,3]thiadiazole was prepared as described in literature.[44,45] The Stille-type cross coupling of 4-bromo-7-methylbenzo[2,1,3]thiadiazole (472 mg, 2.06 mmol) and 2,6-bis(tributylstannyl)-4,4-bis(2-ethylhexyl)-4H-cyclopenta[2,1-*b*:3,4-*b*′]dithiophene (1.01 g, 1.03 mmol) with Pd-$(PPh_3)_2Cl_2$ (11 mg, 15.45 μmol) as catalyst was carried out in dry toluene/THF (4/1, 50 mL) for 12 h under reflux. After purification (column chromatography, silica, *n*-hexane/toluene 1/1), the oligomer CPDTBT was obtained as a red solid. Yield: 703 mg (1.01 mmol, 98%). ^{1}H NMR ($C_2D_2Cl_4$, 400 MHz, 295 K): 0.58−0.65 (m, 12H), 0.88−1.07 (m, 18H), 1.94−2.04 (m, 4H), 2.72 (s, 6H), 7.34−7.38 (d, 7.4 Hz, 2H), 7.71−7.75 (m, 2H), 7.92−7.97 (m, 2H). ^{13}C NMR ($C_2D_2Cl_4$, 100 MHz, 295 K): 10.9, 14.3, 18.1, 23.0, 27.6, 28.6 34.4, 35.3, 43.0, 54.1, 122.2, 124.2, 126.1, 128.6, 129.5, 138.5, 139.8, 152.0, 156.0, 158.8. MS(FD) m/z = 698.3. UV−vis ($CHCl_3$): λ_{max} [nm] = 312, 371, 514. PL (λ_{ex} = 510 nm, $CHCl_3$): $\lambda_{em,max}$ [nm] = 658.

2.2. Sample Preparation. Pristine film samples of all studied materials were prepared from solution. The polymers and the oligomer have been dissolved in toluene (Chromasolv, Sigma-Aldrich) with concentrations of 10 and 20 mg/mL. To ensure good solubility, the solutions were stirred for several hours on a heating plate at 70 °C. The film samples have been prepared on microscope glass substrates by spin coating a volume of 80 μL at a speed of 1800 rpm for 2 min resulting in thin and homogeneous films with optical densities between 0.1 and 0.6 and a thickness between 50 and 150 nm. To prevent any oxidation or adsorption of water of the film samples, all steps were done in nitrogen atmosphere. Final encapsulation with thin microscope cover glass slides (about 100 μm thickness) using a vacuum glue (TORR SEAL, Thorlabs) allowed us to conduct our optical measurements in laboratory atmosphere without using vacuum to avoid photo-oxidation or other degradation phenomena.

Spectroscopy on chemically generated cations is described in details elsewhere.[17,46]

PL of all studied materials has been recorded with an automated UV−vis NIR PL spectrometer (Fluorolog, Horiba) using the same samples as measured in the ultrafast spectroscopic studies.

2.3. Ultrafast Spectroscopy. Time-resolved measurements were performed using a home-built femtosecond pump−probe setup. A Ti:sapphire regenerative amplifier (Quantronix, Integra C) was used as a laser source, delivering 100 fs pulses at a central wavelength of 800 nm with 1 mJ pulse energy at a repetition rate of 1 kHz. For the excitation pulses, a single-stage optical parametric amplifier (OPA), pumped at 400 nm, allowed the choice of a desired pump wavelength from 500 to 900 nm. UV wavelengths and wavelengths shorter than 500 nm were obtained by frequency doubling of the output of the OPA. Excitation pulse intensities were kept in the range between 5 and 50 μJ/cm^2. In order to minimize bimolecular effects, the lowest possible excitation density has been chosen, which still provides a sufficient signal-to-noise ratio for clearly resolving the spectroscopic bands of all species. White light generated with a 2 and 3 mm-thick sapphire plate was used for probing in the visible from 450 to 780 nm and in the NIR from 820 to 1100 nm, respectively. For a spectrally resolved detection of the probe light, a spectrograph and CCD array (Stresing Entwicklungsbüro) were used.[47] The temporal chirp of the stretched white light pulse was carefully taken into account during the analysis and evaluation of the obtained two-dimensional (wavelength and time) $\Delta T(\lambda,t)/T$ maps before extraction of the spectral and temporal data with a homemade software. Overall, a temporal resolution of at least 150 fs was achieved for all excitation wavelengths.

dx.doi.org/10.1021/ja309252a | J. Am. Chem. Soc. 2013, 135, 4282−4290

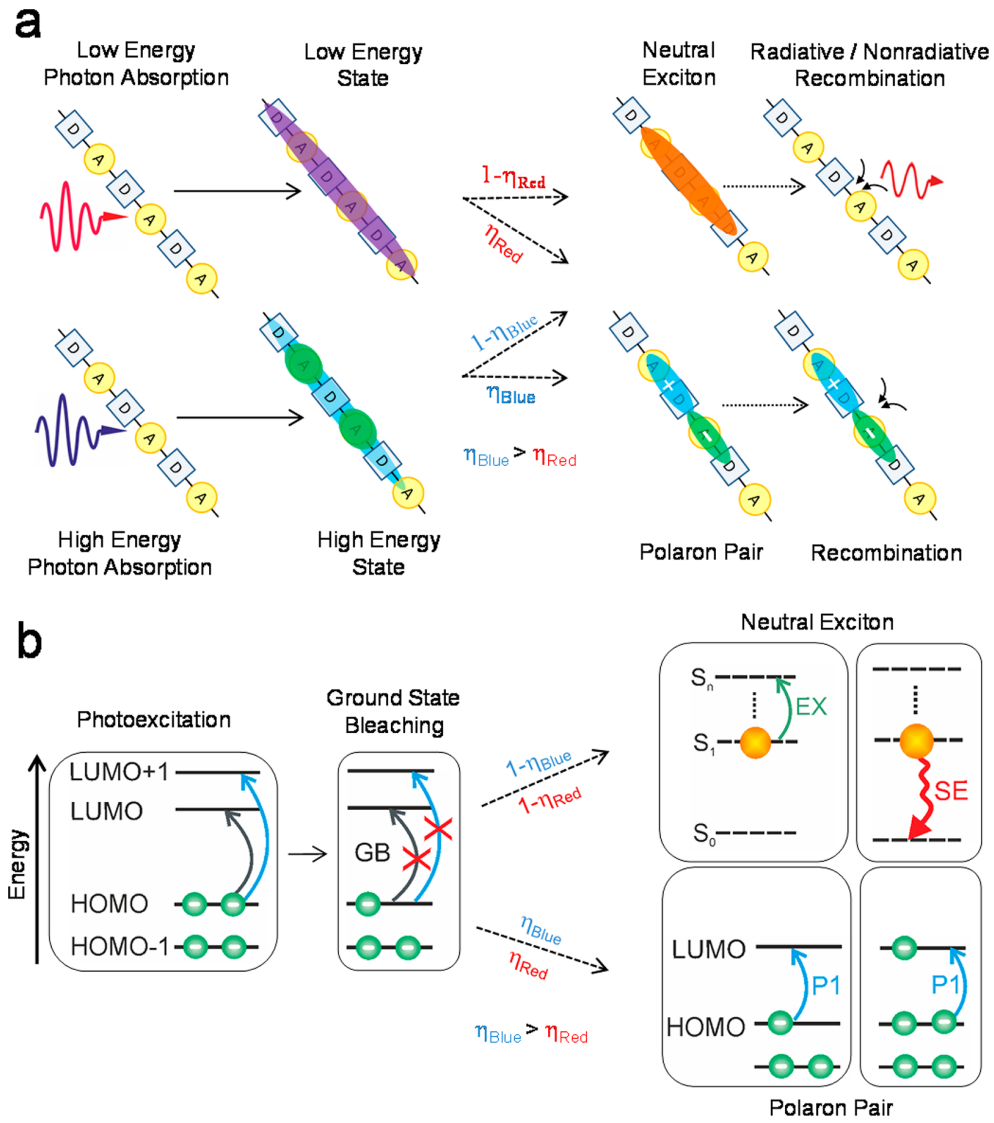

Figure 1. (a) Illustration of the photoinduced processes in donor–acceptor materials. Upon absorption of photons with high energy, states with more pronounced spatial separation of electron and hole wave functions are accessed. Upon relaxation from these excited states, pairs of charged polarons are formed with a yield η varying with excitation energy (η_{Red} and η_{Blue}) as well as neutral excitons with a yield $1 - \eta$. D and A denote donor and acceptor moieties in the molecular backbone. (b) Schematic visualization of the relevant energy levels for photoexcitation in a simplified single-particle picture. HOMO (LUMO) denotes the highest occupied (lowest unoccupied) molecular orbital and S_n marks exciton energy levels. Ground-state bleaching (GB) and the formed species, i.e., neutral excitons and polaron pairs, can be observed on an ultrafast time scale by their distinct spectroscopic signatures of excitonic absorption (EX), stimulated emission (SE), and polaronic absorption (P1), respectively.

2.4. Theoretical Methods. All calculations are based on density functional theory (DFT) and linear response time-dependent DFT (TD-DFT). The Gaussian09 program suite[48] was used, and all results presented were obtained with the Coulomb-attenuating method Becke three-parameter Lee–Yang–Parr hybrid functional (CAM-B3LYP) and 6-31G* basis set. Orbitals were visualized using GaussView 5 (ref 49). To model the PCPDTBT polymer as closely as possible, calculations were performed on a long but finite-length oligomer consisting of six units as shown in Figure 4; alkyl side chains that are largely uninvolved in the electronic processes studied here were replaced by methyl groups to reduce the computational cost. For CPDTBT, the calculations were done for the molecules used in the experiments including side chains. These have been removed from the visualizations in Figure 4 for clarity. For CPDTBT no symmetry constraints were imposed. Calculations for PCPDTBT were done for C_{2V} symmetry of the molecules, as previous tests show[46] that spectra and electronic states are very similar when considering a C_1 symmetry only. We first optimized the molecular geometry in the electronic ground state and then calculated the lowest electronic singlet excitations. A homogeneous broadening of 100 meV was applied to plot the electronic spectra. Natural transition orbitals (NTOs) were computed separately for the transitions of interest. In the donor–acceptor copolymers studied here, significant charge separation occurs in ground and excited states. To account also for long-range contributions to the electronic exchange interaction of these charges, we used the long-range corrected CAM-B3LYP functional.[46,50,51] Good convergence of the results was obtained with the 6-31G* basis set, which was used in all calculations presented here.

3. RESULTS AND DISCUSSION

3.1. Excess Energy Dependence of Polaron Pair Formation. In Figure 1 we provide a qualitative physical picture for the different steps in the photoinduced polaron pair

dx.doi.org/10.1021/ja309252a | J. Am. Chem. Soc. 2013, 135, 4282–4290

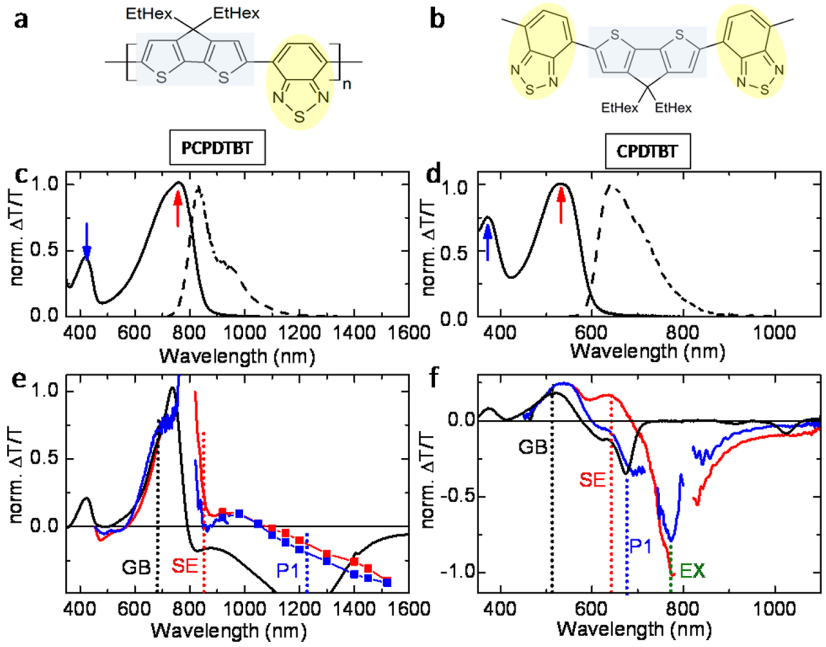

Figure 2. Chemical structures of (a) PCPDTBT and (b) CPDTBT. Gray- and yellow-shaded parts denote the donor and acceptor moieties, respectively. (c,d) Absorption (solid line) and PL (dashed line) spectra of thin film samples. Arrows indicate wavelengths for low- (red) and high-energy (blue) photoexcitation in pump–probe experiments. (e,f) Femtosecond transient absorption spectra for long- (red) and short-wavelength (blue) excitation compared with a spectrum of chemically generated cations (black). (e,f) Vertical dotted lines indicate the spectral position for the evaluation of the temporal dynamics of GB, EX, SE, and P1.

formation occurring at different excitation wavelengths. Figure 1a illustrates the formation of an excited state after photon absorption by the chromophore. Hereby, the energy of the absorbed photons, and hence the excess energy with respect to the gap, plays a crucial role for the degree of charge separation because of relaxation through the excited states. Higher photon energies excite the molecules to high electronic states. These may have a significantly more pronounced spatial separation of the pair of charge carriers (electron and hole) than states accessible at photon energies close to the optical bandgap,[52] as further explained below for our materials. In an intuitive picture, in high excited states a reduced overlap of the electron, and hole wave function is likely to be present causing a reduced Coulomb interaction. Thus, photoexcitations bearing significant excess energy should exhibit increased polaron pair formation yields η, i.e., the ratio of polaron pairs to neutral excitons photoinduced in the system.

Unique spectral signatures of excitons and polarons can be found in each material. A schematic visualization of corresponding energy levels and accessible transitions is presented in Figure 1b. The observation of ground-state bleaching (GB) is considered as a clear indication for the photoexcitation to higher electronic states of the molecules. Different species can be distinguished by their spectral signatures, giving rise to photoinduced absorption or stimulated emission (SE). Neutral excitons can be identified by stimulated emission or by their excited-state absorption band (EX). In contrast, the formation of polarons is visible from the characteristic polaronic absorption band (P1) below the optical bandgap of the neutral molecule.[17]

3.2. Spectroscopic Study of Polaron Pair Formation for Different Excess Energies. In the following section, we discuss in detail our experimental and theoretical results, bearing in mind the qualitative picture we discussed in Figure 1. We have chosen a suitable set of materials, consisting of the copolymer PCPDTBT and the short oligomer CPDTBT. Their chemical structures are shown in Figure 2a,b, with the electron-donating cyclopentadithiophene moieties marked with a gray box and the accepting benzothiadiazole moieties highlighted with a yellow circle. Absorption and PL spectra of the respective materials are shown in Figure 2c,d. Pump–probe experiments with ≈100 fs time resolution and broadband-probe spectral range were performed on thin films of PCPDTBT and CPDTBT. Tuning of the pump wavelength allows us to excite the materials selectively in the low- and high-energy absorption bands, as indicated by red and blue arrows, respectively. In Figure 2e,f, differential transmission ($\Delta T/T$) spectra for low (red) and high (blue) excitation photon energies at 300 fs pump–probe delay are compared to a polaron absorption spectrum (black) obtained by chemical oxidation.[17,53] For better comparison, all spectra shown are normalized to their GB in a range separated from other spectral features and the pump laser wavelength. We have performed the normalization at 690 and 510 nm for the polymer and oligomer, respectively. In selecting these normalization wavelengths we have payed particular attention to maximize the overlap of the GB spectral shapes for the two excitation wavelengths, in a spectral range likely free from overlapping excited-state species, e.g., for the polymer 550–700 nm. In addition, this choice was operated after careful examination of the temporal dynamics of the GB spectra which we report in Figure S1. In particular at these normalization wavelengths, the $\Delta T/T$ spectra do not show appreciable spectral diffusion independently of the excitation wavelength and are therefore suitable to account for the density of photoexcitations induced in the sample by the pump.

dx.doi.org/10.1021/ja309252a | J. Am. Chem. Soc. 2013, 135, 4282–4290

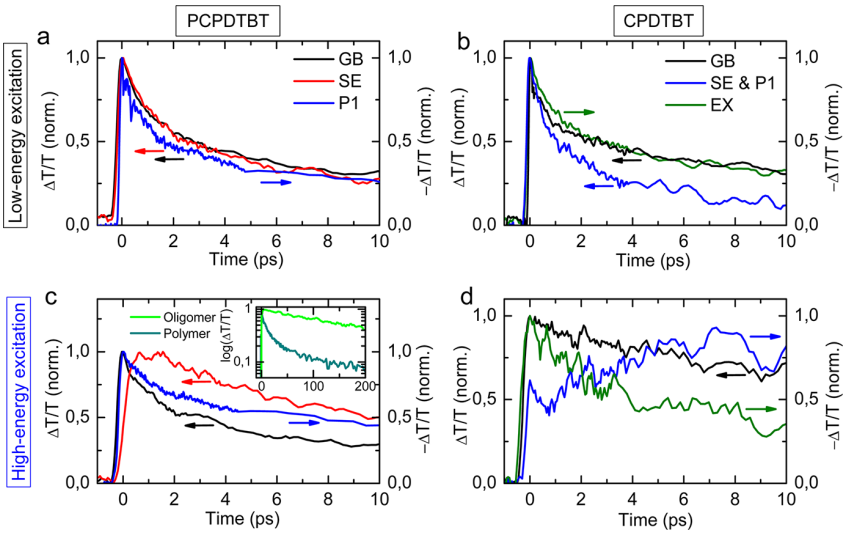

Figure 3. Ultrafast transient dynamics of GB (black), SE (red), P1 (blue), and EX (green) for long-wavelength excitation of (a) PCPDTBT (760 nm) and (b) CPDTBT (530 nm). (c,d) Dynamics for short-wavelength excitation at 400 and 370 nm are shown, respectively. For better comparison, the modulus of all normalized signals is plotted. Clear differences in the temporal dynamics between long- and short-wavelength excitation can be found for PCPDTBT in going from panels (a) to (c). Those are even more pronounced for the oligomer in panels (b) and (d). Spectral positions of respective probe wavelengths are indicated by vertical dotted lines in Figure 2e,f. The inset in panel (c) shows clearly longer decay dynamics for the polaron pair signal in the oligomer (light green) than in the polymer (dark green), both excited with excess energy.

For PCPDTBT in Figure 2e, both $\Delta T/T$ spectra upon 760 nm (red) and 400 nm (blue), as well as the chemical doping spectrum show a prominent GB from 570 up to 745 nm and a clear positive contribution peaking at 935 nm. Because of the good agreement with the spectral shape of the separately measured PL as shown in Figure 2c, an assignment of this latter contribution to stimulated emission is immediate. We note here that differences in the shape of the absorption spectrum and the GB are intrinsically connected to the dynamic nature of the GB. The GB spectrum measures the ground-state absorption blocking due to the population of excited states, which are no longer empty for an absorption process. The excited-state population evolves on a short time scale and involves potential energy surfaces which may be different from those probed in a linear absorption spectrum. At longer wavelengths up to 1100 nm the stimulated emission competes with the negative signal of the polaronic photoinduced absorption. Spectral features arising from polaron absorption range from ~800 nm and go up to 1400 nm, as seen in the spectrum of chemically generated cations; at 1100 nm polaron absorption becomes more prominent due to the vanishing stimulated emission, and the overall $\Delta T/T$ curve turns negative. Our results demonstrate the presence of photogenerated polaron pairs for both excitation wavelengths with the polaron absorption bands exhibiting different amplitudes. When the excitation is performed at short wavelength (400 nm), a less-pronounced stimulated emission and enhanced polaronic absorption are an indication for a higher polaron-to-exciton ratio, i.e., $\eta_{Blue} > \eta_{Red}$.

When looking at the $\Delta T/T$ spectrum of the oligomer CPDTBT we observe a similar pattern of spectroscopic features (Figure 2f), but in addition it exhibits photoinduced absorption at 780 nm, which does not correspond to the PL or the radical cation (polaron) spectrum and occurs for both excitation wavelengths. For this material, the larger bandgap and thus blue-shifted absorption compared to the polymer allows to access the EX, which is located at lower energy compared to the polaron absorption, ranging between 700 and 1100 nm and peaking at 775 nm. As in the case of the polymer, excitation with high-energy photons with respect to the gap leads to a higher generation yield of polaron pairs. Because of the large overlap between SE and P1 in this material, the $\Delta T/T$ completely changes in the range around 630 nm. In agreement with our interpretation of a higher polaron pair generation yield when exciting at higher energy, the EX signal is reduced since its origin is excitonic.

The decay dynamics of all spectral features described in the polymer spectrum are shown in Figure 3a,c for 760 and 400 nm excitation, respectively. The polaron pair signal shows a rapid initial decay of 1.1 ps, followed by a slow decay with a time constant of 16 ps. Previous measurements of polaron pair dynamics, based on the decay of the mid-infrared absorption band P2 (ref 17), exhibit similar recombination dynamics with a first component lifetime of 2.6 ps and a second of 16 ps. Although we tried to stay at excitation densities as low as possible, the required densities for a broadband spectral detection of all species within one measurement did not allow us to completely suppress a residual contribution of bimolecular processes. Thus the discrepancy of the first component in the P1 lifetime with respect to the value in our previous experiments is likely due to the increased laser fluence resulting in an excitation density of 5×10^{18} cm^3, this is also likely the origin of the biexponential decay dynamics with 1.1 and 18 ps in the stimulated emission. The increased laser fluence compared to our previous experiments (excitation density 7×10^{17} cm^3) may have an effect on the generation of polaron pairs, since in some materials it has been reported that high excitation densities promote polaron pair formation. We have investigated this effect for our polymers and found that the $\Delta T/T$ signal amplitude for P1 and the first time constant shows a weak dependence on laser fluence, whereas the SE and GB signals are more affected (Figure S2). Therefore, we exclude that the higher excitation densities used in the experiments presented here have a significant influence on the polaron pair generation yield.

dx.doi.org/10.1021/ja309252a | J. Am. Chem. Soc. 2013, 135, 4282−4290

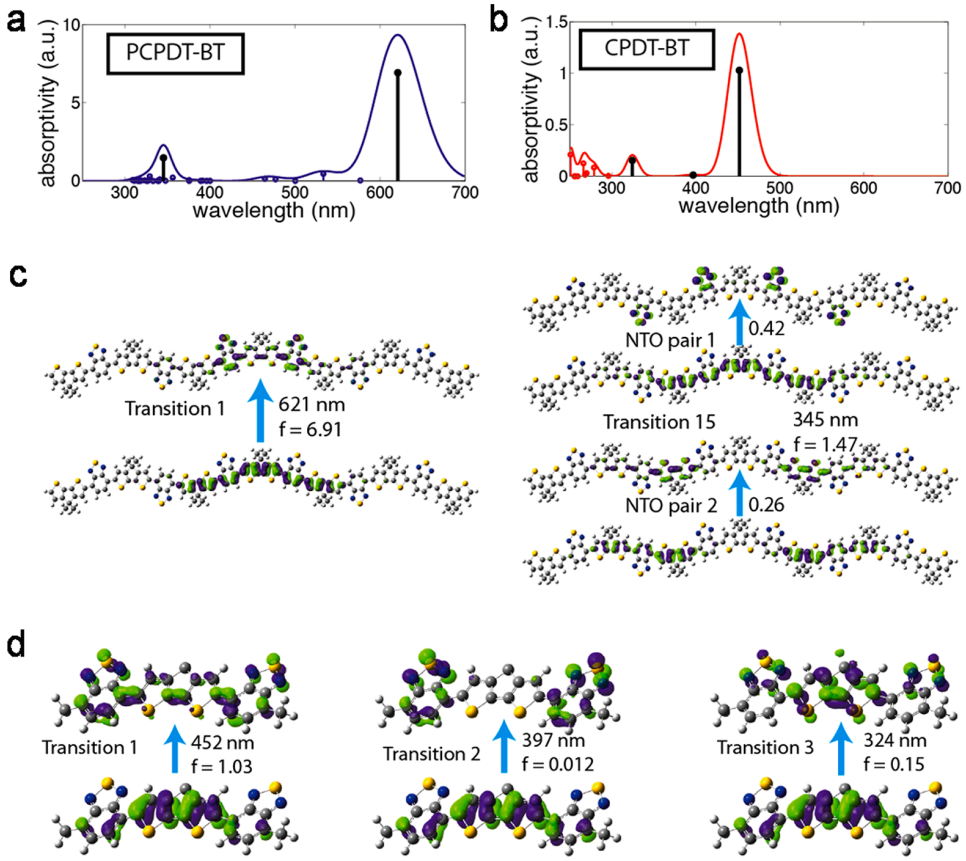

Figure 4. Calculated absorption spectra (a) and (b) and analysis of excitations in terms of natural transition orbitals (NTOs) for the copolymer PCPDTBT (c) and the oligomer CPDTBT (d). Stick spectra represent wavelength and oscillator strength of each transition in (a) and (b); those transitions used for the NTO analysis are shown in black. For both copolymer in (a) and oligomer in (b), only one transition with large oscillator strength contributes to the long-wavelength absorption peak. The corresponding pairs of NTOs are depicted in panels (c) and (d), respectively, showing a delocalized nature and direct spatial overlap of the wave functions. In contrast, transitions corresponding to the absorption band at shorter wavelength exhibit a much lower oscillator strength (denoted as *f*).

The GB has contributions from both polaron pairs and excitons since it measures the depletion of the ground-state absorption with no distinction on whether this originates from neutral or charged excited species. Interestingly, it has very similar decay dynamics to the stimulated emission and confirms the fact that excitons are formed predominantly when the polymer is excited at 760 nm. At short wavelength excitation, the fast initial decay component of the polaron pair signal is less pronounced, as shown in Figure 3c. In this case, the GB decays with a fast time constant of 1.2 ps and a second longer decay of 16 ps. These dynamics are comparable to that of polaron pair absorption, which show a biexponential decay with 1.6 and 17 ps time constants. While the values of the decay times are not identical overall, this suggests that a larger contribution of polaron pairs to the bleaching signal is present. In agreement with other studies,[51] a slower rise time can be observed for stimulated emission due to vibrational relaxation of the hot excited state preceding photon emission. Measurements on another donor–acceptor copolymers with a similar chemical structure (Figure S3) show qualitatively the same effect of a decreasing stimulated emission and increasing polaronic absorption for larger excess excitation photon energies. Excitation energies exceeding the optical bandgap twice did not show any indication of multiexciton or multipolaron pair formation, as known for other organic materials like pentacene[54−56] or carbon nanotubes.[57] This result confirms what has been recently observed by Bange et al. on ladder-type polymers.[58]

The temporal dynamics for the oligomer is shown in Figure 3b,d and confirms the hypothesis that excitation at higher energy leads to a more pronounced formation of polaron pairs. While in the long-wavelength excitation case the GB decay follows almost exactly the dynamics of the EX band (Figure 3b), it appears to be clearly slower when excited at higher energy (Figure 3d) and more similar to the P1 dynamics. We believe that a larger contribution of longer living polaron pairs is the reason for this prominent difference. When excited at 530 nm, the temporal dynamics of the spectral region from 600 to about 700 nm, where SE and P1 absorption are overlapping, is clearly dominated by SE. Although originating from the same species, i.e. excitons, the SE shows faster decay dynamics compared to EX. Most likely this occurs due to a spectrally overlapping polaron absorption signal. However, the most interesting results are obtained when molecules are excited at 370 nm. Here, a long-lived signal with negative amplitude due to polaron absorption follows the GB dynamics and, according to our assignment, is another strong indication that polaron pairs are the mainly formed species. What seems to be a slow buildup of polaron pair absorption can be explained as decay of SE having opposite sign. Indeed measurements of the P1

dx.doi.org/10.1021/ja309252a | *J. Am. Chem. Soc.* 2013, 135, 4282−4290

dynamics further into the red part of the spectrum at 700 nm instead of 640 nm (as in Figure 3d) do not exhibit such a rise on a picosecond time scale (Figure S4).

In summary, the materials show a higher polaron pair yield η for excitation with higher photon energies compared to excitations close to the optical bandgap, i.e., $\eta_{Blue} > \eta_{Red}$. This effect is present for the donor−acceptor copolymer PCPDTBT (and a similar polymer reported in Figure.S3) and is found to be significantly pronounced for the shorter oligomer CPDTBT. Interestingly, as shown in the inset in Figure 3c, the lifetime of the polaron pairs excited at high energy in the oligomer is 164 ps, an order of magnitude larger than the long component in the lifetime of the same species in the polymer, which is 16 ps.

3.3. Wave Function Localization of Photoexcited States. To obtain a deeper understanding and provide a more comprehensive explanation on the photon energy dependence of the polaron pair generation process, we investigated by quantum chemical modeling the optical transitions in PCPDTBT and CPDTBT (see Experimental and Computational Methods section for details). Figure 4a,b shows calculated linear absorption spectra. Comparing these computed spectra with experimental absorption spectra in Figure 2c,d, we note a consistent overall shift of calculated transitions to shorter wavelengths. More importantly, however, relative positions of transitions in the spectrum and relative oscillator strengths of the different peaks are well represented by the calculations. Figure 4c,d provides NTOs for the relevant optical transitions in PCPDTBT and CPDTBT. In the case of the polymer, excitation with low photon energy results in a transition (Figure 4c, transition 1) where both electron and hole wave function are delocalized over several benzothiadiazole (BT) and dithiophene units in the center of the chromophore. The resulting large wave function overlap and the common center of mass lead to a strong Coulomb interaction and explain the favored formation of neutral excitons with respect to spatially separated polaron pairs. The wave function distribution appears different, when electron and hole are excited with significant excess energy, as shown by the dominant NTO pairs 1 and 2 of transition 15 in Figure 4c (CI coefficients 0.42 and 0.26). This transition carries the main oscillator strength leading to the high-energy absorption band in the polymer, and the corresponding dominant NTOs clearly show its significant charge-transfer character. In the dominant contributions, the electron wave function is mostly localized on the BT units, whereas the hole wave function is delocalized in nature. The resulting spatial separation of electron and hole wave function leads to a reduced Coulomb interaction and consequently favors the formation of a weakly bound polaron pair. We note that we have found almost identical NTOs to those reported in Figure 4 for transitions calculated in the equilibrium geometries of the corresponding excited states.

An even more pronounced difference can be found for CPDTBT, as shown in panel Figure 4d. The long wavelength arises from a transition that is delocalized over the entire oligomer backbone. Both electron and hole wave functions are calculated to be spread out with their center of mass located in the middle of the molecule. Transition 3 in Figure 4d is responsible for the higher-energy absorption band in the oligomer and is accessible at high photon energy. This transition also appears to be very delocalized in nature with significant spatial overlap of electron and hole wave functions. However, following excitation of this transition, we assume that the system undergoes ultrafast relaxation through the manifold of excited states.[51] During this relaxation the system may transit through another excited state which is optically almost dark but has very pronounced *charge-transfer character* according to the involved NTOs shown in Figure 4d. In this state, the overlap between electron and hole wave functions is strongly reduced which could be the explanation for the increased polaron formation yield found at higher excitation energies for this system. The pronounced *charge-transfer character* of the excited states at higher energies explains also the lower oscillator strength for those transitions with a lower wave function overlap of initial and final state.[59] This can be seen in the measured (Figure 2c,d) and calculated (Figure 4a,b) absorption spectra showing lower absorption in the high-energy peaks. The corresponding oscillator strengths for the relevant transitions are given in Figure 4c,d.

We assume that topological restrictions due to a limited chain length of the oligomer further promote the localization of the electron wave function. This together with the longer lifetime of the polaron pairs in the oligomer clearly points toward dynamics involving intermolecular processes. In the oligomeric sample, it is likely that a close spacing between donor and acceptor units belonging to nearest-neighbor molecules is present in three dimensions. In case of favorable packing and orientation, this may favor the formation of stabilized long-lived polaron pairs, as was observed in copolymer heterojunctions.[60] While these aspects are important in trying to establish a quantitative comparison between the polymer and the oligomer, the experimental evidence for a higher polaron pair yield upon excitation with high photon energy can be rationalized by the intramolecular wave function characteristics shown in Figure 4. Simulations involving intermolecular polaronic states, for example in dimers, are likely to provide more information on the dynamics of polarons in both systems but involve a large number of degrees of freedom connected to the crystallinity and, in general, to the structure of the two materials. Such studies will be reported elsewhere. PCPDTBT is a semicrystalline polymer,[61] and we have indications that CPDTBT forms polycrystalline films, thus the two material systems have structural similarities. CPDTBT is a rather new compound, and a full structural characterization has not been carried out. Certainly molecular packing and crystallinity may be involved in the polaron pair recombination process, less likely in the generation which starts from the intramolecular wave function shown in Figure 4, since those are mainly responsible for light absorption.

4. CONCLUSIONS

In conclusion, we have studied the influence of excess excitation energy on charge photogeneration in organic donor−acceptor materials with different chain length. Both materials studied, i.e., PCPDTBT and CPDTBT, show consistently higher polaron pair yields for shorter excitation wavelengths together with a reduced occurrence of stimulated emission. With broadband ultrafast pump−probe spectroscopy, we demonstrated a significantly higher polaron-to-exciton formation ratio η for high-energy photons already within the temporal resolution of the setup of 150 fs ($\eta_{Blue} > \eta_{Red}$). This effect is observable in PCPDTBT and more pronounced for a short oligomer with the same chemical structure, CPDTBT.

We explain the higher polaron pair formation yield η observed at shorter wavelengths with the more pronounced initial charge-transfer character of the higher-lying excited states absorbing light, likely caused by the variation of the molecular

dx.doi.org/10.1021/ja309252a | J. Am. Chem. Soc. 2013, 135, 4282−4290

on-chain energy landscape present in these materials. This interpretation is supported by our quantum chemical calculations. During the relaxation through the excited states in the oligomer CPDTBT, pronounced localization of the electron at the BT acceptor moieties occurs when excited at 370 nm. In contrast, the excitations stay delocalized over the entire molecule for 530 nm excitation. A similar effect occurs in PCPDTBT, although less pronounced. The reduced overlap between electron and hole leads to a decreased Coulomb attraction and a lower binding energy. We therefore conclude that a more pronounced charge separation in the initial excitations dynamically favors polaron pair formation instead of relaxation into a strongly bound and emissive Frenkel exciton.

The finding of a high polaron pair formation yield over the high energy part of the absorption spectrum indicates that an optimization of materials in terms of higher yields might be interesting for more efficient organic solar cells. Due to a lower binding energy, the extraction of polaron pairs might be favorable in terms of a reduced voltage loss for their separation compared to strongly bound Frenkel excitons. We believe that the knowledge gained about the nature of higher photoexcitations and the influence of the molecular size is crucial for reaching this goal. Interestingly, we report an increase by 1 order of magnitude in the lifetime of polaron pairs in the oligomer, which can represent an intrinsic advantage for organic photovoltaics. The increased lifetime may be related to a different crystalline, solid-state packing of the small molecules if compared to the semicrystalline polymer PCPDTBT; further detailed structural investigations are required to address this important difference.

■ ASSOCIATED CONTENT

Ⓢ Supporting Information

Transient absorption spectra at several pump−probe delay times, transients at different excitation fluencies, photophysics of polymer PCPDT2TBT, SE transients of CPDTBT. This material is available free of charge via the Internet at http://pubs.acs.org.

■ AUTHOR INFORMATION

Corresponding Author

edc25@bath.ac.uk

Notes

The authors declare no competing financial interest.

■ ACKNOWLEDGMENTS

Financial support by the DFG for funding through the SPP1355 "Fundamental processes in organic photovoltaics" and the Nanosystems Initiative Munich (NIM) as well as by the Bavarian Ministry for Science through the initiative "Solar Technologies Go Hybrid" (SolTech) is gratefully acknowledged. R.T., E.D.C., G.S., and G.C. are grateful for the financial support by the European Community Access to Research Infrastructure Action, contract RII3-CT-2003-506350 (Centre for Ultrafast Science and Biomedical Optics, LASERLAB-EUROPE). G.C. acknowledges partial support by the PRIN Project 2008 JKBBK4 "Tracking ultrafast photoinduced intra- and intermolecular processes in natural and artificial photosensors". The Paderborn group acknowledges financial support from the DFG (GRK 1464) and a grant for computing time at PC^2 Paderborn Center for Parallel Computing. We are grateful for open discussions with L. Luer, D. Polli, and M. T. Carlson.

■ REFERENCES

(1) Vardeny, Z.; Ehrenfreund, E.; Brafman, O.; Nowak, M.; Schaffer, H.; Heeger, A. J.; Wudl, F. *Phys. Rev. Lett.* **1986**, *56*, 671−674.
(2) Kersting, R.; Lemmer, U.; Mahrt, R. F.; Leo, K.; Kurz, H.; Bässler, H.; Göbel, E. O. *Phys. Rev. Lett.* **1993**, *70*, 3820−3823.
(3) Kersting, R.; Lemmer, U.; Deussen, M.; Bakker, H. J.; Mahrt, R. F.; Kurz, H.; Arkhipov, V. I.; Bässler, H.; Göbel, E. O. *Phys. Rev. Lett.* **1994**, *73*, 1440−1443.
(4) Barth, S.; Bässler, H. *Phys. Rev. Lett.* **1997**, *79*, 4445−4448.
(5) Hoofman, R.; de Haas, M. P.; Siebbeles, L. D. A.; Warman, J. M. *Nature* **1998**, *392*, 54−56.
(6) Schweitzer, B.; Arkhipov, V. I.; Bässler, H. *Chem. Phys. Lett.* **1999**, *304*, 365−370.
(7) Miranda, P. B.; Moses, D.; Heeger, A. J. *Phys. Rev. B* **2001**, *64*, 4.
(8) Hendry, E.; Schins, J. M.; Candeias, L. P.; Siebbeles, L. D. A.; Bonn, M. *Phys. Rev. Lett.* **2004**, *92*, 196601.
(9) Bässler, H. *Nat. Phys.* **2006**, *2*, 15−16.
(10) Virgili, T.; Marinotto, D.; Manzoni, C.; Cerullo, G.; Lanzani, G. *Phys. Rev. Lett.* **2005**, *94*, 117402.
(11) Scheblykin, I. G.; Yartsev, A.; Pullerits, T.; Gulbinas, V.; Sundström, V. *J. Phys. Chem. B* **2007**, *111*, 6303−6321.
(12) Banerji, N.; Cowan, S.; Leclerc, M.; Vauthey, E.; Heeger, A. J. *J. Am. Chem. Soc.* **2010**, *132*, 17459−17470.
(13) Deschler, F.; Da Como, E.; Limmer, T.; Tautz, R.; Godde, T.; Bayer, M.; von Hauff, E.; Yilmaz, S.; Allard, S.; Scherf, U.; Feldmann, J. *Phys. Rev. Lett.* **2011**, *107*, 127402.
(14) Grancini, G.; Martino, N.; Antognazza, M. R.; Celebrano, M.; Egelhaaf, H. J.; Lanzani, G. *J. Phys. Chem. C* **2012**, *116*, 9838−9844.
(15) Etzold, F.; Howard, I. A.; Forler, N.; Cho, D. M.; Meister, M.; Mangold, H.; Shu, J.; Hansen, M. R.; Mullen, K.; Laquai, F. *J. Am. Chem. Soc.* **2012**, *134*, 10569−10583.
(16) Sheng, C. X.; Tong, M.; Singh, S.; Vardeny, Z. V. *Phys. Rev. B* **2007**, *75*, 085206.
(17) Tautz, R.; Da Como, E.; Limmer, T.; Feldmann, J.; Egelhaaf, H.-J.; von Hauff, E.; Lemaur, V.; Beljonne, D.; Yilmaz, S.; Dumsch, I.; Allard, S.; Scherf, U. *Nat. Commun.* **2012**, *3*, 970.
(18) Rolczynski, B. S.; Szarko, J. M.; Son, H. J.; Liang, Y. Y.; Yu, L. P.; Chen, L. X. *J. Am. Chem. Soc.* **2012**, *134*, 4142−4152.
(19) Arkhipov, V. I.; Emelianova, E. V.; Bassler, H. *Phys. Rev. Lett.* **1999**, *82*, 1321−1324.
(20) Gadermaier, C.; Cerullo, G.; Sansone, G.; Leising, G.; Scherf, U.; Lanzani, G. *Phys. Rev. Lett.* **2002**, *89*, 4.
(21) Gao, J.; Hegmann, F. A. *Appl. Phys. Lett.* **2008**, *93*, 3.
(22) Hegmann, F. A.; Tykwinski, R. R.; Lui, K. P. H.; Bullock, J. E.; Anthony, J. E. *Phys. Rev. Lett.* **2002**, *89*, 4.
(23) Paquin, F.; Latini, G.; Sakowicz, M.; Karsenti, P. L.; Wang, L. J.; Beljonne, D.; Stingelin, N.; Silva, C. *Phys. Rev. Lett.* **2011**, *106*, 197401.
(24) Brabec, C. J.; Zerza, G.; Cerullo, G.; De Silvestri, S.; Luzzati, S.; Hummelen, J. C.; Sariciftci, S. *Chem. Phys. Lett.* **2001**, *340*, 232−236.
(25) Aryanpour, K.; Sheng, C. X.; Olejnik, E.; Pandit, B.; Psiachos, D.; Mazumdar, S.; Vardeny, Z. V. *Phys. Rev. B* **2011**, *83*, 5.
(26) Herrmann, D.; Niesar, S.; Scharsich, C.; Kohler, A.; Stutzmann, M.; Riedle, E. *J. Am. Chem. Soc.* **2011**, *133*, 18220−18233.
(27) Yan, M.; Rothberg, L. J.; Papadimitrakopoulos, F.; Galvin, M. E.; Miller, T. M. *Phys. Rev. Lett.* **1994**, *72*, 1104−1107.
(28) Mizes, H. A.; Conwell, E. M. *Phys. Rev. B* **1994**, *50*, 11243−11246.
(29) Hertel, D.; Bässler, H. *ChemPhysChem* **2008**, *9*, 666−688.
(30) Wang, Z. D.; Mazumdar, S.; Shukla, A. *Phys. Rev. B* **2008**, *78*, 235109.
(31) Hallermann, M.; Haneder, S.; Da Como, E. *Appl. Phys. Lett.* **2008**, *93*, 053307.
(32) Gong, X.; Tong, M. H.; Brunetti, F. G.; Seo, J.; Sun, Y. M.; Moses, D.; Wudl, F.; Heeger, A. J. *Adv. Mater.* **2011**, *23*, 2272−2277.
(33) Beaujuge, P. M.; Tsao, H. N.; Hansen, M. R.; Amb, C. M.; Risko, C.; Subbiah, J.; Choudhury, K. R.; Mavrinskiy, A.; Pisula, W.; Bredas, J. L.; So, F.; Mullen, K.; Reynods, J. R. *J. Am. Chem. Soc.* **2012**, *134*, 8944−8957.

(34) Chen, H. Y.; Hou, J. H.; Zhang, S. Q.; Liang, Y. Y.; Yang, G. W.; Yang, Y.; Yu, L. P.; Wu, Y.; Li, G. *Nat. Photonics* **2009**, *3*, 649−653.
(35) Svensson, M.; Zhang, F. L.; Veenstra, S. C.; Verhees, W. J. H.; Hummelen, J. C.; Kroon, J. M.; Inganas, O.; Andersson, M. R. *Adv. Mater.* **2003**, *15*, 988−991.
(36) Boudreault, P. L. T.; Najari, A.; Leclerc, M. *Chem. Mater.* **2011**, *23*, 456−469.
(37) Carsten, B.; Szarko, J. M.; Son, H. J.; Wang, W.; Lu, L. Y.; He, F.; Rolczynski, B. S.; Lou, S. J.; Chen, L. X.; Yu, L. P. *J. Am. Chem. Soc.* **2011**, *133*, 20468−20475.
(38) De, S.; Pascher, T.; Maiti, M.; Jespersen, K. G.; Kesti, T.; Zhang, F. L.; Inganas, O.; Yartsev, A.; Sundstrom, V. *J. Am. Chem. Soc.* **2007**, *129*, 8466−8472.
(39) Soci, C.; Hwang, I. W.; Moses, D.; Zhu, Z.; Waller, D.; Gaudiana, R.; Brabec, C. J.; Heeger, A. J. *Adv. Funct. Mater.* **2007**, *17*, 632−636.
(40) Muhlbacher, D.; Scharber, M.; Morana, M.; Zhu, Z. G.; Waller, D.; Gaudiana, R.; Brabec, C. *Adv. Mater.* **2006**, *18*, 2884−2889.
(41) Lin, Y. Z.; Li, Y. F.; Zhan, X. W. *Chem. Soc. Rev.* **2012**, *41*, 4245−4272.
(42) Walker, B.; Kim, C.; Nguyen, T. Q. *Chem. Mater.* **2011**, *23*, 470−482.
(43) Zhu, Z.; Waller, D.; Gaudiana, R.; Morana, M.; Muhlbacher, D.; Scharber, M.; Brabec, C. *Macromolecules* **2007**, *40*, 1981−1986.
(44) Vanelle, P.; Liegeois, C. T.; Meuche, J.; Maldonado, J.; Crozet, M. P. *Heterocycles* **1997**, *45*, 955−962.
(45) Jorgensen, M.; Krebs, F. C. *J. Org. Chem.* **2005**, *70*, 6004−6017.
(46) Wiebeler, C.; Tautz, R.; Feldmann, J.; von Hauff, E.; Da Como, E.; Schumacher, S. *J. Phys. Chem. B* **2013**, DOI: 10.1021/jp3084869.
(47) Polli, D.; Luer, L.; Cerullo, G. *Rev. Scien. Instrum.* **2007**, *78*, 103108.
(48) Frisch, M. J.; Trucks, G. W.; Scuseria, G. E.; Robb, M. A.; Cheeseman, J. R.; Scalmani, G.; Barone, V.; Mennucci, B.; Petersson, G. A.; Nakatsuji, H.; Caricato, M.; Li, X.; Hratchian, H. P.; Izmaylov, A. F.; Bloino, J.; Zheng, G.; Sonnenberg, J. L.; Hada, M.; Ehara, M.; Toyota, K.; Fukuda, R.; Hasegawa, J.; Ishida, M.; Nakajima, T.; Honda, Y.; Kitao, O.; Nakai, H.; Vreven, T.; Montgomery, J. A., Jr.; Peralta, J. E.; Ogliaro, F.; Bearpark, M.; Heyd, J. J.; Brothers, E.; Kudin, K. N.; Staroverov, V. N.; Kobayashi, R.; Normand, J.; Raghavachari, K.; Rendell, A.; Burant, J. C.; Iyengar, S. S.; Tomasi, J.; Cossi, M.; Rega, N.; Millam, J. M.; Klene, M.; Knox, J. E.; Cross, J. B.; Bakken, V.; Adamo, C.; Jaramillo, J.; Gomperts, R.; Stratmann, R. E.; Yazyev, O.; Austin, A. J.; Cammi, R.; Pomelli, C.; Ochterski, J. W.; Martin, R. L.; Morokuma, K.; Zakrzewski, V. G.; Voth, G. A.; Salvador, P.; Dannenberg, J. J.; Dapprich, S.; Daniels, A. D.; Farkas, Ö.; Foresman, J. B.; Ortiz, J. V.; Cioslowski, J.; Fox, D. J. *Gaussian 09*, revision B.01; Gaussian, Inc.: Wallingford, CT, 2009.
(49) Dennington, R.; Keith, T.; Millam, J. *GaussView*, Semichem Inc.: Shawnee Mission KS, 2009.
(50) Zaikowski, L.; Kaur, P.; Gelfond, C.; Selvaggio, E.; Asaoka, S.; Wu, Q.; Chen, H. C.; Takeda, N.; Cook, A. R.; Yang, A.; Rosanelli, J.; Miller, J. R. *J. Am. Chem. Soc.* **2012**, *134*, 10852−10863.
(51) Fazzi, D.; Grancini, G.; Maiuri, M.; Brida, D.; Cerullo, G.; Lanzani, G. *Phys. Chem. Chem. Phys.* **2012**, *14*, 6367−6374.
(52) Kohler, A.; dos Santos, D. A.; Beljonne, D.; Shuai, Z.; Bredas, J. L.; Holmes, A. B.; Kraus, A.; Mullen, K.; Friend, R. H. *Nature* **1998**, *392*, 903−906.
(53) Di Nuzzo, D.; Aguirre, A.; Shahid, M.; Gevaerts, V. S.; Meskers, S. C. J.; Janssen, R. A. J. *Adv. Mater.* **2010**, *22*, 4321.
(54) Siebbeles, L. D. A. *Nat. Chem.* **2010**, *2*, 608−609.
(55) Wilson, M. W. B.; Rao, A.; Clark, J.; Kumar, R. S. S.; Brida, D.; Cerullo, G.; Friend, R. H. *J. Am. Chem. Soc.* **2011**, *133*, 11830−11833.
(56) Chan, W. L.; Ligges, M.; Jailaubekov, A.; Kaake, L.; Miaja-Avila, L.; Zhu, X. Y. *Science* **2011**, *334*, 1541−1545.
(57) Gabor, N. M.; Zhong, Z. H.; Bosnick, K.; Park, J.; McEuen, P. L. *Science* **2009**, *325*, 1367−1371.
(58) Bange, S.; Scherf, U.; Lupton, J. M. *J. Am. Chem. Soc.* **2012**, *134*, 1946−1949.
(59) Lanzani, G. *The Photophysics behind Photovoltaics and Photonics*, 1st. ed.; Wiley-VCH: Weinheim, 2012.
(60) Sreearunothai, P.; Morteani, A. C.; Avilov, I.; Cornil, J.; Beljonne, D.; Friend, R. H.; Phillips, R. T.; Silva, C.; Herz, L. M. *Phys. Rev. Lett.* **2006**, *96*.
(61) Gu, Y.; Wang, C.; Russell, T. P. *Adv. Energy Mater.* **2012**, *2*, 683−690.

9.7 Aims of the Investigations Based on Nonadiabatic Dynamics

In order to better understand the motivation for investigating the nonadiabatic dynamics of CPDTBT based on TSH, the relevant information that can be found in the included article[6] will be summarized from this perspective. The relevant figures from the article are shown in figure 9.2.

In experiment, excitation at high and low energies was employed to investigate pristine films of CPDT-BBT using transient absorption spectroscopy. More information on the experimental techniques can be found in reference [120]. Even without the presence of acceptor material as it is needed for a BHJSC, ultrafast charge separation takes place. After low-energy excitation, the signal of the ground state bleaching (GB) mainly follows the exciton absorption (EX). Due to this, it is concluded that low-energy excitation mainly leads to the formation of strongly bound excitons. In contrast to this, excitation with high energy leads in the end to a signal of theGB that follows the combined signal of stimulated emission (SE) and polaron absorption (P1). Therefore, such an excitation mainly leads to the formation of weakly bound polarons. Furthermore it can be investigated if during the relaxation charge transfer (CT) between two molecules occurs. To sum things up, the dependence on the excitation energy of the nonadiabatic dynamics for uni- and bimolecular systems is investigated in sections 9.8 and 9.9.

9.8 Nonadiabatic Dynamics of the Intramolecular Relaxation

Before the actual investigation of the intramolecular relaxation after excitation, the spectra based on VEA were determined using two different functionals for the DFT-based calculations and RI-ADC(2)[121–123] was used as wave function-based method. Owing to the facts that the latter treats excitations with and without CT character on equal footing and that it has already been used successfully to study CT transitions in aromatic hydrocarbon - tetracyanoethylene complexes, it is chosen as method of reference.[124]

As can be seen on the left in figure 9.3, the general structure of the spectra is similar for calculations with the two functionals and with the wave function-based method. The first and third transitions are relatively bright and the second transition is dark. The main difference is found in the position of the peaks. The first three excitation energies calculated with B3LYP are much lower than with the other two methods that yield similar results compared to each other. Finally it is worth mentioning that the energy difference between S_1 and S_2 is 0.18 eV for B3LYP and about 0.38 eV for the other two methods. In figure 4 of reference [6], it can be seen that this transition has the strongest CT character of the three analyzed transitions. This characterization also holds for the RI-ADC(2) calculation. So B3LYP already underestimates the energy of the CT excitation within this single molecule, indicating the need to use a long-range corrected functional to describe this small molecule consisting of a donor and two acceptor units.

The simulated spectrum employing NEA is shown on the right of figure 9.3. The quantum chemical method used for the spectrum simulation was CAM-B3LYP/6-31G* and

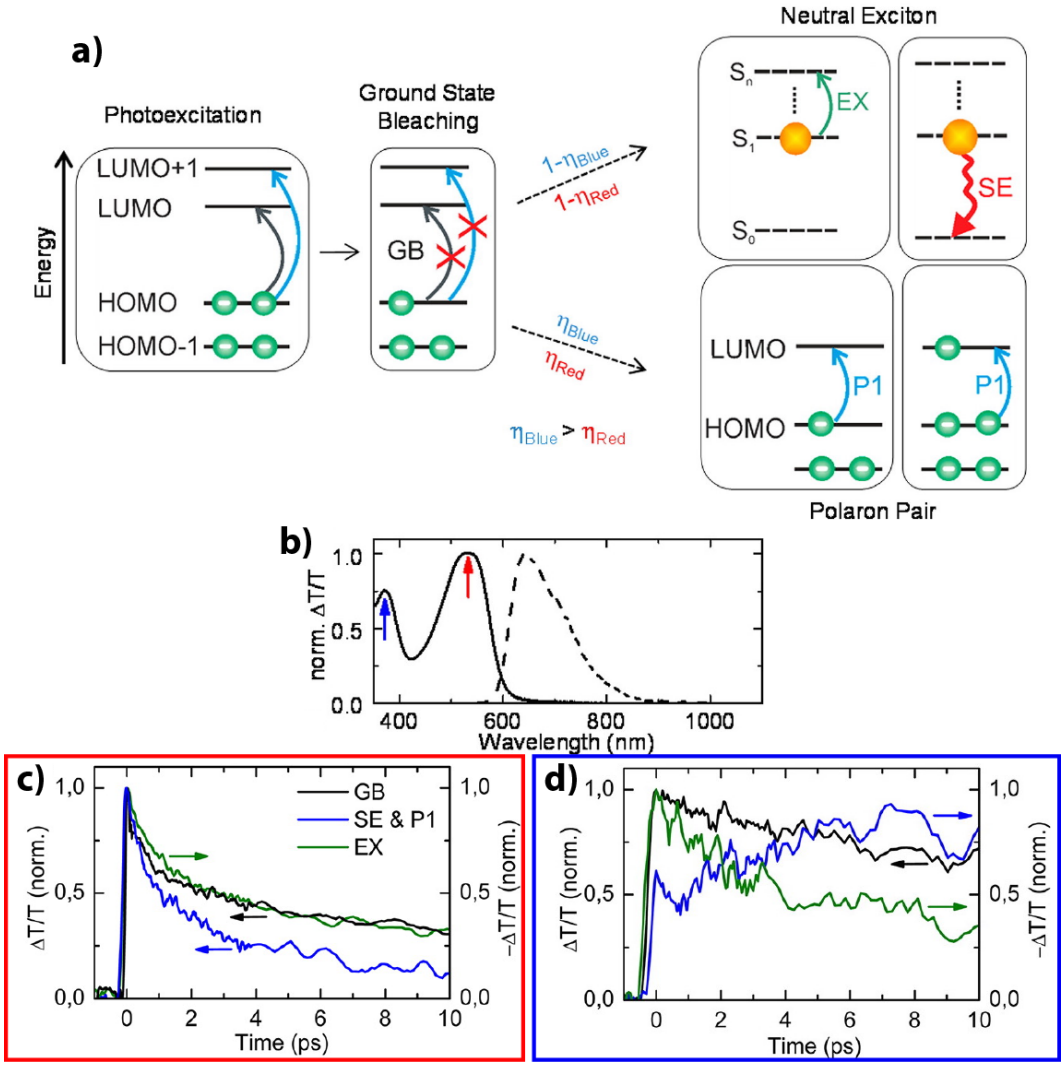

Figure 9.2: Illustration of the main findings from reference [6] for CPDT-BBT that are of relevance for the subsequent discussion of the dynamics of charge separation. In a), the processes after excitation that lead to the different signals in ultrafast transient absorption spectroscopy are depicted. The arrows in b) indicate the wavelengths that are used for the low- and high-energy excitations and the measured absorption (solid) and fluorescence (dashed) spectra are shown. The transients after low-energy absorption are depicted in c) and it can be seen that the signals of GB (black) and EX (green) are similar. The corresponding transients for high-energy absorption show a different behavior for larger times, as can be seen in d). In this case, the signals of GB (black) and P1 (blue) behave similar. Note that the steady increase in the signal of P1 and SE after excitation is caused by the decay of the latter. This decay of the SE leads therefore to an increase in the absorption.

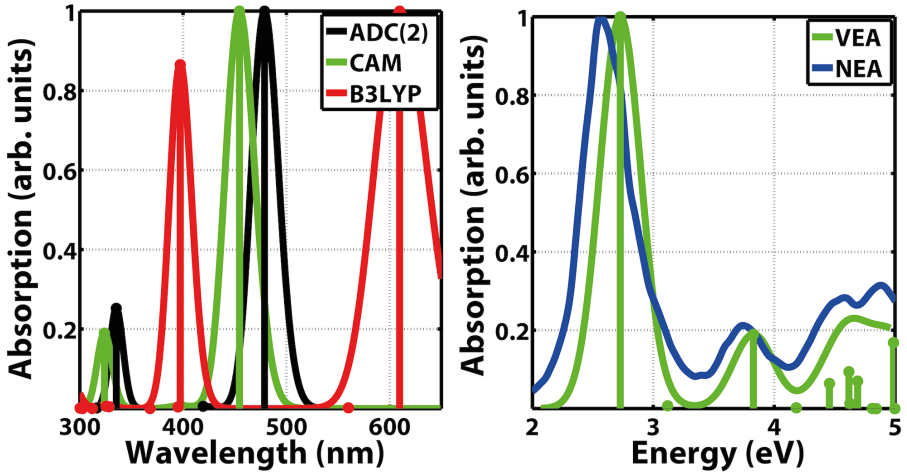

Figure 9.3: On the left, absorption spectra based on VEA calculated with B3LYP/6-31G* (red), CAM-B3LYP/6-31G* (green), and RI-ADC(2)/cc-pVDZ (black) are shown together with the corresponding stick spectra; On the right, the spectra for VEA (green) and NEA (blue) employing CAM-B3LYP/6-31G* are presented. On the left, it can be seen that already for the single molecule, the calculation with the long-range corrected functional yields a result that is closer to RI-ADC(2) than the calculation employing a widely used functional for organic molecules. The comparison between the spectra calculated with VEA and NEA reveals that the simulated spectrum is shifted a bit to lower energies, but the shape stays similar. Further information on how the simulated spectrum was used for the generation of initial conditions are given in the text.

500 geometries obtained from a Wigner-distribution were considered. In order to generate the initial conditions for the NA-AIMD, energy windows centered at the maximum of the first and second peak of the simulated spectrum and with a width of 0.011 eV and 0.015 eV, respectively, were used. The low-energy excitation lead to 21 accepted initial conditions that are all starting in S_1. For the high-energy excitation, 18 initial conditions starting in S_3 and 2 initial conditions starting in S_4 are generated.

Before the actual production runs for the dynamics, the reliability of the parameters that are used for the calculation of the NACs based on LD and OVL and the time step had to be tested. To achieve this, preliminary trajectories were calculated with parameters and a time step similar to the ones used in reference [119]. Then the time-dependence of the quantum mechanical populations was investigated and a part of a trajectory with significant transfer between the populations of adiabatic states in a certain time was chosen. This was taken as the starting point for the calculation of trajectories without any random events, i.e. no surface hops, no decoherence correction,[125] and no thermostat.

Comparing the results for the different parameter sets as defined in table 9.1, see the left part of figure 9.4, it can be concluded that the values of β, n_{core}, and n_{disc} in

set	Method	dt /fs	β	n_{core}	n_{disc}	real time/min
1:	LD	0.5	$5 \cdot 10^{-3}$	60	300	4.1 (3.4)
2:	LD	0.25	$5 \cdot 10^{-3}$	60	300	4.0 (3.4)
3:	LD	0.5	$5 \cdot 10^{-4}$	60	300	29.0 (28.4)
4:	LD	0.5	$5 \cdot 10^{-3}$	30	150	10.4 (9.7)
5:	LD	0.25	$5 \cdot 10^{-4}$	30	150	78.8 (78.2)
6:	OVL	0.5	$5 \cdot 10^{-3}$	60	300	4.4 (3.8)

Table 9.1: Methods, time steps, parameters used to assess the reliability of the calculated NACs, and the time needed for the propagation of the quantum amplitudes. Method refers to the algorithm used for the propagation of the quantum amplitudes, dt is the time step used for the propagation of the nuclear coordinates, β, n_{core}, and n_{disc} are parameters for the overlap calculations. The first is the screening threshold, the second one is the number of frozen occupied orbitals and the third one the number of discarded virtual orbitals. More information on the methods and parameters can be found in reference [119]. Finally, real time is the time needed for the propagation of the quantum amplitudes. Apart from the total time for the algorithm also the time needed for the actual calculation of the overlaps is given in brackets.

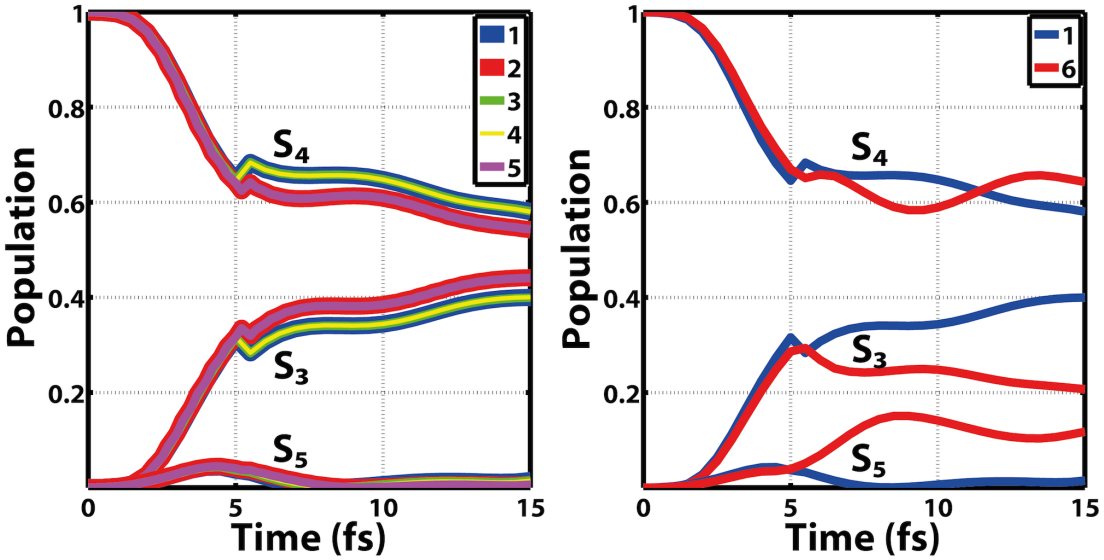

Figure 9.4: Time-dependence of the populations for the adiabatic states S_3, S_4, and S_5 shown for the parameter sets listed in table 9.1. All trajectories start with the same initial condition and there is significant transfer of population from S_4 to S_3. As can be seen on the left, all parameter sets using LD yield in principle similar results and only the change of the time step has a noticeable influence. However, using OVL leads to a significant population of S_5 resulting in a qualitatively different behavior compared to the other parameter sets as can be seen on the right.

set **1** are already converged. Only the use of a smaller time step leads to quantitative, but not qualitative differences in the populations. Bearing in mind that the method used for the propagation of the quantum amplitudes is already an approximation, it is sufficient to use the parameter set with one of the lowest times needed for the overlap calculations.[126] However, in all trajectories a kink in the population of S_3 and S_4 is found and will be investigated in more detail in future research. Finally, the use of OVL does not lead to kinks in the populations but it yields significant population in the S_5 state, see the right part of figure 9.4. The latter is not the case for the methodology using LD that is considered to be more stable.[119] Therefore, LD with parameter set **1** is used for TSH-based dynamics of the monomer.

Having determined an appropriate quantum chemical method, the initial conditions and a set of parameters for TSH, the actual production runs could be started. All trajectories were calculated twice, once with and the other time without the use of a thermostat. If a thermostat is used, the relaxation of the total energy takes place in about 100 fs. The results of typical trajectories for low and high energy excitations without the use of a thermostat are shown in figures 9.5 and 9.6, respectively.

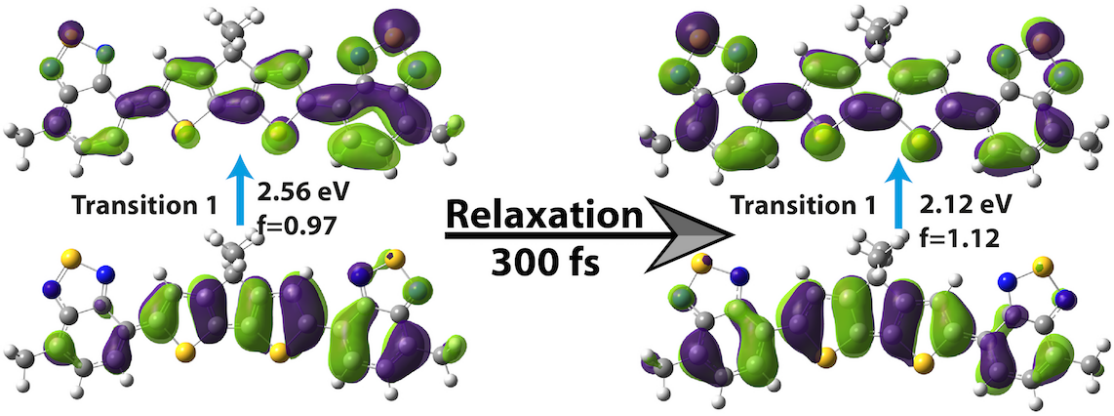

Figure 9.5: Results for a typical trajectory of TSH-based dynamics upon low-energy excitation obtained using a thermostat. The initial active state is S_1 and during the 300 fs of dynamics no surface hopping event occurs. Therefore, the final active state is also S_1. Overall, the total energy of the system is lowered by 0.44 eV and the oscillator strength increases by 0.15. However, the NTOs involved in the electronic transition remain about the same.

Investigating the low-energy excitation and using a thermostat, in 18 from 21 trajectories no hopping occurs. Furthermore one trajectory with hops is in the end again in S_1. Without the use of a thermostat, there are only 9 trajectories without any hopping events but still 15 trajectories finish the dynamics in the S_1 state. So in both cases, the majority of the trajectories is in the beginning and at the end in the same state, but the use of a thermostat has a significant influence on the number of hopping events.

The latter conclusion also holds for the dynamics after high-energy excitation. Using a thermostat, 17 of 20 trajectories are at the end of the dynamics in one of the states that have been chosen as active states for the initial condition, i.e. S_3 or S_4. Therefore,

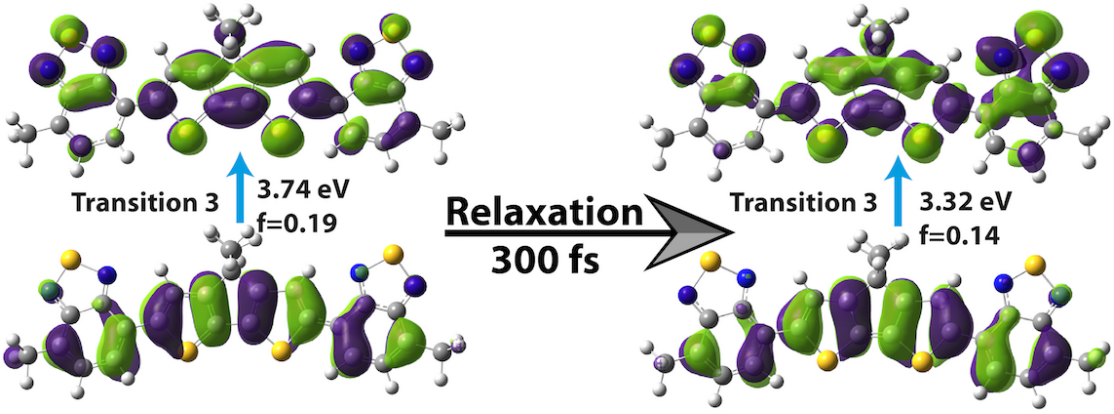

Figure 9.6: Results for a typical trajectory of TSH-based dynamics after high-energy excitation obtained using a thermostat. The initial active state is S_3 and no surface hopping event occurs during the 300 fs of dynamics. Therefore, the final active state is also S_3. Overall, the total energy of the system is lowered by 0.42 eV, the oscillator strength decreases by 0.05 and the NTOs involved in the electronic transition remain about the same.

only 3 trajectories reach one of the two lower lying states. In the absence of a thermostat, already 8 trajectories have reached S_1 within 300 fs of dynamics. Furthermore, 3 trajectories are in the S_2, which might be favorable for polaron pair formation. Finally, it is noteworthy that employing an analogous approach using B3LYP as functional leads to similar results compared to the ones obtained with CAM-B3LYP.

Owing to the significant influence of a thermostat, its proper implementation wtihin the methodology and comparison with experiment are crucial steps to understand the nonadiabatic dynamics. In addition, it might be insightful to analyze how long trajectories remain in S_2 to see if there is sufficient time for charge separation from this state. Finally, it has to be investigated how intermolecular interactions between two molecules have an influence on the nonadiabatic dynamics. For this purpose, first steps have been undertaken and are presented in the next section.

9.9 Nonadiabatic Dynamics of the Intermolecular Relaxation

In order to simulate intramolecular interactions, π-π stacking is assumed. Therefore, the second molecule was placed 4 angstroms directly above the first one in such a way that the conjugated systems were parallel to each other. This structure was optimized with RI-MP2/cc-pVDZ similar to the calculations in reference.[124] After these preparations, the steps presented in the previous section could be used to investigate this system. However, so far only the spectra based on VEA, generation of initial conditions and preliminary trajectory calculations have been done.

The spectrum based on VEA shown in figure 9.7 confirms the conclusions found for the spectrum calculation of the single molecule. The results obtained with B3LYP deviate more pronounced from the RI-ADC(2) results than it is the case for CAM-B3LYP. In

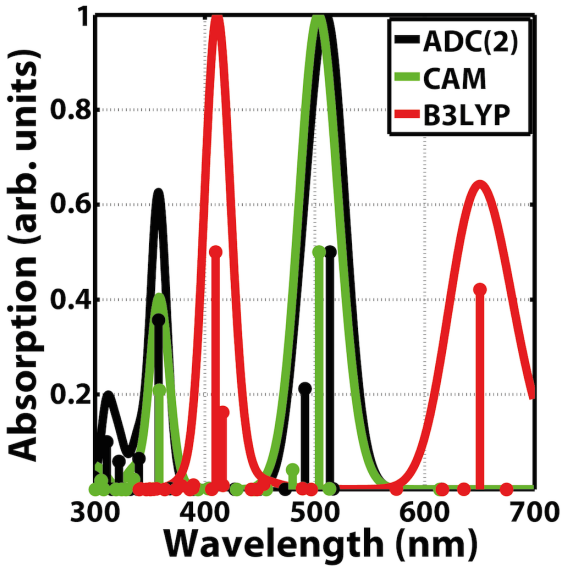

Figure 9.7: Absorption spectra based on VEA calculated with B3LYP/6-31G* (red), CAM-B3LYP/6-31G* (green), and RI-ADC(2)/cc-pVDZ (black) are shown together with the corresponding stick spectra. It can be seen that for the bimolecular system, the calculation with CAM-B3LYP yields a result that is is similar to RI-ADC(2). This is in contrast to the calculation employing B3LYP, which does not only yield red-shifted absorption peaks, but also two dark states at 897 nm and 764 nm that are not shown.

particular, B3LYP yields ample CT states that are located near the bright transitions. Using CAM-B3LYP or RI-ADC(2), the number of these states is significantly reduced. So B3LYP yields artificial low-lying CT states that are energetically close to bright transitions and therefore may influence the TSH-based dynamics.

For initial condition generation and TSH-based dynamics, the basis set was reduced to 3-21G* in order to save computational time without losing much accuracy regarding excited state energy calculations. Having generated initial conditions for the bimolecular system, preliminary trajectories for low- and high-energy excitations were calculated. The parameters were chosen so that the calculation of the wave function overlaps is relatively fast, i.e. 10 minutes. However, it remains to be tested if these parameters are already sufficient to obtain qualitatively correct NACs. Trajectories for low- and high-energy excitations are shown in figures 9.8 and 9.9, respectively.

For the trajectory that is calculated upon the excitation with low energy, the characteristics of the MOs that are mainly contributing to the electonic transition of the active state do not change much, see figure 9.8. The corresponding occupied MOs at the beginning and the end of the dynamics are delocalized over both molecules, whereas the corresponding unoccupied MOs are delocalized over one molecule only. Therefore, the overlap between those orbitals is relatively large which can be associated with strongly bound exctions and not weakly bound polarons.

In contrast to that, upon high-energy excitation the system relaxes through some

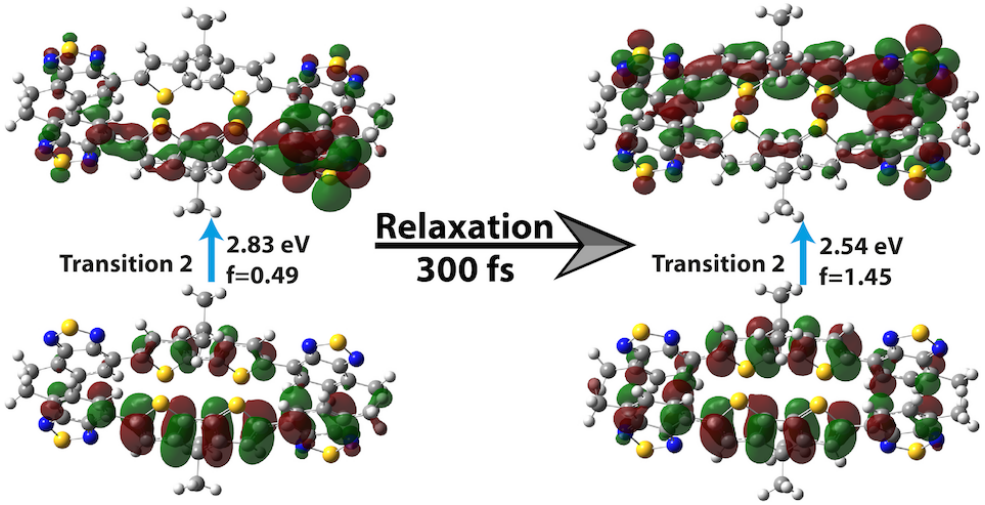

Figure 9.8: Results for a trajectory of TSH-based dynamics upon low-energy excitation obtained using a thermostat. The initial active state is S_2 and the final active state is also S_2. Overall, the total energy of the system is lowered by 0.29 eV, the oscillator strength increases by 0.96 and the characteristics of the MOs that are mainly involved in the electronic transition remain about the same.

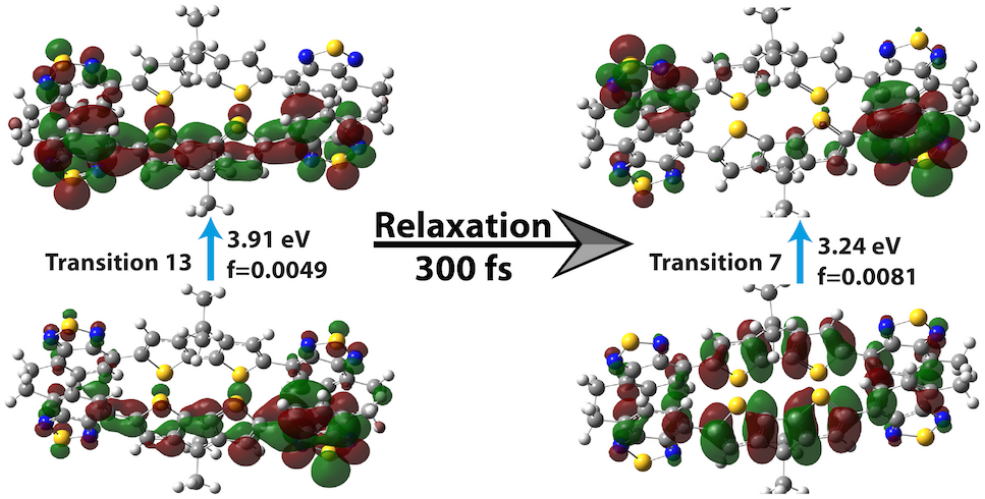

Figure 9.9: Results for a trajectory of TSH-based dynamics upon high-energy excitation obtained using a thermostat. The initial active state is S_{13} and the final active state is S_7. Overall, the total energy of the system is lowered by 0.67 eV and the oscillator strength increases by 0.0032. The occupied MOs in the beginning and at the end of the dynamics that are mainly contributing to the electronic transitions into the corresponding active states are delocalized over one or both molecules, respectively. The mainly contributing unoccupied MO is at the beginning delocalized over one molecule and at the end of the dynamics the mainly contributing unoccupied MO is localized at two acceptor units that are located at different molecules.

excited states into a lower lying state, see figure 9.9. At the end of the dynamics, the unoccupied MO that is mainly involved in the electronic transition of the active state is localized at two BT units and the corresponding occupied MO is delocalized over both molecules mainly located at the CPDT units. So in this final state, the CT character is more pronounced than for the active state at the beginning of the dynamics. It might be the precursor for weakly bound polarons, due to the small overlap between the orbitals mainly involved in the electronic transition into the active state explaining the higher polaron pair formation yield for high-energy excitation.

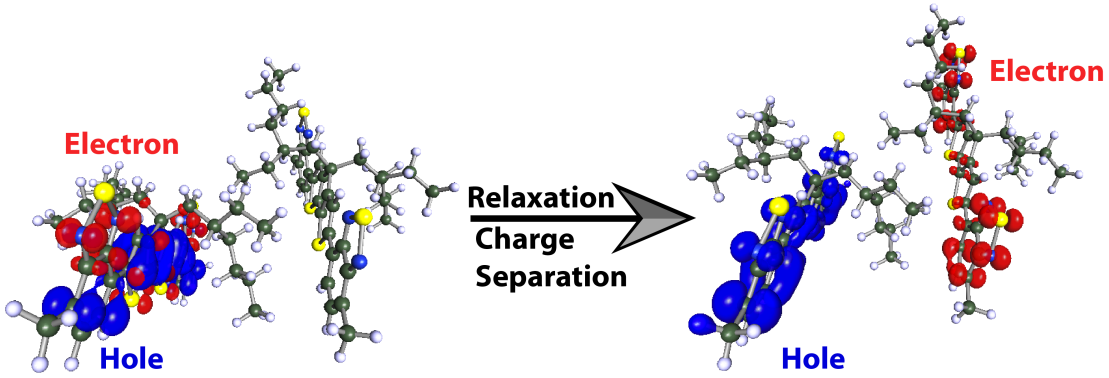

Figure 9.10: Results for a trajectory of TSH-based dynamics that is found for low- and high-energy excitation obtained using B3LYP as functional and employing a thermostat. The graphical user interface for Turbomole is used for the visualization of the orbitals.[127] In the beginning the occupied MO that is mainly contributing to the electronic transition into the active state is delocalized over one molecule and denoted as hole. The mainly contributing unoccupied MO is delocalized over the same molecule and denoted as electron. In the end of the dynamics, the hole is still delocalized over the left molecule. However, the electron is now localized at the acceptor units of the right molecule.

Finally, also TSH-based dynamics with B3LYP as functional was determined. In this case, excitation with low- and high energies lead to trajectories that are similar to the one shown in figure 9.10. After the relaxation, the hole is localized at the BT units of one molecule and the electron is delocalized over the other molecule. This might explain the ultrafast charge separation observed in experiment, but no dependence on the excitation energy is apparent. Finally, the dynamics might be influenced by some artificial low-lying CT states due to the facts that these have been found in the calculated absorption spectrum and that CAM-B3LYP does not yield such results for the separation of electron and hole. So B3LYP does not yield reliable results and it is important to use a method for electronic structure calculation that at least correctly describes the absorption spectrum.

10 Supplement: Advanced Quantum Chemical Methods

> It therefore becomes desirable that approximate practical methods of applying quantum mechanics should be developed, which can lead to an explanation of the main features of complex atomic systems without too much computation.
>
> *(Paul Dirac[128])*

In this chapter the more advanced methods that have been used in the quantum chemical investigations will be described. Therefore, basic knowledge of Gaussian 09[129] and Turbomole[127,130] is assumed, i.e. structure optimizations, calculation of vibrational frequencies and determination of absorption spectra with both programs should be not much of a problem. Furthermore, the general way of generating various inputs for Newton-X[109] should be known.

10.1 Calculation of Vibronic Spectra Using G09

For the calculation of vibronic spectra using FCA as presented in the Supporting Information of the paper by Vollbrecht et al.[3] Gaussian 09 has been used and the following approach has proven most successful:

1. Preliminary optimization of the S_0 geometry
2. Optimization of the geometry of the excited state of interest without symmetry constraints
3. Calculation of vibrational frequencies for the optimized excited state with a header for the input similar to the following:

Listing 10.1: Header for the optimization of the first excited state

```
%nprocshared=12
%mem=24GB
%chk=FreqS1.chk
#p freq=savenormalmodes td=(root=1)/6-31g(d)
nosymm geom=connectivity rpbe1pbe
```

4. Optimization of the S_0 based on the structure obtained from the excited state optimization and done without symmetry constraints

5. Calculation of vibrational frequencies for the optimized ground state

6. Calculation of vibronic spectra using an input similar to the following:

Listing 10.2: Input for the calculation of vibronic spectra

```
%nprocshared=12
%mem=24GB
%Chk=FreqS0.chk
#p Geom=AllCheck Freq=(ReadFC,FC,SaveNM,ReadFCHT) NoSymm

MAXINT=10000 MAXBANDS=8 PRTINT=0.001 NORELI00
SPECMIN=17400 SPECMAX=30200 SPECHWHM=200.0 SPECRES=10.0

FreqS1.chk
```

In this example the vibrational frequencies of the ground state calculation are found in FreqS0.chk and this is used as the standard checkpoint-file. The vibrational frequencies of the excited state calculation are given at the end of the input. The keywords written in capital letters are connected to the calculation of vibronic spectra and more information on them can be found elsewhere.[58] In this case, the first two keywords influence the convergence of the FC-spectrum and the third keyword determines which transitions are printed in the output. "NORELI00" in combination with "SPECMIN" and "SPECMAX" allows to set the energy window for the spectrum calculation in absolute values with the dimension cm^{-1}. "SPECRES" is the distance between two data points of the spectrum in cm^{-1}. Finally, "SPECHWHM" defines the half-width at half-maximum for the convolution of each vibronic using a gaussian function. The combination of the last five keywords allows to easily calculate vibronic spectra for several excited states and generate a total spectrum as the sum of the single electronic transitions.

10.2 NEA for Spectra Calculation Using Newton-X interfaced to G09

In order to calculate spectra employing the NEA as presented in the paper by Riesen et al.,[2] Newton-X interfaced with Gaussian was used and the procedure is as follows:

1. At the beginning, a standard S_0 geometry optimization with subsequent vibrational frequency calculation is done using Gaussian 09

2. A first input-file for the spectrum calculation is generated. There are some requirements, so that the input-file will be processed properly by Newton-X and it should look similar to the following example:

Listing 10.3: Gaussian 09 input for spectrum calculation as required by Newton-X

```
%chk=gaussian.chk
%nprocshared=16
%mem=48GB
#p td=(nstates=20) rcam-b3lyp/def2svp scrf=(solvent=acetonitrile)
nosymm
```

3. The log-file containing the information of the frequency calculation, a file "geom" with the molecular geometry in Newton-X format, for example obtained by using the Newton-X script "xyz2nx" and a directory "JOB_AD" containing the gaussian input have to be in one directory. After that, execution of "nxinp" is used in this directory to generate a file "initqp_input" that contains in principle the following information:

Listing 10.4: Input for the generation of initial conditions with calculation of transition energies

```
&dat
  nact = 2
  numat = 40
  npoints = 1000
  file_geom = geom
  iprog = 4
  file_nmodes = OptFreqClosed.log
  anh_f = 1
  chk_e = 1
  nis = 1
  nfs = 21
  kvert = 1
  de = 1000
  prog = 6.5
  iseed = -1
  lvprt = 1
&end
```

4. The calculation of the transition energies can be split and merged using the scripts "split_initcond.pl" and "merge_initcond.pl", respectively. The jobs can be run on the OCuLUS-Cluster using the following script:

Listing 10.5: Script for running Newton-X on OCuLUS

```
#! /bin/sh
#CCS -m abe
#CCS -M wiebeler@mail.upb.de
#CCS --res=rset=1:ncpus=16:mem=63g
#CCS -N NX-job

#Load modules and specify settings
. /etc/profile.d/modules.sh
```

```
module -s add g09/d01
export g09root=/cm/shared/apps/pc2/GAUSSIAN/g09-d01
export GAUSS_PDEF=16
module add nx/1.4.0

#Current Settings
echo $NX
echo $PATH
echo $NCPUS
echo $TMPDIR

#Start of NX application
$NX/initcond.pl > initcond.log

#ccsinfo $CCS_REQID
exit 0
```

5. After the jobs have finished, they can be merged and the simulated spectrum can be determined using "nxinp" with the appropriate options.

The procedure described above does not only allow to calculate spectra based on the NEA, but it is also a possible approach to sample the initial conditions for NA-AIMD. The next steps to do this kind of calculation employing Newton-X interfaced with Gaussian 09 will be described in section 10.4.

10.3 Trajectory Surface Hopping Using Turbomole

The NA-AIMD for the cycloreversion reaction of DAEs has been calculated for several molecules with the same approach[4,5] that is described in the following:

1. Optimization of the S_0 geometry. For executing Turbomole calculations on the OCuLUS-Cluster, a script like the following has to be used:

Listing 10.6: Script for running Turbomole on OCuLUS

```
#!/bin/sh

#Load Turbomole module
. /etc/profile.d/modules.sh
module -s add turbomole

#Add to PATH
export PATH="$TURBODIR/bin/`sysname`:$PATH"

#Specify Turbomole Settings
export PARNODES=$NCPUS
export TURBOTMPDIR=$TMPDIR
```

```
#Current Settings
sysname
echo $PATH
echo $PARNODES
echo $TURBOTMPDIR

#Start of Turbomole Calculation
jobex -c 200 >jobex.out

exit $?
```

However, depending on the type of the job different programs have to be executed in the script. Therefore, the second last line has to be changed for different types of calculation, but the remainder stays the same.

2. Calculation of BOMD using the following inputs that are created using the Turbomole scripts "define" and "mdprep":

Listing 10.7: file "control" for BOMD

```
$title
BOMD
$operating system unix
$symmetry c1
$coord    file=coord
$user-defined bonds    file=coord
$atoms
c   1-4,6-11,16,20-23,30-32,34,38-42,44,46  \
    basis =c def2-SVP
s   5,12 \
    basis =s def2-SVP
h   13-15,17-19,33,35-37,43,45,47-52 \
    basis =h def2-SVP
f   24-29 \
    basis =f def2-SVP
$basis    file=basis
$rundimensions
   dim(fock,dens)=185910
   natoms=52
   nshell=262
   nbf(CAO)=608
   nbf(AO)=574
   dim(trafo[SAO<->AO/CAO])=676
   rhfshells=1
$scfmo    file=mos
$closed shells
 a       1-130                                          ( 2 )
$scfiterlimit      300
$thize     0.10000000E-04
$thime        5
```

```
$scfdump
$scfintunit
 unit=30       size=0        file=twoint
$scfdiis
$scforbitalshift  automatic=.1
$drvopt
   cartesian  on
   basis      off
   global     off
   hessian    on
   dipole     on
   nuclear polarizability
$interconversion  off
   qconv=1.d-7
   maxiter=25
$optimize
   internal   off
   cartesian  on
   global     off
   basis      off   logarithm
$coordinateupdate
   dqmax=0.3
   interpolate  on
   statistics    5
$forceupdate
   ahlrichs numgeo=0  mingeo=3 maxgeo=4 modus=<g|dq> dynamic fail=0.3
   threig=0.005  reseig=0.005  thrbig=3.0  scale=1.00  damping=0.0
$forceinit on
   diag=default
$energy    file=energy
$grad    file=gradient
$forceapprox    file=forceapprox
$lock off
$dft
   functional pbe0
   gridsize   m3
$scfconv   6
$scfdamp   start=0.700  step=0.050  min=0.050
$last step     define
$end
```

Listing 10.8: file “mdmaster” for BOMD

```
# A I M D : master file
#
$nsteps     4000
$natoms       52
$log file=mdlog.1
$current file=mdlog.1
$turbomole file=control
```

```
$seed 1351133921
$title BOMD
$log_history
  maxlog      4000
       0                        mdlog.1
$ke_control
  length      50
  response       1
$barrier
$constraints
  algorithm    none
  tolerance   0.1000000E-01
  corpercyc   0.2500000
$md_status
  canonical  T=   300.00 t=   500.00
  from t= -50.0000000000        until t=   0.00000000000
$md_action
$end
```

Furthermore, the files “basis”, “coord”, “mdlog.1”, “mos”, and a script for running the dynamics are needed in the same directory.

3. Selection of initial geometries and velocities for TSH. For this purpose the following self-written C-program is used:

Listing 10.9: Program for the random selection of initial geometries and velocities.

```
#include <stdio.h>
#include <math.h>
#include <stdlib.h>
#include <time.h>

const double Steps = 2969.0;
const int RandomNumbers = 100;
const double timestep = 50.0;

int cmpfunc (const void * a, const void * b)
{
   return ( *(int*)a - *(int*)b );
}

int main()
{
        int i ;
        double xi[RandomNumbers];
        int zi[RandomNumbers];
        srand(time(NULL));

        for (i = 0; i < RandomNumbers; i++)
        {
```

```
                xi[i] = rand()/(RAND_MAX+1.0)*Steps;
                zi[i]= ceil(xi[i]);
                printf(" %d;", zi[i]);
        }
        printf("\n");

        qsort(zi, RandomNumbers, sizeof(int), cmpfunc);

        printf("\nSorted Output:\n");
        for( i = 0 ; i < RandomNumbers; i++ )
        {
                printf(" %d;", zi[i]);
        }
        printf("\n");

    printf("\nSorted Output (Time):\n");
    for( i = 0 ; i < RandomNumbers; i++ )
        {
               xi[i]=zi[i]*timestep;
               printf(" %d: %.0f\n", i, xi[i]);
        }
    printf("\n");
    return (0);
}
```

4. Generation of a first input for TSH with “define” and “mdmaster”. Furthermore some additions have to be added manually into the files “control” and “mdmaster”:

Listing 10.10: file “control” for TSH

```
$title
TSH
$operating system unix
$symmetry c1
$coord    file=coord
$user-defined bonds    file=coord
$atoms
c   1-4,6-11,16,20-23,30-32,34,38-42,44,46
\
   basis =c def2-SVP
s   5,12
\
   basis =s def2-SVP
h   13-15,17-19,33,35-37,43,45,47-52
\
   basis =h def2-SVP
f   24-29
\
   basis =f def2-SVP
$basis    file=basis
```

```
$rundimensions
   dim(fock,dens)=185910
   natoms=52
   nshell=262
   nbf(CAO)=608
   nbf(AO)=574
   dim(trafo[SAO<—>AO/CAO])=676
   rhfshells=1
$scfmo   none   file=mos
$closed shells
 a       1-130                                          ( 2 )
$scfiterlimit      300
$thize     0.10000000E-04
$thime        5
$scfdump
$scfintunit
 unit=30       size=0        file=twoint
$scfdiis
$scforbitalshift  automatic=.1
$drvopt
   cartesian  on
   basis      off
   global     off
   hessian    on
   dipole     on
   nuclear polarizability
$interconversion  off
   qconv=1.d-7
   maxiter=25
$optimize
   internal   off
   cartesian  on
   global     off
   basis      off   logarithm
$coordinateupdate
   dqmax=0.3
   interpolate  on
   statistics    5
$forceupdate
   ahlrichs numgeo=0  mingeo=3 maxgeo=4 modus=<g|dq> dynamic fail=0.3
   threig=0.005  reseig=0.005  thrbig=3.0  scale=1.00  damping=0.0
$forceinit on
   diag=default
$energy    file=energy
$grad    file=gradient
$forceapprox    file=forceapprox
$lock off
$dft
   functional pbe0
```

```
   gridsize    m3
   weight derivatives
$scfconv    6
$scfdamp    start=0.700  step=0.050  min=0.050
$scfinstab ciss
$soes
 a            2
$rpacor  16000
$denconv 1d-7
$escfiterlimit 200
$surface_hopping
$nacme
$nac
$exopt 1
$ex_energies file=ex_energies
$integral_ex file=integral_ex
$sh_coeffs file=sh_coeffs
$nac_matrix file=nac_matrix
$last step     define
$end
```

Listing 10.11: file “mdmaster” for TSH

```
# A I M D : master file
#
$nsteps      2000
$natoms        52
$log file=mdlog.1
$current file=mdlog.1
$turbomole file=control
$title TSH
$log_history
  maxlog      2000
       0                        mdlog.1
$ke_control
  length      50
  response       1
$barrier
$constraints
  algorithm    none
  tolerance  0.1000000E-01
  corpercyc  0.2500000
$surface_hopping
$md_status
  free
  from t= -40.0000000000        until t=  0.00000000000
$md_action
 fix total energy     from t=  0.00000000000
$end
```

Additionally, the files “basis”, “coord”, “mdlog.1”, and a script for running dynamics in excited states are needed in the same directory. Note that starting with version 6.5 of Turbomole the multi-threaded parallelization has to be used for SMP calculations.[131]

5. In order to calculate for example a swarm of 100 trajectories, the initial input as shown above has to be copied 100 times in different trajectories before a first test calculation is started. In each directory, the geometry found in “coord” and “mdlog.1” has to be replaced with the randomly selected geometry. In addition, the velocities corresponding to this geometry have to be copied in “mdlog.1” substituting the original velocities. Finally, each trajectory is calculated separately and the data obtained can be analyzed.

The method described above allows the calculation of NA-AIMD starting in S_1 and considering only the coupling between this state and S_0. The calculation of NACs between excited states has already been demonstrated.[132] However, in Turbomole this functionality is not included so far. Therefore, in order to consider couplings and hops between excited states, a different approach has to be used, e.g. using Turbomole/ Gaussian09 interfaced with Newton-X. This is for example necessary to investigate the photocyclization reaction of CMTE or to understand the ultrafast process of charge separation in OPVs. Such an approach is described in section 10.4.

10.4 Nonadiabatic Dynamics Using Newton-X interfaced to G09

The NA-AIMD for CPDT-BBT that has first been characterized in an own article[6] has been calculated using an approach analogous to the one described in this section. The results of this method regarding the ultrafast charge separation for this molecule are presented in chapter 9.

1. Having simulated a spectrum using the nuclear-ensemble approach, the directory with the merged results for the absorption is copied in another directory. Using the option to generate multiple initial states in the script “nxinp”, an energy window has to be specified. The excitation energy is defined in such a way that it resembles the experimental conditions, e.g. excitation at absorption maximum of the simulated spectrum. The width of the energy window then determines how many trajectories are generated.

2. The output files found in “SELECTED_INITIAL_CONDITIONS” that are containing more than the reference geometry are copied in separate directories for the dynamics and have to be renamed into “final_output”. Furthermore, each of these directories has to contain a directory “JOB_AD” with the input-file “gaussian.com” similar to the one used for NEA and with a file “basis” that only contains a single line defining the basis, e.g. “6-31g(d)”. In addition, each of the directories for the

dynamics has to include the following files: “control.dyn”, “jiri.inp”, “sh.inp”, and “therm.inp”. The latter only if a thermostat should be used. Exemplary input files for nonadiabatic dynamics of CMTE are listed in the following:

Listing 10.12: file “control.dyn” for NAD

```
&input
   nat = 40
   nstat = 6
   nstatdyn = 2
   dt = 0.5
   tmax = 500
   prog = 6.5
   thres = 100
   killstat = 1
   timekill = 0
   ndamp = 0
   lvprt = 1
   kt = 1
   Etot_jump = 1000
   Etot_drift = 1000
&end
```

Listing 10.13: file “jiri.inp” for NAD

```
&jirinp
   kross = 1
   cascade = 0
   current = 1
   never_state = 0
   include_pair = 0
   e_ci = 0.2
   ci_cons = 1
   cio_options = "-t 5e-3 -e -1"
   ndisc=218
   ncore=30
&end
```

Listing 10.14: file “sh.inp” for NAD

```
&shinp
   vdoth = -1
   ms = 0
   getphase = 1
   nohop = 0
   nrelax = 0
   seed = 1
   probmin = 0
   integrator = 6
   tully = 1
   decay = 0.1
```

```
  mom = 1
  adjmom = 0
  popdev = 0.05
&end
```

Note that apart from the value in "nstatdyn" found in "control.dyn" and denoting the initial states, the inputs are rather general. Therefore, they should in principle be the same in each directory for TSH starting from different excited states and only "nstatdyn" has to be changed.

3. Using "nxinp" within a directory for the dynamics, further directories for each trajectory are generated. After having copied the script for the dynamics in each of these directories, the calculation of the NA-AIMD can be started in each directory of the trajectories separately and this is repeated for all directories for the dynamics.

It has to be mentioned that the options "ndisc" and "ncore" in "jiri.inp" are only used correctly, if a modified Newton-X script for the NA-AIMD with Gaussian 09 is used. Furthermore, a security test is passed in this script to further decrease the computation time of the overlaps for the NACs. Without the modified script the overlap calculations for a molecule consisting of about 40 atoms would take hours.

The method for calculating the NA-AIMD as described in this section is more elaborate than the approach using Turbomole only. It allows to consider hops between excited states and to simulate excitations. However, there are also some drawbacks: First, due to the absence of analytical expressions for the NACs, they have to be calculated numerically. This leads to new parameters regarding the overlap calculations for which convergence has to be tested and a smaller time step has to be used. Second, CIs between the ground and excited states have to be treated with care, because TDDFT without TDA is used[100] and no hop is enforced when the energy of the excited state is lower than the energy of S_0.[85]

11 Scientific Contributions

> Sapere Aude! Habe Mut, dich deines eigenen Verstandes zu bedienen!
>
> *(Immanuel Kant[133])*

The faculty of sciences at the University of Paderborn requires that publications related to this thesis are listed and the contributions of the candidate are highlighted. This is done in the following. In addition, a list of conference contributions and invited talks are included in this chapter.

11.1 List of Publications and Author Contributions

1. C. Wiebeler and S. Schumacher. *Quantum Yields and Reaction Times of Photochromic Diarylethenes: Nonadiabatic Ab Initio Molecular Dynamics for Normal- and Inverse-Type.* J. Phys. Chem. A **118**, 36, 78167823 (2014).

   In this contribution, we discuss and compare results for two prototypical diarylethene molecuIes. This two molecules have been used in previous quantum chemical calculations to understand the fundamental differences between normal- and inverse-type diarylethenes. We compare excitation energies that are obtained from density functional theory- and wave function-based calculations. We determine the nonadiabatic ab inito molecular dynamics of the cycloreversion reaction, in order to obtain quantum yields and reaction times allowing us to explain the differences that are found in experiment for this two kinds of diarylethenes. Finally, these differences can be explained by investigation of the involved potential energy surfaces.

   I have been in charge for this paper. Therefore, I have done all the quantum chemical calculations and I have also composed the paper.

2. C. Wiebeler, C. A. Bader, C. Meier, and S. Schumacher. *Optical Spectrum, perceived color, refractive index, and non-adiabatic dynamics of the photochromic diarylethene CMTE.* Phys. Chem. Chem. Phys. **16**, 14531-14538 (2014).

   This contribution is dedicated to the characterization of a specific diarylethene abbreviated CMTE, that will be used for the functionalization of an inorganic microdisk resonator. We compare the calculated absorption spectra based on density

functional theory with wave function-based calculations and experimental measurements, determine the perceived color from the absorption spectrum, calculate the frequency-dependent refractive index and compare it with experimental results. In order to improve the understanding the cycloreversion reaction, we determine potential energy surfaces and nonadiabatic ab initio molecular dynamics of the cycloreversion reaction. The latter even allows the determination of quantum yields and reaction times. Quantities that are hard to estimate based on standard quantum chemical calculations.

I have done all the presented quantum chemical calculations that are shown in the paper and have written large parts of the paper. I have elaborated the methodology for the investigation of the frequency-dependent refractive index and the determination of the perceived color. Finally, I have discussed all the results shown.

3. J. Vollbrecht, H. Bock, C. Wiebeler, S. Schumacher, and H. Kitzerow. *Polycyclic Aromatic Hydrocarbons Obtained by Lateral Core Extension of Mesogenic Perylenes: Absorption and Optoelectronic Properties.* Chem. Eur. J. **20**, 38, 12026-12031 (2014).

   Two series of extended perylene derivatives have been synthesized and characterized by experimental measurement, e.g. absorption spectra. Two trends are found: the extension of the aromatic system does not lead to a red-shift of the energetically lowest lying absorption and the absorption in the UV range gains intensity relative to the absorption in the visible range. Both findings are also confirmed by our quantum chemical calculations and the characterization of the orbitals that are involved in the electronic excitations explains them. In order to explain all the absorption peaks that are found in experiment, we calculated vibronically resolved spectra for the lowest electronic transitions of these molecules.

   I have done all the presented quantum chemical calculations that are shown in the paper and its supplement and discussed the results.

4. H. Riesen, C. Wiebeler, and S. Schumacher. *Optical Spectroscopy of Graphene Quantum Dots: The Case of C132.* J. Phys. Chem. A **118**, 28, 5189-5195 (2014).

   In experimental measurements, graphene quantum dots show low lying peaks of absorption that are overshadowed by higher lying and brighter transtions. Therefore, this transitions can only be seen as shoulders in the corresponding spectra. Quantum chemical calculations for the optimized geometry show that the first two electronic transitions are much darker than found in experiment. Due to this, the transitions are not visible in the calculated spectra. Employing the nuclear-ensemble approach, it is confirmed that the shoulders found in the experimental spectra belong to the two lowest electronic excitations. So intensity borrowing

leads to brighter transitions for the first two electronic excitations. Finally, this confirms that the shoulders found in experiment are not caused by impurities but belong to the graphene quantum dots.

I have done all the presented quantum chemical calculations that are shown in the paper and its supplement, except for the optimization of the electronic excited S_1 state.

5. R. Tautz, E. Da Como, C. Wiebeler, G. Soavi, I. Dumsch, N. Frhlich, G. Grancini, S. Allard, U. Scherf, G. Cerullo, S. Schumacher, and J. Feldmann. *Charge Photogeneration in Donor-Acceptor Conjugated Materials: Influence of Excess Excitation Energy and Chain Length.* J. Am. Chem. Soc. **135**, 11, 4282 - 4290 (2013).

   Based on the investigation of the previously published paper, we have employed the quantum chemical method on a shorter oligomer that is also used in experiment. In addition to the characterization of the electronic transitions, we also explain the reason why an excitation with higher energy favors the formation of polarons. For this purpose, the natural transition orbitals that are involved in the electronic excitations are investigated and their localization at acceptor units or delocalization across the whole molecule is discussed.

   I have done all the presented quantum chemical calculations that are shown in the paper.

6. C. Wiebeler, R. Tautz, J. Feldmann, E. von Hauff, E. Da Como, and S. Schumacher. *Spectral Signatures of Polarons in Conjugated Co-polymers.* J. Phys. Chem. B **117**, 16, 4454 - 4460 (2013).

   In this paper, we have modeled the linear absorption spectra of neutral and charged polymers using quantum chemical calculations for sufficiently long oligomers. natural transition orbitals are used to analyze the electronic transitions that are involved in the polaron absorption of Co-polymers. This approach allows to explain why the symmetry of polaron absorption for cations and anions that is observed in homo-polymers is absent in co-polymers.

   I have done all the presented quantum chemical calculations that are shown in the paper.

11.2 Conference Presentations and Invited Talks

1. C. Wiebeler and S. Schumacher. *Six Years of Research in the RTG: Nonlinear Optics, Computational Spectroscopy and Nonadiabatic Dynamics.* Meeting of the

Graduate Program 1464 "Micro- and Nanostructures in Optoelectronics and Photonics", Paderborn, 2014 (**Talk**).

2. C. Wiebeler, F. Plasser, and S. Schumacher. *Non-adiabatic Dynamics of Photochromic Diarylethenes and Conjugated Systems.* Symposium on Theoretical Chemistry, Vienna, 2014 (**Poster**).

3. C. Wiebeler and S. Schumacher. *Non-adiabatic Dynamics of Photochromic Diarylethenes and Conjugated Polymers.* Seminar of the Dreuw Group, IWR, University of Heidelberg 2014 (**Talk**).

4. C. Wiebeler and S. Schumacher. *Non-adiabatic Dynamics of Photochromic Diarylethenes and Conjugated Polymers.* Recent progress in adiabatic and non-adiabatic methods in quantum dynamics, Lausanne, 2014 (**Poster**).

5. C. Wiebeler, R. Tautz, J. Feldmann, E. von Hauff, E. Da Como, and S. Schumacher. *Charge Photogeneration and Spectral Signatures of Polarons in Conjugated Co-polymers.* Charge Transport in Organic Materials, Bremen, 2014 (**Poster**).

6. C. Wiebeler, C. A. Bader, C. Meier, and S. Schumacher. Diarylethenes: Photochromism & Non-adiabatic Dynamics. Meeting of the Graduate Program 1464 "Micro- and Nanostructures in Optoelectronics and Photonics", Paderborn, 2013 (**Talk**).

7. C. Wiebeler and S. Schumacher. *Nonadiabatic Dynamics of the Cycloreversion of Diarylethenes: Normal- vs. Inverse-Type.* Excited States and Complex Environments, Münster, 2013 (**Poster**).

8. C. Wiebeler, C. A. Bader, C. Meier, and S. Schumacher. *Electronic and Optical Properties of Photochromic Diarylethenes.* 15th International Conference on Density Functional Theory and its Applications, Durham, 2013 (**Poster Prize**).

9. C. Wiebeler and S. Schumacher. *Spectral Signatures of Polarons in Conjugated Homo- and Co-polymers.* Meeting of the Graduate Program 1464 "Micro- and Nanostructures in Optoelectronics and Photonics", Paderborn, 2012 (**Poster**).

12 Bibliography & Acknowledgments

> If I have seen further it is by standing on the shoulders of giants.
>
> *(Isaac Newton[134])*

12.1 Bibliography

[1] C. Wiebeler, R. Tautz, J. Feldmann, E. von Hauff, E. Da Como, and S. Schumacher. Spectral Signatures of Polarons in Conjugated Co-polymers. *J. Phys. Chem. B*, 117:4454–4460, 2013.

[2] H. Riesen, C. Wiebeler, and S. Schumacher. Optical Spectroscopy of Graphene Quantum Dots: The Case of C132. *J. Phys. Chem. A*, 118:5189–5195, 2014.

[3] J. Vollbrecht, H. Bock, C. Wiebeler, S. Schumacher, and H. Kitzerow. Polycyclic Aromatic Hydrocarbons Obtained by Lateral Core Extension of Mesogenic Perylenes: Absorption and Optoelectronic Properties. *Chem. Eur. J.*, 20:12026–12031, 2014.

[4] C. Wiebeler, C. A. Bader, C. Meier, and S. Schumacher. Optical spectrum, perceived color, refractive index, and non-adiabatic dynamics of the photochromic diarylethene CMTE. *Phys. Chem. Chem. Phys.*, 16:14531–14538, 2014.

[5] C. Wiebeler and S. Schumacher. Quantum Yields and Reaction Times of Photochromic Diarylethenes: Nonadiabatic Ab Initio Molecular Dynamics for Normal- and Inverse-Type. *J. Phys. Chem. A*, 118:7816–7823, 2014.

[6] R. Tautz, E. Da Como, C. Wiebeler, G. Soavi, I. Dumsch, N. Fröhlich, G. Grancini, S. Allard, U. Scherf, G. Cerullo, S. Schumacher, and J. Feldmann. Charge Photogeneration in Donor-Acceptor Conjugated Materials: Influence of Excess Excitation Energy and Chain Length. *J. Am. Chem. Soc.*, 135:4282–4290, 2013.

[7] A. J. Durán. *Pasiones, piojos, dioses... y matemáticas - La condición humana a la luz de la ciencia más antigua.* Ediciones Destino, 2009.

[8] `www.light2015.org/`. Official Website (June 19, 2015).

[9] `http://www.uni-paderborn.de/nachricht/67842/`. Press Release Universität Paderborn (June 19, 2015).

[10] G. Wittke. *Farbstoffchemie*. Studienbücher Chemie. Diesterweg Sauerländer, 1992.

[11] B. Schrader and P. Rademacher. *Kurzes Lehrbuch der organischen Chemie*. Walter de Gruyter, Berlin, 3. auflage edition, 2009.

[12] M. Born and R. Oppenheimer. Zur Quantentheorie der Molekeln. *Ann. Phys.*, 389(20):457–484, 1927.

[13] A. Szabo and N. S. Ostlund. *Modern Quantum Chemistry - Introduction to Advanced Electronic Structure Theory*. Dover Publications, Mineola, New York, 1996.

[14] M. E. Casida, B. Natarajan, and T. Deutsch. Non-Born-Oppenheimer Dynamics and Conical Intersections. In M. A. L. Marques, N. T. Maitra, F. M. S. Nogueira, E. K. U. Gross, and A. Rubio, editors, *Fundamentals of Time-Dependent Density Functional Theory*, volume 837 of *Lecture Notes in Physics*, chapter 14, pages 279–299. Springer Heidelberg, 2012.

[15] J. Franck. Elementary processes of photochemical reactions. *Trams. Faraday Soc.*, 21:536–542, 1926.

[16] E. Condon. A Theory of Intensity Distribution in Band Systems. *Phys. Rev.*, 28:1182–1201, 1926.

[17] M. Kasha. Characterization of Electronic Transitions in Complex Molecules. *Discuss. Faraday Soc.*, 9:14–19, 1950.

[18] M. Barbatti. Photorelaxation Induced by Water-Chromophore Electron Transfer. *J. Am. Chem. Soc.*, 136(29):10246–10249, 2014.

[19] `http://www.uni-paderborn.de/nachricht/67161/`. Press Release Universität Paderborn (June 19, 2015).

[20] `https://weierstrass-jahr.uni-paderborn.de/`. Official Website (June 19, 2015).

[21] C. Wiebeler. Elektronische Strukturberechnungen für Diarylethene. Master's thesis, Universität Paderborn, 2015.

[22] C. Adamo and D. Jacquemin. The calculations of excited-state properties with Time-Dependent Density Functional Theory. *Chem. Soc. Rev.*, 42:845–856, 2013.

[23] A. D. Laurent and D. Jacquemin. TD-DFT benchmarks: A review. *Int. J. Quant. Chem.*, 113(17):2019–2039, 2013.

[24] A. D. Laurent, C. Adamo, and D. Jacquemin. Dye chemistry with time-dependent density functional theory. *Phys. Chem. Chem. Phys.*, 16(28):14334–14356, 2014.

[25] R. Dennington, T. Keith, and J. Millam. GaussView Version 5.0.9. Semichem Inc. Shawnee Mission KS 2009.

[26] A. J. Heeger. Semiconducting and Metallic Polymers: The Fourth Generation of Polymeric Materials (Nobel Lecture). *Angew. Chem. Int. Ed.*, 40(14):2591–2611, 2001.

[27] A. J. Heeger, N. S. Sariciftci, and E. B. Namdas. *Semiconducting and Metallic Polymers*. Oxford Graduate Texts. Oxford University Press, Oxford, 2010.

[28] M. Geoghegan and G. Hadziioannou. *Polymer Electronics*. Oxford Master Series in Physics. Oxford University Press, Oxford, 2013.

[29] I. D. W. Samuel and G. A. Turnbull. Organic Semiconductor Lasers. *Chem. Rev.*, 107(4):1272–1295, 2007.

[30] J. Clark and G. Lanzani. Organic photonics for communications. *Nat. Photon.*, 4(7):438–446, 2010.

[31] G. Lanzani. Materials for bioelectronics: Organic electronics meets biology. *Nat. Mater.*, 13(8):775–776, 2014.

[32] Richard L. Martin. Natural transition orbitals. *J. Chem. Phys.*, 118(11):4775 – 4777, 2003.

[33] H. Wiebeler. *DFT-Rechnungen zu biomimetischen Kupfer-Komplexen (Cu_A-Modelle)*. Bachelor's thesis, Universität Paderborn, 2013.

[34] N. Banerji, E. Gagnon, P.-Y. Morgantini, S. Valouch, A. R. Mohebbi, J.-H. Seo, M. Leclerc, and A. J. Heeger. Breaking Down the Problem: Optical Transitions, Electronic Structure, and Photoconductivity in Conjugated Polymer PCDTBT and in Its Separate Building Blocks. *J. Phys. Chem. C*, 116(21):11456–11469, 2012.

[35] C. Risko, M. D. McGehee, and J.-L. Brédas. A quantum-chemical perspective into low optical-gap polymers for highly-efficient organic solar cells. *Chem. Sci.*, 2(7):1200–1218, 2011.

[36] A. Dkhissi, F. Ouhib, A. Chaalane, R. C. Hiorns, C. Dagron-Lartigau, P. Iratçabal, J. Desbrieres, and C. Pouchan. Theoretical and experimental study of low band gap polymers for organic solar cells. *Phys. Chem. Chem. Phys.*, 14(16):5613–5619, 2012.

[37] P. Peumans, S. Uchida, and S. R. Forrest. Efficient bulk heterojunction photovoltaic cells using small-molecular-weight organic thin films. *Nature*, 425(6954):158–162, 2003.

[38] P. Peumans, A. Yakimov, and S. R. Forrest. Small molecular weight organic thin-film photodetectors and solar cells. *J. Appl. Phys.*, 93(7):3693–3723, 2003.

[39] T. R. Clarke and J. R. Durrant. Charge Photogeneration in Organic Solar Cells. *Chem. Rev.*, 110(11):6736–6767, 2010.

[40] C. W. Tang. Two-layer organic photovoltaic cell. *Appl. Phys. Lett.*, 48(2):183–185, 1986.

[41] G. Yu, J. Gao, J. C. Hummelen, F. Wudl, and A. J. Heeger. Polymer Photovoltaic Cells: Enhanced Efficiencies via a Networt of Internal Donor-Acceptor Heterojunctions. *Science*, 270(5243):1789–1791, 1995.

[42] B. Kippelen and J.-L. Brédas. Organic Photovoltaics. *Energy Environ. Sci.*, 2(3):251–261, 2009.

[43] S. Few, J. M. Frost, and J. Nelson. Models of charge pair generation in organic solar cells. *Phys. Chem. Chem. Phys.*, 17(4):2311–2325, 2015.

[44] F. Gao and O. Inganäs. Charge generation in polymer-fullerene bulk-heterojunction solar cells. *Phys. Chem. Chem. Phys.*, 16(38):20291–20304, 2014.

[45] G. Grancini, M. Maiuri, D. Fazzi, A. Petrozza, H.-J. Egelhaaf, D. Brida, G. Cerullo, and G. Lanzani. Hot exciton dissociation in polymer solar cells. *Nat. Mater.*, 12(1):29–33, 2013.

[46] A. K. Geim. Nobel Lecture: Random walk to graphene. *Rev. Mod. Phys.*, 8(3):851–862, 2011.

[47] A. K. Geim. Graphene: Status and Prospects. *Science*, 324(5934):1530–1534, 2009.

[48] J. T.-W. Wang, J. M. Ball, E. M. Barea, A. Abate, J. A. Alexander-Webber, J. Huang, M. Sailba, I. Mora-Sero, J. Bisquert, H. J. Snaith, and R. J. Nicholas. Low-Temperature Processed Electron Collection Layers of Graphene/ TiO_2 Nanocomposites in Thin Film Perovskite Solar Cells. *Nano Lett.*, 14(2):724–730, 2014.

[49] P. Atkins and R. Friedman. *Molecular Quantum Mechanics*. Oxford University Press, Oxford, 5th edition, 2011.

[50] N. J. Turro, V. Ramamurthy, and J. C. Scaiano. *Principles of Molecular Photochemistry - An Introduction*. University Science Books, Sausalito, 2009.

[51] J. J. Sakurai. *Modern Quantum Mechanics*. Addison-Wesley Publishing Company, Reading, Massachusetts, revised edition, 1994.

[52] R. Crespo-Otero and M. Barbatti. Spectrum simulation and decomposition with nuclear ensemble: formal derivation and application to benzene, furan and 2-phenylfuran. *Theor. Chem. Acc.*, 131(6), 2012.

[53] M. Barbatti, A. J. A. Aquino, and H. Lischka. The UV absorption of nucleobases: semi-classical ab initio spectra simulations. *Phys. Chem. Chem. Phys.*, 12(19):4959–4967, 2010.

[54] S. Schumacher. Photophysics of graphene quantum dots: Insights from electronic structure calculations. *Phys. Rev. B*, 83(081417), 2011.

[55] M. Karplus. Spinach on the Ceiling: A Theoretical Chemist's Return to Biology. *Ann. Rev. Biophys. Biomol. Struct.*, 35(1):1–47, 2006.

[56] S. R. Forrest. Ultrathin Organic Films Grown by Organic Molecular Beam Deposition and Related Techniques. *Chem. Rev.*, 97(6):1793–1896, 1997.

[57] L. Schmidt-Mende, A. Fechtenkötter, K. Müllen, E. Moons, R. H. Friend, and J. D. MacKenzie. Self-Organized Discotic Liquid Crystals for High-Efficiency Organic Photovoltaics. *Science*, 293(5532):1119–1122, 2001.

[58] V. Barone, J. Bloino, and M. Biczysko. Vibrationally-resolved electronic spectra in GAUSSIAN 09. *http://compchem.sns.it/pdf/vibronic_spectra_G09-A02.pdf*, 2009.

[59] A. D. Becke. Density-functional thermochemistry. III. The role of exact exchange. *J. Chem. Phys.*, 98(7):5648–5652, 1993.

[60] C. Lee, W. Yang, and R. G. Parr. Development of the Colle-Salvetti correlation-energy formula into a functional of the electron density. *Phys. Rev. B*, 37(2):785–789, 1988.

[61] J. P. Perdew, K. Burke, and M. Ernzerhof. Generalized Gradient Approximation Made Simple. *Phys. Rev. Lett.*, 77(18):3865–3868, 1996.

[62] C. Adamo and V. Barone. Toward Reliable Density Functional Methods without Adjustable Parameters: The PBE0 Model. *J. Chem. Phys.*, 110(13):6158–6170, 1999.

[63] T. Yanai, D. P. Tew, and N. C. Handy. A new hybrid exchange-correlation functional using the Coulomb-attenuating method (CAM-B3LYP). *Chem. Phys. Letters*, 393(1-3):51–57, 2004.

[64] B. Champagne, V. Liégeois, and F. Zutterman. Pigment violet 19 - a test case to define a simple method to simulate the vibronic structure of absorption spectra of organic pigments and dyes in solution. *Photochem. Photobiol. Sci.*, 14(2):444–456, 2015.

[65] M. Oltean, A. Calborean, G. Mile, M. Vidrighin, M. Iosin, L. Leopold, D. Maniu, N. Leopold, and V. Chis. Absorption spectra of PTCDI: A combined UV-Vis and TD-DFT study. *Spectrochim. Acta Mol. Biomol. Spectros.*, 97:703–710, 2012.

[66] R. P. Feynman, R. B. Leighton, and M. Sands. *The Feynman Lectures on Physics*, volume 1. Pearson Addison Wesley, the definitive edition, 2006.

[67] M. Irie. Diarylethenes for Memories and Switches. *Chem. Rev.*, 100(5):1685–1716, 2000.

[68] M. Irie. Photochromism of diarylethene molecules and crystals. *Proc. Jpn. Acad., Ser. B*, 86(5):472–483, 2010.

[69] G. H. Brown, editor. *Photochromism*, volume III of *Techniques of Chemistry*. John Wiley & Sons, 1971.

[70] H. Dürr and H. Bouas-Laurent, editors. *Photochromism: Molecules and Systems*. Elsevier, 2003.

[71] M. Irie and M. Mohri. Thermally Irreversible Photochromic Systems. Reversible Photocyclization of Diarylethene Derivatives. *J. Org. Chem.*, 53(4):808–810, 1988.

[72] M. Irie, Y. Yokoyama, and T. Seki, editors. *New Frontiers in Photochromism*. Springer Japan, 2013.

[73] M. Irie, T. Fukaminato, K. Matsuda, and S. Kobatake. Photochromism of Diarylethene Molecules and Crystals: Memories, Switches, and Actuators. *Chem. Rev.*, 114(24):12174–12277, 2014.

[74] A. Spangenberg, J. A. P. Perez, A. Patra, J. Piard, A. Brosseau, R. Métivier, and K. Nakatani. Probing photochromic properties by correlation of UV-visible and infra-red absorption spectroscopy: a case study with cis-1,2-dicyano-1,2-bis(2,4,5-trimethyl-3-thienyl)ethene. *Photochem. Photobiol. Sci.*, 9:188–193, 2010.

[75] A. Spangenberg, R. Métivier, R. Yasukuni, K. Shibata, A. Brosseau, J. Grand, J. Aubard, P. Yu, T. Asahi, and K. Nakatani. Photoswitchable interactions between photochromic organic diarylethene and surface plasmon resonance of gold nanoparticles in hybrid thin films. *Phys. Chem. Chem. Phys.*, 15:9670–9678, 2013.

[76] K. A. Piegdon, M. Lexow, G. Grundmeier, H.-S. Kitzerow, K Pärschke, D. Mergel, D. Reuter, A. D. Wieck, and C. Meier. All-optical Tunability of Microdisk Lasers via Photo-adressable Polyelectrolyte Functionalization. *Opt. Express*, 20(6):6060–6067, 2012.

[77] S. Nakamura, K. Uchida, and M. Hatakeyama. Potential Energy Surfaces and Quantum Yields for Photochromic Diarylethene Reactions. *Molecules*, 18:5091–5103, 2013.

[78] S. Nakamura, T. Kobayashi, A. Takata, K. Uchida, Y. Asano, A. Murakami, A. Goldberg, D. Guillaumont, S. Yokojima, S. Kobatake, and M. Irie. Quantum yields and potential energy surfaces: a theoretical study. *J. Phys. Org. Chem.*, 20:821–829, 2007.

[79] D. Guillaumont, T. Kobayashi, K. Kanda, H. Miyasaka, K. Uchida, S. Kobatake, K. Shibata, S. Nakamura, and M. Irie. An ab Initio MO Study of the photochromic Reaction of Dithienylethenes. *J. Phys. Chem. A*, 106(31):7222–7227, 2002.

[80] Y. Asano, A. Murakami, T. Kobayashi, A. Goldberg, D. Guillaumont, S. Yabushita, M. Irie, and S. Nakamura. Theoretical Study on the Photochromic Cycloreversion Reactions of Dithienylethenes; on the Role of the Conical Intersections. *J. Am. Chem. Soc.*, 126:12112–12120, 2004.

[81] B. G. Levine and T. J. Martínez. Isomerization Through Conical Intersections. *Annu. Rev. Phys. Chem.*, 58:613–634, 2007.

[82] M. Boggio-Pasqua, M. Ravaglia, M. J. Bearpark, M. Garavelli, and M. A. Robb. Can Diarylethene Photochromism Be Explained by a Reaction Path Alone? A CASSCF Study with Model MMVB Dynamics. *J. Phys. Chem. A*, 107:11139–11152, 2003.

[83] J. C. Tully. Molecular Dynamics with Electronic Transitions. *J. Chem. Phys.*, 93(2):1061–1071, 1990.

[84] A. Köhn and C. Hättig. Analytic gradients for excited states in the coupled-cluster model CC2 employing the resolution-of-the-identity approximation. *J. Chem. Phys.*, 119(10):5021–5036, 2003.

[85] E. Tapavicza, A. M. Meyer, and F. Furche. Unravelling the Details of Vitamin D Photosynthesis by Non-adiabatic Molecular Dynamics Simulations. *Phys. Chem. Chem. Phys.*, 13:20986–20998, 2011.

[86] A. Chantzis, J. Cerezo, A. Perrier, F. Santoro, and D. Jacquemin. Optical Properties of Diarylethenes with TD-DFT: 0-0 Energies, Fluorescence, Stokes Shift, and Vibronic Shapes. *J. Chem. Theory Comput.*, 10(9):3944–3957, 2014.

[87] W. Humphrey, A. Dalke, and K. Schulten. VMD: Visual Molecular Dynamics. *J. Mol. Graphics*, 14:33–38, 1996.

[88] H. Poincaré. *Science et méthode*. Flammarion, Paris, 1947.

[89] I. Fleming. *Pericyclic Reactions*. Oxford Chemistry Primers. Oxford University Press, 1998.

[90] J. Clayden, N. Greeves, S. Warren, and P. Wothers. *Organic Chemistry*. Oxford University Press, 2001.

[91] K. P. C. Vollhardt and N. E. Schore. *Organische Chemie*. Wiley-VCH Verlag, Weinheim, 4. auflage edition, 2009.

[92] I. Fleming. *Frontier Orbitals and Organic Chemical Reactions*. John Wiley & Sons, 1976.

[93] R. B. Woodward and R. Hoffmann. The Conservation of Orbital Symmetry. *Angew. Chem. Int. Ed.*, 8(11):781–853, 1969.

[94] M. H. Beck, A. Jäckle, G. A. Worth, and H.-D. Meyer. The Multiconfiguration Time-dependent Hartree (MCTDH) Method: a Highly Efficient Algorithm for Propagating Wavepackets. *Phys. Rep.*, 324:1–105, 2000.

[95] M. Ben-Nun, J. Quenneville, and T. J. Martínez. Ab Initio Multiple Spawning: Photochemistry from First Principles Quantum Molecular Dynamics. *J. Phys. Chem. A*, 104(22):5161–5175, 2000.

[96] X. Li, J. Tully, B. Schlegel, and M. J. Frisch. Ab Initio Ehrenfest dynamics. *J. Chem. Phys.*, 123(084106), 2005.

[97] A. Perrier, S. Aloïse, M. Olivucci, and D. Jacquemin. Inverse versus Normal Dithienylethenes: Computational Investigation of the Photocyclization Reaction. *J. Phys. Chem. Lett.*, 4:2190–2196, 2013.

[98] Y. Ishibashi, M. Mukaida, M. Falkenström, H. Miyasaka, S. Kobatake, and M. Irie. One- and multi-photon cycloreversion reaction dynamics of diarylethene derivative with asymmetrical structure, as revealed by ultrafast laser spectroscopy. *Phys. Chem. Chem. Phys.*, 11:2640–2648, 2009.

[99] B. G. Levine, C. Ko, J. Quenneville, and T. J. Martínez. Conical Intersections and Double Excitations in Time-dependent Density Functional Theory. *Mol. Phys.*, 104(5-7):1039–1051, 2006.

[100] E. Tapavicza, I. Tavernelli, U. Röthlisberger, C. Filippi, and M. E. Casida. Mixed Time-dependent Density-functional Theory/Classical Trajectory Surface Hopping Study of Oxirane Photochemistry. *J. Chem. Phys.*, 129(124108):124108, 2008.

[101] K. Morimitsu, S. Kobatake, and M. Irie. Control of Cycloreversion Quantum Yields of Diarylethenes by Introduction of Substituents at the Reactive Carbons. *Mol. Cryst. Liq. Cryst.*, 431:151–154, 2005.

[102] Y. Ishibashi, T. Umesato, S. Kobatake, M. Irie, and H. Miyasaka. Femtosecond Laser Photolysis Studies on Temperature Dependence of Cyclization and Cycloreversion Reactions of a Photochromic Diarylethene Derivative. *J. Phys. Chem. C*, 116:4862–4869, 2012.

[103] H. Jean-Ruel, R. R. Cooney, M. Gao, C. Lu, M. A. Kochman, C. A. Morrison, and R. J. D. Miller. Femtosecond Dynamics of the Ring Closing Process of Diarylethene: A Case Study of Electrocyclic Reactions in Photochromic Single Crystals. *J. Phys. Chem. A*, 115:13158–13168, 2011.

[104] H. Jean-Ruel, M. Gao, M. A. Kochman, C. Lu, L. C. Liu, R. R. Cooney, C. A. Morrison, and R. J. D. Miller. Ring-Closing Reaction in Diarylethene Captured by Femtosecond Electron Crystallography. *J. Phys. Chem. B*, 117(49):15894–15902, 2013.

[105] J. von Liebig. *Chemische Briefe, zweiter Brief.* C. F. Winter, Leipzig und Heidelberg, 1878.

[106] M. Barbatti, R. Shepard, and H. Lischka. Computational and Methodological Elements for Nonadiabatic Trajectory Dynamics Simulations of Molecules. In W. Domcke, D. R. Yarkony, and H. Köppel, editors, *Conical Intersections. Theory, Computation and Experiment*, volume 17 of *Advanced Series in Physical Chemistry*, chapter 11. World Scientific Publishing, 2011.

[107] H.-D. Meyer and W. H. Miller. A classical analog for electronic degrees of freedom in nonadiabatic collision processes. *J. Chem. Phys.*, 70(7):3214–3223, 1979.

[108] E. Fabiano, Z. Lan, Y. Lu, and W. Thiel. Nonadiabatic Trajectory Calculations with Ab Initio and Semiempirical Methods. In W. Domcke, D. R. Yarkony, and H. Köppel, editors, *Conical Intersections. Theory, Computation and Experiment*, volume 17 of *Advanced Series in Physical Chemistry*, chapter 12. World Scientific Publishing, 2011.

[109] M. Barbatti, M. Ruckenbauer, F. Plasser, J. Pittner, G. Granucci, M. Persico, and H. Lischka. Newton-X: a surface-hopping program for nonadiabatic molecular dynamics. *WIREs: Comp. Mol. Sci.*, 4(1):26–33, 2014.

[110] S. Hammes-Schiffer and J. C. Tully. Proton transfer in solution: Molecular dynamics with quantum transitions. *J. Chem. Phys.*, 101(6):4657–4667, 1994.

[111] J. Pittner, H. Lischka, and M. Barbatti. Optimization of mixed quantum-classical dynamics: Time-derivative coupling terms and selected couplings. *Chem. Phys.*, 356(1-3):147–152, 2009.

[112] B. F. E. Curchod, T. J. Penfold, U. Röthlisberger, and I. Tavernelli. Nonadiabatic ab initio molecular dynamics using linear-response time-dependent density functional theory. *Cent. Eur. J. Phys.*, 11(9):1059–1065, 2013.

[113] M. Barbatti, Z. Lan, R. Crespo-Otero, J. J. Szymczak, H. Lischka, and W. Thiel. Critical appraisal of excited state nonadiabatic dynamics simulations of 9H-adenine. *J. Chem. Phys.*, 137(22):22A503, 2012.

[114] F. Plasser, R. Crespo-Otero, M. Pederzoli, J. Pittner, H. Lischka, and M. Barbatti. Surface Hopping Dynamics with Correlated Single-Reference Methods: 9H-Adenine as a Case Study. *J. Chem. Theory Comput.*, 10(4):1395–1405, 2014.

[115] B. F. E. Curchod, U. Röthlisberger, and I. Tavernelli. Trajectory-Based Nonadiabatic Dynamics with Time-Dependent Density Functional Theory. *ChemPhysChem*, 14(7):1314–1340, 2013.

[116] R. Send and F. Furche. First order nonadiabatic couplings from time-dependent hybrid density functional response theory: Consistent formalism, implementation, and performance. *J. Chem. Phys.*, 132(4):044107, 2010.

[117] F. Furche, R. Ahlrichs, C. Hättig, W. Klopper, M. Sierka, and F. Weigend. Turbomole. *WIREs: Comp. Mol. Sci.*, 4(2):91–100, 2014.

[118] E. Tapavicza, G. D. Bellchambers, J. C. Vincent, and F. Furche. Ab Initio Non-adiabatic Molecular Dynamics. *Phys. Chem. Chem. Phys.*, 15:18336–18348, 2013.

[119] F. Plasser, G. Granucci, J. Pittner, M. Barbatti, M. Persico, and H. Lischka. Surface hopping dynamics using a locally diabatic formalism: Charge transfer in the ethylene dimer cation and excited state dynamics in the 2-pyridone dimer. *J. Chem. Phys.*, 137(22):22A514, 2012.

[120] R. Tautz. *Charge Separation in Organic Photovoltaics: Enhanced Formation of Weakly Bound Polaron Pairs in Donor-Acceptor-Copolymers*. PhD thesis, Ludwig-Maximilians-Universität München, 2013.

[121] J. Schirmer. Beyond the Random-phase Approximation: A new Approximation Scheme for the Polarization Propagator. *Phys. Rev. A*, 26(5):2395–2416, 1982.

[122] A. B. Trofimov and J. Schirmer. An Efficient Polarization Propagator Approach to Valence Electron Excitation Spectra. *J. Phys. B: At., Mol. Opt. Phys.*, 28:2299–2324, 1995.

[123] C. Hättig. Structure Optimizations for Excited States with Correlated Second-Order Methods: CC2 and ADC(2). *Adv. Quantum Chem.*, 50:37–60, 2005.

[124] A. A. J. Aquino, I. Borges, Jr., R. Nieman, A. Köhn, and H. Lischka. Intermolecular Interactions and Charge Transfer Transitions in Aromatic Hydrocarbon-Tetracyanoethylene Complexes. *Phys. Chem. Chem. Phys.*, 16(38):20586–20597, 2014.

[125] G. Granucci and M. Persico. Critical appraisal of the fewest switches algorithm for surface hopping. *J. Chem. Phys.*, 126:134114, 2007.

[126] F. Plasser. Private Communication, 2014.

[127] TURBOMOLE V6.5 2013, a development of University of Karlsruhe and Forschungszentrum Karlsruhe GmbH, 1989-2007, TURBOMOLE GmbH, since 2007, available from
`http://www.turbomole.com`.

[128] P. A. M. Dirac. Quantum Mechanics of Many-Electron Systems. *Proceedings of the Royal Society of London. Series A, Containing Papers of a Mathematical and Physical Character*, 123(792):714–733, 1929.

[129] M. J. Frisch, G. W. Trucks, H. B. Schlegel, G. E. Scuseria, M. A. Robb, J. R. Cheeseman, G. Scalmani, V. Barone, B. Mennucci, G. A. Petersson, H. Nakatsuji, M. Caricato, X. Li, H. P. Hratchian, A. F. Izmaylov, J. Bloino, G. Zheng, J. L. Sonnenberg, M. Hada, M. Ehara, K. Toyota, R. Fukuda, J. Hasegawa, M. Ishida,

T. Nakajima, Y. Honda, O. Kitao, H. Nakai, T. Vreven, J. A. Montgomery, Jr., J. E. Peralta, F. Ogliaro, M. Bearpark, J. J. Heyd, E. Brothers, K. N. Kudin, V. N. Staroverov, R. Kobayashi, J. Normand, K. Raghavachari, A. Rendell, J. C. Burant, S. S. Iyengar, J. Tomasi, M. Cossi, N. Rega, J. M. Millam, M. Klene, J. E. Knox, J. B. Cross, V. Bakken, C. Adamo, J. Jaramillo, R. Gomperts, R. E. Stratmann, O. Yazyev, A. J. Austin, R. Cammi, C. Pomelli, J. W. Ochterski, R. L. Martin, K. Morokuma, V. G. Zakrzewski, G. A. Voth, P. Salvador, J. J. Dannenberg, S. Dapprich, A. D. Daniels, Ö. Farkas, J. B. Foresman, J. V. Ortiz, J. Cioslowski, and D. J. Fox. Gaussian 09 Revision D.01. Gaussian Inc. Wallingford CT 2009.

[130] F. Furche, R. Ahlrichs, C. Hättig, W. Klopper, M. Sierka, and F. Weigend. Turbomole. *WIREs: Comp. Mol. Sci.*, 4(2):91–100, 2014.

[131] C. Van Wüllen. Shared-Memory Parallelization of the TURBOMOLE Programs AOFORCE, ESCF, and EGRAD: How to Quickly Parallelize Legacy Code. *J. Comput. Chem.*, 32(6):1195–1201, 2011.

[132] I. Tavernelli, B. F. E. Curchod, A. Laktionov, and U. Röthlisberger. Non-adiabatic coupling vectors for excited states within time-dependent density functional theory in the Tamm-Dancoff approximation and beyond. *J. Chem. Phys.*, 133:194104, 2010.

[133] I. Kant. Beantwortung der Frage: Was ist Aufklärung. Essay, 1784.

[134] I. Newton. Letter to Robert Hooke dated February 5, 1676.

12.2 Acknowledgments

First and foremost I thank my supervisor **Jun.-Prof. Dr. Stefan Schumacher** for being part in his research group and giving me the opportunity to do research related to quantum chemistry and molecular materials. His continuous support and the regular discussions were essential for my PhD studies. Furthermore, he organized the collaborations with the research groups from experiment.

I thank **Prof. Torsten Meier** not only for investing time and effort in reviewing my PhD thesis, but also for the circumstance that I was allowed to start my research work in his research group and to spend the first years of research in his group.

This thesis is based on articles that came into being due to collaborations with research groups doing the experiments allowing a close connection between experimental applications and theoretical calculations. My thanks go to the research groups of **Prof. Jochen Feldmann**, **Prof. Heinz-Siegfried Kitzerow**, **Prof. Cedrik Meier**, and **Prof. Hans Riesen**. In particular, I thank **Dr. Raphael Tautz**, **Christina Bader**, and **Joachim Vollbrecht** for the discussions regarding the corresponding research projects. These discussions were important for guiding my theoretical investigations in the directions that were of highest interest. I thank **Dr. Felix Plasser** for his assistance regarding the investigation of the ultrafast charge separation in PCPDT-BBT and his information regarding nonadiabatic dynamics.

A crucial part of scientific work is devoted to the presentation and discussion of research results. Therefore, I am grateful to the Zentrum für Sprachlehre that it is offering courses in scientific English. In particular, I thank **Marion Zurborg** and **Mirja Gehring** for their help improving my English.

Research in the field of molecular materials is an interdisciplinary endeavor. As a physicist I am grateful to the department of chemistry that I had the chance to take part in chemistry classes. In particular, thanks go to the lecturers of the classes I attended during my PhD studies: **Prof. Christian Ducho**, **PD Hans Egold**, **Prof. Gregor Fels**, **Prof. Gerald Henkel**, **Prof. Klaus Huber**, **PD Karamali Khanbabaee**, **Prof. C. Schmidt**, and **Prof. René Wilhelm**.

I thank my brother **Hendrik** for the discussions regarding chemistry, the use of NTOs and electron density differences to characterize electronic transitions, and the superposition of molecular structures. Furthermore, I thank him for covering my back during the final days of my thesis writing.

I am grateful for the good working atmosphere in theoretical physics and in particular my thanks go to **Dominik Breddermann**, **Dirk Heinze**, **Rebecca Hölscher**, **Przemyslaw Lewandowski**, **Reinold Podzimski**, and **Dr. Matthias Reichelt** for the joint activities. In addition, I thank Simone Lange for her assistance regarding administration. Furthermore thanks go to my friends and former fellow students, in particular **Martin Babilon** and **Peter Olenburger**, for their support.

Finally, I am grateful to all the persons that looked through my thesis. All comments have been valuable and have contributed to improve this text. Therefore, I thank them again for all their efforts.

Last but not least, I am thanking the institutions that made this research possible: **The Friedrich-Ebert-Stiftung (FES)** not only for the funding of my PhD, but also for the regular conventions that made me think about the presentation of my research for interested laymen, **the German Research Foundation (DFG)** for the Qualifizierungsstipendium and the funding of the GRK 1464, and **the Paderborn Center for Parallel Computing (PC^2)** for computing time and technical support. Without them, my research would have not been possible.